

---

**Spectral Properties  
of  
Quasi One-dimensional Quantum Antiferromagnets  
Perturbative Continuous Unitary Transformations**

---

Inaugural-Dissertation  
zur  
Erlangung des Doktorgrades  
der Mathematisch-Naturwissenschaftlichen Fakultät  
der Universität zu Köln

vorgelegt von  
**Kai Phillip Schmidt**  
aus Neunkirchen

2004

Berichterstatter: Priv.-Doz. Dr. G.S. Uhrig  
Prof. Dr. M. Braden  
Prof. Dr. F. Mila

Vorsitzender der Prüfungskommission: Prof. Dr. A. Freimuth

Tag der mündlichen Prüfung: 5. November 2004

# 1 Abstract

In this work a perturbative realization of particle conserving continuous unitary transformations is applied to study the energies and the spectral properties of quasi one-dimensional quantum anti-ferromagnets. The systems considered are defined on a lattice and they allow for a perturbative decomposition. The unperturbed part is chosen to be a fully dimerized state. The groundstate is a product-state of singlets and the excitation spectrum is equidistant. The related energy quantum is called a triplon because it has total spin one. The continuous unitary transformation leads to an effective triplon-conserving Hamiltonian and effective, experimentally relevant observables.

The effective operators are obtained in a high-order series expansion in the perturbation parameters. All calculations are performed on finite clusters in real space and yield exact results in the thermodynamic limit due to the linked cluster theorem.

The results are exact in the given order. In order to improve the representation of the results extrapolation techniques are used. A detailed description of extrapolation tools like standard Padé and dlogPadé extrapolation, optimized perturbation theory and the use of internal parameters is given.

The dimerized and frustrated spin-chain is analysed first. At zero frustration, a detailed investigation of the spectral weights shows that even in the limit of vanishing dimerization, the one-dimensional Heisenberg model, almost the total spectral weight is situated in the two-triplon sector. So, besides spinons, triplons may be used as elementary excitations for the one-dimensional Heisenberg model. The case of strong frustration is not yet settled.

An extensive review of one- and two-triplon spectral densities at large and intermediate value of the dimerization for various values of the frustration is presented. The findings are compared with field theoretical results. In addition, the Raman response and the infrared absorption are investigated. Second, the antiferromagnetic two-leg Heisenberg ladder plus additional four-spin interaction is investigated. The transformation starts from the limit of isolated rung dimers. The excitations are rung-triplons. The relative energies of one-triplon states, the two-triplon bound states and the multi-triplon continua are given for various couplings. Optical observables are discussed in detail. The extent of the rung-singlet phase is calculated in the whole parameter space. It is shown that the experimental realizations of two-leg ladder systems are always situated in the rung-singlet phase. In the experimentally relevant regime, most of the spectral weight is captured by the one- and the two-triplon sector, but also three- and four-triplon contributions become sizable.

The current understanding of the spectroscopic signatures of magnetic excitations in cuprate ladders measured with inelastic neutron scattering, Raman spectroscopy and infrared absorption is presented. The results obtained are compared with experimental findings. The first experimental evidence of a triplon-triplon bound state in a ladder system is found.



# Contents

<b>1</b>	<b>Abstract</b>	<b>3</b>
<b>2</b>	<b>Introduction</b>	<b>9</b>
2.1	High-temperature superconductors . . . . .	9
2.1.1	Undoped cuprates . . . . .	12
2.1.2	Doped Mott insulators . . . . .	13
2.1.3	Inhomogeneity . . . . .	16
2.2	Continuous unitary transformations . . . . .	18
<b>3</b>	<b>Perturbative CUT</b>	<b>21</b>
3.1	Introduction . . . . .	21
3.1.1	Starting point . . . . .	22
3.1.2	Setup . . . . .	23
3.2	The structure of effective operators . . . . .	24
3.2.1	The effective Hamiltonian . . . . .	24
3.2.2	Effective observables . . . . .	30
3.3	Transformation of the Hamiltonian . . . . .	33
3.4	Transformation of observables . . . . .	35
3.5	Effective lattice . . . . .	38
3.6	Choice of the cluster . . . . .	39
3.6.1	Hamiltonian . . . . .	40
3.6.2	Observables . . . . .	45
3.7	Translational invariance . . . . .	47
3.7.1	Hamiltonian . . . . .	48
3.7.2	Observable . . . . .	52
3.8	Chapter summary . . . . .	54
<b>4</b>	<b>Spectral densities for effective operators</b>	<b>56</b>
4.1	General considerations . . . . .	56
4.1.1	One-particle spectral density . . . . .	57
4.1.2	Two-particle spectral density . . . . .	57
4.1.3	$N$ -particle spectral density . . . . .	58
4.1.4	Limitations . . . . .	58
4.2	Terminators for one-dimensional gapped systems . . . . .	59
4.3	Chapter summary . . . . .	61

<b>5</b>	<b>Extrapolation</b>	<b>64</b>
5.1	Padé-extrapolation	64
5.2	DlogPadé-extrapolation	65
5.2.1	Biased dlogPadé extrapolation	66
5.3	Optimised perturbation theory	67
5.4	Internal parameters	69
5.5	Chapter summary	72
<b>6</b>	<b>Dimerized and frustrated spin-chain</b>	<b>73</b>
6.1	Model	74
6.1.1	Phase diagram and excitations	74
6.1.2	Spectral properties	82
6.2	Method	84
6.2.1	Perturbative CUT	88
6.2.2	Observables	88
6.2.3	Extrapolation	93
6.3	Spectral weights	94
6.3.1	The dimerized chain ( $\alpha = 0$ )	94
6.3.2	Finite frustration	104
6.3.3	Intermediate conclusion	106
6.4	$S=1$ excitations	107
6.4.1	One-triplon contribution	109
6.4.2	Two-triplon contribution	110
6.4.3	Comparison with field theory results	113
6.5	$S=0$ excitations	118
6.5.1	Case $R_{NN,weak}^{S=0}$	118
6.5.2	Case $R_{NNN}^{S=0}$	120
6.5.3	Raman spectroscopy	120
6.5.4	IR-absorption	122
6.6	Chapter summary	130
6.7	Chapter conclusion	132
<b>7</b>	<b>The antiferromagnetic two-leg ladder</b>	<b>134</b>
7.1	Model	134
7.2	Materials	135
7.3	Method	138
7.3.1	Observables for the two-leg ladder	139
7.4	Spectral weights	142
7.4.1	$S = 1$	142
7.4.2	$S = 0$	142
7.5	Energy properties	144
7.5.1	Ground state energy	144

7.5.2	One-triplon dispersion . . . . .	145
7.5.3	Two-triplon continuum and bound states . . . . .	147
7.5.4	Multi-triplon continua . . . . .	148
7.6	$S = 1$ excitations . . . . .	151
7.6.1	One-triplon contribution . . . . .	151
7.6.2	Two-triplon contribution . . . . .	153
7.7	$S = 0$ excitations . . . . .	155
7.8	Chapter summary . . . . .	158
<b>8</b>	<b>The antiferromagnetic two-leg ladder with four-spin interactions</b>	<b>160</b>
8.1	Model . . . . .	160
8.2	Method . . . . .	162
8.3	Rung-singlet phase . . . . .	164
8.4	Spectral weights . . . . .	169
8.4.1	$S=1$ . . . . .	169
8.4.2	$S=0$ . . . . .	171
8.5	Energy properties . . . . .	171
8.5.1	Ground state energy . . . . .	171
8.5.2	One-triplon dispersion . . . . .	172
8.5.3	Two-triplon continuum and bound states . . . . .	174
8.5.4	Multi-triplon continua . . . . .	176
8.6	$S = 1$ excitations . . . . .	177
8.6.1	One-triplon contribution . . . . .	177
8.6.2	Two-triplon contribution . . . . .	178
8.7	$S = 0$ excitations . . . . .	181
8.7.1	Two-triplon contribution . . . . .	181
8.7.2	Raman spectroscopy . . . . .	183
8.7.3	IR-absorption . . . . .	187
8.8	Cuprate Ladders . . . . .	192
8.8.1	Undoped telephone number compound . . . . .	192
8.8.2	Structural modulations . . . . .	195
8.8.3	$\text{SrCu}_2\text{O}_3$ and $\text{Sr}_{14}\text{Cu}_{24}\text{O}_{41}$ . . . . .	200
8.9	Chapter summary . . . . .	201
<b>9</b>	<b>Concluding summary</b>	<b>203</b>
9.1	Methodical aspects . . . . .	203
9.2	Chains . . . . .	204
9.3	Ladders . . . . .	205
9.3.1	Two-leg Heisenberg ladder . . . . .	206
9.3.2	Heisenberg ladder with four-spin interaction . . . . .	207
9.4	Perspectives . . . . .	209

<b>References</b>	<b>211</b>
<b>List of publications</b>	<b>223</b>
<b>Danksagungen</b>	<b>225</b>
<b>Kurze Zusammenfassung</b>	<b>227</b>
<b>Erklärung</b>	<b>229</b>
<b>Lebenslauf</b>	<b>231</b>



## 2 Introduction

### 2.1 High-temperature superconductors

The history of high-temperature superconductivity starts in 1986 when Bednorz and Müller discovered a superconducting transition in  $\text{La}_{2-x}\text{Ba}_x\text{CuO}_4$  [1]. In contrast to conventional superconductors which can be understood by the theory of Bardeen, Cooper and Schrieffer [2] based on phonon mediated pairing and transition temperatures below 30 K, the family of cuprate superconductors display a variety of anomalous properties and rather high transition temperatures up to 133 K [3, 4]. The pairing mechanism and the unconventional normal properties of the cuprate materials are still under intensive debate. This introductory chapter cannot provide a complete discussion of the cuprate problem. It gives a rather general framework and establishes connections between the topics discussed in this thesis and some open questions in the field of high-temperature cuprate superconductors.

A schematic phase diagram of cuprate superconductors is displayed in Fig. 2.1. At low temperatures and zero doping, an antiferromagnetic phase is realized (green area). The antiferromagnet (AF) is destroyed at low hole concentrations ( $x < 0.03$ ). The red area corresponds to the superconducting phase, the so-called superconducting dome (SC). The superconducting phase is realized at zero temperature between  $x \approx 0.05$  and  $x \approx 0.25$ . The carrier concentration with maximal transition temperature is defined as optimal doping. Lower carrier concentration defines the underdoped region and larger doping levels the overdoped regime. The normal state is divided into pseudo-gap (PG), non-Fermi liquid (NFL) and Fermi liquid (FL) regime. For doping levels when antiferromagnetism has disappeared and superconductivity has not been realized, various forms of local or incommensurate magnetism survives. The dynamical properties at intermediate levels are those of a spin glass (SG) [5].

In 1987, Anderson identified some key ingredients for a theory of cuprate superconductors [6]. The most important structural unit is believed to be the two-dimensional copper-oxide planes such that couplings between the planes are weak. This is illustrated in the left panel of Fig. 2.2 for the case of  $\text{La}_{2-x}\text{Sr}_x\text{CuO}_4$ . The undoped parent compound of this family of cuprate superconductors is  $\text{La}_2\text{CuO}_4$ . It contains one hole per site which is located in the  $3d$ -shell. The hole occupies the  $3d_{x^2-y^2}$  orbital and a local magnetic moment with total spin  $S = 1/2$  and  $g$ -factor of about 2. The properties of the undoped cuprates, which mainly result from superexchange interactions via the oxygen  $p$ -orbitals, are discussed in the next section.

Substituting  $\text{La}^{3+}$  by  $\text{Sr}^{2+}$  injects additional holes in the copper-oxide planes which are mainly located at the oxygen-ion. The relevant orbitals of the copper and oxygen ions are illustrated in the right panel of Fig. 2.2. Therefore the cuprates should be described by a three-band Hubbard model [7–9]. However, it is commonly accepted that the essential physics of the cuprates is cap-

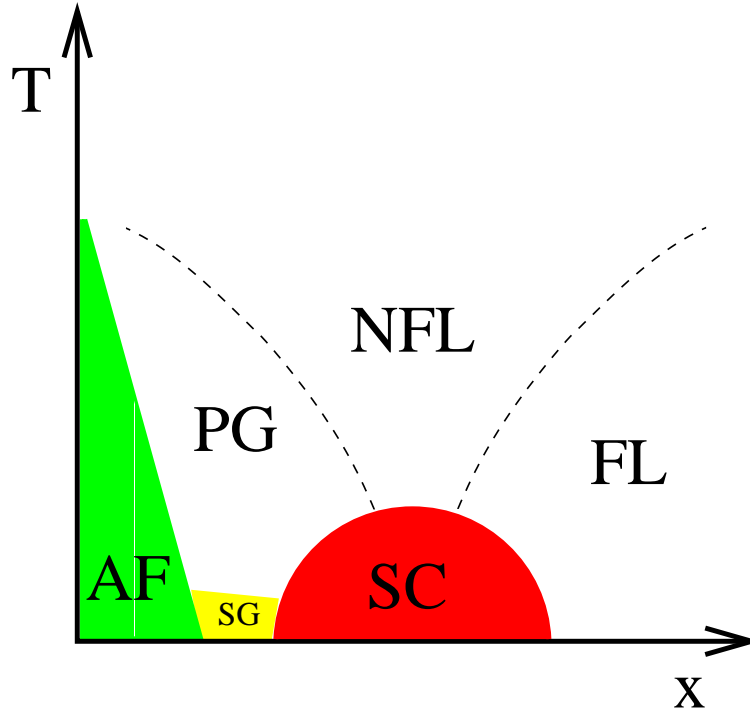


Fig. 2.1: Schematic phase diagram of high-temperature superconductors depending on temperature  $T$  and carrier concentration  $x$ . The green area displays the antiferromagnetic phase and the red area the so-called superconducting dome. The carrier concentration with maximal critical temperature  $T_c$  for the superconducting phase is called optimal doping. Less doping is referred to as the underdoped regime and higher doping as the overdoped regime. The normal state phases are divided into the pseudo-gap regime (PG), the non-Fermi liquid (NFL) phase and a Fermi liquid at high doping levels. The dashed lines stand for crossovers, not for phase transitions.

tured by an effective one-band Hubbard model as suggested early by Anderson [6]. The reason is the existence of the Zhang-Rice singlet band [10] as the first electron removal state. Here the system is considered as a Mott-Hubbard system with the Zhang-Rice singlet band playing the role of the lower Hubbard band and Cu-derived band as the upper Hubbard band.

The one-band Hubbard model contains a single kinetic energy term proportional to the nearest-neighbor hopping amplitude  $t$  and a Hubbard  $U$  originating from the Coulomb interaction. The Hubbard Hamiltonian reads

$$H = -t \sum_{\langle ij \rangle, \sigma} (c_{i\sigma}^\dagger c_{j\sigma} + h.c.) + U \sum_i n_{i\uparrow} n_{i\downarrow}. \quad (2.1.1)$$

Here  $c_{i\sigma}^\dagger$  ( $c_{i\sigma}$ ) creates (annihilates) an electron or hole on site  $i$  with spin  $\sigma$ ,  $\langle ij \rangle$  corresponds to nearest-neighbor pairs, and  $n_{i\sigma} = c_{i\sigma}^\dagger c_{i\sigma}$  is the number operator. In the strong coupling limit ( $U \gg t$ ) the doubly occupied states can be projected out [12]. In this way the one-band and the

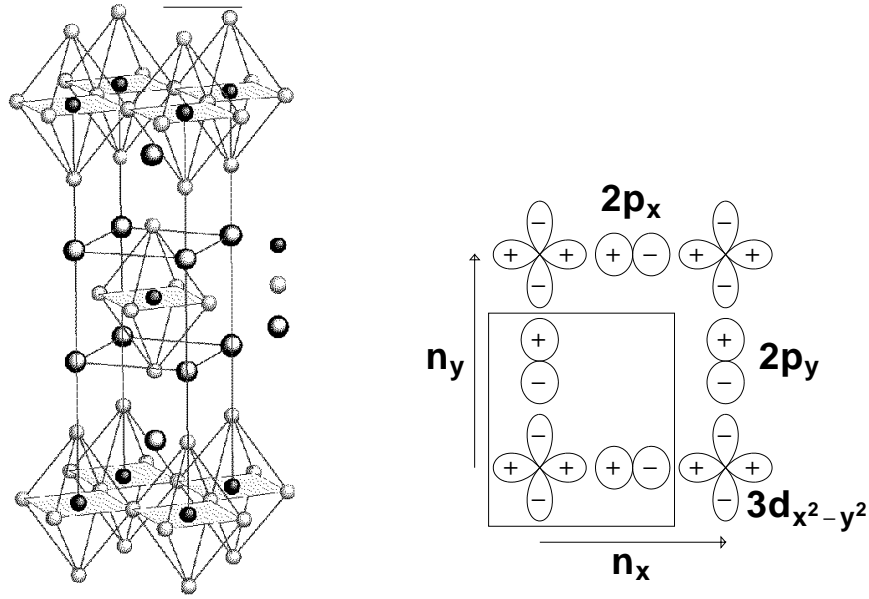


Fig. 2.2: (Left panel) Crystal structure of  $\text{La}_{2-x}\text{Sr}_x\text{CuO}_4$  [11]. Small dark circles denote copper sites, small light circles denote oxygen sites and larger circles correspond to La/Sr. The key structural unit are the  $\text{CuO}_2$  planes. (Right panel) Orbital structure of the copper-oxide planes. The oxygen sites are  $p_\sigma$ -orbitals and the copper sites  $d$ -orbitals.

three-band Hubbard-model simplify in leading order in  $t/U$  to the  $t - J$  Hamiltonian

$$H = -t \sum_{\langle ij \rangle, \sigma} (\tilde{c}_{i\sigma}^\dagger \tilde{c}_{j\sigma} + h.c.) + J \sum_{\langle ij \rangle} (\mathbf{S}_i \cdot \mathbf{S}_j - \frac{n_i n_j}{4}). \quad (2.1.2)$$

The operator  $\tilde{c}_{i\sigma} = c_{i\sigma}(1 - n_{i-\sigma})$  excludes double occupancy and  $J = 4t^2/U$  denotes the antiferromagnetic exchange coupling constant.  $\mathbf{S}_i$  denote  $S = 1/2$  spin operators.

At half-filling ( $x = 0$ , i.e. one electron per Cu site in a  $3d_{x^2-y^2}$  orbital), the  $t - J$  Hamiltonian is equivalent to the two-dimensional Heisenberg model. Here the antiferromagnetic state results from the fact that the electron gain energy by virtual hopping to neighboring sites which is only possible for antiparallel alignment due to Pauli's principle [13]. Away from half-filling, the  $t - J$  model describes a so-called doped antiferromagnet, i.e. a system of interacting spins and mobile holes.

The cuprate superconductors are therefore often considered as doped antiferromagnets [5]. One major complication of the problem is the destruction of the long-range ordered antiferromagnet by doping resulting in a spin-liquid state. It is generically believed that many unusual properties of cuprate superconductors are related to the interplay between holes and magnetic fluctuations of the spin-liquid state. The standard BCS theory [2] is not the appropriate foundation for the physics of cuprate superconductors.

This has led to the development of various different theories for the description of high-temperature superconductors. Among them there are the resonating valence bond (RVB) state and related spin-charge separation pictures [6, 14–26], inhomogeneities like stripes [5, 27–41] or the concept of

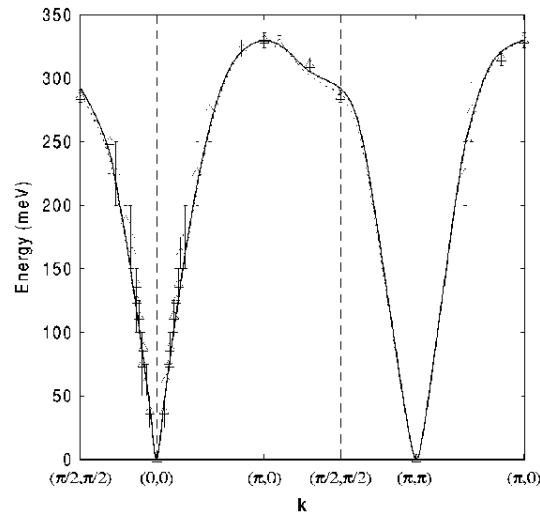


Fig. 2.3: One-magnon dispersion along high-symmetry directions in the 2D Brillouin zone obtained by spin-wave theory in Ref. [67] (solid line). The triangles are the experimental results of Coldea et al. [57] for  $\text{La}_2\text{CuO}_4$  at 10K.

quantum criticality [42–50].

It can be concluded from the discussion of the last paragraphs that the nature of the magnetic fluctuations and their interactions with the hole carriers in the two-dimensional copper-oxide planes is one of the central issues in the field of high-temperature superconductivity. Nevertheless, also the role of phonons in the pairing mechanism of cuprate superconductors is still under discussion [51, 52]. At this point, the focus is laid on the magnetic excitations ignoring phonons and the fermionic degrees of freedom in order to establish three different connections to the physics described in the following chapters:

i) The spectral properties of magnetic excitations in the undoped compounds are discussed. This is related to Chapt. 8 which discusses spectral properties of cuprate ladder systems displaying similar physical properties. ii) The nature of the magnetic excitations in the quantum spin liquid realized for the doped quantum antiferromagnet is described. This is connected to the discussion of fractional and integer excitations of spin-chains in Chapt. 6. iii) The occurrence of inhomogeneity in cuprate superconductors like the formation of one-dimensional stripe-structures is discussed. In this way one-dimensional quantum magnetism is relevant for the physics of cuprate superconductors.

### 2.1.1 Undoped cuprates

The undoped cuprates like  $\text{La}_2\text{CuO}_4$  and  $\text{Sr}_2\text{CuO}_2\text{Cl}_2$  are considered usually as realizations of the two-dimensional spin 1/2 Heisenberg model [53]. Effects like intra-layer coupling, anisotropies in spin-space, Dzyaloshinski-Moriya interactions and spin-orbit coupling are present in these materials but usually of minor importance [54].

The presence of long-range ordered antiferromagnetism below the Néel temperature was estab-

lished by neutron scattering experiments [54]. One observes well-defined dispersing peaks [55, 56] which are identified as magnons which are the elementary excitations of a Néel-ordered state. In recent years a complete magnon dispersion was measured [57]. The antiferromagnetic correlation length diverges exponentially for decreasing temperatures which indicates long-range order at  $T = 0$  [54, 58, 59]. These experimental results agree with the field theoretical analysis of the two-dimensional Heisenberg model in terms of the non-linear  $\sigma$  model [42] and of spin-wave approaches [60]. Summarizing these points, the low-energy magnetic excitations of the undoped cuprates are identified with renormalized magnons [53].

It turned out that the two-dimensional Heisenberg model does not capture the full physics of the low-energy magnetic excitations [57]. The Hamiltonian has to be extended by the so-called ring-exchange term which consists of four-spin interactions. It is the dominant correction to the nearest-neighbor Heisenberg model [61–66]. In this way the complete magnon dispersion can be understood in terms of spin-wave theory [67] (see Fig. 2.3).

In contrast to the obviously well-understood low-energy one-magnon properties, the high-energy spin excitations show several anomalies not captured by the standard spin-wave techniques. This is most clearly seen in optical probes like Raman spectroscopy [69, 70] and infrared absorption [71–73]. Typical results for both experiments are shown in Fig. 2.4. The optical spectra show similar results. There is a low-energy peak usually referred to as a two-magnon peak. The position of this peak is in agreement with spin-wave theory [73, 74]. The width and also the high-energy spectral weight cannot be explained in terms of standard spin-wave theory [73, 74]. In addition, the one-magnon part of the inelastic neutron scattering experiments only accounts for about 50% of the total spectral weight [75–77].

Altogether, one can conclude that quantum fluctuations are strong in these compounds, i.e. on the one hand a more sophisticated spin-wave theory has to be done treating magnon-magnon interactions and multi-magnon contributions properly or on the other hand, a theory not based on the Néel state has to be constructed which implies to introduce new kinds of excitations. The nature of the incoherent high-energy excitations is currently under strong debate [22, 77–79].

In Chapt. 8 these questions are discussed for cuprate ladders. Cuprate ladders show similar spectroscopical properties concerning optical experiments. The two-leg ladder is the archetype model for a resonating valence bond state. It is gapped and has shortrange spin-spin correlations. It is seen that the quantitative treatment of two-particle interactions and multi-particle continua is essential to understand the full physics of the high-energy excitations and their spectral weight.

### 2.1.2 Doped Mott insulators

The problem of doped two-dimensional antiferromagnets with holes has two complementary aspects. On the one hand it is important to understand the effect of the antiferromagnetic correlations on the charge carriers and on the other hand it is crucial to investigate the influence of the holes on the antiferromagnetic state itself. Here only magnetic phases and their excitations are discussed.

Experimentally it can be seen clearly that the antiferromagnet is destroyed by doping resulting in a magnetically paramagnetic state. Having in mind that spin fluctuations may be important for the

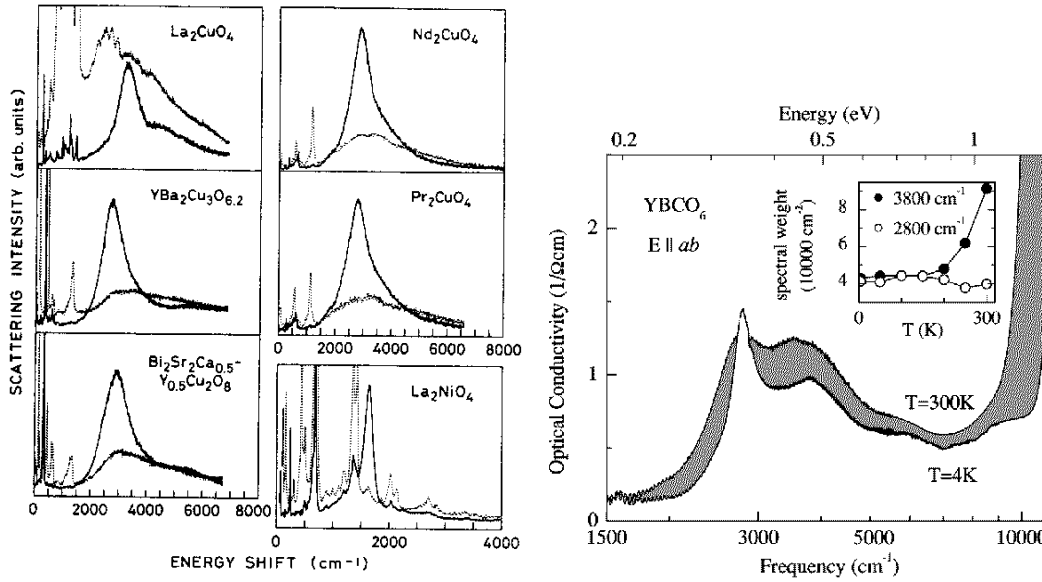


Fig. 2.4: (Left panel) Polarized Raman spectra at 30 K from Ref. [69]. The upper left corresponds to the undoped  $\text{La}_2\text{CuO}_4$ . It displays the typical two-magnon peak with additional spectral weight at high frequencies. (Right panel) Optical conductivity  $\sigma(\omega)$  of  $\text{YBCO}_6$  at 4 and 300 K taken from Ref. [73]. The spectra display a low-energy two-magnon peak plus significant additional spectral weight at higher frequencies.

pairing mechanism of cuprate superconductors, it is therefore decisive to study the nature of the magnetic excitations in the doped regime. As the long-range order is absent, it is expected that the excitations are different in nature compared to magnons reflecting the local correlations of the system [6, 80]. The system has become a spin-liquid.

Therefore doping tunes the long-range ordered Néel ordered state into a quantum disordered paramagnetic state. Some principal issues of this transition can be explained in terms of quantum criticality [80]. The quantum critical point separates the antiferromagnetically ordered phase from a quantum disordered phase. Above the critical point the quantum critical regime is located. The principal setting is illustrated in the left panel of Fig. 2.5. One possible quantum disordered phase is a valence bond solid. In such a state, neighboring states form singlets, resulting in an ordered pattern of valence bonds. This phase breaks translational symmetry and displays a finite spin gap [81]. A second class of quantum paramagnetic states are valence bond liquids which do not break translational symmetry [81]. A sketch of the Néel-ordered state and a valence bond solid is given in the right panel of Fig. 2.5.

The nature of the elementary excitations in the disordered phases and the connection between the different excitations in the different phases is important. Fractional and integer excitations are discussed for the quantum disordered phase [6, 80]. The integer excitation is identified with an elementary triplet excitation (or triplon [82]). It has total spin one and exists with three different

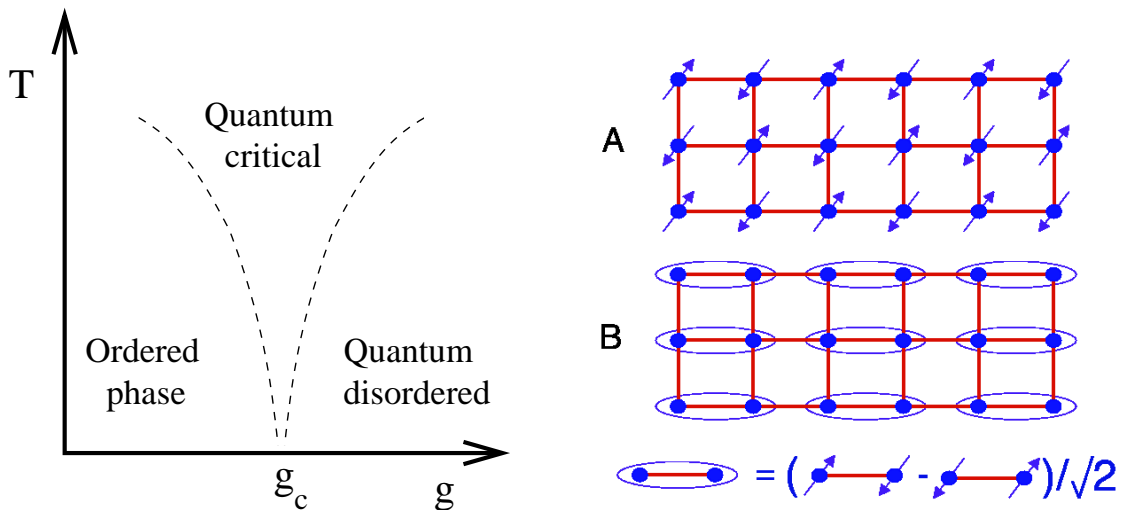


Fig. 2.5: (Left panel) Generic crossover phase diagram near a quantum critical point. The variable  $g$  denotes a tuning parameter, e.g. hole doping, and  $T$  is the temperature of the system. The quantum critical point is denoted by  $g_c$ . There is an ordered phase, a quantum critical regime and a quantum disordered phase. (Right panel) (A) The magnetic Néel ground state on the square lattice. The spins fluctuate quantum-mechanically in the ground state, but they have an ordered nonzero magnetic moment, which is oriented along the direction shown. (B) A valence bond solid quantum paramagnet. The spins are paired in singlet valence bonds, which resonate among the different ways the spins can be paired. The valence bonds crystalize so that the pattern of bonds shown has a larger weight in the ground state wavefunction than its symmetry-related partners. The right figure is taken from Ref. [81].

flavours. In terms of the valence bond solid it can be visualized as the excitation of a local singlet to a local triplet plus a polarization cloud. In the triplon language the ordered state corresponds to a condensation of two triplon flavours. This condensate represents the magnon excitations of the ordered phase. A possible fractional nature of the elementary excitations of the quantum disordered phase is also under strong debate [6, 22]. Here the decay of the electron into a spinon and holon pair is assumed. The spinon carries the spin  $1/2$  and it can be excited only in pairs. Recently, a new kind of deconfined quantum critical point is discussed for the order-to-disorder transition in two-dimensional cuprate systems [81]. It is argued that the triplon in the quantum disordered phase fractionalizes at the quantum critical point which results in new properties of the quantum critical regime.

The necessity to introduce fractional excitations in the description of cuprate superconductors is an open issue. In Chapt. 6 one-dimensional spin-chains are analysed with respect to these questions. One-dimensional quantum antiferromagnets are commonly known to have fractional spinon excitations [83]. Therefore they are important systems to study the relationship between the spinon and the triplon picture. Interestingly, it is found that both excitations can be viewed as elementary excitations of these systems [82].

### 2.1.3 Inhomogeneity

Next the aspect of inhomogeneity in cuprates is briefly discussed. Here the term “inhomogeneity” is equivalent to a static or dynamic order in a sense that hole-rich and hole-poor regions are formed in the considered system. A static order corresponds to an ordered phase like the longranged ordered Néel state and a dynamic order corresponds to a quantum disordered phase in the proximity of a quantum critical point such that strong dynamic fluctuations are present. At the moment mostly quasi one-dimensional inhomogeneity is discussed, the so-called stripe phase [5, 32, 84–88]. But also two-dimensional checkerboard inhomogeneity is discussed [27, 89] which is seen in recent surface-sensitive scanning tunneling microscopy investigations [90]. In this introduction, the focus is laid on stripe structures.

The best way to detect such stripe-ordered or fluctuating stripes is to measuring the appropriate magnetic dynamical structure factor. Indeed, x-ray and neutron scattering studies have provided the best evidence of ordered and fluctuating stripe phases [32, 88, 91, 92]. The existence of stripe order manifests itself in superstructure satellites around  $\mathbf{Q}_{AF}$  [5, 93] which is the antiferromagnetic wave vector. Precursors of incommensurate Bragg peaks are dispersion minima at incommensurate positions in the Brillouin zone. These low-energy incommensurate peaks are measured in  $\text{La}_{1.6-x}\text{Nd}_{0.4}\text{Sr}_x\text{CuO}_4$  [94–96],  $\text{La}_{2-x}\text{Ba}_x\text{CuO}_4$  [97],  $\text{La}_{2-x}\text{Sr}_x\text{CuO}_4$  [96, 98–102],  $\text{La}_2\text{CuO}_{2+\delta}$  [109] and recently in  $\text{YBa}_2\text{Cu}_3\text{O}_{6+\delta}$  [110–115]. Therefore the low-energy incommensurate peaks are a universal feature of cuprate superconductors<sup>1</sup>.

A second feature strongly discussed in the field of cuprate superconductors is the so-called resonance peak which appears in the superconducting phase at the antiferromagnetic wave vector  $\mathbf{Q}_{AF}$  at finite energies (e.g. 41 meV in optimally doped  $\text{YBa}_2\text{Cu}_3\text{O}_{7-\delta}$ ) [117–124]. An  $S=1$  collective mode identified with the resonance peak in the superconducting phase is a prominent feature of many different theoretical scenarios. Its interpretation ranges from a particle-hole bound state (see Refs. in [124, 125]) to a particle-particle bound state in  $\text{SO}(5)$  theory [40, 126–128].

The last two points are the most striking features of the magnetic excitation spectrum in the superconducting phase located at low energies. Very recently an experimental progress has been made in preparing large single crystals [115, 129] which implies the possibility of investigating the magnetic excitation spectrum also at energies above and below the resonance mode. The experimental result is shown in Fig. 2.6 for the stripe-ordered compound  $\text{La}_{1.875}\text{Ba}_{0.125}\text{CuO}_4$  [129] and for underdoped superconducting  $\text{YBa}_2\text{Cu}_3\text{O}_{6.6}$  [115].

Interestingly, the magnetic excitation spectra of the stripe-ordered compound and the superconducting compound look very similar. Three generic features can be extracted: i) at low energies there are four incommensurate satellites around the antiferromagnetic wave vector, ii) the satellites merge at intermediate energies into the resonance mode located at  $\mathbf{Q}_{AF}$  and iii) the excitation spectra above the resonance mode is rotated by  $45^\circ$  compared to the square formed by the low-energy satellite peaks. These experimental findings suggest a common physical origin of the observed structures.

The choice of the microscopic model is straightforward for the stripe-ordered phase. Indeed, an

<sup>1</sup>Note that there are also explanations of the incommensurability observed by neutron scattering experiments based on Fermi surface nesting [103–108].



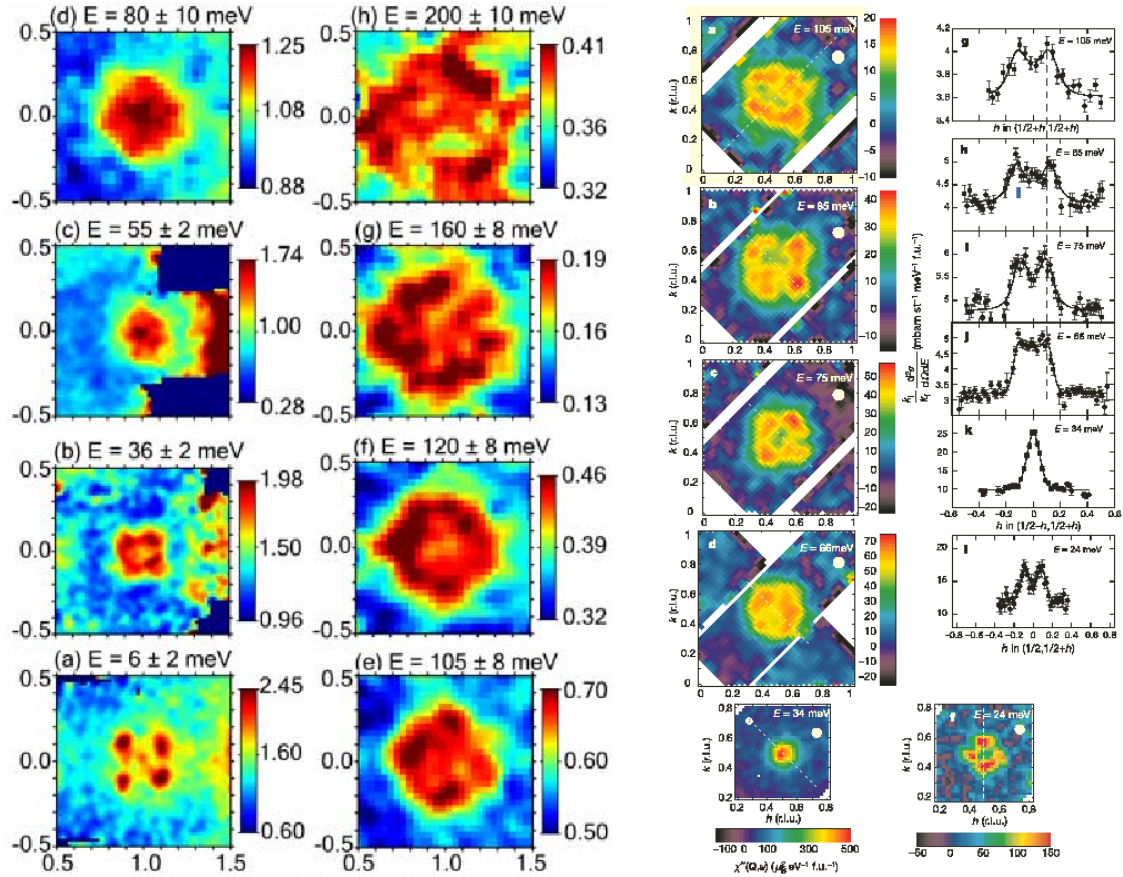


Fig. 2.6: (Left panel) Constant-energy slices through the experimentally measured magnetic structure factor from stripe-ordered  $\text{La}_{1.875}\text{Ba}_{0.125}\text{CuO}_4$  taken from Ref. [129]. The intensity is measured at  $T = 12\text{K}$  ( $> T_c$ ) within a single antiferromagnetic zone (magnetic Brillouin zone is rotated by  $45^\circ$ ). The data show incommensurate peaks at low energies forming a square, a resonance peak at  $44\text{ meV}$  and a diamond shape structure at higher energies. (Right panel) Images of the spherical magnetic scattering in underdoped  $\text{YBa}_2\text{Cu}_3\text{O}_{6.6}$  at  $T = 10\text{K}$  from Ref. [115]. Note that this data is not rotated by  $45^\circ$ . Analogous structures to the stripe-ordered compounds are found: incommensurate peaks at low energy, a resonance peak at  $34\text{ meV}$  and a  $45^\circ$ -rotated (compared to the low-energy peaks) intensity pattern at high energies.

effective magnetic model consisting of coupled two-leg ladders is able to capture all observed experimental structures on a quantitative level [130, 131]. Qualitatively similar results were also obtained by a coupled dimer calculation [132], a spin wave approach [116, 133] and a recent study using time-dependent Gutzwiller approximation for the one-band Hubbard model [134].

The stunning similarities between the magnetic excitations of a stripe-ordered and a superconducting cuprate compound on the one hand and the quantitative description of these data based on coupled one-dimensional spin systems on the other hand, establish the importance of one-dimensional quantum magnetism in cuprate superconductors. In this thesis dynamical correlations for one-dimensional spin systems are calculated which can serve as a starting point for the descrip-

tion of anisotropic two-dimensional systems.

## 2.2 Continuous unitary transformations

Here a brief general discussion of the method chosen in this thesis is given before entering the detailed investigations in the next chapters. In this work the method of continuous unitary transformation is used which was independently proposed by Wegner [135] and Głazek and Wilson [136, 137] in 1994. Ref. [138] is referred to as an introductory paper and Ref. [139] as a recent review about the method.

The main idea of the method is to find an optimal description of the considered quantum many-body system by choosing an appropriate basis. Changing the basis is equivalent to a unitary transformation. Famous examples of unitary transformations are the bosonic Bogoliubov transformation or the fermionic transformation leading to the BCS wave function. These two transformations work in the case of bilinear Hamiltonians. They are often used in mean-field treatments. The method of continuous unitary transformations extends this concept beyond bilinear Hamiltonians.

The unitary transformation is performed in a continuous fashion, i.e. a continuous parameter  $l$  is introduced such that  $l = 0$  refers to the initially given system and  $l = \infty$  corresponds to the finally effective system which corresponds to an easier physical picture. The transformation can be set up such that processes at larger energy are treated before those at lower energies. This renormalizing property is similar to Wilson's renormalization group approach [140].

Let  $U$  be the unitary transformation which diagonalizes the Hamiltonian  $H$  and  $H(l) = U^\dagger(l)HU(l)$ . Then this unitary transformation is equivalent to performing an infinite sequence of unitary transforms  $e^{-\eta(l)dl}$  with the antihermitian generator

$$\eta(l) = -U^\dagger(l)\partial_l U(l) \quad . \quad (2.2.1)$$

This results in the so-called flow equation

$$\partial_l H(l) = [\eta(l), H(l)] \quad (2.2.2)$$

which defines the change of the Hamiltonian during the flow. Clearly, the choice of the antihermitian generator is the crucial point of the method. At the moment, mainly two different generators are in use. First, the originally generator proposed by Wegner [135] reads

$$\eta^W(l) = [H_d(l), H_{nd}(l)] = [H_d(l), H(l)] \quad (2.2.3)$$

where  $H_d$  denotes the diagonal part and  $H_{nd}$  the non-diagonal part of the Hamiltonian. Second, a quasi-particle conserving generator is in use [141–145]. Let  $Q$  be the operator counting the number of elementary excitations and choose the matrix elements of  $\eta^{\text{MKU}}$  as

$$\eta_{i,j}^{\text{MKU}} = \text{sgn}(q_i(l) - q_j(l)) H_{i,j}(l) \quad (2.2.4)$$

in the eigenbasis of  $Q$ , then the final Hamiltonian satisfies  $[Q, H(\infty)] = 0$ , i.e. the number of elementary excitations is a conserved quantity after the transformation. In addition, it is found

that the latter generator sorts the eigenvalues in ascending order of the particle number of the corresponding eigen vectors [141, 143]. This can be proven for finite-dimensional Hilbert spaces. The commutator  $[\eta(I), H(I)]$  produces generically for both generators  $\eta^W$  and  $\eta^{MKU}$  new terms not contained in the original Hamiltonian. In this way a proliferating number of new terms are generated so that the flow equations are an infinitesimal set of coupled differential equations. For most practical purposes, one has to truncate at some point. One obtains a closed set of equations which can be solved in order to receive the effective system. Therefore the truncation is essential to capture the relevant physics in the effective system.

The method has been applied to various systems mostly in condensed matter physics. The resulting flow equations are solved in an analytical way (usually in some perturbative treatment in first order) or numerically. Among these systems studied there are impurity models [146–154], dissipative systems [155, 156], electron-phonon coupling [157–159], two-dimensional Hubbard model [160–164], one-dimensional fermionic [165, 166] and bosonic systems [167, 168]. Truncation schemes vary from perturbative arguments, Hartee-Fock decoupling, locality to consideration on the structure of operators. These applications correspond to a renormalized realization of the continuous unitary transformations.

In addition, the continuous unitary transformations can be also realized perturbatively to high orders in the perturbation parameters. This can be either done for Wegner's [144, 169, 170] or the particle conserving generator [143, 171, 172]. Here the Hamiltonian  $H$  and the antihermitian generator  $\eta$  are expanded in a series to some order such that the resulting coupled equations can be solved. In contrast to the renormalizing continuous unitary transformation, the choice of the truncation scheme is straightforward. All terms in a given order are taken into account so that no truncation error is made in the obtained perturbative order.

In this work the perturbative realization of particle conserving continuous unitary transformation is applied to low-dimensional quantum antiferromagnets. It is shown that the perturbative realization of the continuous unitary transformation is an efficient tool to calculate the energy and the spectral properties of gapped spin liquids. The perturbative treatment is performed about a totally dimerized state. Then the ground state is the product-state of singlets on the dimers and the excitations are local triplets. Assuming that the ground state and the elementary excitations of the non-interacting system are continuously connected to the ground state and the excitations of the full system, the elementary excitations of the interacting system are elementary triplets or *triplons* [82]. Triplons can be visualized as local triplets plus a magnetic polarization cloud. The resulting effective Hamiltonian after the continuous unitary transformation is blockdiagonal in the number of triplons, i.e. the number of triplons is a conserved quantity.

The property of triplon conservation gives a rather intuitive picture of the physics of the system. The ground state is the triplon vacuum and the excitations of the system are the triplons. The blockdiagonality of the effective Hamiltonian also implies that the ground state energy can be computed by the zero-triplon block, the one-triplon dispersion by the one-triplon block, and the  $n$ -triplon energies by the  $n$ -triplon block. In this sense the complex many-body problem has reduced to a few-body problem.

In analogy to the Hamiltonian, the *same* continuous unitary transformation has to be applied to

the observables in order to study the spectral properties of the system. The effective observables do not conserve the number of triplons but they can be classified by the number of excitations they inject or annihilate in the system. This property enables the independent computation of the  $n$ -triplon contribution to the spectral weight and to the spectral density.

The reduction of the system to a few-body problem is true if the chosen quasi-particle picture is appropriate for the system under study, i.e. if only a few number of excitations are sufficient to capture the physics of the system. The quality of the quasi-particle picture can be investigated by analyzing the  $n$ -triplon spectral weights. If most of the spectral weight is in the channels with a small triplon number, one would call the quasi-particle picture appropriate. If the spectral weight is distributed equally over a large number of triplon channels, one would call the quasi-particle inappropriate.

The effective Hamiltonian describes the system finally by *interacting* quasi-particles, i.e. the  $n$ -triplon block comprises triplon-triplon interactions<sup>2</sup>. In this thesis the zero-, one- and two-triplon properties are studied. Therefore also the two-triplon interaction has to be treated.

The quasi-particles introduced by the particle conserving continuous unitary transformations can be viewed as an extension of the idea of Landau's Fermi liquid-like quasi-particles [173, 174]. Here the low-energy properties of many-body systems are described by effectively *non-interacting* particles such that the bare interactions present in the original system renormalize the one-particle properties. The quasi-particles obtained in this thesis do *interact*. But the resulting interacting problem can be solved because only a small number of quasi-particles are necessary to describe the physics of the considered systems. In this way it should be possible to describe the physics of a large class of many-body systems.

In the next chapter the perturbative particle conserving continuous unitary transformation is described in detail. Chapt. 4 deals with the calculation of spectral densities for the effective operators. Chapt. 5 give an overview about possible extrapolation technique. Chapt. 6, Chapt. 7 and Chapt. 8 applies the method to spin-chain and two-leg ladder systems. Chapt. 9 summarizes the findings of this work and gives a brief outlook.

---

<sup>2</sup>Note that not only two-triplon interactions are present. In general, the  $n$ -triplon block contains all possible multi-triplon interactions of  $n$  triplons.

## 3 Perturbative CUT

For many-particle systems defined on lattices the global structure of effective Hamiltonians and observables obtained by means of a suitable basis transformation are investigated. Transformations are studied which lead to effective Hamiltonians conserving the number of excitations. The *same* transformations must be used to obtain effective observables. The analysis of the structure shows that effective operators give rise to a simple and intuitive perspective on the initial problem. The systematic calculation of  $n$ -particle irreducible quantities becomes possible constituting a significant progress. Details how to implement the approach perturbatively for a large class of systems are presented.

### 3.1 Introduction

Effective models are at the very center of theoretical physics since they allow to focus on the essential physics of a problem without being distracted by unnecessary complexity. Hence it is very important to dispose of *systematic* means to derive effective models. In this chapter the mathematical structure of a certain kind of effective models is presented, namely effective models where the elementary excitations above the ground state can be viewed as particles above a complex vacuum. This type of view is very common in low-temperature physics. Many experiments can be understood on the basis of this picture.

In this chapter, the global structure of the Hamiltonian and of the observables will be elucidated if the model is transformed to a model which *conserves* the number of particles. Such a mapping is often possible and renders the subsequent calculation of physical quantities much easier. The determination of the effective Hamiltonian is facilitated by the decomposition into  $n$ -particle irreducible parts. A classification is set up for *strong-coupling* situations at zero temperature, i.e. no weak-coupling limit is needed and no non-interacting fermions or bosons are required. Generically, this thesis deals with hard-core bosons relevant for quantum spin systems.

The necessity for the decomposition into  $n$ -particle irreducible parts has arisen in perturbative calculations of the effective Hamiltonians because only the  $n$ -particle irreducible interactions are independent of the system size. The second main point of this chapter is the perturbative computation of effective Hamiltonians and observables. Such computations are a standard technique for ground state energies (0-particle terms) and dispersion relations (1-particle terms), see Ref. [175] and references therein. But the possibility to compute multi-particle contributions has only recently been realized [142, 176, 177] and continues to be exploited intensively. The key ingredient is to define a similarity transformation on the operator level (see below).

A promising alternative route, which will be only sketched in this article, consists in the non-perturbative, renormalizing realization of the transformation of the initial model to the effective

model which conserved the number of particles. Examples of this approach are realized already in fermionic models [165, 166, 178].

### 3.1.1 Starting point

The Models considered are defined on a lattice  $\Gamma$ . At each site of the lattice the system can be in a number  $d$  of states spanning the local Hilbert space. Let us assume that  $d$  is finite. The dynamics of the system is governed by a Hamiltonian  $H$  acting in the tensor-product space of the local Hilbert spaces. For simplicity one does not consider antisymmetric, fermionic situations although this is also possible. The focus is on physical systems which can be described in terms of hard-core bosons.

The Hamiltonian  $H$  is assumed to be of finite range. This means that it is composed of *local* operators  $h_\nu$  acting on a *finite* number of sites in the vicinity of the site  $\nu$ .

$$H = \sum_{\nu \in \Gamma} h_\nu . \quad (3.1.1)$$

One further assumes, that  $H$  can be split as

$$H(x) = H_0 + xV , \quad (3.1.2)$$

so that the spectrum of  $H_0$  is simple (see below) and that the system does not undergo a phase transition from  $x = 0$  to the range of values of final interest. These requirements do not necessarily imply that  $x$  has to be small. But it is helpful if this is the case.

The ground state of  $H_0$  and its eigen states and eigen energies shall be known. The latter will be viewed as elementary excitations from which the whole spectrum can be built. It is assumed that the elementary excitations above the ground state can be viewed as (quasi-)particles above the vacuum. For simplicity, the prefix 'quasi-' will be dropped. Henceforth, it is understood that 'particle' is a synonym for elementary excitation.

It is assumed that the physical picture sketched for  $H(x = 0) = H_0$  is linked *continuously* to the range  $0 \leq x \leq x_c$  where  $x_c$  is the critical value at which a phase transition occurs. At the critical value  $x_c$  the picture breaks down and cannot be used beyond  $x = x_c$ . Generically, a mode of  $H(x)$  will become soft at  $x_c$ .

Furthermore, the particles for  $x = 0$  shall be local in the sense that a site can be assigned to each of them. Let  $Q$  be the operator that counts the number of particles.

As a concrete example, the reader may think of an antiferromagnetic Heisenberg model made up from strongly coupled (coupling  $J$ ) pairs of spins ('dimers') which are weakly coupled (coupling  $xJ$ ) among themselves, e.g. [143, 176]. At  $x = 0$ , the ground state is the product state with singlets on all dimers; the elementary excitations are local triplets. The number of these local triplets, i.e. the number of dimers which are not in the singlet state, shall be given by the operator  $Q$ .

A considerable simplification of the problem can be achieved by mapping the initial problem  $H(x)$  to an effective Hamiltonian  $H_{\text{eff}}(x)$  in which the number of elementary excitations does not change. That is the number of particles should be a conserved quantity. Then the computation of many physical quantities is significantly simplified.

In this thesis, the use of a continuous unitary transformation (CUT) [135, 141, 143, 144] is advocated in order to achieve a systematically controlled mapping of the kind described above which leads to

$$[H_{\text{eff}}, Q] = 0, \quad (3.1.3)$$

i.e.  $H_{\text{eff}}$  conserves the number of particles. Such an approach has three major advantages:

1. Conceptual clarity

Using a unitary transformation guarantees that no information of the original model is lost. In particular, it is clear that the *same* transformation [135, 155, 179, 180] can be applied to obtain the effective observables  $\mathcal{O}_{\text{eff}}$  from the original observables  $\mathcal{O}$ .

2. Technical simplicity

To implement the unitary transformation in a continuous fashion only the computation of commutators is required since the mapping is split into infinitesimal steps leading to a differential equation [135]

$$\partial_\ell H = [\eta(\ell), H(\ell)] \quad (3.1.4)$$

where  $\ell \in [0, \infty]$  is an auxiliary parameter parametrizing the continuous transformation with starting point  $\ell = 0$  and end point  $\ell = \infty$ .

3. Good controllability

By an appropriate choice of the infinitesimal generator  $\eta$  of the transformation it can be designed such that it preserves block-band diagonality [141, 143]. Moreover, it is renormalizing in the sense that matrix elements between energetically very different states are transformed more rapidly than those between energetically adjacent states [141, 165, 166].

Note, that the general structure of operators does not depend on the details of the method by which the effective particle-conserving model is obtained. Also other methods than CUTs are conceivable, e.g. orthogonal transformation are used [177, 181, 184].

In the present treatment the focus is laid on perturbative realizations of the CUTs. This approach [143] was the first which realized the computation of bound states in higher orders [142, 176]. The concept of a similarity transformation is indispensable for a conceptually clear computation of multi-particle effects [177, 181].

### 3.1.2 Setup

In Sect. 3.2 the global structural aspects of effective operators are analysed. The basic prerequisite will be Eq. 3.1.3. Furthermore, it is shown that the linked cluster property holds. Therefore the effective operators which hold in the thermodynamic limit can be computed in finite systems.

Sect. 3.3 is a preparatory section in which the perturbative CUT for Hamilton operators of a certain kind is constructed. Gapped low-dimensional spin models on lattices are among the models which can be treated in this way.

Sect. 3.4 contains a detailed description of how the perturbative CUT can be extended to transform general observables. Series expansions in  $x$  for the effective observables are obtained

which allow to compute the experimentally relevant spectral functions. So the extension from Hamiltonians to observables is an important one.

This chapter is summarized in Sect. 3.8.

## 3.2 The structure of effective operators

In this section, it is *assumed* that one is able to construct a mapping such that  $H_{\text{eff}}$  fulfills Eq. 3.1.3. The eigen-states of the particle number operator  $Q$  serve as a basis for the Hilbert space of the system. If the mapping is realized perturbatively, the matrix elements of  $H_{\text{eff}}$  and  $\mathcal{O}_{\text{eff}}$  are polynomials in  $x$ .

### 3.2.1 The effective Hamiltonian

#### 3.2.1.1 Global structure

It is shown that  $H_{\text{eff}}$  can be written as

$$H_{\text{eff}} = H_0 + H_1 + H_2 + H_3 + \dots, \quad (3.2.1)$$

where  $H_n$  is an  $n$ -particle irreducible operator, i.e.  $H_n$  measures  $n$ -particle energies. Moreover, each thermodynamic matrix element of any of the components  $H_n$  can be obtained on finite clusters for a given order in  $x$  if the original Hamiltonian is of finite range. The components  $H_n$  can be defined recursively in ascending order in  $n$ .

Eq. 3.2.1 comprises already a route to determine the properties of  $H_{\text{eff}}$  in a sequence of approximate treatments. The very first step is to know the ground state energy which defines  $H_0$ . The second level is to describe the dynamics of a single particle (elementary excitations) correctly which is possible by knowing  $H_1$ . The third level is reached if  $H_2$  is included which contains the information on the interaction of two particles. True three-particle interactions are contained in  $H_3$  and so on. From the generic experience in condensed matter theory, the three- and more particle terms can very often be neglected. So the first three terms in Eq. 3.2.1 provide the systematically controlled starting point of a broad class of problems.

First some notation is clarified. The following eigen-states of the particle number operator  $Q$  are defined as

$$\begin{aligned} |0\rangle & \quad \text{ground state (particle vacuum)} \\ |i\rangle & \quad \text{state with 1 particle on site } i \\ |i_1 i_2\rangle & \quad \text{state with 2 particles on sites } i_1 \text{ and } i_2 \\ & \quad \vdots \end{aligned}, \quad (3.2.2)$$

i.e.  $Q|0\rangle = 0|0\rangle$ ,  $Q|i\rangle = 1|i\rangle$  and  $Q|ij\rangle = 2|ij\rangle$  and so on. These states span the global Hilbert space  $\mathcal{E}$  of the physical system under study. Dealing with (hard-core) bosons  $|i_1 i_2\rangle$  and  $|i_2 i_1\rangle$  are identical states. This indistinguishability causes a certain ambiguity. This ambiguity can be remedied for instance by assuming that coefficients depending on several indices  $i_1 i_2 \dots i_n$  are even



under permutation of any pair of these indices<sup>1</sup>. For simplicity, the ground state  $|0\rangle$  is assumed to be unique.

Let  $\mathcal{R}$  be an arbitrary operator acting on  $\mathcal{E}$  and conserving the number of particles  $[\mathcal{R}, Q] = 0$ . By  $\mathcal{R}|_n$  one denotes the restricted operator acting on  $\mathcal{E}_n \subset \mathcal{E}$  spanned by all states with exactly  $n$  particles.

Now the operators  $H_n$  are defined

$$H_0 := E_0 \mathbf{1} \quad (3.2.3a)$$

$$H_1 := \sum_{i,j} t_{j,i} e_j^\dagger e_i \quad (3.2.3b)$$

$$H_2 := \sum_{i_1 i_2; j_1 j_2} t_{j_1 j_2; i_1 i_2} e_{j_1}^\dagger e_{j_2}^\dagger e_{i_2} e_{i_1} \quad (3.2.3c)$$

$\vdots$

$$H_n := \sum_{i_1 \dots i_n; j_1 \dots j_n} t_{j_1 \dots j_n; i_1 \dots i_n} e_{j_1}^\dagger \dots e_{j_n}^\dagger e_{i_n} \dots e_{i_1}. \quad (3.2.3d)$$

where  $\mathbf{1}$  is the identity operator. Note that these operators are defined on the full Hilbert space  $\mathcal{E}$ . The operators  $e_i^{(\dagger)}$  are *local* operators that annihilate (create) particles at site  $i$ . They are bosonic operators. Their definition can be tailored to include a hard-core repulsion between the particles to account for the common situation that at maximum one of the particles may be present at given site  $i$ . If the particles have additional internal quantum numbers, i.e. if there can be different particles at each site, the indices  $i$  and  $j$  are substituted by multi-indices  $\mathbf{i}$  and  $\mathbf{j}$ . Note that the operators are ordered such that the creation operators are all left from the annihilation operators. The importance is discussed below.

As an example a situation is considered where one has three kinds of particles per site, but that at maximum one of these particles can occupy a given site. Then each site corresponds to a four-level system; the particles are hard-core bosons. Such a situation arises in antiferromagnetic dimerized spin systems where each dimer represents a four-level system. The ground state is the unique singlet while the three particles are given by the three-fold degenerate triplet states. In this case one has the multi-indices  $\mathbf{i} = (i, \alpha)$ , where  $i$  denotes the site and  $\alpha$  takes for instance the three values of the  $S^z$  component  $\alpha \in \{-1, 0, 1\}$ . In the local basis  $\{|i, s\rangle, |i, -1\rangle, |i, 0\rangle, |i, 1\rangle\}$ ,

---

<sup>1</sup>Another way to deal with the ambiguity would be to introduce a certain ordering among the indices. Then only one representative of the two (or more) identical states needs to be kept [176, 179].

where  $s$  denotes the singlet, the local creation operators  $e_{i,\alpha}^\dagger$  are the  $4 \times 4$ -matrices

$$e_{i,-1}^\dagger = \begin{pmatrix} 0 & 0 & 0 & 0 \\ 1 & 0 & 0 & 0 \\ 0 & 0 & 0 & 0 \\ 0 & 0 & 0 & 0 \end{pmatrix}, \quad (3.2.4a)$$

$$e_{i,0}^\dagger = \begin{pmatrix} 0 & 0 & 0 & 0 \\ 0 & 0 & 0 & 0 \\ 1 & 0 & 0 & 0 \\ 0 & 0 & 0 & 0 \end{pmatrix}, \quad (3.2.4b)$$

$$e_{i,1}^\dagger = \begin{pmatrix} 0 & 0 & 0 & 0 \\ 0 & 0 & 0 & 0 \\ 0 & 0 & 0 & 0 \\ 1 & 0 & 0 & 0 \end{pmatrix}. \quad (3.2.4c)$$

It is understood that the action at all other sites but  $i$  is the identity so that the operators in (3.2.4) are defined on the whole Hilbert space. The annihilation operators  $e_{i,\alpha}$  are given by the hermitian conjugate matrices. All possible commutators can easily be computed within the matrix representation. Finite matrix elements in the lower right  $3 \times 3$  block can be viewed as combined annihilation & creation processes: The matrix  $M_{\alpha,\beta}$  with all elements zero except the one at  $(\alpha,\beta)$  corresponds to the process  $e_{i,\alpha}^\dagger e_{i,\beta}$ . A finite matrix element in the upper left  $1 \times 1$  block, i.e. the singlet-singlet channel, can be expressed in normal-ordered fashion as  $\mathbf{1}_4 - \sum_{\alpha} e_{i,\alpha}^\dagger e_{i,\alpha}$ . In this way the operators (3.2.4) and their hermitian conjugate define a complete algebra which in turn enables one to classify contributions of the Hamiltonian according to the number of particles affected as done in Eqs. 3.2.1 and (3.2.3).

The decomposition (3.2.1) is physically very intuitive [171]. Yet the next important question is whether and how the operators  $H_n$  are unambiguously defined. This issue is addressed by noting that  $H_n|_m$  vanishes for  $m < n$ . This follows directly from the normal-ordering of the creation and annihilation operators in Eq. 3.2.3. Then one can proceed iteratively by requiring that  $H_{\text{eff}}$  applied to  $n$  particles corresponds to  $H_0 + H_1 + \dots + H_n$  ( $n$  arbitrary but fixed). Solving for  $H_n$  yields the recursions

$$H_0|_0 := H_{\text{eff}}|_0 \quad (3.2.5a)$$

$$H_1|_1 := H_{\text{eff}}|_1 - H_0|_1 \quad (3.2.5b)$$

$$H_2|_2 := H_{\text{eff}}|_2 - H_0|_2 - H_1|_2 \quad (3.2.5c)$$

⋮

$$H_n|_n := H_{\text{eff}}|_n - \sum_{i=0}^{n-1} H_i|_n. \quad (3.2.5d)$$

Assuming that  $H_{\text{eff}}$  is calculated beforehand one starts by evaluating  $E_0$  by means of the first definition. The result entirely defines  $H_0$ . The restriction  $H_0|_1$  is then used in the second equation to extract the  $t_{j,j}$  of  $H_1$  and so on. Generally,  $H_n$  is defined on the full many-particle Hilbert

space, not only for  $n$  particles. But it is sufficient to know the action of  $H_n$  on the subspace of  $n$  particles to determine all its matrix elements in (3.2.3). It is the essential merit of the notation in second quantization (3.2.3) that it provides the natural generalization of the action of a part of the Hamiltonian on a *finite* number of particles to an *arbitrary* number of particles. Since Eq. 3.2.5d holds for any number of particles and since  $H_n|_m$  vanishes for  $m < n$  one obtains Eq. 3.2.1, neglecting the precise definition of convergence which is beyond the scope of the present chapter.

In conventional many-body language,  $H_n$  stands for the  $n$ -particle irreducible interaction. The subtractions in Eq. 3.2.5 ensure that  $H_n$  contains no reducible contributions, i.e. contributions which really act only on a lower number of particles. It should be emphasized that the formalism above does not require that a simple *free* fermionic or bosonic limit exists. It is possible to start from any type of elementary particles counted by some operator  $Q$ .

Moreover, the formalism presented in this section does not depend on how  $H_{\text{eff}}$  is obtained. It does not matter whether a perturbative, a renormalizing procedure or a rigorously exact method was used to obtain  $H_{\text{eff}}$ .

### 3.2.1.2 Cluster additivity

Here the focus is laid on formal aspects of a perturbative approach [171] generalizing results obtained previously for 0-particle properties [182] and for 1-particle properties [183]. The feature that the Hamiltonian is of finite range on the lattice is exploited. Then the Eqs. 3.2.5 can be evaluated on finite subsystems (clusters, see below). Still, the thermodynamically relevant matrix elements of the operators  $H_n$  are obtained as will be shown in the following paragraphs.

To proceed further definitions are needed. A *cluster*  $C$  of the thermodynamic system is a *finite* subset of sites of the system and their linking bonds. By  $\mathcal{R}^C$  one denotes an operator which acts only on the Hilbert space  $\mathcal{E}^C$  of  $C$ . If  $\bar{C}$  denotes the sites of the total system which are not included in  $C$ , the restricted operator  $\mathcal{R}^C$  is lifted naturally to an operator  $\mathcal{R}$  in the total Hilbert space  $\mathcal{E} = \mathcal{E}^C \otimes \mathcal{E}^{\bar{C}}$  by

$$\mathcal{R} := \mathcal{R}^C \otimes \mathbf{1}^{\bar{C}} . \quad (3.2.6)$$

Note that it is not possible to define a restricted operator  $\mathcal{R}^C$  from an arbitrary operator  $\mathcal{R}$  acting on  $\mathcal{E}$  since  $\mathcal{R}$  will in general not have the product structure (3.2.6).

Two clusters  $A$  and  $B$  are said to form a *disconnected cluster*  $C = A \cup B$  iff they do not have any site in common  $A \cap B = \emptyset$  and there is no bond linking sites from  $A$  with sites from  $B$ . Otherwise the clusters  $A$  and  $B$  are said to constitute together a *linked cluster*  $C = A \cup B$ . Given a disconnected cluster  $C = A \cup B$  an operator  $\mathcal{R}^C$  is called *cluster additive* iff it can be decomposed as

$$\mathcal{R}^C = \mathcal{R}^A \otimes \mathbf{1}^B + \mathbf{1}^A \otimes \mathcal{R}^B . \quad (3.2.7)$$

With these definitions it is shown that  $H_{\text{eff}}$  and  $H_n$  are cluster additive. But  $H_{\text{eff}}|_n$  is not! This is another important reason to introduce the  $H_n$ .

The cluster additivity of  $H_{\text{eff}}^C$  is obvious since  $A$  and  $B$  are assumed to be disconnected. So they can be viewed as physically independent systems. Hence

$$H_{\text{eff}}^C = H_{\text{eff}}^A \otimes \mathbf{1}^B + \mathbf{1}^A \otimes H_{\text{eff}}^B . \quad (3.2.8)$$

Similarly, the operators  $H_n^A$  and  $H_n^B$  are deduced from (3.2.5) which act on  $\mathcal{E}^A$  and  $\mathcal{E}^B$ , respectively. Then it is straightforward to verify that the operators

$$H_n^C = H_n^A \otimes \mathbf{1}^B + \mathbf{1}^A \otimes H_n^B \quad (3.2.9)$$

fulfill the recursion (3.2.5) for the operators defined for the cluster  $C$ . Hence the operators  $H_{\text{eff}}$  and  $H_n$  are indeed cluster additive.

It is instructive to see that  $H_{\text{eff}}|_n$  is *not* cluster additive, contrary to what one might have thought. Let us consider the tentative identity

$$H_{\text{eff}}^C|_n = H_{\text{eff}}^A|_n \otimes \mathbf{1}^B + \mathbf{1}^A \otimes H_{\text{eff}}^B|_n . \quad (3.2.10)$$

This equation cannot be true since on the left hand side the number of particles is fixed to  $n$  while on the right hand side the number of particles to which the identities  $\mathbf{1}^A$  and  $\mathbf{1}^B$  are applied is not fixed. So no cluster additivity is given for the  $H_{\text{eff}}|_n$ .

The fact that cluster additivity holds only for particular quantities was noted previously for  $n = 1$  [183]. For  $n = 2$ , the subtraction procedure was first applied in the calculations in Ref. [142] (though not given in detail). In Refs. [176, 177, 181, 184] the subtractions necessary to obtain the irreducible 2-particle interaction were given in more detail. The general formalism presented in this article shows on the *operator* level why such subtractions are necessary and where they come from. Thereby, it is possible to extend the treatment to the general  $n$ -particle irreducible interaction.

The notation in terms of second quantization (3.2.3) renders the cluster additivity almost trivial. This is so since the creation and annihilation operators are defined locally for a certain site. It is understood that the other sites are not affected. Hence the same symbol  $e_i^\dagger$  can be used independent of the cluster in which the site  $i$  is embedded. In particular, one identifies automatically  $e_i^{\dagger,C}$  with  $e_i^{\dagger,A} \otimes \mathbf{1}^B$  if  $i \in A$  and with  $\mathbf{1}^A \otimes e_i^{\dagger,B}$  if  $i \in B$ . Hence cluster additivity is reduced to trivial statements of the kind that

$$H_1^A = \sum_{i,j \in A} t_{j;i} e_j^\dagger e_i \quad (3.2.11a)$$

$$H_1^B = \sum_{i,j \in B} t_{j;i} e_j^\dagger e_i \quad (3.2.11b)$$

implies

$$H_1^C = \sum_{i,j \in C} t_{j;i} e_j^\dagger e_i \quad (3.2.12a)$$

$$= \sum_{i,j \in A} t_{j;i} e_j^\dagger e_i + \sum_{i,j \in B} t_{j;i} e_j^\dagger e_i \quad (3.2.12b)$$

$$= H_1^A \otimes \mathbf{1}^B + \mathbf{1}^A \otimes H_1^B . \quad (3.2.12c)$$

In this sense, the notation in second quantization is the most natural way to think of cluster additivity.

Following Gelfand and co-workers [175, 182, 183] one concludes that the cluster additive quantities possess a cluster expansion. Hence all the irreducible matrix elements  $t_{j;i}$  possess a cluster expansion and can be computed on finite clusters.

## 3.2.1.3 Computational aspects

Since  $H_{\text{eff}}$  conserves the number of particles, i.e. Eq. 3.1.3, its action is to shift existing particles. The relevant matrix elements for a linked cluster  $A$  are denoted by

$$E_0^A := \langle 0 | H_{\text{eff}}^A | 0 \rangle \quad (3.2.13a)$$

$$a_{j;i}^A := \langle j | H_{\text{eff}}^A | i \rangle \quad (3.2.13b)$$

$$a_{j_1 j_2; i_1 i_2}^A := \langle j_1 j_2 | H_{\text{eff}}^A | i_1 i_2 \rangle \quad (3.2.13c)$$

$$\vdots$$

where the indices  $i, j, \dots$  may be multi-indices from now on. Put differently,  $E_0^A$  is the matrix element of  $H_{\text{eff}}^A | 0$ , the  $a_{j;i}^A$  are the matrix elements of  $H_{\text{eff}}^A | 1$ , the  $a_{j_1 j_2; i_1 i_2}^A$  those of  $H_{\text{eff}}^A | 2$  and so on. The number  $E_0^A$  is the ground state energy of cluster  $A$ . The recursive definitions (3.2.5) imply

$$t_{j;i}^A = a_{j;i}^A - E_0^A \delta_{ji} \quad (3.2.14a)$$

$$t_{j_1 j_2; i_1 i_2}^A = a_{j_1 j_2; i_1 i_2}^A - E_0^A \delta_{j_1 i_1} \delta_{j_2 i_2} - E_0^A \delta_{j_1 i_2} \delta_{j_2 i_1} - t_{j_2; i_2}^A \delta_{j_1 i_1} - t_{j_1; i_2}^A \delta_{j_2 i_1} - t_{j_2; i_1}^A \delta_{j_1 i_2} - t_{j_1; i_1}^A \delta_{j_2 i_2} \quad (3.2.14b)$$

$$t_{j_1 j_2 j_3; i_1 i_2 i_3}^A = a_{j_1 j_2 j_3; i_1 i_2 i_3}^A - A_0 - A_1 - A_2 \quad (3.2.14c)$$

$$\vdots$$

where  $A_0$  comprises six terms resulting from  $H_0$ ,  $A_1$  comprises 18 terms resulting from  $H_1$  and  $A_2$  comprises 36 terms resulting from  $H_2$ . The explicit formulae are given in the Appendix of Ref. [171]. The recipe in deriving the above equations is straightforward. For a given  $n$ -particle process  $\{i_m\} \rightarrow \{j_m\}$  ( $m \in \{1, \dots, n\}$ ) one has to subtract all possible processes which move less than  $n$  particles. Since the  $m$ -particle processes with  $m < n$  have been computed before the procedure is recursive. Note that all coefficients must be computed for the *same* cluster.

The cluster additivity or, equivalently, the existence of a cluster expansion can be exploited to compute the irreducible matrix elements on finite clusters given that the Hamiltonian is of finite range. There are two strategies to do so.

The first strategy is to choose a cluster large enough to perform the intended computation without finite-size effects. This strategy works particularly well if the dimensionality of the problem is low. Let us assume for simplicity that the Hamiltonian links only nearest-neighbour sites. Aiming at a given matrix element, for instance  $t_{j_1 j_2; i_1 i_2}^A$ , which shall be computed in a given order  $k$ , the large enough cluster  $C_l$  contains all possible subcluster  $C_s$  with two properties: (i) they have  $k$  or less bonds, (ii) they link the concerned sites  $j_1, j_2, i_1, i_2$  among themselves<sup>2</sup>. Clearly,  $C_l$  depends on the order  $k$ . But it depends also on the sites  $j_1, j_2, i_1, i_2$  under study so that the notation  $C_l^{(k)}(\{j_1, j_2, i_1, i_2\})$  is appropriate. Note, that the order of the sites does not matter. If some sites

<sup>2</sup>Depending on the details of the interaction on the bonds it may be sufficient to consider smaller clusters than mentioned in the main text, for instance a pure nearest-neighbour spin exchange reduces the range of virtual excursions. Frustration is another mechanism which reduces the range of the effective processes, see e.g. the Shastry-Sutherland model [176, 185, 191].

are omitted the constraints for the subclusters  $C_s$  are diminished since less sites must be linked. This implies in particular  $C_j^{(k)}(\{j_1, j_2, i_1, i_2\}) \subset C_j^{(k)}(\{j_1, i_1\})$ . Hence there can be a cluster  $A$  which contains  $C_j^{(k)}(\{j_1, j_2, i_1, i_2\})$  but does *not* contain  $C_j^{(k)}(\{j_1, i_1\})$  so that the hopping matrix element  $t_{j_1; i_1}^A$  is *not* the thermodynamic one, but the interaction  $t_{j_1 j_2; i_1 i_2}^A$  is without finite-size correction. So intermediate steps in the calculations (3.2.14) can display finite-size effects although the final result does not. In Refs. [142, 143, 176, 179] this strategy was used.

The second strategy is to compute, for a given order  $k$ , the *net* contributions of all clusters  $C$  with  $m \leq k$  bonds which link the sites under study. The advantage of this approach is that only smaller clusters need to be treated ( $\leq k$  bonds). The price to pay is an overhead in determining the *net* contribution. This requires to deduct from the total contribution of  $C$  the contributions of all subcluster of  $C$  with less bonds which link the points under study. This must be done in order to avoid double counting. More details on this strategy can be found in Ref. [175].

For Hamiltonians with relatively simple topology, the second strategy is more powerful. For more complicated Hamiltonians, however, the task to implement the overhead without flaw can quickly become impracticable while the first strategy can still be used, at least up to a certain order of the perturbation.

### 3.2.2 Effective observables

An effective Hamiltonian conserving the number of particles is useful to determine characteristic energies of the considered systems. But it is not sufficient to determine physical quantities which require more knowledge than the eigen-energies of the system. In particular, one is interested in the determination of dynamic correlations such as  $\langle \mathcal{O}(t) \mathcal{O}(0) \rangle$ . Then the mapping of the original Hamiltonian  $H$  to the effective Hamiltonian  $H_{\text{eff}}$  must be extended to a mapping of the original observable  $\mathcal{O}$  to the effective observables  $\mathcal{O}_{\text{eff}}$ . Here it is assumed that this has been achieved by an appropriate unitary transformation, for instance in a continuous fashion as described in the introduction.

#### 3.2.2.1 Global structure

The structure of the observables can be described best by using the notation of second quantization. Thereby it can be denoted clearly how many particles are involved. The most important difference compared to the Hamiltonian is that there is no particle conservation. Generically an observable creates and annihilates excitations, i.e. particles. Hence one defines the operators

$$\mathcal{O}_{d,n} := \sum_{i_1 \dots i_n; j_1 \dots j_{n+d}} w_{j_1 \dots j_{n+d}; i_1 \dots i_n} e_{j_1}^\dagger \dots e_{j_{n+d}}^\dagger e_{i_n} \dots e_{i_1}. \quad (3.2.15)$$

The local operators  $e_i$  have been described after Eq. 3.2.3. Again they shall appear normal-ordered, i.e. all creation operators are sorted to the left of the annihilation operators. The first index  $d$  indicates how many particles are created ( $d \geq 0$ ) or annihilated ( $d < 0$ ) by application of  $\mathcal{O}_{d,n}$ . The second index  $n \geq 0$  denotes how many particles have to be present before the operator  $\mathcal{O}_{d,n}$  becomes active. The result of  $\mathcal{O}_{d,n}$  acting on a state with less than  $n$  particles is zero.

In analogy to Eq. 3.2.1 the effective observables can be decomposed into partial observables like

$$\mathcal{O}_{\text{eff}} = \sum_{n=0}^{\infty} \sum_{d \geq -n} \mathcal{O}_{d,n}. \quad (3.2.16)$$

The additional feature in comparison to Eq. 3.2.1 is the sum over  $d$ . Tab. 3.1 sketches the structure of the terms appearing in the partial observables  $\mathcal{O}_{d,n}$

$d \downarrow / n \rightarrow$	0	1	2	3
...	...	...	...	...
-3	0	0	0	eee
-2	0	0	ee	$e^\dagger eee$
-1	0	e	$e^\dagger ee$	$e^\dagger e^\dagger eee$
0	1	$e^\dagger e$	$e^\dagger e^\dagger ee$	$e^\dagger e^\dagger e^\dagger eee$
1	$e^\dagger$	$e^\dagger e^\dagger e$	$e^\dagger e^\dagger e^\dagger ee$	$e^\dagger e^\dagger e^\dagger e^\dagger eee$
2	$e^\dagger e^\dagger$	$e^\dagger e^\dagger e^\dagger e$	$e^\dagger e^\dagger e^\dagger e^\dagger ee$	$e^\dagger e^\dagger e^\dagger e^\dagger e^\dagger eee$
...	...	...	...	...

Table 3.1: List of terms appearing in the partial observables  $\mathcal{O}_{d,n}$  which form together the effective observable  $\mathcal{O}_{\text{eff}}$  according to Eq. 3.2.16. No prefactors or indices are given for clarity.

It is assumed that  $\mathcal{O}_{\text{eff}}$  is computed by some technique, for instance by a continuous unitary transformation. Then the partial observables can be determined recursively by

$$\mathcal{O}_{d,0}|_{0 \rightarrow 0+d} := \mathcal{O}_{\text{eff}}|_{0 \rightarrow 0+d} \quad (3.2.17a)$$

$$\mathcal{O}_{d,1}|_{1 \rightarrow 1+d} := \mathcal{O}_{\text{eff}}|_{1 \rightarrow 1+d} - \mathcal{O}_{d,0}|_{1 \rightarrow 1+d} \quad (3.2.17b)$$

$$\mathcal{O}_{d,2}|_{2 \rightarrow 2+d} := \mathcal{O}_{\text{eff}}|_{2 \rightarrow 2+d} - \mathcal{O}_{d,0}|_{2 \rightarrow 2+d} - \mathcal{O}_{d,1}|_{2 \rightarrow 2+d}$$

$$\vdots$$

$$\mathcal{O}_{d,n}|_{n \rightarrow n+d} := \mathcal{O}_{\text{eff}}|_{n \rightarrow n+d} - \sum_{i=0}^{n-1} \mathcal{O}_{d,i}|_{n \rightarrow n+d}. \quad (3.2.17c)$$

Here  $|_{n \rightarrow n+d}$  denotes the restriction of an operator to act on the  $n$ -particle subspace  $\mathcal{E}_n$  (domain) and to yield states in the  $(n+d)$ -particle subspace  $\mathcal{E}_{n+d}$  (co-domain). The recursion is set-up in analogy to (3.2.5). It is again used that an operator  $\mathcal{O}_{d,n}$  effectively vanishes if it is applied to *less* than  $n$  particles. Barring possible problems of convergence, the validity of the recursion (3.2.17) for all  $d$  and  $n$  implies the decomposition (3.2.16).

As for the Hamiltonian the partial observables  $\mathcal{O}_{d,n}$  can be viewed as the  $n$ -particle irreducible part of the particular observable. The notation in second quantization elegantly resolves the question how the observables act on clusters as was explained in the section 3.2.1.2. Hence the definition (3.2.15) ensures cluster additivity and there exist cluster expansions for the partial observables. So they can be computed on finite clusters.

If dynamical correlations at zero temperature  $T = 0$  shall be described, the observables are applied to the ground state  $|0\rangle$  which is the particle vacuum [166]. Then only the partial observables  $\mathcal{O}_{d,0}$

with  $d \geq 0$  matter. According to (3.2.17a) no corrections are necessary, i.e. the structure of the relevant part of the effective observable is given by

$$\mathcal{O}_{\text{eff}}^{T=0} = \mathcal{O}_{0,0} + \mathcal{O}_{1,0} + \mathcal{O}_{2,0} + \mathcal{O}_{3,0} + \dots \quad (3.2.18)$$

This structure has been used so far in a number of investigations of spectral weights [82, 186] and spectral densities [179, 180, 187]. It turned out that it is indeed sufficient to consider a restricted number of particles [82, 179, 180]. But the question how many particles are required to describe a certain physical quantity sufficiently well depends on the considered model, on the chosen basis (What is called a particle?) and on the quantity under study.

At finite temperatures a certain number of particles will already be present in the system due to thermal fluctuations. Then the action of the partial observables  $\mathcal{O}_{d,n}$  with  $n \geq 1$  will come into play as well. This constitutes an interesting route to extend the applicability of effective models to finite temperatures, even though they were derived in the first place at zero temperature.

### 3.2.2.2 Computational aspects

The recursive equations for matrix elements which can be derived from (3.2.17) are very similar to those obtained for the Hamiltonian (3.2.14). This is illustrated for the matrix elements of  $\mathcal{O}_{1,n}$ . Let the bare matrix elements on a cluster  $A$  be

$$v_j^A := \langle j | \mathcal{O}_{\text{eff}}^A | 0 \rangle \quad (3.2.19a)$$

$$v_{j_1 j_2; i}^A := \langle j_1 j_2 | \mathcal{O}_{\text{eff}}^A | i \rangle \quad (3.2.19b)$$

$$\vdots$$

From (3.2.17) one obtains the irreducible elements as

$$w_j^A = v_j^A \quad (3.2.20a)$$

$$w_{j_1 j_2; i}^A := v_{j_1 j_2; i}^A - w_{j_1}^A \delta_{j_2 i} - w_{j_2}^A \delta_{j_1 i} \quad (3.2.20b)$$

$$\vdots$$

As for the irreducible interactions the strategy is straightforward. One has to subtract from the reducible  $n$ -particle matrix elements  $v^A$  the contributions which come from the  $m$ -particle irreducible matrix elements  $w^A$  with  $m < n$ . With this strategy also other irreducible matrix elements can be determined in a straightforward manner.

So far all considerations were general in the sense that it did not matter how the mapping is achieved. Next the focus is led on the actual *perturbative* evaluation of the matrix elements on finite clusters. For simplicity, it is assumed as before that the perturbative part of the Hamiltonian links only nearest-neighbour sites. One can consider for instance  $w_{j_1 j_2; i}^A$ . Assuming that the observable  $\mathcal{O}$  is also local, i.e. acts on a certain site only, or is a sum of such terms. If the observable is a sum of local terms then the transformation of each term separately and subsequent summation yields the result. So without loss of generality  $\mathcal{O}$  is considered to affect only site  $p$ . Then one has to compute the matrix elements for clusters linking the *four* sites  $j_1, j_2, i, p$ . If  $\mathcal{O}$  itself is a product of



operators affecting several sites  $p_i$  then the observable  $\mathcal{O}$  itself links these sites  $p_i$ . Apart from this difference to the matrix elements of the effective Hamiltonian, one may copy the remaining steps from there:

There are again the two strategies. Either the calculation in order  $k$  is performed on a cluster  $C_l$  large enough so that all subclusters of  $k$  bonds linking the relevant sites  $j_1, j_2, i, p$  are comprised in  $C_l$  [179, 180, 188, 189]. Or one has to add the *net* contributions of all different clusters with  $k$  or less bonds which link the relevant sites  $j_1, j_2, i, p$  [187]. In either way the results for spectral densities can be obtained.

### 3.3 Transformation of the Hamiltonian

So far no particular property of the transformation providing the effective operators  $H_{\text{eff}}$  and  $\mathcal{O}_{\text{eff}}$  was assumed. The only prerequisites were the existence of a counting operator  $Q$ , which counts the number of elementary excitations, i.e. particles, and the conservation of this number of particles by  $H_{\text{eff}}$ :  $[H_{\text{eff}}, Q] = 0$ .

Here a particular transformation is specified leading to  $[H_{\text{eff}}, Q] = 0$ . This section is a very brief summary of Ref. [143] which is necessary to present the ideas and to fix the notation for the subsequent section dealing with the transformation yielding the effective observables.

For simplicity one restricts the considered systems in the following way: The problem can be formulated as perturbation problem as in Eq. 3.1.2 with the properties

- (A) The unperturbed part  $H_0$  has an equidistant spectrum bounded from below. The difference between two successive levels is the energy of a particle, i.e.  $Q = H_0$ .
- (B) There is a number  $\mathbb{N} \ni N > 0$  such that the perturbing part  $V$  can be split as  $V = \sum_{n=-N}^N T_n$  where  $T_n$  increments (or decrements, if  $n < 0$ ) the number of particles by  $n$ :  $[Q, T_n] = nT_n$ .

Condition (A) allows to introduce the particularly simple and intuitive choice  $Q = H_0$ . Note that the restrictions of (A) are not too serious in practice since very often the deviations from an equidistant spectrum can be put into the perturbation  $V$ . Conditions (A) and (B) together imply that the starting Hamiltonian  $H$  has a block-band-diagonal structure as depicted in Fig. 3.1. The perturbation  $V$  connects states of different particle numbers only if the difference is a finite number  $\leq N$ . Note that very many problems in physics display this property, for a discussion of interacting fermions see Ref. [165, 166]. So far, most applications consider  $N = 1$  [176, 190] and  $N = 2$  [82, 142–144, 179, 180, 188, 189, 191, 192], but calculations for higher  $N$  are also possible [193–195].

The flow equation (3.1.4) is solved for the Hamiltonian (3.1.2) obeying the conditions (A) and (B) perturbatively, that means up to a certain order in the expansion parameter  $x$ . The *ansatz* used is

$$H(x; \ell) = H_0 + \sum_{k=1}^{\infty} x^k \sum_{|\underline{m}|=k} F(\ell; \underline{m}) T(\underline{m}), \quad (3.3.1)$$

with unknown real functions  $F(\ell; \underline{m})$  for which the flow equation (3.1.4) yields non-linear recursive

differential equations [143]. The notation comprises

$$\underline{m} = (m_1, m_2, m_3, \dots, m_k) \quad \text{with} \quad (3.3.2a)$$

$$m_i \in \{0, \pm 1, \pm 2, \dots, \pm N\} \quad (3.3.2b)$$

$$|\underline{m}| = k \quad (3.3.2c)$$

$$T(\underline{m}) = T_{m_1} T_{m_2} T_{m_3} \cdots T_{m_k} \quad (3.3.2d)$$

$$M(\underline{m}) = \sum_{i=1}^k m_i . \quad (3.3.2e)$$

The second sum in ansatz (3.3.1) runs over all indices  $\underline{m}$  of length  $|\underline{m}| = k$ . Thereby,  $H(x; \ell)$  includes all possible virtual excitation processes  $T(\underline{m})$  in a given order  $x^k$  multiplied by the weight  $F(\ell; \underline{m})$ .

The optimum choice for the infinitesimal generator  $\eta$  of the unitary transformation reads

$$\eta(x; \ell) = \sum_{k=1}^{\infty} x^k \sum_{|\underline{m}|=k} \text{sgn}(M(\underline{m})) F(\ell; \underline{m}) T(\underline{m}). \quad (3.3.3)$$

In the eigen-basis  $\{|n\rangle\}$  of  $Q$ , i.e.  $Q|n\rangle = n|n\rangle$ , the matrix elements of the generator  $\eta$  read

$$\eta_{i,j}(x; \ell) = \text{sgn}(Q_i - Q_j) H_{i,j}(x; \ell) , \quad (3.3.4)$$

with the convention  $\text{sgn}(0) = 0$ . This choice keeps the flowing Hamiltonian block-band diagonal also at intermediate values of  $\ell$  [141, 143]. For  $\ell \rightarrow \infty$  the generator (3.3.4) eliminates all parts of  $H(x; \ell)$  changing the number of particles so that  $[H_{\text{eff}}, Q] = 0$  with  $H_{\text{eff}} := H(\ell = \infty)$ .

For the functions  $F(\ell; \underline{m})$  a set of coupled differential equations is determined by inserting Eqs. 3.3.1 and 3.3.3 in the flow equation (3.1.4) and comparing coefficients. The differential equations are recursive [143]. The functions  $F$  of order  $k + 1$ , i.e.  $F(\ell; \underline{m})$  with  $|\underline{m}| = k + 1$ , are determined by the functions  $F$  of order  $k$ . The initial conditions are  $F(0; \underline{m}) = 1$  for  $|\underline{m}| = 1$  and  $F(0; \underline{m}) = 0$  for  $|\underline{m}| > 1$ . The functions are sums of monomials with structure  $(p/q)\ell^i \exp(-2\mu\ell)$ , where  $p, q, i, (\mu > 0)$  are integers. This allows to implement a computer-aided iterative algorithm for the computation of the functions  $F$  [143].

The following symmetry relations hold

$$F(\ell; \underline{m}) = F(\ell; (-m_k, \dots, -m_1)) \quad (3.3.5a)$$

$$F(\ell; \underline{m}) = F(\ell; (-m_1, \dots, -m_k)) (-1)^{|\underline{m}|+1} . \quad (3.3.5b)$$

Relation (3.3.5a) reflects the hermiticity of the Hamiltonian. The block-band diagonality for all  $\ell$  implies

$$F(\ell; \underline{m}) = 0 \quad \text{for} \quad |M(\underline{m})| > N . \quad (3.3.6)$$

In the limit  $\ell \rightarrow \infty$  the coefficients  $C(\underline{m}) := F(\infty; \underline{m})$  are obtained. They are available in paper form [143, 190] and electronically [196]. The effective Hamiltonian is given by the general form

$$H_{\text{eff}}(x) = H_0 + \sum_{k=1}^{\infty} x^k \sum_{\substack{|\underline{m}|=k \\ M(\underline{m})=0}} C(\underline{m}) T(\underline{m}) , \quad (3.3.7)$$

where  $M(\underline{m}) = 0$  reflects the conservation of the number of particles. The action of  $H_{\text{eff}}$  can be viewed as a weighted sum of particle-number conserving virtual excitation processes each of which is encoded in a monomial  $T(\underline{m})$ . One has to emphasize that the effective Hamiltonian  $H_{\text{eff}}$  with known coefficients  $C(\underline{m})$  can be used straightforwardly in all perturbative problems that meet conditions (A) and (B).

$H_{00}$	$H_{01}$		
$H_{10}$	$H_{11}$	$H_{12}$	
	$H_{21}$	$H_{22}$	$H_{23}$
		$H_{32}$	$H_{33}$

Fig. 3.1: Block-band diagonal Hamilton matrix for  $N = 1$  in the eigen-basis  $\{|n\rangle\}$  of the operator  $Q$  which counts the number of particles. The unperturbed Hamiltonian  $H(x = 0) = H_0$  and the effective Hamiltonian  $H_{\text{eff}}$  have matrix elements in the dark areas only:  $[H_{\text{eff}}, Q] = 0$ . For non-degenerate ground state  $H_{00}$  is a  $1 \times 1$  matrix. The dimension of  $H_{nn}$  grows roughly like  $L^n$  with system size  $L$ . The perturbation  $V$  can lead to overlap matrices indicated as light boxes. The empty boxes contain vanishing matrix elements only.

### 3.4 Transformation of observables

To calculate physical quantities which do not depend only on the eigen-energies the relevant observables must also be known. The conceptual simplicity of unitary transformations implies that the observables must be subject to the *same* unitary transformation as the Hamiltonian. In this section it is described how the perturbative CUT method can be extended to serve this purpose.

Consider the observable  $\mathcal{O}$ . It is mapped according to the flow equation

$$\frac{\partial \mathcal{O}(x; \ell)}{\partial \ell} = [\eta(x; \ell), \mathcal{O}(x; \ell)] , \quad (3.4.1)$$

where the *same* generator  $\eta(x; \ell)$ , given in Eq. 3.3.3, as in Eq. 3.1.4 is to be used to generate the transformation. In analogy to Eq. 3.3.1 one employs the ansatz

$$\mathcal{O}(x; \ell) = \sum_{k=0}^{\infty} x^k \sum_{i=1}^{k+1} \sum_{|\underline{m}|=k} G(\ell; \underline{m}; i) \mathcal{O}(\underline{m}; i) , \quad (3.4.2)$$

where the  $G(\ell; \underline{m}; i)$  are real-valued functions for which the flow equation (3.4.1) yields recursive differential equations. The operator products  $\mathcal{O}(\underline{m}; i)$  are given by

$$\mathcal{O}(\underline{m}; i) := T_{m_1} \cdots T_{m_{i-1}} \mathcal{O} T_{m_i} \cdots T_{m_k} , \quad (3.4.3)$$

where the notation of the Eqs. (3.3.2) is used. Note that  $G(\ell; \underline{m}; i)$  does not depend on  $\mathcal{O}$ . The integer  $i$  denotes the position in  $\mathcal{O}(\underline{m}, i)$  at which the operator  $\mathcal{O}$  is inserted in the sequence of the  $T_m$ . The starting condition is  $\mathcal{O}(x; 0) = \mathcal{O}(x)$  and the final result is found at  $\ell = \infty$ :  $\mathcal{O}_{\text{eff}}(x) := \mathcal{O}(x; \infty)$ .

Inserting the ansatz (3.4.3) for  $\mathcal{O}(x; \ell)$  and the generator  $\eta(x; \ell)$  from (3.3.3) into the flow equation (3.4.1) yields

$$\begin{aligned} \sum_{k=0}^{\infty} x^k \sum_{|\underline{m}|=k} \sum_{i=1}^{k+1} \frac{\partial}{\partial \ell} G(\ell; \underline{m}; i) \mathcal{O}(\underline{m}; i) = \\ \sum_{k_1=1}^{\infty} \sum_{k_2=0}^{\infty} x^{k_1+k_2} \sum_{\substack{|\underline{m}'|=k_1 \\ |\underline{m}''|=k_2}} \sum_{i=1}^{k_2+1} F(\ell; \underline{m}') G(\ell; \underline{m}''; i) \times \\ \times \text{sgn}(M(\underline{m}')) [T(\underline{m}'), \mathcal{O}(\underline{m}''; i)] . \end{aligned} \quad (3.4.4)$$

The functions  $F(\ell; \underline{m})$  are known from the calculations described in the previous section 3.3 pertaining to the transformation of the Hamiltonian. The sums denoted by expressions of the type  $|\underline{m}| = k$  run over all multi-indices  $\underline{m}$  of length  $k$ .

Comparing coefficients in Eq. 3.4.4 yields a set of recursive differential equations for the functions  $G(\ell; \underline{m}, i)$ . To ease the comparison of coefficients one splits a specific  $\underline{m}$  with  $k$  fixed in two parts as defined by  $i$

$$\underline{m} = (\underline{m}_l, \underline{m}_r) , \quad (3.4.5)$$

with  $|\underline{m}_l| = i - 1$  and  $|\underline{m}_r| = k - i + 1$  such that the splitting reflects the structure of  $\mathcal{O}(\underline{m}; i)$  in Eq. 3.4.3. Then the explicit recursions can be denoted by

$$\begin{aligned} \frac{\partial}{\partial \ell} G(\ell; \underline{m}; i) = \\ \sum_{\substack{\underline{m}_l = (\underline{m}_a, \underline{m}_b) \\ \underline{m}_a \neq 0}} \text{sgn}(M(\underline{m}_a)) F(\ell; \underline{m}_a) G(\ell; (\underline{m}_b, \underline{m}_r); i - |\underline{m}_a|) \\ - \sum_{\substack{\underline{m}_r = (\underline{m}_a, \underline{m}_b) \\ \underline{m}_b \neq 0}} \text{sgn}(M(\underline{m}_b)) F(\ell; \underline{m}_b) G(\ell; (\underline{m}_l, \underline{m}_a); i) . \end{aligned} \quad (3.4.6)$$

The recursive nature of these equations becomes apparent by observing that the summations  $\underline{m}_l = (\underline{m}_a, \underline{m}_b)$  and  $\underline{m}_r = (\underline{m}_a, \underline{m}_b)$  are performed over all non-trivial breakups of  $\underline{m}_l$  and  $\underline{m}_r$ . For instance, the restriction  $\underline{m}_l = (m_1, m_2, \dots, m_{i-1}) \doteq (\underline{m}_a, \underline{m}_b)$  with  $\underline{m}_a \neq 0$  means, that one has to sum over the breakups

$$\begin{aligned} \underline{m}_a &= (m_1) & \text{and} & \underline{m}_b &= (m_2, \dots, m_{i-1}) \\ \underline{m}_a &= (m_1, m_2) & \text{and} & \underline{m}_b &= (m_3, \dots, m_{i-1}) \\ &\vdots & & & \vdots \\ \underline{m}_a &= (m_1, m_2, \dots, m_{i-1}) & \text{and} & \underline{m}_b &= () . \end{aligned} \quad (3.4.7)$$

This implies that the  $G(\ell; \underline{m}; i)$  appearing on the right side of Eq. 3.4.6 are of order  $k - 1$  or less. Once they are known the function on the left hand side of order  $k$  can be computed. By iteration,

all functions can be determined. The initial conditions follow from  $\mathcal{O}(x; \ell = 0) = \mathcal{O}$  and read

$$G(0; \underline{m}; 1) = 1 \text{ for } |\underline{m}| = 0 \quad (3.4.8a)$$

$$G(0; \underline{m}; i) = 0 \text{ for } |\underline{m}| > 0. \quad (3.4.8b)$$

By iteration of (3.4.6), all functions can be determined.

Two examples are briefly discussed to illustrate how the Eqs. 3.4.6 work. It is assumed that  $N = 2$ . All zero order functions  $G(\ell; (), 1)$  are equal to 1. Since there is no breakup of  $()$ , as would be required by the sums on the right hand side of Eqs. 3.4.6, the right hand sides vanish identically, whence  $G(\ell; (); 1) = 1$  for all values of  $\ell$ .

The first order function  $G(\ell; (1); 2)$  is given by

$$\begin{aligned} \frac{\partial}{\partial \ell} G(\ell; \underbrace{(1)}_{m_1}; 2) &= \text{sgn}[M((1))] F(\ell; (1)) \cdot G(\ell; (); 1) \\ &= e^{-\ell} \cdot 1, \end{aligned} \quad (3.4.9)$$

where  $F(\ell; (1)) = e^{-\ell}$  is taken from Eq. 15 in Ref. [143]. With the initial condition  $G(0; (1); 2) = 0$  from (3.4.8) the differential equation (3.4.9) yields

$$G(\ell; (1); 2) = 1 - e^{-\ell} \xrightarrow{\ell \rightarrow \infty} 1. \quad (3.4.10)$$

As a second example a second order function is considered where one can use the above result

$$\begin{aligned} \frac{\partial}{\partial \ell} G(\ell; \underbrace{(-2, 1)}_{m_1}; 3) &= \\ &\text{sgn}[M((-2, 1))] F(\ell; (-2, 1)) G(\ell; (), 1) \\ &\quad + \text{sgn}[M((-2))] F(\ell; (-2)) G(\ell; (1), 2) \end{aligned} \quad (3.4.11a)$$

$$= - (e^{-3\ell} - e^{-\ell}) \cdot 1 - e^{-2\ell} \cdot (1 - e^{-\ell}) \quad (3.4.11b)$$

$$= e^{-\ell} - e^{-2\ell}. \quad (3.4.11c)$$

Again the functions  $F$  are taken from Eq. 15 in Ref. [143]. Integrating the result (3.4.11c) using the initial condition (3.4.8) leads to

$$G(\ell; (-2, 1); 3) = -e^{-\ell} + \frac{1}{2}e^{-2\ell} + 1 - \frac{1}{2} \xrightarrow{\ell \rightarrow \infty} \frac{1}{2}. \quad (3.4.12)$$

This kind of calculation carries forward to higher orders. The functions  $G$  – like the functions  $F$  – are sums of simple monomials  $(p/q)\ell^i \exp(-2\mu\ell)$ , where  $p, q, i, (\mu > 0)$  are integers. Thus the integrations are always straightforward

$$\int_0^\ell d\ell' \ell'^i = \frac{1}{i+1} \ell^{i+1} \quad (3.4.13a)$$

$$\int_0^\ell d\ell' \ell'^i e^{-2\mu\ell'} = \frac{i!}{2\mu} \left[ \frac{1}{(2\mu)^i} - e^{-2\mu\ell} \sum_{j=0}^i \frac{\ell^j}{j!(2\mu)^{i-j}} \right] \quad (3.4.13b)$$

and can easily be implemented in a computer-algebraic programme. The remaining implementation follows very much the same line as described previously for the functions  $F$  [143].

In analogy to Eqs. (3.3.5) for  $F$  two symmetry relations hold for  $G$ . With  $\underline{m} = (m_1, \dots, m_k)$  they read

$$G(\ell; \underline{m}; i) = G(\ell; (-m_k, \dots, -m_1); k - i + 2) \quad (3.4.14a)$$

$$G(\ell; \underline{m}; i) = G(\ell; (-m_1, \dots, -m_k); i)(-1)^{|\underline{m}|} \quad (3.4.14b)$$

as can be shown by induction. The first symmetry (3.4.14a) holds if  $\mathcal{O}$  is hermitian. Unfortunately, there is no equivalence to Eq. 3.3.6 so that a possible initial block-band structure in  $\mathcal{O}(x; 0)$  is generically lost in the course of the transformation, i.e. for  $\ell > 0$ .

In the limit  $\ell \rightarrow \infty$  the coefficients  $\tilde{C}(\underline{m}; i) := G(\infty; \underline{m}; i) \in \mathbb{Q}$  are obtained as rational numbers. So one retrieves finally

$$\mathcal{O}_{\text{eff}}(x) = \sum_{k=0}^{\infty} x^k \sum_{i=1}^{k+1} \sum_{|\underline{m}|=k} \tilde{C}(\underline{m}; i) \mathcal{O}(\underline{m}; i) \quad (3.4.15)$$

similar to Eq. 3.3.7. The coefficients  $\tilde{C}(\underline{m}; i)$  are available electronically [196]. Note that  $\mathcal{O}_{\text{eff}}$  is *not* a particle-conserving quantity as is obvious from the fact that the sum over  $|\underline{m}|$  is not restricted to  $M(\underline{m}) = 0$ . In order to see the net effect of  $\mathcal{O}_{\text{eff}}(x)$  on the number of particles explicitly it is helpful to split the bare operator accordingly  $\mathcal{O} = \sum_{n=-N'}^{N'} T'_n$ , where  $T'_n$  increments (or decrements, if  $n < 0$ ) the number of particles by  $n$ :  $[Q, T'_n] = nT'_n$ .

The difference between the bare initial observable  $\mathcal{O}$  and the representation (3.4.15) must be viewed as vertex correction which comes into play since the bare initial excitations are not the true eigen-excitations of the interacting system. It is stressed that the formalism presented introduces the notions of  $n$ -particle irreducibility, vertex correction and so on *without* starting from the limit of *non-interacting* conventional particles such as bosons or fermions.

### 3.5 Effective lattice

In this section an effective lattice  $\Gamma_{\text{eff}}$  is introduced on which the effective operators act. The reason behind it is mainly that the language one uses for the spin systems has dimers as basic building blocks and no longer the underlying spins which act on the initial lattice  $\Gamma$ . The same reasoning holds also true for more general applications. The effective lattice is illustrated on the level of the Hamiltonian for a dimerized chain which will be later discussed in detail in the first application chapter. The effective lattice is the same for the Hamiltonian and the observables.

The dimerized spin chain is depicted in Fig. 3.2

$$\begin{aligned} H &= J_0 \sum_{i=1}^{2N} (1 + \delta(-1)^i) \mathbf{S}_i \mathbf{S}_{i+1} \\ &= H_0 + xV = J \sum_{j=1}^N \mathbf{S}_{2j} \mathbf{S}_{2j+1} + xJ \sum_{j=1}^N \mathbf{S}_{2j} \mathbf{S}_{2j-1} \end{aligned} \quad (3.5.1)$$

where  $J = J_0(1 + \delta)$  and  $x = (1 - \delta)/(1 + \delta)$ . The summation index  $i$  counts the sites in the original lattice  $\Gamma$ , depicted as small black circles in Fig. 3.2, while  $j$  counts the number of dimers, i.e. the sites of the effective lattice  $\Gamma_{\text{eff}}$ , depicted as big grey circles. The ground state of system

of isolated dimers, i.e.  $H_0$ , is given by singlets on all dimers. An elementary excitation of  $H_0$  is a single triplet on one of the dimers which means it sits on two neighbourings (strong bonds) sites of the initial lattice  $\Gamma$  or on one site in the effective lattice  $\Gamma_{\text{eff}}$ . The effective lattice represents therefore the connection of the basic building blocks defined by the unperturbed Hamiltonian  $H_0$ . It is easily verified that  $H$  matches the conditions (A) and (B) for using the perturbative realization of the particle conserving continuous unitary transformations.

The effective Hamiltonian  $H_{\text{eff}}$  conserves the number of triplets. The important point is that  $H_{\text{eff}}$  engenders a hopping of these triplets from dimer to dimer and also the interaction is a dimer-dimer interaction, i.e. from site to site in the effective lattice  $\Gamma_{\text{eff}}$ . In other words, it suffices to study the action of  $H_{\text{eff}}$  on  $\Gamma_{\text{eff}}$ , which comprises only half of the number of sites of the original lattice  $\Gamma$ . From now on it is understood that the action of  $H_{\text{eff}}$  is evaluated on the corresponding effective lattice.

The same conclusion can be made for the effective observables  $\mathcal{O}_{\text{eff}}$ . The reason is that the unperturbed observable is expressed in similar operators  $T'$  as the unperturbed Hamiltonian  $H_0$ . Additionally, one uses the same generator for the observables as for the Hamiltonian. It follows that the action of  $\mathcal{O}_{\text{eff}}$  on some initial state, e.g. the ground state  $|\tilde{0}\rangle$ , generates only effective particles which can be classified by the sites of the effective lattice  $\Gamma_{\text{eff}}$ . The latter point will be used in the following chapters.

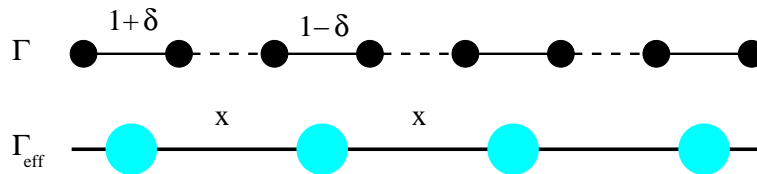


Fig. 3.2: A simple example to illustrate the difference between the original lattice  $\Gamma$ , on which the original model is defined, and the effective lattice  $\Gamma_{\text{eff}}$ . Small black circles corresponds to spins of the initial lattice  $\Gamma$ . Two sites connected by a thick solid black line denote a dimer. Big grey circles are the sites of the effective lattice  $\Gamma_{\text{eff}}$  and correspond to dimers in the original model. The action of the effective operators  $H_{\text{eff}}$  and  $\mathcal{O}_{\text{eff}}$  is restricted to the effective lattice  $\Gamma_{\text{eff}}$ .

### 3.6 Choice of the cluster

In this section general considerations are made how to choose the appropriate cluster size for a given perturbation order for the various quantities of interest in order to obtain results in the thermodynamic limit. The amplitudes for a  $n$ -triplon quantity are in general cluster dependent and one has to subtract contributions from triplon sectors with smaller triplon numbers. The latter points will be illustrated for the zero-, one- and two-triplon sector and also for the effective observables.

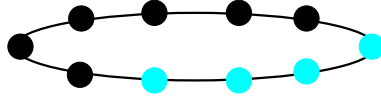


Fig. 3.3: A periodically closed cluster of ten sites.  $H_{\text{eff}}$  to third order connects at maximum four neighbouring sites by activated bonds (see text). The connected rungs are printed in grey.

### 3.6.1 Hamiltonian

#### 3.6.1.1 Zero triplon: $H_0$

Let  $|0\rangle$  denote the triplon vacuum. This is the state where all sites in  $\Gamma_{\text{eff}}$  are occupied by singlets. Clearly,  $|0\rangle$  is the ground state of  $H(x=0) = H_0$ . The one-triplon gap separates the corresponding ground state energy from the first excited level. In Ref. [166] it was shown on general grounds that the particle vacuum  $|0\rangle$  remains the ground state of  $H_{\text{eff}}$  for finite  $x$  unless a phase transition occurs (e.g. a mode softening at some critical value  $x_c$ ). Since  $H_{\text{eff}}$  conserves the number of triplons one concludes that  $\langle 0|H_{\text{eff}}(0 < x < x_c)|0\rangle$  is the ground state energy. The point  $x = x_c$  is in general a singular point where a phase transition occurs.

Since the action of  $H_0$  on  $|0\rangle$  coincides with the action of  $H_{\text{eff}}$  on this state (see Ref. [171]), every order of the ground state energy per site  $\epsilon_0$  can be calculated in the thermodynamic limit on a finite minimum cluster by

$$\epsilon_0 = \langle 0|H_{\text{eff}}|0\rangle/(2N), \quad (3.6.1)$$

where  $N$  is the number of sites used in the minimum cluster.

The minimum cluster is now specified. At first, it is clear that one needs a *closed* segment of the effective lattice. This ensures that there are no end sites, which are linked to the cluster by one inter-site bond only. They would not contribute the same amount of energy as the fully linked rungs in the middle of the cluster. Fig. 3.3 shows a cluster of a generic one-dimensional spin-system which has been closed to a ring.

$H_{\text{eff}}$  connects usually a maximum of  $l+1$  sites on a finite cluster of  $N$  sites in  $l^{\text{th}}$  order. In other words: A maximum of  $l$  bonds between neighbouring sites can be *activated* in  $l^{\text{th}}$  order. A bond  $\nu$  is said to be activated, if a part of  $H_{\text{eff}}$ , i.e., the specific local operator  $\mathcal{T}_n(\nu)$  in  $T_n = \sum_{\nu} \mathcal{T}_n(\nu)$  of  $H_{\text{eff}}$ , has acted on the two sites connected by  $\nu$ .

The linked cluster theorem states that only those processes induced by the  $T_{\underline{m}}$  of  $H_{\text{eff}}$  contribute to the ground state energy (and all other extensive quantities), in which all activated bonds are linked. Processes involving disconnected active-bond distributions cannot contribute. The basic argument is sketched in Fig. 3.4. This means in our case, that a cluster of  $l+1$  sites is sufficient to calculate the  $l^{\text{th}}$  order contribution avoiding *wrap-arounds*.

$$\begin{aligned} & \text{Minimum number of sites to calculate} \\ & \text{the } l^{\text{th}} \text{ order contribution to } \epsilon_0 \text{ in the} \\ & \text{thermodynamic limit} \\ & = l + 1 . \end{aligned} \quad (3.6.2)$$



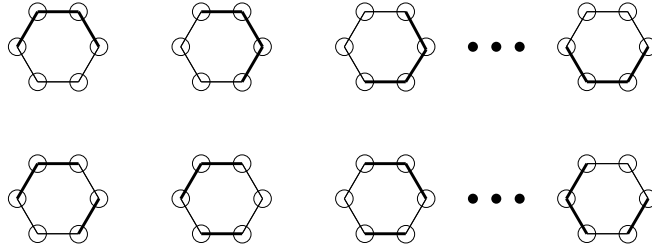


Fig. 3.4: A closed segment of six sites. Sites are depicted by circles and (active) bonds between sites by (thick) solid lines. In a process of order  $l = 3$  a maximum of 3 bonds can be active. On a closed cluster of  $N = 6$  there are 6 possibilities to arrange *linked* bonds (top row). One clearly sees that this number grows linearly in  $N$ . The given example of 3 *disconnected* active bonds (bottom row) has 12 possibilities, which would lead to a super-extensive contribution  $\propto N^2$  to the extensive quantity under study. Thus they do not contribute.

Once the minimum cluster is specified it is straight forward to calculate  $\epsilon_0$ .

### 3.6.1.2 One triplon: $H_1$

One defines  $|i\rangle$  to denote the eigen state of  $H_0$  with one triplon on site  $i$  of  $\Gamma_{\text{eff}}$  and singlets on all other sites. The magnetic quantum number  $m$  of the triplon at site  $i$  is of no importance in the following considerations, since  $H_{\text{eff}}$  usually conserves  $m$  and the total spin  $S$ . Thus it is not denoted explicitly.

Since  $H_{\text{eff}}(x)$  conserves the number of triplons the action of  $H_{\text{eff}}(x)$  on the state  $|i\rangle$  is a hopping of the triplon. One defines the hopping coefficients

$$a_{i,j}^{\text{cl}}(x) = \langle i | H_{\text{eff}}(x) | j \rangle . \quad (3.6.3)$$

The superscript cl indicates that the hopping coefficient might depend on the cluster on which it was calculated.

The hopping coefficients  $t_{i,j}$  of the irreducible one-particle operator  $H_1$  read (see Eqs.9 in Ref. [171])

$$t_{i,j} = \langle i | H_1 | j \rangle = \langle i | H_{\text{eff}} - H_0 | j \rangle = a_{i,j}^{\text{cl}} - E_0^{\text{cl}} \delta_{i,j} . \quad (3.6.4)$$

Since  $H_1$  is a cluster additive, i.e., an extensive, operator, the coefficients  $t_{i,j}$  can be calculated for the infinite system on finite clusters up to some finite order. This is the reason why the superscript cl is dropped from  $t_{i,j}$ . The cluster ground state energy  $E_0^{\text{cl}}$  must be calculated on the *same* cluster as the “raw” hopping coefficients  $a_{i,j}^{\text{cl}}$ .

For each order of the coefficient  $t_{i,j}$  there exists a minimum cluster which must contain the two rungs  $i$  and  $j$ . To classify the size of the minimum cluster one studies how far the triplon motion extends in a given order  $l$ . Only processes, which take place on *linked* clusters of active bonds (see previous section), contribute to the extensive thermodynamic hopping coefficients  $t_{i,j}$ . The minimum cluster must be a linked cluster, which contains the rungs  $i$  and  $j$ .

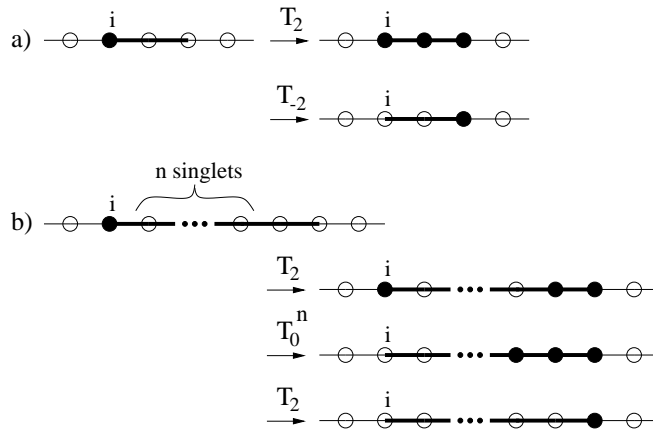


Fig. 3.5: Processes of  $H_{\text{eff}}$  that lead to a motion of the initial triplon on rung  $i$ . Active bonds are depicted by thick lines. All processes that contribute to thermodynamic extensive hopping coefficients take place on linked clusters of active bonds. Part a) shows a second order process moving the initial triplon by two sites. Part b) is a process of order  $n + 2$  moving the triplon by  $n + 2$  sites.

The action of a single  $T_0$  operator (first order process) on  $|i\rangle$  is to shift the triplon by one. Somewhat more intricate is the case of the operator  $T_2$  acting on  $|i\rangle$ . In any operator-product  $T(\underline{m})$  an operator  $T_2$  is always accompanied by a destruction operator  $T_{-2}$ . The operator  $T_2$  creates two triplons on neighbouring sites (triplon-pair) if both of them are occupied by singlets. Suppose that  $T_2$  is immediately followed by the  $T_{-2}$  operator. Then there can be a hopping of the initial triplon by two rungs, if the triplon-pair was created in the immediate vicinity of the triplon at site  $i$  to produce a three-triplon state. The situation is depicted in Fig. 3.5a. This is a second order process. It moves the triplon by two rungs. One could go on like this ( $\dots T_{-2}T_2T_{-2}T_2$ ) or one could start to build up a linked chain by iterative application of  $T_2$  operators, say, to the right of the triplon at site  $i$  and then destroy the chain from the left (e.g.  $T_{-2}T_{-2}T_2T_2$ ). All these processes lead to a maximum motion of the initial triplon by  $l$  rungs in  $l^{\text{th}}$  order. The creation of a triplon-pair *not* connected to the initial triplon on site  $i$  does not lead to any motion of the latter unless there is a sufficient number of  $T_0$  operators moving the triplon at site  $i$  towards the isolated triplon-pair until they form a state with three adjacent triplons as depicted in Fig. 3.5b. This also leads to a maximum motion of the initial triplon by  $l$  sites in  $l^{\text{th}}$  order.

All possible combinations of the  $T_2$ ,  $T_0$  and  $T_{-2}$  operators that can appear in a  $T(\underline{m})$ -product of  $H_{\text{eff}}$  can now be viewed as a product of the processes discussed. So one concludes

$$\begin{aligned} &\text{maximum motion of one triplon under the action} \\ &\text{of } H_{\text{eff}} \text{ in } l^{\text{th}} \text{ order} = l \text{ sites} . \end{aligned} \quad (3.6.5)$$

Therefore, the minimum cluster to calculate the hopping coefficient  $t_{i,j}$  in order  $l$  in the thermodynamic limit must contain the two sites  $i$  and  $j$ , which must not be further apart than  $l$  sites. Additionally the minimum cluster must contain all  $l$  bonds that can be activated in all processes

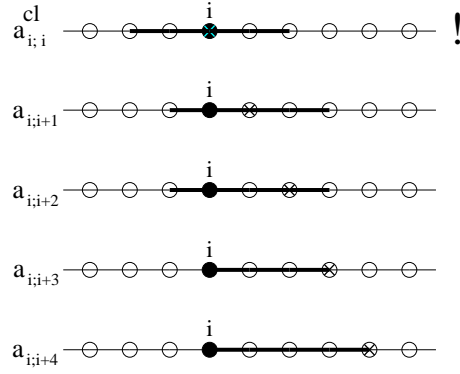


Fig. 3.6: All possible hopping coefficients that can be calculated in 4<sup>th</sup> order. Again, active bonds are depicted by thick lines. All processes that have to be considered take place on linked clusters. The initial (final) triplon positions are depicted by a filled circle (cross). They are contained in the minimum cluster (cl), which is defined by all active bonds for each coefficient. The exclamation mark next to the  $a_{i,i}^{cl}$  cluster is a reminder that one has to subtract the cluster energy  $E_0^{cl}$  to get the cluster independent hopping coefficient  $t_{i,i} = t_0$ , c.f. Eq. 3.6.4

moving the triplon from rung  $i$  to rung  $j$ . Fig. 3.6 illustrates the situation for all coefficients that can be calculated in fourth order.

### 3.6.1.3 Two triplons: $H_2$

One defines the states  $|i,j\rangle$ , denoting the eigen state of  $H_{\perp}$  with triplon 1 on site  $i$ , triplon 2 on site  $j$  and singlets on all other sites. Two triplons together can form an  $S = 0$  singlet, an  $S = 1$  triplet or an  $S = 2$  quintuplet bound state. Tab. 3.2 summarizes these nine states sorted by their total spin  $S$  and magnetic quantum number  $m$ .

By construction  $H_{\text{eff}}$  conserves the total spin  $S$  and the magnetic quantum number  $m$ . Therefore it is convenient to work in the basis given in Tab. 3.2. This table defines the states  $|i,j\rangle^{S,m}$  by the linear combinations in the third column.

Again, due to triplon conservation the action of  $H_{\text{eff}}$  on the state  $|i,j\rangle$  is to shift the triplons to site  $i'$  and site  $j'$  conserving also  $S$  and  $m$ . Nothing else is possible. In analogy to Eq. 3.6.3 of the preceding section one defines the interaction coefficients

$$a_{ij;kl}^{S,cl}(x) = {}^S\langle i,j|H_{\text{eff}}(x)|k,l\rangle^S. \quad (3.6.6)$$

The coefficients depend on the total spin  $S$  but not on the magnetic quantum number  $m$ . Hence the  $m$ -index is dropped here and in the following.

The exchange parity is determined by the total spin  $S$

$$|i,j\rangle^S = (-1)^S |j,i\rangle^S. \quad (3.6.7)$$

This means that the description can be restricted to those states  $|i,j\rangle$  for which  $i < j$ .

S	m	$ S, m \rangle, 0 \text{ triplon}$
0	0	$ s, s \rangle$
S	m	$ S, m \rangle, 1 \text{ triplon}$
1	1	$ s, t^1 \rangle$
1	0	$ s, t^0 \rangle$
1	-1	$ s, t^{-1} \rangle$
S	m	$ S, m \rangle, 2 \text{ triplon}$
2	2	$ t^1, t^1 \rangle$
2	1	$1/\sqrt{2}( t^1, t^0 \rangle +  t^0, t^1 \rangle)$
2	0	$1/\sqrt{6}( t^{-1}, t^1 \rangle + 2 t^0, t^0 \rangle +  t^1, t^{-1} \rangle)$
2	-1	$1/\sqrt{2}( t^{-1}, t^0 \rangle +  t^0, t^{-1} \rangle)$
2	-2	$ t^{-1}, t^{-1} \rangle$
1	1	$1/\sqrt{2}( t^1, t^0 \rangle -  t^0, t^1 \rangle)$
1	0	$1/\sqrt{2}( t^1, t^{-1} \rangle -  t^{-1}, t^1 \rangle)$
1	-1	$1/\sqrt{2}( t^0, t^{-1} \rangle -  t^{-1}, t^0 \rangle)$
0	0	$1/\sqrt{3}( t^0, t^0 \rangle -  t^1, t^{-1} \rangle -  t^{-1}, t^{11} \rangle)$

Table 3.2: The  $|S, m \rangle$  states. The notation is a short form of the tensor product state of any two sites situated somewhere in  $\Gamma_{\text{eff}}$

Making use of the above the irreducible two-triplon interaction coefficients  $t_{ij;kl}^S$  follow from

$$\begin{aligned}
t_{ij;kl}^S &= {}^S\langle i, j | H_2 | k, l \rangle^S = {}^S\langle i, j | H_{\text{eff}} - H_1 - H_0 | k, l \rangle^S \\
&= a_{ij;kl}^{S,\text{cl}} - E_0^{\text{cl}} \delta_{i,k} \delta_{j,l} \\
&\quad - t_{i;k}^{\text{cl}} \delta_{j,l} - t_{j;l}^{\text{cl}} \delta_{i,k} - t_{i;l}^{\text{cl}} \delta_{j,k} (-1)^S - t_{j;k}^{\text{cl}} \delta_{i,l} (-1)^S.
\end{aligned} \tag{3.6.8}$$

analogous to Eq. 9 in Ref. [171]. Again,  $E_0^{\text{cl}}$  and the one-triplon hopping coefficients  $t_{ij}^{\text{cl}}$  must be calculated on the *same* cluster as the “raw” two-triplon coefficients  $a_{ij;kl}^{\text{cl}}$ . The cluster hopping coefficients  $t_{j;l}^{\text{cl}}$  are needed only in the intermediate steps of the calculation of the irreducible interaction coefficients.

There will be no  $t_{ii;kl}$  or  $t_{ij;kk}$  since it is not possible to have two triplons on one rung at the same time. This constraint can be viewed as a hardcore repulsion interaction.

The construction of the minimum cluster needed to calculate the  $t_{ij;kl}$  in the thermodynamic limit follows the same line of argumentation as in the one-particle section. Generally, the cluster must be large enough to encompass all possible processes in order  $l$ . The minimum cluster has to include all linked bonds that can be activated in any possible interaction process of length  $l$  which leads to state  $|i', j'\rangle$  if one starts with state  $|i, j\rangle$ . Obviously the sites  $i, j, i'$  and  $j'$  must be contained in the minimum cluster and they must be connected by active bonds. All interaction coefficients of order  $l$  can be calculated on a cluster containing  $l + 1$  rungs.

For particular systems there may be symmetries, e.g., spin rotation invariance, or other particularities, e.g., nearest-neighbour exchange coupling only, which prevent certain processes from

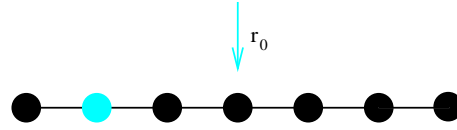


Fig. 3.7: General situation for a local observable acting on site  $r_0$  of the effective lattice. Black filled circles denote sites being in a singlet configuration. Here one triplon is created out of the triplon vacuum two sites left from  $r_0$ . The triplon is marked as a filled grey circle.

generating non-vanishing coefficients. This will be described and used later in the application chapters.

### 3.6.2 Observables

The consideration concerning the cluster size for the observables are very similar to the previously described case for the Hamiltonian. This can be seen in the formal structure of the effective observable (Eq. 3.4.15). The new part one has to account for is the creation (or annihilation) of triplons. In this work only  $T = 0$  properties are calculated. One therefore has not to perform any subtractions in the  $n$ -triplon sector of contributions with less triplons.

A locally acting observable is considered which creates triplons out of the triplon vacuum at a fixed site  $r_0$  in the system (see Fig. 3.7). In this thesis the maximum number of triplons which can be created (annihilated) by an local operator is restricted to  $N = 2$ . In the following the case of  $N = 1$  is considered, i.e. the monomials for the effective Hamiltonian and the effective observables consists only of  $\{T_0; T_{\pm 1}\}$  and  $\{T'_0; T'_{\pm 1}\}$ . The generalizations of the obtained conclusions are straightforward.

First, one-triplon configurations are considered in  $(l - 1)^{\text{th}}$  order in the perturbation operator  $x$ , i.e. there are  $(l - 1)$  operations from the Hamiltonian and one operation from the observable. The total number of operations is therefore  $l$ . One needs one operator to create the triplon, i.e. there are  $l - 1$  operations left. The linked cluster theorem then states that only processes contribute to the local observable in which all activated bonds are linked. It follows that only states occur where the triplon is connected by active bonds with the site  $r_0$ . In the latter subsection it is argued that maximum motion of one triplon is  $l$  sites in  $l^{\text{th}}$  order. One can conclude that all one-triplon states being created by the local observable are located in an interval of length  $2l - 2$  centered around  $r_0$ . All possible one-triplon states are shown in Fig. 3.8 for  $l = 4$ . Note that there are often additional symmetries like the inversion about  $r_0$ . Then one has to compute less amplitudes. This will be explained in detail in the application chapters.

It is clear that there are no operations left for the extreme states (the triplon at the maximum distance left/right from site  $r_0$ ). For these cases the minimum cluster to get the correct amplitude in the thermodynamic limit is equal to the cluster which includes the triplon site and the site  $r_0$  of the local observable. In all other cases operations are left in a given order which represent virtual fluctuations around the considered configurations, i.e. virtual hopping, interaction or creation (annihilation) processes. Here the minimum cluster has to include all bonds that can be activated

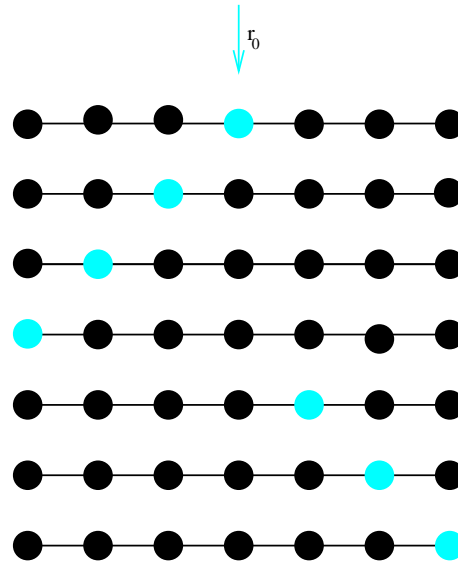


Fig. 3.8: All possible one-triplon states in third order in perturbation parameter  $x$  created by a local observable acting on site  $r_0$ . Black filled circles denote singlets and grey filled circles denote triplons.

in all processes creating the triplon at some site  $r$  by the local observable at site  $r_0$ . This is illustrated in Fig. 3.9 for  $l = 4$ .

The case of creating two triplons can be treated similarly. In  $l^{\text{th}}$  order one needs two operations to create two triplons (remember  $N = 1$ ), e.g. twice the operator  $T_1$  would give two connected triplons. This means there are only  $l - 2$  operations left. The linked cluster theorem imposes that only clusters contribute consisting of active bonds containing the sites of the two triplons and the site of the local observable  $r_0$ . The minimal cluster to get the correct amplitude for two triplons is therefore smaller than in the one-triplon case. This is illustrated for the fourth order case in Fig. 3.10.

The latter considerations are generalized easily to more than two triplons. The number of operations to get the triplons excited plus connecting the triplons is growing and therefore the number of reachable states is reduced. Additionally, the size of the minimal clusters is getting smaller. In the previous example, four-triplon states consist of four triplons on neighboring sites including site  $r_0$  because for the creation of four triplons one already needs four operations. Consequently, the creation of five triplons is not possible in fourth order.

The case of  $N > 1$  is done in the same manner as  $N = 1$ . In the application chapter the cases  $N = 1$  and  $N = 2$  are studied. Any characteristics of the  $N = 2$  case (compared to  $N = 1$ ) will be point out in the application chapters. Note that the size of the chosen clusters can be tested by enlarging the cluster. The result should not change on the larger cluster.

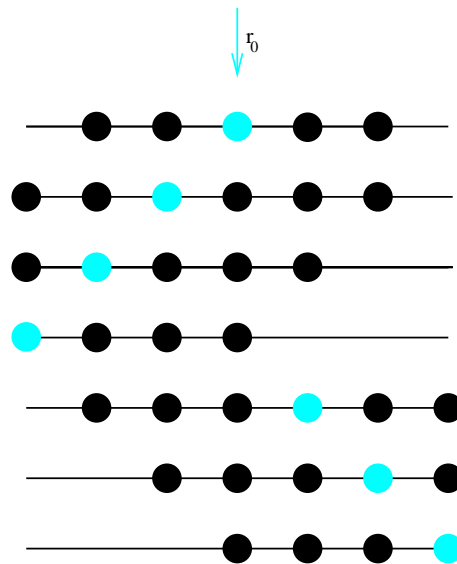


Fig. 3.9: Minimal clusters for all possible one-triplon states in third order in the perturbation parameter  $x$  created by a local observables acting on site  $r_0$ . Black filled circles denote singlets and grey filled circles denote triplons.

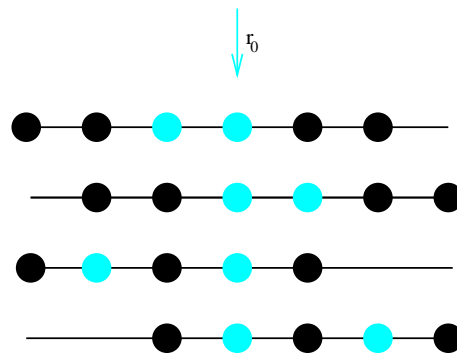


Fig. 3.10: Minimal clusters for all possible two-triplon states in third order in the perturbation parameter  $x$  created by a local observables acting on site  $r_0$ . Black filled circles denote singlets and grey filled circles denote triplons.

### 3.7 Translational invariance

In Sect. 3.3 an effective Hamiltonian is derived which is block diagonal (to the calculated order) with respect to the number of particles. A sketch of the situation is shown in Fig. 3.11. The representation of the Hamiltonian can be simplified, if the system under inspection exhibits translational symmetry. In this case it is useful to switch to a momentum basis. This will be the case for all models to be studied in this work. In the first subsection this will be elaborated for the one- and two-particle block of the effective Hamiltonian  $H_{\text{eff}}$ . The structure of the corresponding one- and two-particle matrices of  $\mathcal{O}_{\text{eff}}$  is inspected in the second subsection. In addition, also multi-particle

matrices for  $\mathcal{O}_{\text{eff}}$  are discussed focusing on the case of three particles. The results will be used in the application Chapt. 6 and Chapt. 7.

With respect to these applications the quasi-particles for each site of  $\Gamma_{\text{eff}}$  are assumed to be triplets  $t^i$ , where  $i \in \{-1, 0, 1\}$  denotes the z-component, defined above a singlet (s) ground state (triplet-vacuum). The sites of  $\Gamma_{\text{eff}}$  are equivalent to dimers as illustrated in the last section. Triplons are defined as the elementary triplets on the dimers. All quantities throughout this work will refer to the triplon as elementary particle.

### 3.7.1 Hamiltonian

The effective Hamiltonian  $H_{\text{eff}}$  is considered to be invariant under translations of the effective lattice  $\Gamma_{\text{eff}}$ . A one-triplon state is denoted by  $|r\rangle$  where  $r$  refers to the state of one triplon at site  $r$  of  $\Gamma_{\text{eff}}$  and all other sites being a singlet. For the case of two triplons the states  $|r, r'\rangle^{S, m}$  are introduced with one triplon at site  $r$  and the other at site  $r'$ . Here  $S$  is the total spin and  $m$  is the  $S^z$  component of the two-triplon state. It is assumed that the Hamiltonian conserves total spin and the total  $S^z$ -component of the spin. All models which will be studied in this work will have these additional symmetries. In Tab.3.2 all states  $|S, m\rangle$  that can be constructed for zero, one and two triplons are summarized.

In the following the structure of the one- and two-triplon sector in the momentum basis will be investigated in detail. The particular simplicity of the obtained expressions is mainly due to triplon conserving property of  $H_{\text{eff}}$ .

#### 3.7.1.1 One-triplon sector

From the thermodynamic cluster-independent hopping coefficients the one-triplon energies are constructed. The Fourier-transformed are defined as states

$$|k\rangle = \frac{1}{\sqrt{N}} \sum_r e^{-ikr} |r\rangle, \quad (3.7.1)$$

$N$  is the total number of sites in  $\Gamma_{\text{eff}}$ . Calculating the action of  $H_1$  on these states yields

$$H_1 |k\rangle = \frac{1}{\sqrt{N}} \sum_{r, d=-l_{\text{max}}}^{l_{\text{max}}} e^{-ikr} t_d |r+d\rangle \quad (3.7.2a)$$

$$= \frac{1}{\sqrt{N}} \sum_{r, d=-l_{\text{max}}}^{l_{\text{max}}} e^{-ik(r-d)} t_d |r\rangle \quad (3.7.2b)$$

$$= \sum_{d=-l_{\text{max}}}^{l_{\text{max}}} e^{ikd} t_d \underbrace{\frac{1}{\sqrt{N}} \sum_j e^{-ikj} |j\rangle}_{|k\rangle}. \quad (3.7.2c)$$

Making use of the inversion symmetry  $t_d = t_{-d}$  yields the real one-triplon dispersion

$$\omega(k; x) = \langle k | H_1(x) | k \rangle = t_0 + 2 \sum_{d=1}^{l_{\text{max}}} t_d \cos(dk), \quad (3.7.3)$$

where  $l_{\text{max}}$  is the maximum order of the perturbation series.



### 3.7.1.2 Two-triplon sector

Due to the translational invariance the momentum  $k$  is a good quantum number in the one-triplon sector and the diagonal matrix elements of the Fourier transformed states  $|k\rangle$  are the eigen energies  $\omega(k)$ . With two triplons present only the *total* momentum  $K$  is a good quantum number. The relative momentum  $q$  is not conserved and generally leads to the formation of a two-triplon continuum.

To make use of the conserved total momentum one turns to a new basis. As a first step the center-of-mass coordinates are used, i.e.,  $|i, j\rangle^S \rightarrow |r, r+d\rangle^S = (-1)^S |r+d, r\rangle^S$ , with  $r = i$  and  $d = j - i$ . The restriction  $i < j$  (see text below Eq. 3.6.7) translates to  $d > 0$ . A suitable origin is chosen, say  $k = 0$ , and the matrix element is renamed

$$t_{d;r,d'} \equiv \langle r, r+d' | H_2 | 0, d \rangle = \langle i, j | H_2 | k, l \rangle = t_{ij;kl} , \quad (3.7.4)$$

with  $d = l$ ,  $r = i$  and  $r+d' = j$ . From Eq. 3.6.8 one obtains

$$\begin{aligned} t_{d;r,d'}^S &= a_{d;r,d'}^{S,\text{cl}} - E_0^{\text{cl}} \delta_{0,r} \delta_{d,r+d'} - t_{r;0}^{\text{cl}} \delta_{d,r+d'} - t_{d;r+d'}^{\text{cl}} \delta_{0,r} \\ &\quad - t_{0;r+d'}^{\text{cl}} \delta_{d,r} (-1)^S - t_{d;r}^{\text{cl}} \delta_{0,r+d'} (-1)^S \end{aligned} \quad (3.7.5)$$

in the new basis. This is equivalent to the equations emerging from considering the special cases

$$t_{d;0,d'}^S = a_{d;0,d'}^{S,\text{cl}} - t_{d'-d}^{\text{cl}} - \delta_{d,d'} (t_0^{\text{cl}} + E^{\text{cl}}) \quad (3.7.6a)$$

$$t_{d;d-d',d'}^S = a_{d;d-d',d'}^{S,\text{cl}} - t_{d-d'}^{\text{cl}} - \delta_{d,d'} (t_0^{\text{cl}} + E^{\text{cl}}) \quad (3.7.6b)$$

$$t_{d;-d',d'}^S = a_{d;-d',d'}^{S,\text{cl}} - t_{-d-d'}^{\text{cl}} (-1)^S \quad (3.7.6c)$$

$$t_{d;d,d'}^S = a_{d;d,d'}^{S,\text{cl}} - t_{d+d'}^{\text{cl}} (-1)^S . \quad (3.7.6d)$$

Otherwise the interaction coefficients  $t_{d;r,d'}^S$  and  $a_{d;r,d'}^S$  are identical.

As a second step the states  $|r, r+d\rangle^S$  are Fourier transformed with respect to the center-of-mass variable  $(r+d/2)$

$$\begin{aligned} |K, d\rangle^S &:= \frac{1}{\sqrt{N}} \sum_r e^{iK(r+d/2)} |r, r+d\rangle^S \\ &= (-1)^S \frac{1}{\sqrt{N}} \sum_r e^{iK(r+d/2)} |r+d, r\rangle^S \\ &\stackrel{r \rightarrow r-d}{=} (-1)^S \frac{1}{\sqrt{N}} \sum_r e^{iK(r-d/2)} |r, r-d\rangle^S \\ &= (-1)^S |K, -d\rangle^S , \end{aligned} \quad (3.7.7)$$

where  $K$  is the conserved total momentum in the Brillouin zone and  $N$  is the number of sites in  $\Gamma_{\text{eff}}$ . For fixed  $K$  and  $S$  the relative distance  $d > 0$  between two triplons is the only remaining quantum number one has to keep track of.

To obtain the complete two-triplon excitation energies one has to calculate the action of

$$H_{\text{eff}} - H_0 = H_1 + H_2 \quad (3.7.8)$$

on the two-triplon states  $|K, d\rangle$ . The two addends on the right hand site are considered separately in the following.

The operator  $H_1$  can move one of the two triplons at maximum. A short calculation yields

$$\begin{aligned}
H_1|K, d\rangle^S &= \\
\frac{1}{\sqrt{N}} \sum_r e^{iK(r+d/2)} \sum_{\substack{n=-l_{\max} \\ n \neq d}}^{l_{\max}} t_n (|r+n, r+d\rangle^S + |r, r+d-n\rangle^S) \\
&= \sum_{\substack{n=-l_{\max} \\ n \neq d}}^{l_{\max}} t_n (e^{iKn/2} + e^{-iKn/2}) \times \\
&\quad \times \underbrace{\frac{1}{\sqrt{N}} \sum_r e^{iK(r+(d-n)/2)} |r, r+d-n\rangle^S}_{|K, d-n\rangle} \\
&= 2 \sum_{\substack{n=-l_{\max} \\ n \neq d}}^{l_{\max}} t_n \cos\left(K\frac{n}{2}\right) [\text{sgn}(d-n)]^S |K, |d-n\rangle^S. \tag{3.7.9}
\end{aligned}$$

Here the previously calculated matrix-elements  $t_n = t_{-n}$  (inversion symmetry) are used. Since  $d$  is restricted to  $d > 0$  the sgn-function enters the result by Eq. 3.7.7. For fixed  $K$ ,  $H_1$  now appears as a semi-infinite band matrix in the remaining quantum number  $d$ . Independent of the size of the initial distance  $d > 0$  between the two triplons,  $H_1$  will produce states where the distances between the triplons are incremented or decremented by  $l_{\max}$  at maximum. If the initial distance  $d$  is larger than  $l_{\max}$ ,  $H_1$  continues to produce the same matrix elements on and on for all  $d > l_{\max}$ , i.e. the matrix representing  $H_1$  in the chosen basis for fixed  $K$  is semi-infinite with a repeated pattern in the tail. The head of  $H_1$ , i.e., the  $l_{\max} \times l_{\max}$  block between states with  $d \leq l_{\max}$ , contains matrix elements with a somewhat more complicated structure. Here the matrix element between the starting distance  $d$  and the final distance  $d'$  is a sum of the direct process  $d \rightarrow d'$ , where one of the triplons has hopped  $n$  rungs to the right ( $n > 0$ ) or to the left ( $n < 0$ ) with  $d - n = d' > 0$ , and the indirect process with  $d - n = -d' < 0$ . The situation is sketched in Fig. 3.11. The matrix  $H_1$  comprises the full thermodynamic one-triplon dynamics in the two-triplon sector for the given order  $l_{\max}$ .

The situation is more complex for  $H_2$ . In a first step one finds

$$\begin{aligned}
H_2|K, d\rangle^S &= \\
\frac{1}{\sqrt{N}} \sum_r e^{iK(r+d/2)} \sum_{\substack{\max\{n+d', d-n\} \\ \leq l_{\max}}} t_{d;n,d'} |r+n, r+n+d'\rangle^S &= \\
\sum_{\substack{\max\{n+d', d-n\} \\ \leq l_{\max}}} t_{d;n,d'} e^{iK(-n+(d-d')/2)} |K, d'\rangle^S, \tag{3.7.10}
\end{aligned}$$

with the two integers  $n \in \mathbb{Z}$  and  $d' \in \mathbb{N}$  as summation indices. The positive distances  $d$  and  $d'$  must be smaller or equal to  $l_{\max}$ , since a maximum of  $l_{\max}$  linked bonds can be produced in this order and all four triplons sites (the two initial sites and the two final sites) must be contained in

the resulting linked cluster. The  $t_{d;n,d'}$  are the matrix elements of  $H_2$  defined in Eq. 3.7.5. The last equality follows from substituting the summation-index  $r \rightarrow r + n$ .

To simplify the expression further inversion symmetry is used. One has

$$t_{d;r',d'} = \langle r'', r'' + d' | H_2 | r, r + d \rangle, \quad (3.7.11)$$

with  $r' = r'' - r$ . The thermodynamic interaction coefficient  $t_{d;r',d'}$  is associated with a fixed constellation of initial and final triplon pairs. A configuration CON is defined by the set of four positions given by these two pairs  $\text{CON} = \{r, r + d, r'', r'' + d'\}$ . Let  $s$  denote the middle of this configuration  $s = (\max(\text{CON}) - \min(\text{CON}))/2$ . Reflecting a configuration about  $s$  and interchanging the triplon positions in both initial and final triplon pairs gives

$$\begin{aligned} t_{d;r',d'} &= \langle r'', r'' + d' | H_2 | r, r + d \rangle \\ &= \langle 2s - r'' - d', 2s - r'' | H_2 | 2s - r - d, 2s - r \rangle \\ &= t_{d;d-d'-r',d'}. \end{aligned} \quad (3.7.12)$$

Possible minus signs cancel since they appear twice. One can now split the sum over  $n$  in Eq. 3.7.10 in three parts,  $n > (d - d')/2$ ,  $n < (d - d')/2$  and  $n = (d - d')/2$ . The second sum is indexed back to  $n > (d - d')/2$  by making use of  $\sum_{n < j} a_n = \sum_{n > j} a_{2j-n}$  where  $j := (d - d')/2$

$$\begin{aligned} H_2 |K, d\rangle^S &= \sum_{\substack{\max\{n+d', d-n\} \leq l_{\max} \\ n > (d-d')/2 \in \mathbb{Z}}} \left[ t_{d;n,d'} e^{iK(-n+(d-d')/2)} |K, d'\rangle^S \right. \\ &\quad \left. + t_{d;d-d'-n,d'} e^{iK(n-(d-d')/2)} |K, d'\rangle^S \right] \\ &\quad + \sum_{\substack{\max\{n+d', d-n\} \leq l_{\max} \\ n = (d-d')/2 \in \mathbb{Z}}} t_{d;(d-d')/2,d'} |K, d'\rangle^S \\ &= 2 \sum_{\substack{\max\{n+d', d-n\} \leq l_{\max} \\ n > (d-d')/2 \in \mathbb{Z}}} t_{d;n,d'} \cos[K(n - (d - d')/2)] |K, d'\rangle^S \\ &\quad + \sum_{\substack{\max\{n+d', d-n\} \leq l_{\max} \\ n = (d-d')/2 \in \mathbb{Z}}} t_{d;(d-d')/2,d'} |K, d'\rangle^S. \end{aligned} \quad (3.7.13)$$

In contrast to  $H_1$  the matrix representing  $H_2$  is of finite dimension due to the finite range of the contributing processes (finite maximum order) expressed by the restrictions of the sums appearing in Eq. 3.7.13. Fig. 3.11 sketches the situation.

Finally, the sum of the two matrixes  $H_1$  and  $H_2$  with respect to basis (3.7.7) comprises the complete two-triplon dynamics. At large distances the two-triplon dynamics is governed by independent one-triplon hopping. At smaller distances an additional two-particle interaction occurs given by  $t_{d;r,d'}$  connecting the state  $|r, r + d'\rangle$  with state  $|0, d'\rangle$ . The sum  $H_1 + H_2$  gives the combined effect of one-triplon hopping and two-triplon interaction.

It is important to note in which sense the used approach treats processes of a certain range. Taking the perturbation expansion up to order  $l_{\max}$  allows to calculate the irreducible two-particle interaction up to a distance  $l$  between the two particles correctly within order  $l_{\max}$ . No processes involving larger distances appear. But the part of the two-particle sector that can be described by

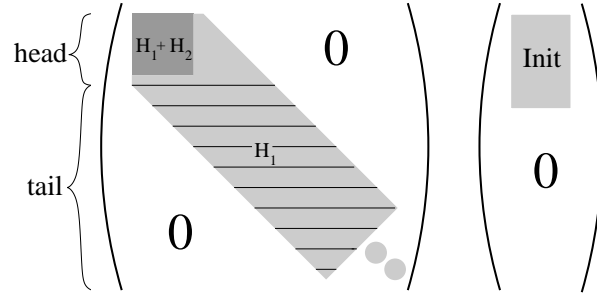


Fig. 3.11: The left part of the figure schematically shows the matrix representation of  $H_1$  and  $H_2$  in the two-triplon  $\{|K, d\rangle\}$  basis (3.7.7). The matrix  $H_1$  has elements in the whole grey area, while  $H_2$  has elements in the dark grey area only.  $H_2$  is a finite  $l_{\max}^W \times l_{\max}^W$  matrix and  $H_1$  a semi-infinite band matrix with width  $2l_{\max}^T$ , see Eqs. (3.7.9) and (3.7.13) for further information. The sum of  $H_1$  and  $H_2$  represents  $H_{\text{eff}}$  in the two-triplon sector to the given orders. The right part shows the initial vector  $|\text{Init}\rangle = \mathcal{O}_{\text{eff}}|0\rangle$  as calculated in Sect. 3.7.2 for the two-triplon sector.  $|\text{Init}\rangle$  is a vector of dimension  $l_{\max}^O$  in the  $\{|K, d\rangle\}$  basis. The Green's function  $\mathcal{G}$  (Eq. 4.1.2) is calculated by tridiagonalization, more information in Sect. 4. For  $K$  and  $x$  fixed, the elements of the matrix and the vector reduce to real numbers.

one-particle dynamics alone is taken into account for *all* distances between the two particles and describes hopping processes of range  $\leq l_{\max}$  correctly within order  $l_{\max}$ .

### 3.7.2 Observable

The effective operators  $\mathcal{O}_{\text{eff}}$  can be decomposed in a sum of cluster-additive operators  $\mathcal{O}_{d,n}$ , see Eq. 3.2.16, for which the linked cluster theorem can be used. Here  $d$  indicates how many particles are created ( $d \geq 0$ ) or destroyed ( $d < 0$ ) by  $\mathcal{O}_{d,n}$ . The subindex  $n \geq 0$  indicates the minimum number of particles that must be present for  $\mathcal{O}_{d,n}$  to have a non zero action. The action of the operator  $\mathcal{O}_{d,n}$  on a state containing less than  $n$  particles is zero.

To be more specific, let  $\mathcal{O}$  be a *locally* acting observable injecting triplons at a specific site  $r$  of  $\Gamma_{\text{eff}}$ . Then the effective observable reads

$$\begin{aligned}
 \mathcal{O}_{\text{eff}}(r)|0\rangle &= \sum_{d \geq 0} \mathcal{O}_{d,0}(r)|0\rangle \\
 &= c|0\rangle + \sum_{n=-l_{\max}}^{l_{\max}} c_n|r+n\rangle + \\
 &\quad + \sum_{\substack{n,n' \\ |n|+|n'| \leq l_{\max}}} c_{n,n'}|r+n, r+n'\rangle + \dots .
 \end{aligned} \tag{3.7.14}$$

The restriction  $|n| + |n'| \leq l_{\max}$  for the third sum reflects the fact that the two triplons, after being injected, cannot undergo more site-to-site hops in total than the maximum order  $l_{\max}$ .

Once the coefficients  $c$  are calculated the spectral weights  $l_N$  are accessible, which are contained

in the different triplon-sectors characterized by the number  $N$  of triplons injected

$$\begin{aligned}
I_N &= \langle 0 | \mathcal{O}_{-N,0}(r) \mathcal{O}_{N,0}(r) | 0 \rangle \\
&= \sum_{n_1, \dots, n_N} |\langle r + n_1, \dots, r + n_N | \mathcal{O}_{N,0}(r) | 0 \rangle|^2 \\
&= \sum_{n_1, \dots, n_N} |c_{n_1, \dots, n_N}|^2 .
\end{aligned} \tag{3.7.15}$$

If the total weight  $I_{\text{tot}}$  of the operator is also known, for instance via the sum rule

$$I_{\text{tot}} = \langle 0 | \mathcal{O}^2 | 0 \rangle - \langle 0 | \mathcal{O} | 0 \rangle^2 ; \tag{3.7.16}$$

the *relative* weights of the individual particle sectors  $I_N/I_{\text{tot}}$  can be calculated. They serve as an important criterion to judge the applicability of the approach presented here. If most of the weight can be found in sectors of low quasi-particle number and sectors of higher triplon number can be safely neglected the approach will work fine. The chosen triplons constitute a suitable basis to describe the system. This argument will be used in the application chapters to argue that the triplon is a well-suited particle to describe generically one-dimensional spin systems. It will be found that most of the spectral weight is captured by one and two triplons [82].

So far *local* observables  $\mathcal{O}(r)$  were considered. A real experiment, however, couples to the system in a global fashion. Due to translational invariance the injected particles (here triplons) have a total momentum  $K$ . Thus one defines the *global* observables in momentum space representations

$$\begin{aligned}
\mathcal{O}_{\text{eff}}(K) | 0 \rangle &= \sum_{d \geq 0} \mathcal{O}_{d,n}(K) | 0 \rangle \\
&= \sum_{p \geq 0} \frac{1}{\sqrt{N}} \sum_{r=1}^N e^{iKr} \mathcal{O}_{p,0}(r) | 0 \rangle ,
\end{aligned} \tag{3.7.17}$$

where  $N$  is the number of sites of the effective lattice. The one- and two-triplon sectors can be investigated separately. In the one-triplon sector one has (here  $K$  is the one-triplon momentum  $k$ )

$$\begin{aligned}
\mathcal{O}_{1,0}(k) | 0 \rangle &= \frac{1}{\sqrt{N}} \sum_{r=1}^N e^{ikr} \sum_{n=1-l_{\text{max}}}^{l_{\text{max}}-1} c_n | r + n \rangle \\
&= \sum_n c_n e^{-ikn} \frac{1}{\sqrt{N}} \sum_r e^{ikr} | r \rangle \\
&= \sum_n c_n e^{-ikn} | k \rangle .
\end{aligned} \tag{3.7.18}$$

The same definition is used for  $|k\rangle$  as introduced in Sect. 3.7.1. Due to inversion symmetry  $c_n = c_{-n}$  holds. Thus Eq. 3.7.18 simplifies to

$$\langle k | \mathcal{O}_{1,0}(k) | 0 \rangle = A_k = c_0 + 2 \sum_{n=1}^{l_{\text{max}}-1} c_n \cos(kn) . \tag{3.7.19}$$

Somewhat more complex is the two-triplon sector

$$\begin{aligned}
\mathcal{O}_{2,0}(K)|0\rangle &= \frac{1}{\sqrt{N}} \sum_{r=1}^N e^{iKr} \sum_{n,n'} c_{n,n'} |r+n, r+n'\rangle \\
&= \sum_{n,d} c_{n,n+d} e^{-iK(n+d/2)} \frac{1}{\sqrt{N}} \sum_r e^{iK(r+d/2)} |r, r+d\rangle \\
&= \sum_{n,d} c_{n,n+d} e^{-iK(n+d/2)} |K, d\rangle \\
&= \sum_d A_{K,d} |K, d\rangle, \tag{3.7.20}
\end{aligned}$$

where one defines the relative distance  $d = n' - n$  between the two injected triplons. The definition of  $|K, d\rangle$  is taken from Sect. 3.7.1. Again, inversion symmetry, here  $c_{n,n'} = (-1)^S c_{-n,-n'}$ , can be used to obtain real results for the coefficients  $A_{K,d}$ . The variable  $S \in \{0, 1, 2\}$ , which is a good quantum number, denotes the total spin of the injected triplon pair.

The action of  $\mathcal{O}_{\text{eff}}$  from the ground state into the two-triplon space produces the states  $|K, d\rangle$  with  $0 < d \leq l_{\text{max}}$  in order  $l_{\text{max}}$ . Thus, for fixed  $K$ , the action of  $\mathcal{O}_{\text{eff}}$  may be visualized as a vector in the remaining quantum number  $d$  of which the first  $l_{\text{max}}$  entries are the  $A_{K,d}$  of Eq. 3.7.20. All other entries are zero. This vector, labeled initial vector  $|\text{Init}\rangle$  for reasons given in Ch. 4, is depicted in Fig. 3.11 together with the matrix representing  $H_{\text{eff}}$  for fixed  $K$  in the two-triplon sector.

### 3.8 Chapter summary

In this chapter an approach is presented to calculate energies and observables for quantum multi-particle systems defined on lattices. The chapter has two main parts. In the first part (Sect. 3.2), the existence of a mapping of the original problem to an effective one is assumed in which the number of elementary excitations, the so-called (quasi-)particles, is conserved. The general structure of the effective Hamiltonians and the observables is analysed. It is found that a classification of the various contributions in terms of the number of particles concerned is most advantageous. To this end a notation in second quantization is introduced which does not, however, require non-interacting fermions or bosons. Generically, hard-core bosons are dealt with in this thesis.

The formulation in second quantization is found to be particularly intuitive. It provides the irreducible quantities in a natural way on the *operator level*. They display cluster additivity. One has to emphasize that the definition of irreducible operators is not a trivial task if a strong-coupling situation is considered as was done in the present chapter. No limit of non-interacting bosons or fermions is assumed. Since the definition of irreducible operators is completely general it allows to compute the  $n$ -particle contribution for arbitrary  $n$ .

The *irreducible* interactions and vertex corrections possess a cluster expansion so that they can be computed on finite clusters provided that the Hamiltonian is of finite range. This property is the basis for the real-space treatment of many spin systems.

In the second part (Sects. 3.3 and 3.4), an actual mapping is described which provides effective operators. The mapping is based on continuous unitary transformations. In this thesis the focus

is laid on the perturbatively construction of the mapping. In Sect. 3.3, the treatment of the Hamiltonian is given. The computation of the effective Hamiltonian requires the solution of a set of recursive non-linear differential equations. For the perturbative set-up under study these equations can be solved in full generality, i.e. no particular details of the model need to be known.

In Sect. 3.4, the calculational steps to compute effective observables are given. Again, recursive differential equations have to be solved. But they are linear since the transformation of the Hamiltonian is known. For the perturbative set-up under study also the equations for the observables can be solved in full generality, i.e. no particular details of the model need to be known.

The above approach will be used in the following chapters to compute spectral functions, i.e. dynamical correlations, for low-dimensional quantum spin systems, namely a dimerized and frustrated spin-chain and a two-leg ladder with additional four-spin interaction.

## 4 Spectral densities for effective operators

In the last chapter, the determination of an effective Hamiltonian  $H_{\text{eff}}$  and effective observables  $\mathcal{O}_{\text{eff}}$  obtained by a particle conserving continuous unitary transformation has been described. These can be directly use to study energetical properties or spectral weights. In this chapter the problem of calculating  $T = 0$  spectral densities from these effective operators is tackled. Spectral densities provide informations on the density of excitations and on the dynamical correlations in the considered system. The dynamical correlation are directly measurable in scattering experiments and therefore of great importance. After a general introduction, the calculation of one- and two-particle spectral densities is explained in detail. Translational invariance of  $H_{\text{eff}}$  and  $\mathcal{O}_{\text{eff}}$  is assumed throughout the chapter. This symmetry is present in all applications to be discussed in the later chapters.

### 4.1 General considerations

For some given observable  $\mathcal{O}$  the  $T = 0$  momentum and energy resolved spectral density  $I$  is given by

$$I(\mathbf{k}, \omega) = -\frac{1}{\pi} \text{Im} G^{\mathcal{O}^+}(\mathbf{k}, \omega), \quad (4.1.1)$$

where  $G^{\mathcal{O}^+}(\mathbf{k}, \omega)$  is the retarded zero temperature Green's function

$$G^{\mathcal{O}^+}(\mathbf{k}, \omega) = \left\langle 0 \left| \mathcal{O}^\dagger(\mathbf{k}) \frac{1}{\omega - [H(\mathbf{k}) - E_0] + i0^+} \mathcal{O}(\mathbf{k}) \right| 0 \right\rangle. \quad (4.1.2)$$

The ground state of the system is denoted by  $|0\rangle$ . The ground state energy  $E_0$  is subtracted in order to account for the fact that an actual experiment can measure energy-differences from the ground state only.

The physics contained in spectral densities consists of three parts. The observable  $\mathcal{O}(\mathbf{k})$  creates excitations with total momentum  $\mathbf{k}$  from the vacuum  $|0\rangle$  with some probability depending on the considered observable. Every observable/measurement opens therefore a special window on the system or equally on the Hamiltonian  $H$ . The spectral density is proportional to the energy and momentum resolved intensity of scattering experiments. The second and third part is contained in the Hamiltonian  $H$ . There is single particle motion and two-particle or multi-particle interaction. The interplay of dynamics, interaction and matrix elements defines the physical structure of spectral densities. Spectral densities contain therefore a lot of information about the system and about the measurement.

The next important step is to use the particle number to classify the spectral density of the effective system. In the following it will be shown that the spectral density for the effective model separates



into a sum over all particle channels

$$I_{\text{eff}}(\mathbf{k}, \omega) = \sum_n I_{n,\text{eff}}(\mathbf{k}, \omega). \quad (4.1.3)$$

This can be seen by inserting  $U^\dagger U$  in the equation for  $I(k, \omega)$ :

$$\begin{aligned} I_{\text{eff}}(\mathbf{k}, \omega) &= -\frac{1}{\pi} \text{Im} \left\langle 0 \left| U^\dagger U \mathcal{O}^\dagger(\mathbf{k}) U^\dagger U \frac{1}{\omega - [H(\mathbf{k}) - E_0] + i0^+} U^\dagger U \mathcal{O}(\mathbf{k}) U^\dagger U \right| \right\rangle \\ &= -\frac{1}{\pi} \text{Im} \left\langle \hat{0} \left| \mathcal{O}_{\text{eff}}^\dagger(\mathbf{k}) \frac{1}{\omega - [H_{\text{eff}}(\mathbf{k}) - E_0] + i0^+} \mathcal{O}_{\text{eff}}(\mathbf{k}) \right| \hat{0} \right\rangle \\ &= \sum_n \left\{ -\frac{1}{\pi} \text{Im} \left\langle \hat{0} \left| \mathcal{O}_{\text{eff}}^{n,0\dagger}(\mathbf{k}) \frac{1}{\omega - [H_{\text{eff}}^n(\mathbf{k}) - E_0] + i0^+} \mathcal{O}_{\text{eff}}^{n,0}(\mathbf{k}) \right| \hat{0} \right\rangle \right\}, \quad (4.1.4) \end{aligned}$$

where  $|\hat{0}\rangle = U|0\rangle$  is the transformed ground state. The latter step is a direct consequence of block-diagonality of  $H_{\text{eff}}$ . Therefore one can calculate the contributions of the individual particle sectors separately. In each block the complex many body problem reduces to a few-body problem. In the following the one- and two-particle spectral densities are discussed in detail. A generalization to more particles is straightforward. It will be given after the discussion of the latter cases.

### 4.1.1 One-particle spectral density

In the case of a translational invariance system the calculation of the spectral density in the one-particle channel is particularly simple. Using Dirac's identity

$$\frac{1}{x - x_0 \pm i0^+} = \mathcal{P} \frac{1}{x - x_0} \mp i\pi \delta(x - x_0), \quad (4.1.5)$$

where  $\mathcal{P}$  denotes Cauchy's principle value, one finds

$$\begin{aligned} I_{\text{eff}}^{1,0}(\mathbf{k}, \omega) &= \left\langle \hat{0} \left| \mathcal{O}_{\text{eff}}^{1,0\dagger}(\mathbf{k}) \delta(\omega - H_{\text{eff}}^1) \mathcal{O}_{\text{eff}}^{1,0}(\mathbf{k}) \right| \hat{0} \right\rangle \\ &= |A_{\mathbf{k}}|^2 \langle \mathbf{k} | \delta(\omega - H_{\text{eff}}^1) | \mathbf{k} \rangle \\ &= |A_{\mathbf{k}}|^2 \delta(\omega - \omega(\mathbf{k})). \quad (4.1.6) \end{aligned}$$

The one-particle dispersion  $\omega(\mathbf{k})$  and the one-particle amplitude  $A_{\mathbf{k}}$  are readily given by Eqs. 3.7.3 and 3.7.19, respectively. At each point  $(\mathbf{k}, \omega(\mathbf{k}))$  the corresponding weight is given by the square of the modulus of  $A_{\mathbf{k}}$  which is a polynomial in  $x$ . The result is thus obtained by assigning a  $\delta$ -function with corresponding weight  $|A_{\mathbf{k}}|^2$  to each point  $(\mathbf{k}, \omega(\mathbf{k}))$ .

### 4.1.2 Two-particle spectral density

The evaluation of the two-particle spectral density is done by tridiagonalization. This leads to the continued fraction expression ( [199–201], for overviews see Refs. [202, 203])

$$I_{\text{eff}}^{2,0} = -\frac{1}{\pi} \text{Im} \left[ \frac{\langle \hat{0} | \mathcal{O}_{\text{eff}}^{2,0\dagger}(\mathbf{k}) \mathcal{O}_{\text{eff}}^{2,0}(\mathbf{k}) | \hat{0} \rangle}{\omega - a_0 - \frac{b_1^2}{\omega - a_1 - \frac{b_2^2}{\omega - \dots}}} \right] = -\frac{1}{\pi} \text{Im} \left[ \frac{\langle \hat{0} | \sum_d |A_{\mathbf{k},d}|^2 | \hat{0} \rangle}{\omega - a_0 - \frac{b_1^2}{\omega - a_1 - \frac{b_2^2}{\omega - \dots}}} \right]. \quad (4.1.7)$$

The amplitudes  $A_{\mathbf{k},d}$  are given by Eq. 3.7.20. The repeated application of  $H_{\text{eff}} - H_0 = H_1 + H_2$  on the initial two-particle momentum state  $|\text{init}\rangle = |f_0\rangle = \mathcal{O}_{\text{eff}}^{2,0}(\mathbf{k})|\hat{0}\rangle$  enables the calculation of the coefficients  $a_i$  and  $b_i^2$ . Setting the states  $|f_{n(0)}\rangle$  to zero the recursion

$$|f_{n+1}\rangle = (H_1 + H_2)|f_n\rangle - a_n|f_n\rangle - b_n^2|f_{n-1}\rangle \quad (4.1.8)$$

generates a set of orthogonal states, if the coefficients are defined according to

$$a_n = \frac{\langle f_n|(H_1 + H_2)|f_n\rangle}{\langle f_n|f_n\rangle}, \quad b_{n+1}^2 = \frac{\langle f_{n+1}|f_{n+1}\rangle}{\langle f_n|f_n\rangle}. \quad (4.1.9)$$

In the generated  $\{|f_n\rangle\}$ -basis  $H_{\text{eff}}$  is a tridiagonal matrix, where the  $a_i$  are the diagonal elements and the  $b_i$  are the elements on the second diagonal. All other matrix elements are zero [204].

Fig. 3.11 illustrates the procedure for the two-particle sector. For fixed momentum  $\mathbf{k}$  the relative distance  $d$  between the two particles is the only remaining quantum number. In this basis  $H_1 + H_2$  is represented as a matrix (left side). Its matrix elements are polynomials in the perturbation parameter  $x$ . This matrix has to be applied to the vector  $|f_0\rangle = |\text{init}\rangle$  (right side), whose components  $A_{\mathbf{k},d}$  are also polynomials in  $x$  for fixed  $\mathbf{k}$ .

The pure two-particle interaction  $H_2$  is a finite matrix of dimension  $d_{\text{max}}$  in this basis. The interaction mixes only the first  $d_{\text{max}}$  components in the states  $|f_n\rangle$ . In contrast to this,  $H_1$  is a semi-infinite band matrix generating finite components in the state  $|f_{n+1}\rangle$  for larger  $d$  where there have been zeros in the previous state  $|f_n\rangle$ . The range of non-zero components in  $|f_n\rangle$  grows with each application of  $H_1$ . The width of the band matrix depends of the maximal order of the perturbation. The amount of non-zero components in  $|f_n\rangle$  additionally generated in each application is correlated with the width of  $H_1$  and on the size of the off-diagonal elements.

### 4.1.3 $N$ -particle spectral density

The generalization to calculate the spectral density for more than two particles is straightforward. For  $N$  particles one has to consider the conserved total momentum  $\mathbf{k}$  and  $(n-1)$  relative distances between the particles. Then, for fixed  $\mathbf{k}$ ,  $H_{\text{eff}}$  and  $|\text{init}\rangle$  are represented by a matrix and a vector, but their appearance becomes more complicated for increasing number of particles. The effective Hamiltonian consists of  $N$  parts:  $H_{\text{eff}} = H_1 + H_2 + \dots + H_N$ . It might be a good approximation for many physical systems to approximate the  $N$ -particle effective Hamiltonian by the contributions of small particle number, namely  $H_1$  and  $H_2$ . This approximation means to restrict the physical processes of  $N$  particles to one-particle dynamics and two-particle interactions.

### 4.1.4 Limitations

The chosen method to evaluate the effective spectral densities introduces no quantitative finite size effects. The problem of calculating the spectral density for a given  $N$ -particle effective Hamiltonian and observable comprises the quantum numbers  $\mathbf{k}$  and the relative distances  $d_i$  between the particles. In the two-particle sector one has two quantum numbers, the total momentum  $\mathbf{k}$  and

the relative distance  $d$  between the two particles. The calculations are in the thermodynamic limit. The only limitation which enters the calculation is the range of the relative distances  $d_i$ .

The main error for  $d_i$  is caused by the finiteness of the perturbative processes treated in the calculations. The true many-particle interactions are accounted for, only if all involved particles are within a certain distance to each other. This approximation is controlled, since one generically observes a rather sharp drop of the interaction matrix elements with increasing distances. Especially gapped system which are tackled in this work are well suited due to the finite correlation lengths. Difficulties arises if the correlations drop slowly with increasing distances. This point will be discussed in more detail in the case of the dimerized and frustrated spin-chain where the limit of vanishing dimerization is accompanied by a diverging correlation length.

Another error for  $d$  is introduced by truncating the continued fraction expansion of the effective Green's function. However, allowing  $10^4$  distances as in the one-dimensional spin-systems considered here should guarantee, that this additional error is very small in comparison to the error introduced by truncating the perturbative expansion.

The finiteness of the continued fraction can be partly compensated by suitable terminations as will be discussed in the next section for the two-particle sector of generic one-dimensional gapped systems.

## 4.2 Terminators for one-dimensional gapped systems

The outcome of the tridiagonalization procedure discussed in the last section is a finite continued fraction. The effective Green's function has poles at the zeros of the denominator. The effective spectral density of a truncated continued fraction is therefore a collection of  $\delta$ -peaks representing the true spectral density which consists generically of continua and single states like bound states. A slight broadening of  $I$  via  $\omega \rightarrow \omega + i\delta$  (small  $\delta$ ) in  $\mathcal{G}$  will transform the  $\delta$ -peaks into lorentzians. This process is illustrated in Fig. 4.1. Truncation of the continued fraction introduces therefore a finite resolution. The use of a finite broadening will be often helpful in comparing theoretical calculated spectral densities with experimental data. Here the finite broadening can be used to mimic the finite resolution of the experiment or the amount of disorder or various scattering processes not included in the considered model Hamiltonian  $H$ . However, theoretically the aim is a perfect resolution of  $I(\mathbf{k}, \omega)$  as a smooth function by introducing proper terminators of the continued fraction. To this end, the one-dimensionality of the considered model can be exploited.

The main ingredient for a proper termination of the continued fraction is the fact that the (upper) lower band edges ( $\epsilon_{ub}$ )  $\epsilon_{lb}$  of the two-particle continuum can be calculated directly from the one-particle dispersion  $\omega(\mathbf{k})$  for fixed momentum  $\mathbf{k}$ . All energies of the two-particle continuum are seized by

$$\omega_2(k, q) = \left[ \omega_1 \left( \frac{k}{2} + q \right) + \omega_1 \left( \frac{k}{2} - q \right) \right], \quad (4.2.1)$$

where  $q \in [-\pi, \pi]$  denotes the relative momentum of the two particles. The determination of the band edges is therefore equivalent to the determination of the global maximum and minimum of

$\omega_2(k, q)$

$$\begin{aligned}\epsilon_{\text{ub}}(k) &= \max_q(\omega_2(k, q)) \\ \epsilon_{\text{lb}}(k) &= \min_q(\omega_2(k, q)).\end{aligned}\quad (4.2.2)$$

For fixed  $\mathbf{k}$  the upper and lower band edges  $\epsilon_{\text{ub}}$  and  $\epsilon_{\text{lb}}$  give the values to which the continued fraction coefficients  $a_i$  and  $b_i$  should converge for  $i \rightarrow \infty$ . One finds [202]

$$\begin{aligned}a_\infty &= \frac{\epsilon_{\text{ub}} + \epsilon_{\text{lb}}}{2} \\ b_\infty &= \frac{\epsilon_{\text{ub}} - \epsilon_{\text{lb}}}{4}.\end{aligned}\quad (4.2.3)$$

The next point is to include the knowledge that the system is gapped. The elementary excitations are massive and show quadratic behavior at the dispersion extrema. One concludes that the one-particle dispersion  $\omega_1(\mathbf{k})$  is two-fold continuously differentiable. Obviously  $\omega_2(\mathbf{k}, q)$  has this property, too. It follows that the density of states of the one-dimensional system shows square root singularities at the band edges. The two particles, giving rise to the continuum of states, are assumed to be asymptotically free. In conclusion, a square root termination for the continued fraction is appropriate: all listed properties lead to a convergent behavior of  $a_i$  and  $b_i^2$  [202, 203] with

$$\begin{aligned}a_i &= a_\infty + \mathcal{O}(1/i^3) \\ b_i &= b_\infty + \mathcal{O}(1/i^3)\end{aligned}\quad (4.2.4)$$

and it is well justified to assume  $a_i$  and  $b_i$  to be constant beyond a certain fraction depth  $i$ . Hence one defines the following terminators

$$\begin{aligned}\tau_b &= \frac{1}{2b_\infty^2} \left( \omega - a_\infty + \sqrt{-D} \right), \text{ below continuum} \\ \tau_i &= \frac{1}{2b_\infty^2} \left( \omega - a_\infty - i\sqrt{D} \right), \text{ within continuum} \\ \tau_u &= \frac{1}{2b_\infty^2} \left( \omega - a_\infty - \sqrt{-D} \right), \text{ above continuum,}\end{aligned}\quad (4.2.5)$$

where

$$D = 4b_\infty^2 - (\omega - a_\infty)^2. \quad (4.2.6)$$

The choice of signs in the terminators is a consequence of the asymptotic behavior of Green's functions, namely  $G(\omega) \rightarrow 1/\omega$  for large  $\omega$  and that one aims at the retarded Green's function. The  $b_i^2$  calculated last in Eq. 4.1.7 is multiplied by the appropriate terminator depending on the energy range of interest. Taking the imaginary part of the resulting expression for the case within the continuum yields the continuous part of the spectral density  $I$  in the thermodynamic limit. The continuum is displayed very precisely

For illustration, an elliptic spectral density

$$I(\omega) = \frac{1}{2\pi b^2} \sqrt{4b^2 - (\omega - a)^2}, \quad (4.2.7)$$

is depicted as solid black curve in Fig. 4.1. The corresponding Green's function can be expressed as

$$\mathcal{G}(\omega) = \frac{1}{\omega - a - \frac{b^2}{\omega - a - \frac{b^2}{\dots}}} = \frac{1}{\omega - a - b^2 \tau_i(\omega)}, \quad (4.2.8)$$

with

$$\tau_i(\omega) = \mathcal{G}(\omega) = \frac{1}{2b^2} \left( \omega - a - i\sqrt{4b^2 - (\omega - a)^2} \right) \quad (4.2.9)$$

Extracting the imaginary part of  $\mathcal{G}$  one ends with  $I(\omega) = -\frac{1}{\pi} \text{Im} \mathcal{G}(\omega)$ . This simple example illustrates how the terminator  $\tau_i$  for the continued fraction within a continuum is used. The resulting spectral density is the black line in Fig. 4.1. For systems which are more complicated the coefficients  $a_i$  and  $b_i$  are functions of  $i$  which asymptotically converges to constants for large  $i$ . In these cases one calculates as many coefficients as possible and multiplies the terminator to the last obtained  $b_i^2$ .

In the case of bound states the effective Green's function can be written for fixed total momentum  $\mathbf{k}$

$$g_{\text{eff}}^{\mathcal{O}}(\omega) = \frac{\langle \hat{\mathcal{O}} | \mathcal{O}_{\text{eff}}^{2,0\dagger} \mathcal{O}_{\text{eff}}^{2,0} | \hat{\mathcal{O}} \rangle}{\omega - f(\omega)} \quad (4.2.10)$$

where the function  $f(\omega)$  is a real-valued function (compare terminations  $\tau_b$  and  $\tau_u$ ). The position of possible bound states is given by the zeros of  $g(\omega) = \omega - f(\omega)$ . Let  $\omega_0$  be the energy of a bound state or equivalently a zero of the function  $g(\omega)$ . Then one can expand the function  $g(\omega)$  in  $\omega - \omega_0$  to first order and obtains for the effective Green's function

$$g_{\text{eff}}^{\mathcal{O}}(\omega) \approx \frac{\langle \hat{\mathcal{O}} | \mathcal{O}_{\text{eff}}^{2,0\dagger} \mathcal{O}_{\text{eff}}^{2,0} | \hat{\mathcal{O}} \rangle}{(\omega - \omega_0)(1 - \partial_{\omega} f(\omega))}. \quad (4.2.11)$$

Using Dirac's identity and implying  $G^{\mathcal{O}}$  to be a retarded Green's function, one concludes for the effective spectral density

$$I_{\text{eff}}(\omega)|_{\omega \approx \omega_0} = -\frac{1}{\pi} \text{Im} g_{\text{eff}}^{\mathcal{O}}(\omega) = \frac{\langle \hat{\mathcal{O}} | \mathcal{O}_{\text{eff}}^{2,0\dagger} \mathcal{O}_{\text{eff}}^{2,0} | \hat{\mathcal{O}} \rangle}{1 - \partial_{\omega} f(\omega_0)} \delta(\omega - \omega_0). \quad (4.2.12)$$

Bound states therefore show up as  $\delta$ -functions in the spectral density. The spectral weight of a bound state is given by

$$I_{\text{bound}}^{-1} = \partial_{\omega} (g_{\text{eff}}^{\mathcal{O}}(\omega)^{-1}) |_{\omega = \omega_0}, \quad (4.2.13)$$

which is easy to calculate once the Green's function  $\mathcal{G}$  is evaluated.

### 4.3 Chapter summary

In this chapter it is illustrated how to calculate spectral densities from an effective Hamiltonian and an effective observable. The property of particle conservation of the effective model enables one to calculate the spectral density for each particle sector separately. Assuming that most of the spectral weight is distributed in the particle sectors with small particle number, the determination of the spectral density of a complex many-body system is reduced to the evaluation of few-body

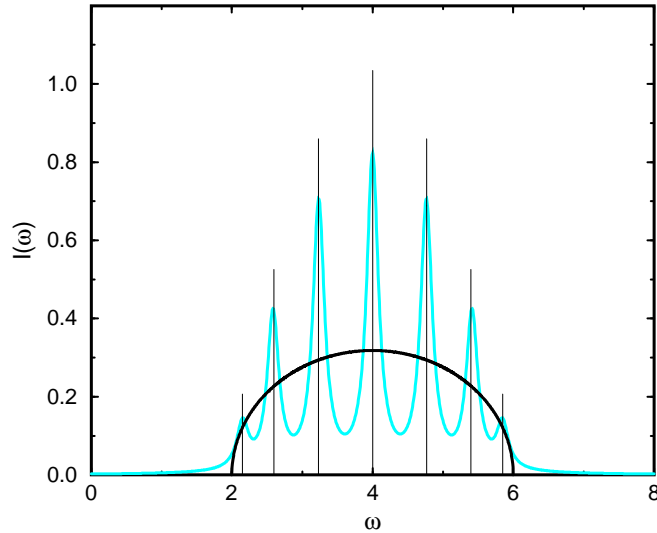


Fig. 4.1: An elliptic spectral density  $I(\omega)$  is considered as an example to illustrate the difference between terminated continued fraction and a continued fraction of finite depth with an additional broadening. The parameters used are  $a = 4$  and  $b = 1$ . The true spectral density is the solid black curve, for which the use of a square-root terminator in the corresponding effective Green's function is illustrated. The vertical lines indicate the  $\delta$ -functions which appear, if the continued fraction expansion of the Green's function was terminated at some finite depth  $N$  (here  $N = 7$ ). The grey curve is the spectral density which results from a terminated Green's function by introducing a broadening by  $\omega \rightarrow \omega + i\delta$  (here  $\delta = 0.1$ ).

spectral densities only.

Assuming translational invariance the one-particle spectral density can be calculated straightforwardly from the results of the preceding chapter, namely the one-particle dispersion and the one-particle momentum resolved spectral weights. The case of two-particle spectral weights is tackled with the continuous fraction technique. The technical details of the approach are explained in detail. The extension to more than two particles is described briefly. There is no principal problem associated with this generalization.

In this work the focus is set on one-dimensional gapped systems. The special properties of these systems are used to construct appropriate terminators allowing to go beyond the truncation at some finite depth of the continued fraction.

It must be stressed that  $H_{\text{eff}}$  and  $O_{\text{eff}}$  are determined in the thermodynamic limit and that also the use of the continuous fraction technique does not induce any finite size error. It is argued that the finiteness of the continued fraction introduces errors for the quantum number  $d$  only which are usually small for the cases considered in this thesis.

The procedure described is mainly restricted by errors arising from the finiteness of the maximum perturbation order. This is no problem for small values of the perturbation. Then even the plain series of the calculated processes converges and the correlation length is very small. In actual

---

applications, however, one is often interested in the case of larger perturbation parameters. Then one has to distinguish two cases. On the one hand the correlation length increases so much that processes are important which are not included in the calculation. In this situation the described approach is not useful anymore. A possible alternative is the use of renormalizing continuous unitary transformation. Especially a formulation in momentum space is able to treat in principle processes of infinite range. On the other hand, if only the plain series of the calculated processes are not valid, but the correlation length is not larger than the range of processes kept, then the use of extrapolation techniques is important. This problem is addressed in the next chapter.

## 5 Extrapolation

In this chapter a variety of extrapolation techniques is described. As discussed in the previous chapters, the outcome of the perturbative treatment of the continuous unitary transformations is a series expansion up to high order for several physical quantities. For small parameters, the truncated series is a valid approximation. It is clear that for larger parameters the truncated series diverges. In order to obtain reliable results for higher values one has to use extrapolation techniques. The first part of this chapter discusses the standard extrapolation tools like Padé- and dlogPadé-extrapolation. The inclusion of additional information and the determination of singularities and their exponents are also described. A review article about these standard tools was written by Guttmann [205]. The second part provides information about optimised perturbation theory (OPT) [172]. The last part describes a different sort of extrapolation tool. Here the system is no longer expressed in terms of external variables but in terms of an internal parameter of the considered system. This improves the convergence of the obtained series [207–211]. Note that it is also possible to combine the technique of internal parameters with Padé extrapolation procedures.

### 5.1 Padé-extrapolation

The basic idea of Padé extrapolation is to consider the obtained plain series as a Taylor expansion of an unknown rational function. The order of the plain series is therefore considered to be the number of coefficients of a Taylor expansion of the unknown rational function. Consider a general plain series

$$F(x) = \sum_{n \geq 0}^{Max} a_n x^n = a_0 + a_1 x + a_2 x^2 \dots \quad (5.1.1)$$

where  $Max$  is the order of the series and  $a_i$  is the real coefficient of the  $i$ -th order term. The  $P[L/M]_F$  Padé extrapolant of  $F(x)$  is defined as

$$P[L/M]_F \equiv \frac{P_L(x)}{Q_M(x)} \equiv \frac{p_0 + p_1 x + \dots + p_L x^L}{q_0 + q_1 x + \dots + q_M x^M}. \quad (5.1.2)$$

where  $p_i$  and  $q_i$  are real coefficients. Here one requires that a Taylor expansion  $\mathcal{T}$  of  $P[L/M]_F$  up to order  $Max$  is equal to  $F(x)$ . In the following a Taylor expansion  $\mathcal{T}$  about  $x = x_0$  of some function  $f(x)$  up to order  $Max$  is denoted by

$$\mathcal{T}[f]_{x=x_0}^{Max} . \quad (5.1.3)$$

This condition leads to a system of linear equations which determine the coefficients  $p_i$  and  $q_i$ . The sum of  $L$  and  $M$  must be equal to  $Max$ . The extrapolation is considered to work in an interval



$I$  if several extrapolants  $P[L/M]_F$  give very similar results in  $I$ . It is important to exclude those extrapolants which show zeros in the denominator in the interval  $I$  or zeros which lie close to  $I$  in the complex plane. If such poles do not represent valid physical behavior they are called *spurious*. The corresponding extrapolant is called *defective*.

It is easy to see that one can control the large  $x$  behaviour by the use of Padé extrapolants. The  $P[L/M]$  Padé behaves like  $x^{L-M}$  for large  $x$ . Detailed information about the limit  $x \rightarrow \infty$ , which is often known for physical systems, can therefore be built in the extrapolation. The Padé extrapolation is also applicable if the quantity of interest undergoes a sign change, i.e. sign changes do not restrict the use of Padé extrapolation.

## 5.2 DlogPadé-extrapolation

The dlogPadé extrapolation can be used for quantities of definite sign like energies and spectral weights. It is usually the most powerful and reliable extrapolation scheme. Consider a general plain series which is normalized in the sense  $a_0 = 1$

$$F(x) = \sum_{n \geq 0}^{Max} a_n x^n = 1 + a_1 x + a_2 x^2 \dots \quad (5.2.1)$$

The dlogPadé extrapolation is a Padé extrapolation on the logarithmic derivative of  $F(x)$

$$\frac{d}{dx} \ln F(x) = \frac{F'(x)}{F(x)} \equiv P[L/M]_{\ln F} = \frac{P_L(x)}{Q_M(x)}. \quad (5.2.2)$$

$P_L(x)$  and  $Q_M(x)$  are again polynomials of order  $L$  and  $M$ . The sum of  $L$  and  $M$  must be equal to  $Max - 1$  because one information is lost due to the derivative in the numerator of Eq. (5.2.2). The  $dP[L/M]_F$  extrapolant can also be viewed as the solution of the differential equation

$$Q_M(x) dF(x) = P_L(x) F(x) \quad (5.2.3)$$

It is sometimes called differential extrapolant due to the latter property. The  $dP[L/M]_F$  extrapolant of  $F$  is therefore

$$dP[L/M]_F(x) = \exp \left( \int_0^x \frac{P_L(x')}{Q_M(x')} dx' \right). \quad (5.2.4)$$

The extrapolation is very sensitive to real poles on the positive real axis and complex poles which are closed to the positive real axis of the rational function  $P_L/Q_M$ . The poles can be of physical origin if the quantity of interest vanishes like the gap of a physical system at a phase transition point. But the poles can also be spurious and one better rejects the extrapolant. In the case of a physical pole at  $x_0$  it is possible to calculate the dominant power-law behaviour  $|x - x_0|^\alpha$  near  $x_0$ . For  $x$  close to  $x_0$  one has

$$dP[L/M](x) \propto \exp \left( \int_0^x \frac{\alpha}{x' - x_0} dx' \right) = \exp \left( \alpha [\ln |x' - x_0|]_0^x \right) = |x - x_0|^\alpha. \quad (5.2.5)$$

The exponent  $\alpha$  is defined as the residuum of  $P_L/Q_M$  at  $x = x_0$

$$\alpha = \left. \frac{P_L(x)}{\frac{d}{dx} Q_M(x)} \right|_{x=x_0}. \quad (5.2.6)$$

The latter property is the main reason to use dlogPadé extrapolation.

### 5.2.1 Biased dlogPadé extrapolation

It is often the case that one has additional information about the function  $F(x)$ , e.g. phase transition points, exponents at a phase transition or the asymptotic behaviour for  $x$  approaching infinity. Assuming a phase transition at point  $x_0$  with an exponent  $\alpha$ , the additional information is added on the level of the logarithmic derivative. A function  $G(x)$  is defined as

$$G(x) = \left( \frac{d}{dx} \ln F(x) \right) (x - x_0) + Ax^{\text{Max}} \quad (5.2.7)$$

where the constant  $A$  is used to incorporate the exponent  $\alpha$  in the extrapolant. The next step is to make a Padé extrapolation  $P[L/M]_G$  for  $G$ . The constant  $A$  is determined by the condition

$$P[L/M]_G|_{x=x_0}(A) \equiv \alpha \quad , \quad (5.2.8)$$

because one wants to have  $dP[L/M]_G = \exp(\int_0^x \frac{\alpha}{x'-x_0} dx') = |x - x_0|^\alpha$  at  $x = x_0$ . The biased  $[L/M]$  dlogPadé extrapolant of  $F$  is defined as

$$dP[L/M]_F = \exp \left( \int_0^x \frac{P[L/M]_G}{x' - x_0} dx \right). \quad (5.2.9)$$

In order to include the asymptotic behaviour of a series  $F(x)$  it is useful to apply an Euler transformation to the logarithmic derivative of  $F$ . Assuming the asymptotic behaviour  $x^\alpha$  for  $x \rightarrow \infty$ , one adds an additional term to the logarithmic derivative of  $F$

$$G(x) = \left( \frac{d}{dx} \ln F(x) \right) + Ax^{\text{Max}} \quad (5.2.10)$$

where  $A$  is a constant which has to be determined in order to include the asymptotic behaviour. The Euler transformation is defined as

$$G(x) \rightarrow \tilde{G}(u) = \sum_0^{\text{Max}} a'_n u^n \quad \text{with} \quad x = \frac{u}{1-u} \quad (5.2.11)$$

which transforms  $G(x)$  in a series  $\tilde{G}(u)$  and  $x \in [0, \infty[$  in  $u \in [0, 1]$ . Similar to the inclusion of the exponent above one determines  $A$  through the equation

$$P[L/M]_{\frac{\tilde{G}}{1-u}}|_{u=1} = \alpha \quad (5.2.12)$$

where  $P[L/M]_{\frac{\tilde{G}}{1-u}}$  is the  $[L/M]$  Padé extrapolant of  $\tilde{G}$  and  $u = 1$  corresponds to  $x = \infty$ . The additional factor  $1 - u$  originates from the transformation of  $dx \rightarrow 1/(1-u)^2 du$ . The second factor  $1 - u$  is included explicitly in the final biased dlogPadé expression

$$BdP[L/M]_F = \exp \left( \int_0^{\frac{x}{1+x}} \frac{P[L/M]_G}{1-u} du \right). \quad (5.2.13)$$

## 5.3 Optimised perturbation theory

Optimised perturbation theory (OPT) is based on the principle of minimal sensitivity [206]. The basic idea is to find an optimum way of splitting the Hamiltonian in an unperturbed part and a perturbing part. Starting from the usual beginning of a perturbational approach

$$H(x) = H_0 + xV \quad (5.3.1)$$

where  $x$  is the expansion parameter, an additional parameter  $a$  is introduced which controls the splitting of  $H$

$$H(x; a) = (1 + a)H_0 + xV - aH_0 \quad (5.3.2)$$

$$= (1 + a)\tilde{H}(\tilde{x}; \tilde{a}) \quad (5.3.3)$$

$$\tilde{H}(\tilde{x}; \tilde{a}) = H_0 + \tilde{x}(V + \tilde{a}H_0). \quad (5.3.4)$$

Here  $\tilde{x}$  is equal to  $x/(1 + a)$  and  $\tilde{a}$  is equal to  $-a/x$ .  $\tilde{x}$  is considered to be the new expansion parameter. The transformed Hamiltonian  $H(x; a)$  is identical to the Hamiltonian  $H(x)$ . However, the truncated series of any eigen-energy  $E_{\text{trunc}}(x; a)$  of  $H(x; a)$  will depend on  $a$ . Since  $E_{\text{trunc}}(x; a)$  should not depend on the unphysical parameter  $a$  one can impose the criterion of minimal sensitivity to determine  $a$  in an optimum way

$$\partial_a E_{\text{trunc}}(x; a)|_{a=a_{\text{opt}}} = 0. \quad (5.3.5)$$

In general the convergence of  $E_{\text{trunc}}(x; a_{\text{opt}})$  is enhanced compared to the plain series  $E_{\text{trunc}}(x)$ . In some cases, the OPT series can be convergent even if the original series diverges, e.g. the standard series expansion of the ground state energy of a harmonic oscillator perturbed by a quartic potential diverges [212] while the series obtained by OPT converges [206].

In the following the specific application of OPT is described. Rewriting the Hamiltonian

$$\tilde{H}(\tilde{x}; \tilde{a}) = H_0 + \tilde{x}(V + \tilde{a}H_0) = (1 + \tilde{a}\tilde{x}) \left[ H_0 + \frac{\tilde{x}}{1 + \tilde{a}\tilde{x}} V \right] \quad (5.3.6)$$

one obtains the corresponding eigenvalues  $\tilde{E}(\tilde{x}; \tilde{a})$  by a simple substitution  $x \rightarrow \tilde{x}/(1 + \tilde{a}\tilde{x})$  in  $E(x)$

$$\tilde{E}(\tilde{x}; \tilde{a}) = (1 + \tilde{a}\tilde{x}) E \left( \frac{\tilde{x}}{1 + \tilde{a}\tilde{x}} \right). \quad (5.3.7)$$

Therefore, if a truncated series  $E_{\text{trunc}}(x)$  has been calculated from  $H_{\text{eff}}$  then one obtains  $E_{\text{trunc}}(x; a)$  by re-expansion in the small parameter  $\tilde{x}$  up to the same order in which one had obtained  $E_{\text{trunc}}(x)$ . In the end a final re-substitution  $\tilde{x} = x/(1 + a)$  and  $\tilde{a} = -a/x$  is done.

In order to do all the above described steps in one an auxiliary variable  $\lambda$  is introduced. The Taylor expansion in  $\tilde{x}$  can be replaced by an expansion in  $\lambda$

$$\tilde{x} = \frac{\lambda x}{1 + a} \quad \text{and} \quad \tilde{a} = -\frac{a}{x}. \quad (5.3.8)$$

The final result  $E_{\text{trunc}}(x; a_{\text{opt}})$  is then obtained by doing first a Taylor expansion  $\mathcal{T}$  of  $E_{\text{trunc}}(x; a)$  about  $\lambda = 0$  and then setting  $\lambda = 1$  at the end of the calculation

$$E_{\text{trunc}}(x; a_{\text{opt}}) = \left[ \mathcal{T} \left\{ (1 + a(1 - \lambda)) E_{\text{trunc}} \left( \frac{\lambda x}{1 + a(1 - \lambda)} \right) \right\} \right]_{\lambda=1; a=a_{\text{opt}}}. \quad (5.3.9)$$

Therefore, no new calculations have to be done. The parameter  $a_{\text{opt}}$  is determined by the criterion of minimal sensitivity.

It is also clear from the above discussion that any other quantity  $A_{\text{trunc}}$  obtained from an effective observable can be optimised in an analogous way

$$A_{\text{trunc}}(x; a) = \left\{ \mathcal{T} \left[ A_{\text{trunc}} \left( \frac{\lambda x}{1 + a(1 - \lambda)} \right) \right] \right\}_{\lambda=1; a=a_{\text{opt}}} . \quad (5.3.10)$$

Here no prefactor  $(1 + a(1 - \lambda))$  occurs because  $A$  is not measured in units of energy in contrast to  $E$ .

The criterion of minimal sensitivity imposes additional structural information on  $a_{\text{opt}}$ . It can be shown [172] that one can always write

$$a_{\text{opt}} = \alpha_{\text{opt}} x . \quad (5.3.11)$$

Let  $F_{\text{trunc}}(x; a)$  be the truncated series expansion of the quantity for which the optimum  $\alpha_{\text{opt}}$  is to be found. In the following  $F$  could be an energy  $E$  or some observable  $A$ . A function  $g(u, v)$  is introduced

$$g(u, v) = \begin{cases} v E_{\text{trunc}}(u/v) & \text{for energies,} \\ A_{\text{trunc}}(u/v) & \text{for observables.} \end{cases} \quad (5.3.12)$$

in order to compactify the notation. The derivative of  $g$  with respect to  $v$  is denoted by  $f(u, v) = \partial_v g(u, v)$ . The problem of determining  $a_{\text{opt}}$  reduces to

$$\begin{aligned} 0 \doteq \partial_a F_{\text{trunc}}(x; a) &= \left\{ \mathcal{T} \left[ \partial_a g(\lambda x, 1 + a(1 - \lambda)) \right]_{\lambda=0}^n \right\}_{\lambda=1} \\ &= \left\{ \mathcal{T} \left[ f(\lambda x, 1 + a(1 - \lambda))(1 - \lambda) \right]_{\lambda=0}^n \right\}_{\lambda=0} . \end{aligned} \quad (5.3.13)$$

For the following argument it is important to see that

$$\mathcal{T} \left[ f(\lambda x, 1 + a(1 - \lambda))(1 - 0\lambda) \right]_{\lambda=0}^n = f_n \lambda^n + (1 - \lambda) \mathcal{T} \left[ f(\lambda x, 1 + a(1 - \lambda)) \right]_{\lambda=0}^{n-1} , \quad (5.3.14)$$

holds, where  $f_n$  denotes the  $n^{\text{th}}$  coefficient in the Taylor expansion of  $f$  with respect to  $\lambda$

$$f_n = \frac{1}{n!} (\partial_\lambda)^n f(\lambda x, 1 + a(1 - \lambda)) . \quad (5.3.15)$$

The second term of the right hand side of Eq. 5.3.14 vanishes for  $\lambda = 1$ . In addition, the structure in Eq. 5.3.15 is such, that in each derivative with respect to  $\lambda$  either an  $x$  or an  $a$  is obtained as internal derivative of the chain rule. Thus, one obtains

$$\partial_a F_{\text{trunc}}(x; a) = f_n \quad (5.3.16)$$

to be a homogeneous polynomial in the variables  $x$  and  $a$ . In an  $n^{\text{th}}$  order expansion the criterion of minimal sensitivity reads

$$0 \doteq \partial_a F_{\text{trunc}}(x; a) \Big|_{a=a_{\text{opt}}} = \sum_{i=0}^n F_i a^i x^{n-i} \Big|_{a=a_{\text{opt}}} , \quad (5.3.17)$$

which clearly shows  $a_{\text{opt}} = \alpha_{\text{opt}}x$ .

The OPT procedure can be used for all physical quantities obtained by the continuous unitary transformation. There is no need for further calculation. The OPT-results are obtained by simple substitutions and re-expansions of the plain results.

The OPT can be also applied in a slightly different form. It is assumed that an optimal  $\alpha_{\text{opt}}$  exists and that it depends mainly on the model and on the order of the expansion. It is then fixed by simultaneously optimising some simpler quantities, e.g. the one-particle gap or bound state energies, which can be determined by reliable dlogPadé extrapolants or different methods. Additionally, the OPT procedure is linear. Denoting the OPT procedure as  $\mathcal{O}[\ ]$  such that

$$f(x; a_{\text{opt}}) = \mathcal{O}[f(x)] \quad (5.3.18)$$

is the optimised series obtained from the plain series  $f(x)$ . Then

$$\mathcal{O} \left[ \sum_i a_i f_i(x) \right] = \sum_i a_i \mathcal{O}[f_i(x)] \quad (5.3.19)$$

holds, where all series are of the same order. Therefore the OPT procedure can be applied in real or in momentum space giving exactly the same results.

It is important to note that OPT does not yield the best approximation one can obtain for a specific quantity. But it is an easy way to approximate in a physically controlled fashion a large number of quantities in one step. Additionally there are no unphysical singularities possible, i.e. the OPT approach is robust.

## 5.4 Internal parameters

Generically, the various physical quantities in a given system depend in a complicated way on the external control parameters. Expanding the quantities under study in terms of one of the external control parameters, let us say  $x$ , yields the bare, truncated series which can only rarely be directly used to compute the quantities. This is so since singularities induced by phase transitions easily spoil the convergence of the series. For instance, a correlation length diverges and the corresponding energy gap closes rendering an expansion about the gapped phase difficult.

If the convergence of the series is deteriorated due to an incipient phase transition it is reasonable to assume that *all* quantities in the particular system behave in a similar fashion. If this is so one may proceed in two separate steps: (i) one extrapolates an internal parameter which may serve as a measure of the distance to the phase transition as reliably as possible. Thereby, a reliable mapping between the external  $x$  and the internal parameter is established. (ii) One expresses all *other* quantities as functions of the internal parameter. According to the above argument the latter dependencies are expected to be much simpler, i.e. they are much less singular. The canonical candidate for the internal parameter measuring the distance to a phase transition or, more generally, to some singular situation is the energy gap  $\Delta$ . It is inversely proportional to the correlation length  $\xi$  which plays the role of the internal control parameter in standard renormalization group treatments.

The one-particle gap  $\Delta(x)$  can usually be extrapolated very reliably using dlogPadé-extrapolants or extrapolation schemes to be described at the end of this section. In this extrapolation one can exploit additional properties of the gap such as its positivity and its asymptotic behavior for  $x \rightarrow \infty$ . In this way, very reliable extrapolations are possible so that step (i) can usually be successfully solved. In general a magnetic system depends on various magnetic exchange coupling  $J_i$  where  $i \in 0 \dots n$ . The one-particle gap is denoted by

$$\Delta(\vec{J}) \equiv \Delta(J_0, J_1, \dots, J_n) = \frac{\Delta(x_1, x_2, \dots, x_n)}{J_0} \quad , \quad (5.4.1)$$

where one measures the gap in units of one magnetic coupling coupling (here  $J_0$ ) and introduces relative magnetic couplings  $x_i = J_i/J_0$ . For step (ii) one defines

$$G(\vec{x}) \equiv G(x_1, \dots, x_n) = 1 - \frac{\Delta(x_1, \dots, x_n)}{(\sum_{i=1}^n (1+x_i)J_0)} = 1 - \frac{\Delta(x_1, \dots, x_n)}{\sum_{i=0}^n J_i} \quad (5.4.2)$$

where one assumes that  $\Delta(x_1 = 0, x_2 = 0, \dots, x_n = 0) = J_0$ . In order to extrapolate only in one single parameter, e.g.  $x_1$ , one introduces  $r_{i-1} = x_i/x_1$  for  $i \in 2, \dots, n$ . They will be kept constant during the extrapolation in  $x_1$ . Then one has

$$G(x_1) = 1 - \frac{\Delta(x_1, r_1 x_1, \dots, r_n x_1)}{\sum_{i=0}^n J_i} \quad . \quad (5.4.3)$$

In units of  $\sum_i J_i$  the gap is unity at  $x_1 = 0$  and it goes to zero on  $x_1 \rightarrow \infty$ . So  $G(x_1)$  varies monotonically between 0 and 1 when  $x_1$  is increased from 0 to  $\infty$ . Since one has  $G \propto x_1$  for small  $x_1$  any expansion in  $x_1$  can be rewritten as expansion in  $G$  of the same order as the series in  $x_1$ , yet with other coefficients! This is done by inverting Eq. 5.4.3, thus completing the second step.

The succesful use of the above scheme depends on the behaviour of the one-particle gap  $\Delta$  concerning the external parameters  $x_i$ . In the following chapters spin-chain and spin-ladder system are examined which show generically different functional behaviour of  $\Delta$  as shown in Fig.5.1. The spin-chain system shows a phase transition at  $x = 1$ . The one-particle gap vanishes with some power-law behaviour, i.e. it changes drastically for small variation in  $x$ . In contrast to the spin-chain, the spin-ladder system becomes critical only for  $x \rightarrow \infty$  showing a slowly varying behaviour. It is found that the reformulation of the obtained series in terms of the internal parameter has not a large effect on the convergence of the spin-chain system while the convergence of the spin-ladder system is enhanced tremendously. In the spin-chain non-analytical dependencies of physical quantities on the one-triplon gap might influence the extrapolation procedure.

As discussed above the use of internal parameters requires reliable extrapolation schemes for  $G(x_1)$ . In the following an advanced extrapolation procedure for the one-particle gap  $\Delta$  is described [209]. Here the one-particle gap  $\Delta$  is determined through an extrapolation of the derivative of  $\Delta$ . One obtains a differential equation in  $\Delta$  for which the solutions represent a reliable extrapolation for the one-particle gap  $\Delta$  depending on the external parameters  $x_i$ . It is also possible to determine phase transition points, i.e. points where the one-particle gap vanishes for a given set of external parameters. This method will be used in a later chapter to calculate the phase diagram of the rung-singlet phase for a  $S = 1/2$  two-leg spin ladder with four-spin interaction [209].

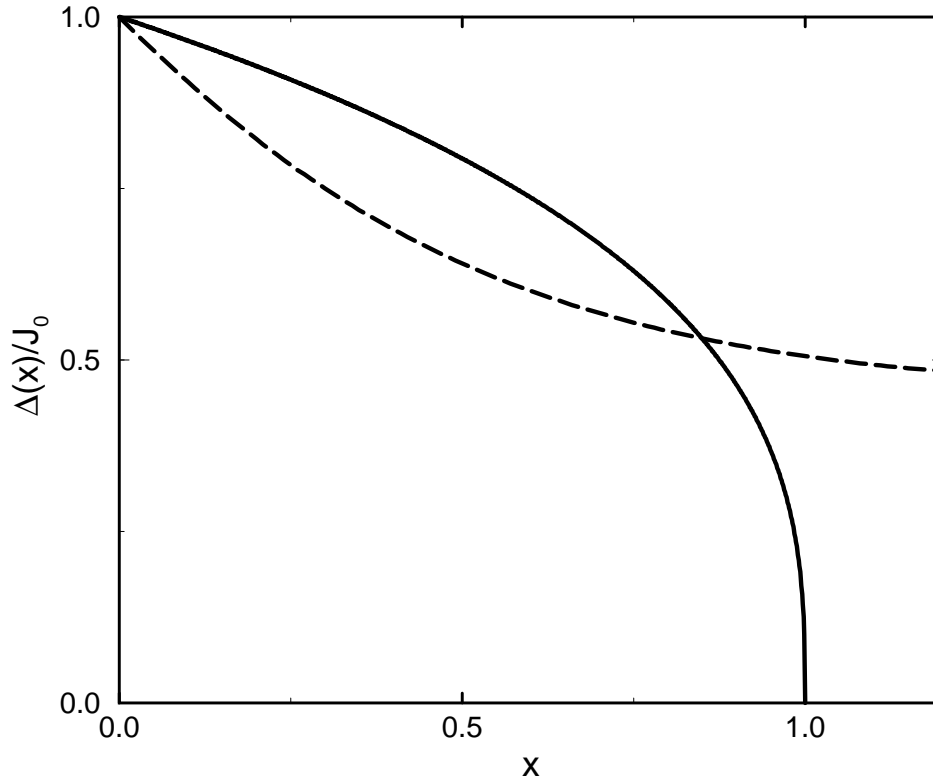


Fig. 5.1: The generic behaviour for the one-particle gap  $\Delta(x)$  depending on the external parameter  $x$  is shown for a spin-chain (solid line) and a spin-ladder (dashed line).

First the derivative of  $\bar{\Delta}(x_1) = \frac{\Delta(x_1, \dots, x_n)}{(\sum_{n=1}^n (1+x_i) J_0)}$  is considered

$$\frac{d\bar{\Delta}(x_1)}{dx_1} = -\frac{dG}{dx_1} . \quad (5.4.4)$$

Substituting  $x_1 = x_1(G)$  in Eq. 5.4.4 one obtains

$$-\frac{dG}{dx_1} = P(G) , \quad (5.4.5)$$

where  $P(G)$  is the truncated series in  $G$ . Note that even the convergence of the truncated series  $P(G)$  is often better than the convergence of the truncated series  $\Delta'(x_1)$  in  $x_1$  [208]. Because the gap is a monotonic decreasing function for  $r_i = \text{const}$  one can use dlogPadé extrapolants for  $P(G)$  since  $-dG/dx_1$  is non-negative. Integrating Eq. 5.4.5 yields

$$-\int_0^{G_0} \frac{dG}{P(G)} = \int_0^{x_0} dx_1 = x_0 . \quad (5.4.6)$$

Therefore, integrating the left hand side to  $G_0 = 1$ , i.e.  $\Delta = 0$ , provides the phase transition point  $[x_0, r_1 x_0, \dots, r_n x_0]$  for a given set of  $r_i$ . For any  $G_0 \in [0, 1[$  the gap is  $\Delta(x_0, r_1 x_0, \dots, r_n x_0)/J_0 = (1 + x_0)(1 - G_0)$ . In this way,  $\Delta(x_1, \dots, x_n)$  is obtained.

Note that one of the advantages of the use of internal variables is the possibility to apply standard Padé and dlogPadé techniques to the transformed quantities depending on the internal parameters. On the other hand one has to admit that this scheme does not work for all considered physical systems. The different behaviours are caused by the different analytic structure of the one-particle gap in physical systems, e.g. spin chain or spin ladder systems. In the spin-chain non-analytical dependencies may influence the reliability of the extrapolation.

## 5.5 Chapter summary

In this chapter a variety of extrapolation tools has been introduced. These tools are necessary in order to enlarge the region of convergence of the truncated series which are obtained by the continuous unitary transformation. The first two sections described the standard Padé and dlogPadé extrapolation. The dlogPadé extrapolation is usually much more reliable but its use is restricted to quantities with definite sign. The extrapolation of energies or spectral weights can therefore be done much better in comparison to the extrapolation of transition amplitudes which may change their sign. In the middle and the last part of this chapter a different way of extrapolation is presented, namely the OPT procedure and the use of internal parameters. The OPT is an easy-to-apply extrapolation scheme which optimises the unperturbed starting point by the criterion of minimal sensitivity. In the last part the concept of internal parameters is introduced. The basic idea is to express all quantities obtained as a series of some external parameter as a series of an internal parameter. This is usually the one-particle gap which is also proportional to the inverse of the correlation length. The physics in terms of the internal parameter is expected to be smoother and thus the obtained series to converge better. In order to get back to the external parameter it is necessary to have a reliable extrapolation of the one-particle gap. At the end of this chapter a method to calculate the one-particle gap by solving a high order differential equation for the one-particle gap is introduced. This method combines high order series expansion and renormalization group ideas.

In the following chapters a variety of spin-chain and spin-ladder systems are studied. Generically the method of internal parameters is used. For signed quantities like energies and spectral weights additional dlog-Padé extrapolants are applied. For all other quantities like transition amplitudes the truncated series or additional Padé extrapolation techniques are used.



## 6 Dimerized and frustrated spin-chain

One-dimensional quantum spin systems have attracted considerable attention over the last decades because most of the interesting and fascinating features observed in these systems are pure quantum effects due to the low dimension. The dimerized and frustrated spin-chain is one generic system to be studied in this context.

In this chapter perturbative particle-conserving continuous unitary transformations is used to study the energetic and spectral properties of the dimerized and frustrated spin-chain. The starting point of the calculation is the limit of isolated dimers. One obtains an effective model at  $T = 0$  up to high order in the perturbation where every order is exact in the thermodynamic limit. The one- and two-particle energies and the spectral densities are discussed as well as the multi-particle spectral weights (up to four particles).

There is a large amount of literature on this model which uses a variety of methods. Among these there are Bethe-Ansatz methods, DMRG or bosonization which are very powerful techniques in one dimension. In contrast to the large amount of results for the energetic properties, results for dynamical correlations are very rare due to the more complex nature of these quantities. In gapped spin liquids, investigations of dynamical correlations are only accessible with exact diagonalization and complete exact diagonalization which have no high resolution in energy and momentum.

The quantitative determination of spectral densities even for large dimerization gives new insights in one-dimensional quantum spin-systems. It is an important achievement to calculate dynamical correlations for various observables in a quantitative manner. The obtained results are directly relevant for experiments like inelastic neutron scattering, Raman scattering or optical absorption. There is a large number of quasi one-dimensional compounds which can be successfully described by the dimerized and frustrated Heisenberg model, e.g., spin-Peierls compounds like  $\text{CuGeO}_3$  [213–216],  $(\text{VO})_2\text{P}_2\text{O}_7$  [217] or organic compounds like  $\text{Cu}_2(\text{C}_5\text{H}_{12}\text{N}_2)_2\text{Cl}_4$  [218] and  $(\text{Cu}(\text{NO}_3)_2 \cdot 2.5\text{D}_2\text{O})$  [219, 220]. But also undimerized cuprate chain compounds like  $\text{KCuF}_3$  [221],  $\text{Sr}_2\text{CuO}_3$  [222] and  $\text{SrCuO}_2$  [223].

The physical most interesting case is the limit of vanishing dimerization. The conventional description is in terms of fractional excitations, so called spinons carrying  $S = 1/2$ . This limit is of course the most difficult situation to address starting from disconnected dimers. Nevertheless it is possible for quantities with definite sign like energies or spectral weights to study the case of zero dimerization using the extrapolation tools described in Chapt. 5. By analyzing the spectral weights it is shown that a description in terms of triplons carrying  $S = 1$  exists even in the limit of vanishing dimerization. This result offers a new route in the description of low-dimensional undoped and doped quantum spin systems. It is a central outcome of this thesis.

In the following the model and its phase diagram is introduced in detail. Methodical aspects for the dimerized and frustrated spin-chain are described next. A discussion of the spectral weights follows which sets the base line of the triplon picture. In the last part of this chapter various results for

energies and spectral densities are shown for large and intermediate dimerization.

## 6.1 Model

The dimerized and frustrated spin-chain investigated is a model in one dimension with spins carrying  $S = 1/2$  and interacting via nearest and next-nearest antiferromagnetic exchange couplings. The dimerization is considered as a given additional alternation of the nearest neighbour coupling. The Hamiltonian for the dimerized and frustrated  $\mathbf{S} = 1/2$  spin-chain reads

$$H = J_0 \sum_i [(1 + \delta(-1)^i) \mathbf{S}_i \mathbf{S}_{i+1} + \alpha_0 \mathbf{S}_i \mathbf{S}_{i+2}], \quad (6.1.1)$$

where  $\delta \in [-1, 1]$  parameterizes the dimerization and  $\alpha_0 \geq 0$  is the relative frustration between next-nearest neighbor spins as shown in Fig. 6.1. the coupling  $J_0$  is the energy scale of the model. In the following the interval for  $\delta$  is reduced to  $[0, 1]$  because of the invariance of the Hamiltonian under the simultaneous transformation  $i \rightarrow i+1$  and  $\delta \rightarrow -\delta$ . Physically this symmetry corresponds to the interchange of strong and weak bonds which does not change the physics of the system. The phase diagram and the energetic properties of the dimerized and frustrated spin-chain are

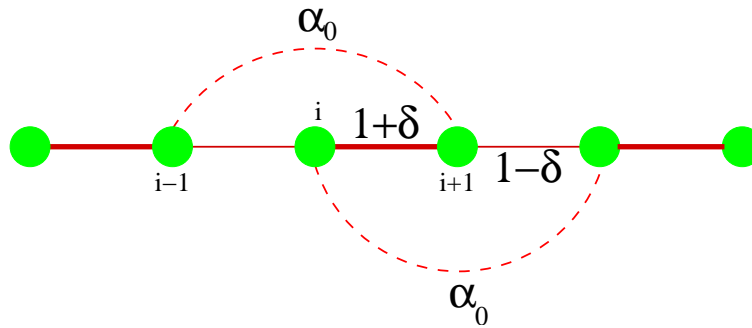


Fig. 6.1: Sketch of the dimerized and frustrated  $S = 1/2$  chain.

described next. This includes a detailed discussion of the nature of the elementary excitations. In a subsequent step the spectral properties of the model are presented.

### 6.1.1 Phase diagram and excitations

The dimerized and frustrated spin-chain exhibits very interesting intrinsic physics. The phase diagram of the model is shown in Fig. 6.2. Basically one has to distinguish between the case of finite and zero dimerization. Most of the work concerning this model has been done for the undimerized case. The most studied situation is the case of zero frustration ( $\alpha = 0$ ) and zero dimerization ( $\delta = 0$ ), i.e. the one-dimensional Heisenberg model. At this point the model is exactly solvable by Bethe Ansatz methods [224–228]. One obtains the ground state and the excited states exactly [83, 229]. In addition, it is possible to determine the thermodynamics of the system

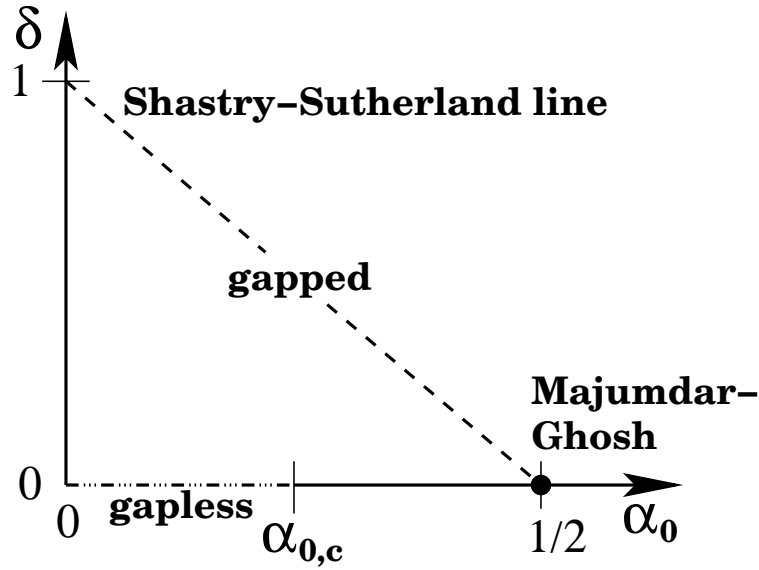


Fig. 6.2: Phase diagram of the dimerized and frustrated Heisenberg chain depending on frustration  $\alpha_0$  and dimerization  $\delta$ . The system is always in a gapped regime except for the interval  $\alpha_0 \in [0, \alpha_{0,c}]$  at zero dimerization. The dashed line marks the Shastry-Sutherland line where the ground state is known exactly.

exactly [230].

The one-dimensional Heisenberg model is a gapless and critical system. For  $|i - j| \rightarrow \infty$ , the correlation functions decay algebraically

$$\langle \mathbf{S}_i \mathbf{S}_j \rangle \propto (-1)^{|i-j|} / |i-j| \quad (6.1.2)$$

$$\langle (\mathbf{S}_i \mathbf{S}_{i+1})(\mathbf{S}_j \mathbf{S}_{j+1}) \rangle \propto (-1)^{|i-j|} / |i-j| \quad (6.1.3)$$

Here multiplicative logarithmic corrections are omitted. The results of Eq. 6.1.2 are supported by findings of bosonization [231, 232] and conformal field theory [234, 235]. The total spin of the ground state is zero. The system is physically situated right at the border between a RVB-state and a Néel-state. The sublattice magnetization is zero and the wave function of the ground state has locally a strong singlet character. These are characteristics of an RVB-state. On the other hand, the system is gapless and exhibits quasi-long-range antiferromagnetic correlations which is typical for a Néel-ordered state.

The focus of interest is the nature of the elementary excitations. The first result on the excitations was obtained by Cloizeaux and Pearson in 1962 [229]. They found a spin one excitation with a dispersion relation

$$\epsilon_{CP}(k) = \frac{1}{2}\pi |\sin k|, \quad -\pi \leq k \leq \pi \quad (6.1.4)$$

Later it became clear that the situation is more delicate. It was found that the true excitation spectrum has to be labeled by two quantum numbers rather than just the one used above [83, 236–238]. Consequently, the elementary excitations have to form a continuum. This leads to the interpretation by Fadeev and Takhtajan [83] that the elementary excitation of the one-dimensional

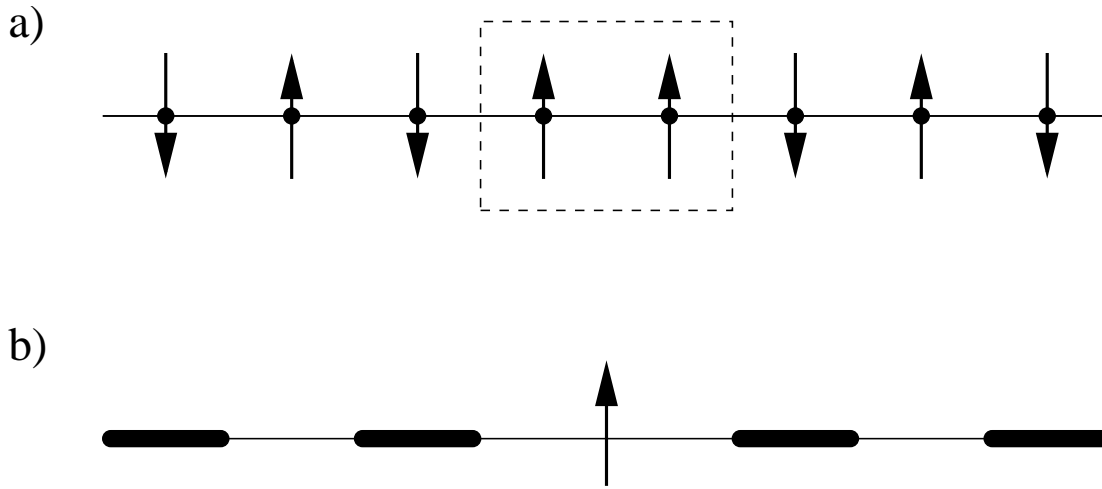


Fig. 6.3: Visualization of a spinon in a Néel-type ordering (a) and in an RVB-like state (b).

Heisenberg model are fractional excitations carrying spin  $1/2$  which are asymptotically free. Later, these particles were named spinons by P. W. Anderson in the context of antiferromagnetism in two dimensions [6]. An illustration of a spinon can be given in the Néel picture and as well as in a RVB-like description. Assuming a Néel-type ordering as visualized in Fig. 6.3a, the spinon can be imagined as a domain wall between two Néel-ordered domains with opposite sublattice magnetization. Even more appealing is the illustration in an RVB-like structure shown in Fig. 6.3b. The filled blocks represent local singlet configurations and the single spin represents the excited spinon. In this picture the total spin  $1/2$  of one spinon can be clearly seen. Of course, both illustrations are only simplified sketches of the complicated true ground state.

The spinons have a dispersion relation

$$\epsilon(k) = \frac{1}{2}\pi \sin k, \quad 0 \leq k \leq \pi \quad . \quad (6.1.5)$$

They can be created only in pairs because the total spin of the system is fixed to be either integer or half-integer. The excitation spectrum of the one-dimensional Heisenberg model is therefore composed of  $2n$ -spinon continua with  $n \in \{1, 2, \dots\}$ . The support of the two-spinon continuum  $\omega(k)$  is shown in Fig. 6.4.

As will be discussed in more detail later in Sect. 6.3, the outcome of the Bethe ansatz is the existence of two quantum numbers in the excitation energies which means there is a continuum of energies for fixed total momentum rather than only one energy. This implies that the elementary excitations cannot be created as single excitations. The interpretation in terms of fractional excitations is the natural consequence, but it will be argued and motivated later that this description is not unique and there there exist an other representation which does not rely on fractionality [82]. At  $\delta = 0$  there are two regimes for finite frustration. For  $\alpha_0 < \alpha_{0,c}$ , the ground state is in the same universality class as the uniform Heisenberg chain. The excitations are massless and the standard description is in terms of unconfined spinons carrying total spin  $S = 1/2$  [83, 229]. At  $\alpha_0 = \alpha_{0,c}$  there is a transition to a spontaneously dimerized phase [216, 239–241]. The ground state is two-

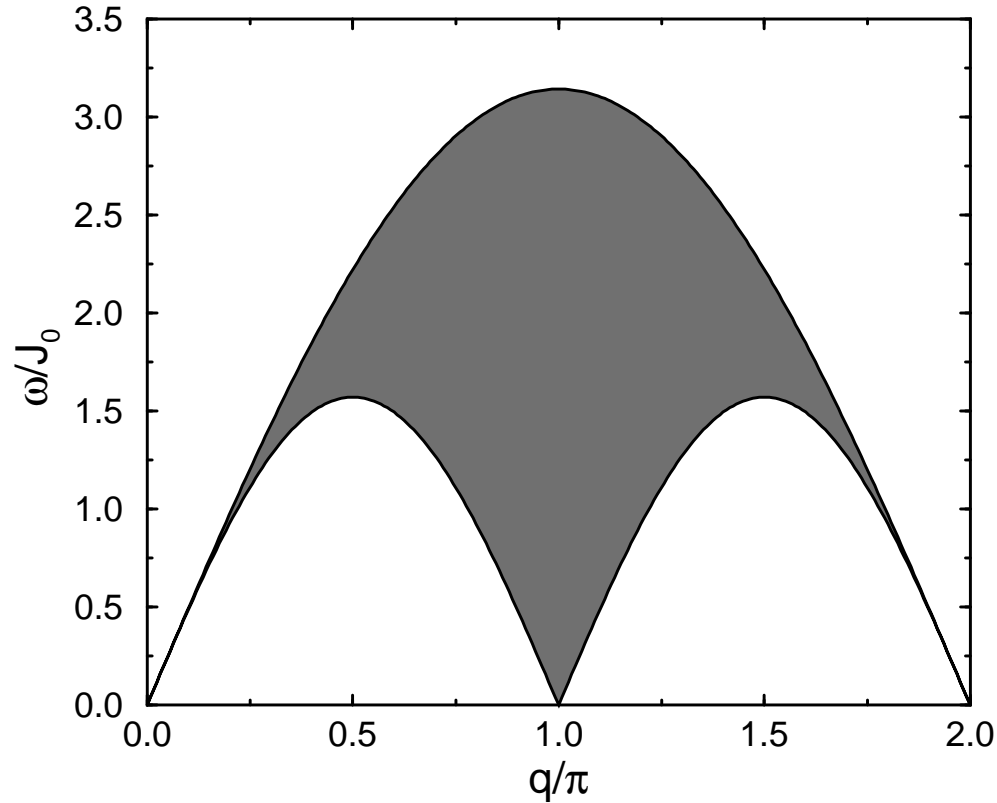


Fig. 6.4: Support of the two-spinon continuum for the one-dimensional Heisenberg model.

fold degenerate and the excitations are massive spinons for  $\alpha_0 > \alpha_{0,c}$ . The value of the critical frustration  $\alpha_{0,c} = 0.241167$  depends on the physics at short distances and is only accessible by numerical techniques [216, 239–241], i.e. it is a non-universal parameter. At the Majumdar-Ghosh point ( $\alpha_0 = 0.5$ ) the ground state is known exactly [242–244].

Haldane has shown that for any finite dimerization  $\delta$  the spinons become confined [245]. The confinement of spinons for finite dimerization is illustrated in Fig. 6.5. Without dimerization the two spinons indicated are asymptotically free, i.e. there is no force between the spinons at large distances. At finite dimerization one dimerization pattern is energetically favored while the other pattern is disfavored. The favored pattern exists left of the left spinon and right of the right spinon. Consequently, the state becomes energetically more and more disfavored for larger distances between the spinons. Equivalently, there is an attractive potential between the spinons which increases monotonically for larger distances. Thus the two spinons are confined.

The spectrum is always gapped [245, 246, 248] and the excitations can be viewed as bound states of two spinons [249–252]. These bound states form three triplet states and a singlet state. The triplet states are lower in energy compared to the singlet state. The energy difference between

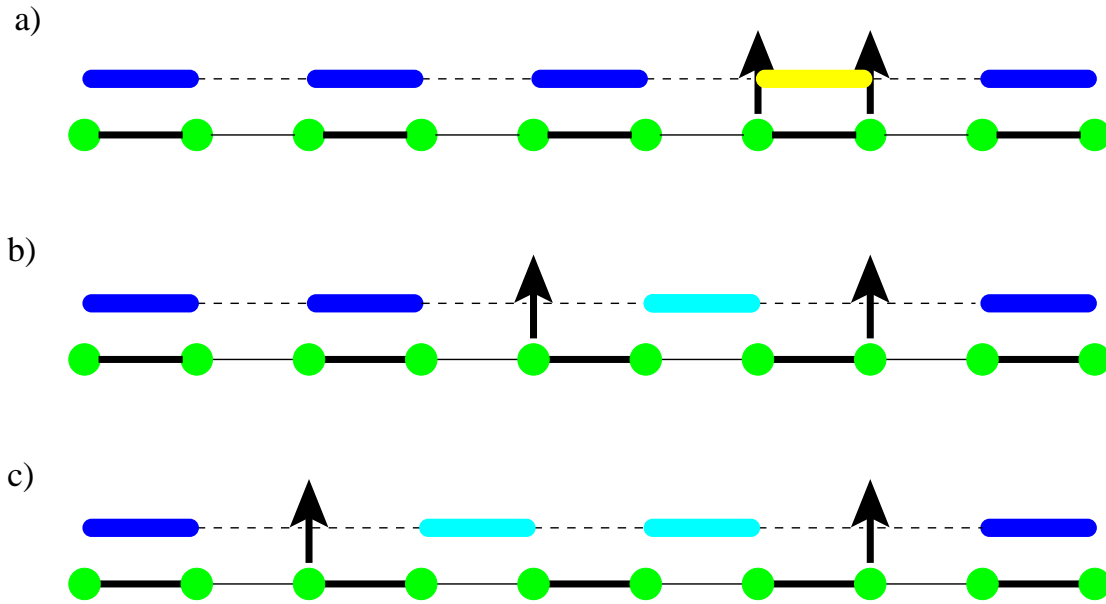


Fig. 6.5: Illustration of the confinement of spinons at finite dimerization. Filled circles correspond to spin positions. Thick solid black lines displays a strong exchange coupling and thin solid black lines a weak exchange coupling. Filled blue dimers denote singlet states on strong bonds and grey dimers are singlets on weak bonds. (a) The figure illustrates the excitation of two spinons (black arrows) on strong bonds. (b-c) The left spinon moves to the left and creates singlets on weak bonds. The latter are energetically disfavored and a confining force is build between the two spinon excitations (see also [263]).

the triplet energy and the ground state energy defines the energy gap  $\Delta$ . These low-lying bound states represent the elementary excitations of the dimerized state. These low-lying triplets are called triplons or elementary triplets [82].

The interaction between the spinons is not exhausted by the confinement and there remains a triplon-triplon interaction which can lead to two-triplon bound states with total spin  $S = 0$  and  $S = 1$  lying below the two-triplon continuum or anti-bound states with total spin  $S = 2$  lying above the two-triplon continuum [177, 181, 246, 251, 254, 255, 257–259].

One way of studying the low-energy physics of the dimerized and frustrated spin-chain at very small dimerization is the use of continuum field theories. In one dimension it is possible to map the spin model either on a fermionic or a bosonic field theory.

First, the main results of fermionic field theories are presented. A Jordan-Wigner transformation [260] is used to transform the spin model to a fermionic model. Concentrating on low-energy excitations, it is reasonable to focus on the dispersion and on the interaction at the Fermi points  $k_F = \pm\pi/2$  and to neglect all other other momentum dependencies. One obtains an effective local model in real space [245, 251]

$$H = \int_{-\infty}^{\infty} \left[ -iv_S \left( \psi_1^\dagger \frac{d}{dx} \psi_1 - \psi_2^\dagger \frac{d}{dx} \psi_2 \right) + m_0 (\psi_1^\dagger \psi_2 + \psi_2^\dagger \psi_1) + 2g_0 \psi_1^\dagger \psi_1 \psi_2^\dagger \psi_2 \right] dx, \quad (6.1.6)$$

which is called the massive Thirring-model. Here  $\psi_{1/2}$  are fermionic fields originating from the two Fermi points, and  $v_s$  is the Fermi velocity. It is exactly equal to  $\pi/2$  for the one-dimensional Heisenberg model as can be seen from Eq. 6.1.5. For  $\alpha_0 < \alpha_c$ ,  $v_s$  is renormalized which can be determined by numerical calculations [255]. The bare fermionic mass  $m_0$  is proportional to the dimerization  $\delta$ . The value of the bare interaction  $g_0$  is not known. But similar to the later discussed bosonic field theories, the interaction parameter can be determined by restoring the rotational invariance of the spin-system. The massive Thirring model can be solved exactly by Bethe ansatz methods [256]. The main results are the renormalization of the fermionic mass

$$m = m_0 \frac{\tan(\pi\gamma)}{\pi(\gamma-1) \exp(\Lambda(1-\gamma))} \quad (6.1.7)$$

$$\text{with } \gamma = \frac{\pi}{2\mu} \text{ and } \cot \mu = -\frac{g_0}{2}, \quad (6.1.8)$$

where  $\Lambda$  is the ultraviolet cut-off of the rapidities. The energies and the momenta of the bound states lying below the continuum with the same particle number as the ground state are

$$E = 2m \sin(n\alpha) \cosh(\gamma\alpha_s) \quad (6.1.9)$$

$$P = 2m \sin(n\alpha) \sinh(\gamma\alpha_s) \quad (6.1.10)$$

$$\text{with } \alpha = \frac{\pi}{2} \left( \frac{\pi}{\mu} - 1 \right); \quad n \in \{1, 2, 3, \dots, [\pi/(2\alpha)]\}. \quad (6.1.11)$$

The inclusion of spin-rotational symmetry in the solution of the fermionic model demands a state with  $E = m$  at  $P = 0$  that completes the missing  $S_z = 0$  state of the  $S = 1$ -multiplet. This condition leads to  $\alpha = \pi/6$  which implies  $\mu = 3\pi/4$ ,  $\gamma = 2/3$  and  $g_0 = 2$ . Using these results one concludes for the renormalized mass  $m \propto m_0^{2/3}$  and  $\Delta E \propto \delta^{4/3}$  where  $\Delta E$  is the change of the ground state energy due to the dimerization. Additionally, for  $\alpha = \pi/6$  there exists a bound state with  $S_z = 0$  at  $E = 2m \sin(2\alpha) = \sqrt{3}m$ . This bound state must be a singlet because there are no degenerate states with  $S_z \neq 0$  for this energy, i.e. for the weakly dimerized spin-chain one expects a singlet bound state at  $k \in \{0, \pi\}$  with the energy  $\sqrt{3}\Delta$ .

The latter results can also be obtained by bosonization [261, 262]. The idea of bosonization is to consider the superposition of particle-hole pairs to be elementary. This is well defined if the fermionic dispersion is linear. In order to bosonize the dimerized and frustrated spin-chain, the first step is again a Jordan-Wigner transformation [260]. Next one switches to a continuum description, i.e. one focuses on the neighborhood of the two Fermi points. The dispersion relation of the fermions are linearized at these points and extended to  $\pm\infty$ . Fermions at the left fermi point are called  $\psi_1$  and fermions at the right fermi point  $\psi_2$ .

Bosonic fields  $\phi(x)$  and  $\Pi(x)$  are introduced [232, 233]

$$\phi(x) = \frac{-i\pi}{L} \sum_{p \neq 0} \frac{1}{p} [\rho_1(p) + \rho_2(p)] \exp(-a|p|/2 - ipx) - N \frac{\pi x}{L} \quad (6.1.12)$$

$$\Pi(x) = \frac{1}{L} \sum_{p \neq 0} [\rho_1(p) + \rho_2(p)] \exp(-a|p|/2 - ipx) + \frac{J}{L}. \quad (6.1.13)$$

Here  $L$  is the length of the chain,  $\rho_{1/2}$  are the Fourier components of the particle density operator of the left/right fermions an  $N = N_1 + N_2$  and  $J = N_1 - N_2$ .  $\phi(x)$  and  $\Pi(x)$  depend on the continuous

space variable  $x$ . The local fermionic problem of the one-dimensional Heisenberg model, can be written as

$$H = \frac{v_S}{2\pi} \int_{-L/2}^{L/2} \left( K(\pi\Pi)^2 + \frac{1}{K}(\partial_x\phi)^2 \right) dx. \quad (6.1.14)$$

$v_S$  is the fermi velocity and  $K$  is the interaction parameter. The bosonic fields  $\phi$  and  $\Pi$  are conjugated fields

$$[\phi(x), \Pi(x)] = i\delta(x - y). \quad (6.1.15)$$

The value of the interaction parameter  $K$  is determined to be  $1/2$  by imposing the spin rotational symmetry on the bosonic model analogue to the fermionic field theory. The Hamiltonian (6.1.14) is a model of free bosons with a linear dispersion.

The frustration term in the spin-model creates umklapp processes in the fermionic model which lead to an additional term in the bosonized version of the system

$$H_U = D \int_{-L/2}^{L/2} dx \cos(4\phi), \quad (6.1.16)$$

which corresponds to an interaction between the bosons. The total system  $H + H_U$  stays gapless for  $K = 1/2$ . The operator  $H_U$  is a marginal operator. From numerical studies one knows that a gap opens for  $\alpha_0 > \alpha_c$  and one concludes  $D \propto (\alpha_0 - \alpha_c)$  [248, 257, 264, 265]. There  $H_U$  becomes relevant. The umklapp processes are marginal relevant for  $\alpha_0 > \alpha_c$  and marginally irrelevant for  $\alpha_0 < \alpha_c$ .

The dimerization  $\delta$  leads to a similarly structured term as the frustration in the bosonized Hamiltonian

$$H_D = -\delta B \int_{-L/2}^{L/2} \cos(2\phi) dx. \quad (6.1.17)$$

The essential difference is the value of the angle. This term is relevant and leads to a finite energy gap even for infinitesimal dimerization  $\delta$ .  $B$  is a non-universal constant.

The bosonized version of the dimerized and frustrated spin-chain therefore reads

$$\begin{aligned} H_{FT} = & \frac{v}{2\pi} \int_{-\infty}^{\infty} \left[ K(\pi\Pi)^2 + K^{-1}(\partial_x\Phi)^2 \right] dx \\ & + \int_{-\infty}^{\infty} [\delta B \cos(2\Phi) + D \cos(4\Phi)] dx, \end{aligned} \quad (6.1.18)$$

which is a double sine-Gordon model which is not exactly solvable. The term originating from the frustration is often omitted due to his marginality. But this is exact only at critical frustration  $\alpha_c$  [264, 265]. For  $\alpha \neq \alpha_c$ , this term decreases to zero for  $\delta \rightarrow 0$  but only logarithmically which means very slowly. Then one is left with a simple sine-Gordon model which is exactly solvable.

For the single sine-Gordon model one obtains similar to the fermionic theory the energy gap  $\Delta \propto \delta^{2/3}$  [266, 267] and the energy of bound states [268–271]

$$\Delta_n = 2\Delta \sin(n\pi\beta/2) \quad (6.1.19)$$

$$\text{with } n \in \{1, 2, 3, \dots, 1/\beta\}, \quad (6.1.20)$$

where for a general cosine term  $\cos(\nu\phi)$  one has

$$\beta = \frac{K\nu^2}{8 - K\nu^2}. \quad (6.1.21)$$



In the case of dimerization one has  $\nu = 2$ , and one again recovers a singlet bound state with energy  $\sqrt{3}\Delta$  equivalent to the result of the fermionic field theory.

In order to study the dimerized phase it is natural to switch from a description in terms of spinons to a triplonic description. A description in terms of triplons is clearly valid for any finite value of the dimerization. It is reasonable to start a triplonic treatment in the limit of isolated dimers ( $\delta = 1, \alpha_0 = 0$ ).

A qualitative understanding of the model can be obtained in a first order calculation. In order to apply a perturbative treatment Eq. 6.1.1 is transformed into

$$H/J = \sum_i [\mathbf{S}_{2i}\mathbf{S}_{2i+1} + \lambda\mathbf{S}_{2i}\mathbf{S}_{2i-1} + \lambda\alpha\mathbf{S}_i\mathbf{S}_{i+2}], \quad (6.1.22)$$

where

$$\begin{aligned} J &= J_0(1 + \delta) \\ \lambda &= \frac{1 - \delta}{1 + \delta} \\ \alpha &= \frac{\alpha_0}{1 - \delta} \end{aligned} \quad (6.1.23)$$

For  $\lambda = 0$  one obtains a local Hamiltonian which has an equidistant spectrum that is bounded from below [251]. In zeroth order in  $\lambda$  the excitations are local triplets on isolated dimers. There is no dispersion and no interaction. In first order in  $\lambda$  the triplet is able to hop with an amplitude  $t_1$  from one dimer to the neighbouring dimer. At the same time, triplets on neighbouring dimers interact with an amplitude  $w_{S_{\text{tot}}}$  depending on the total spin  $S_{\text{tot}}$  of the two triplets. The total spin can be zero, one or two. The corresponding matrix elements are

$$t_1 = -\frac{\lambda}{4}(1 - 2\alpha) \quad (6.1.24)$$

$$w_0 = -\frac{\lambda}{2}(1 + 2\alpha) \quad (6.1.25)$$

$$w_1 = -\frac{\lambda}{4}(1 + 2\alpha) \quad (6.1.26)$$

$$w_2 = \frac{\lambda}{4}(1 + 2\alpha). \quad (6.1.27)$$

One recognizes that the interaction  $w_2$  corresponds to a repulsion between two parallel spins while  $w_0$  and  $w_1$  represent attractive interactions which are strongest for antiparallel spins. This reflects the antiferromagnetic character of the system.

Generically frustration lowers the amount of mobility of the considered particle. The same can be seen in the equation for  $t_1$ . On the other hand the interactions between the triplons are enhanced by the frustration. Calculating the binding energy between the triplons [251] for the different values of the total spin, one obtains a singlet bound state which exists for all momenta, a triplet bound state existing only in a region near  $k = \pi/2$  and a quintuplet anti-bound state existing in the whole Brillouin zone. So even the first order calculation gives generic features of the dimerized and frustrated spin-chain.

In the recent years there was an ongoing activity in extending this first order calculation to a series

expansion up to high order in  $\lambda$ . The used methods are linked cluster expansion and the perturbative realization of the particle conserving continuous unitary transformations to be described here. The calculation of one-triplon energies was first done by Gelfand [183] using the linked cluster expansion and later by Knetter and Uhrig introducing the perturbative continuous unitary transformations for quantum spin systems [143].

For the calculation of bound states at least two-triplon energies are needed. Zheng *et al.* [184] managed to calculate two-triplon energies including a detailed study of two-triplon bound states for the dimerized and frustrated spin-chain using linked cluster expansion techniques. One of the main new features obtained in these studies is the fact that there are more than only one bound state for every spin channel compared to the above first order calculation. These bound states exist at high energies and cannot be treated in field theoretical models which are only valid at low energies.

### 6.1.2 Spectral properties

The calculation of dynamical quantities is a much more difficult task. In the limit of zero dimerization many facts are known. Usually it is very hard to determine correlation functions by Bethe ansatz. But in 1997, Karbach *et al* were able to obtain the exact expression for the two-spinon contribution  $S^{2\text{sp}}$  to the dynamical structure factor  $S(q, \omega)$ , the spectral density for two spinons with total ( $S = 1$ ) [272]. The result is shown in Fig. 6.6.

The two-spinon continuum accounts for 72.89% of the total intensity in  $S(q, \omega)$ . The remaining 27.11% of the total intensity of the dynamical structure factor is distributed in the  $2n$ -multi-spinon continua ( $n \in \{2, 3, 4, \dots\}$ ). The exact structure and spectral weight of these contributions are not fully known at the moment (see Refs. [273–276]).

The two-spinon continuum displays a very interesting behavior at the band edges.  $S^{2\text{sp}}$  vanishes in a square-root cusp at the upper band edge for all momenta  $q$

$$S^{2\text{sp}}(q, \omega) \xrightarrow{\omega \rightarrow \omega_U} \propto \sqrt{\omega_U - \omega}, \quad (6.1.28)$$

where  $\omega_U$  denotes the energy at the upper band edge. The intensity at the lower band edge diverges. One finds a square-root divergence for  $q \neq \pi$  and a stronger infrared divergence for  $q = \pi$

$$S^{2\text{sp}}(q, \omega)|_{q \neq \pi} \xrightarrow{\omega \rightarrow \omega_L} \propto \frac{1}{\sqrt{\omega_L - \omega}} \quad (6.1.29)$$

$$S^{2\text{sp}}(q, \omega)|_{q = \pi} \xrightarrow{\omega \rightarrow \omega_L} \propto \frac{1}{\omega} \sqrt{\ln \frac{1}{\omega}}, \quad (6.1.30)$$

where  $\omega_L$  corresponds to the energy at the lower band edge. Considering the case of the spectral density for total ( $S = 0$ ), or leaving the case of zero frustration and zero dimerization, it is no longer possible to calculate spectral properties using Bethe ansatz.

As discussed above it is possible to map the dimerized and frustrated spin-chain to an effective low-energy bosonic model, the double sine-Gordon model. Ignoring the marginal operator resulting from the frustration, one is left with a single sine-Gordon model. The validity of this step is discussed in more detail later. The spectral properties of the single sine-Gordon are known, i.e. the

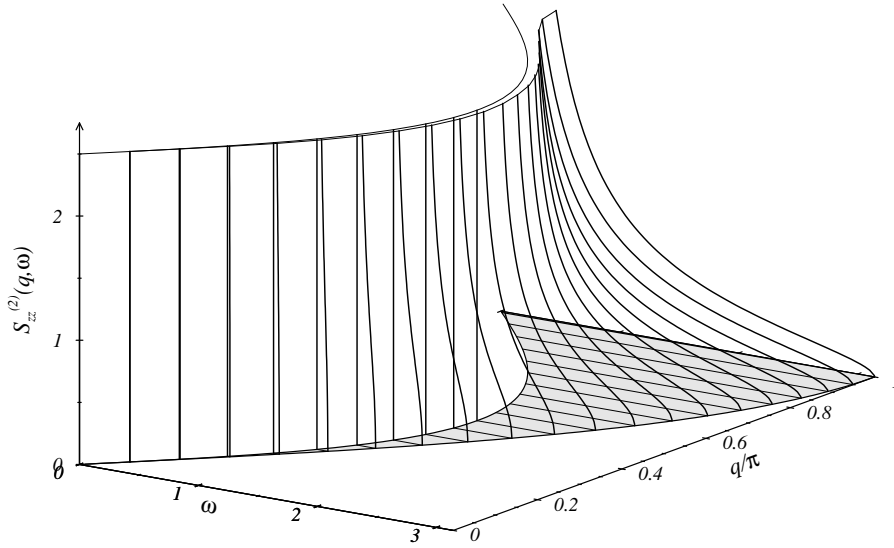


Fig. 6.6: Exact two-spinon dynamical structure factor  $S^{2sp}$  obtained by Bethe ansatz [272]. The shaded region represents the support of the two-spinon continuum as shown in Fig. 6.4. The two-spinon dynamical structure factor displays a singularity at the lower band edge which is cutted in the figure.

shape of the lower band edge near  $k = 0$  or  $k = \pi$  [252].

The energy of the different breather states (depending on the total spin) plays a crucial role concerning the shape of the lower band edge. At infinitely small but finite dimerization the system is always gapped. The lower band edge of the two-triplon continuum (at  $k = \pi$ ) is therefore equal to two times the one-triplon gap  $\Delta$ . Recalling that the triplet bound state corresponding to  $S_z = 0$  is fixed to  $\Delta$  in order to restore the spin rotational symmetry of the spin-model, the second ( $S = 1$ )-breather has a energy of  $2\Delta$  (as can be seen in Eq. 6.1.19 with  $n = 3$ ), i.e. it is degenerate with the lower band edge. In contrast to the  $S = 1$  case, the first singlet-breather has an energy of  $\sqrt{3}\Delta$ . Therefore, this state lies below the continuum and has a finite binding energy. These two cases are sketched in Fig. 6.7(a-b).

One finds that a degeneracy between a breather state and the lower band edge leads to a square-root divergence of the spectral density. This corresponds to a somehow fine-tuned situation which is believed to be protected by spin rotational symmetry. This is true in the limit of extremely small energies. In contrast, the generic case of a bound state lying below the continuum leads to a square-root cusp, i.e. zero intensity at the lower band edge (see Fig. 6.7(a-b)).

The latter observation is also found by a first order calculation about the limit of isolated dimers [251]. It can be shown that the generic situation in this limit corresponds to a vanishing intensity at

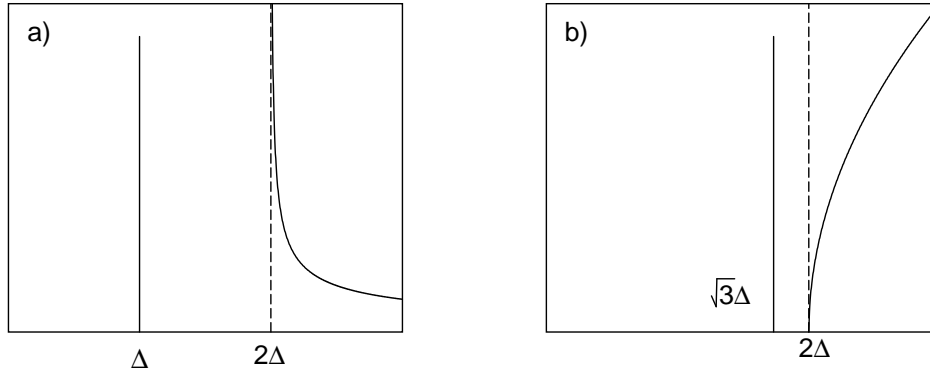


Fig. 6.7: Sketch of the spectral density at the lower band edge at  $k = \pi$  for the single sine-Gordon model with  $K = 1/2$  with total spin one (a) and total spin zero (b). Case (a): The triplet bound state corresponding to  $S_z = 0$  is fixed to  $\Delta$  in order to restore the spin rotational symmetry of the spin-model. The second  $S = 1$ -breather is degenerate with the lower band edge producing a square-root divergence. Case (b): One breather is below the continuum. The lower band edge displays a square-root cusp.

the lower and the upper band edges. Physically this behavior is related to the hardcore constraint on the triplonic interaction, i.e. the hardcore constraint induces a triplon-triplon interaction leading to a square-root cusp instead of a divergence as in the density of states of free bosons.

In the following a triplon-conserving continuous unitary transformation is used to investigate the energetic and especially the spectral properties of the dimerized and frustrated spin-chain. The transformation will be implemented in a perturbative manner up to high order in the perturbation starting from the limit of isolated dimers as explained above. One-triplon and two-triplon contributions to the spectral density for total spin one and total spin zero are presented for all momenta and energies at strong and intermediate dimerization including the influence of frustration. The focus is laid on two-triplon bound states and on the shape of the two-triplon continuum.

The concept of the triplon as an elementary excitation of the system even in the limit of zero dimerization is introduced and discussed in an investigation of the multi-triplon spectral weights. The outcome of the latter analysis is the dominance of the two-triplon spectral weight even at zero dimerization. This leads to a detailed discussion of the connection between the two-triplon contribution at intermediate dimerization and the undimerized case comparing the results obtained by continuous unitary transformations with the above stated results obtained by other methods.

## 6.2 Method

A continuous unitary transformation [135] is used to map the Hamiltonian  $H$  to an effective Hamiltonian  $H_{\text{eff}}$  which conserves the number of triplons on the strong bonds, i.e.  $[H_0, H_{\text{eff}}] = 0$  where  $H_0 := H|_{\lambda=0}$  [143, 171]. As shown in Chapt. 3, the perturbative realization of this transformation

relies on two prerequisites. Assuming the initially given Hamiltonian  $H$  can be formulated as a perturbative problem

$$H = H_0 + xV, \quad (6.2.1)$$

two conditions on the Hamiltonian  $H$  are required:

- A.** The unperturbed Hamiltonian  $H_0$  must have an equidistant spectrum bounded from below. The difference between two adjacent levels is called an energy quantum.
- B.** There is a number  $\mathcal{N} \ni N > 0$  such that the perturbing Hamiltonian  $V$  can be written as  $V = \sum_{n=-N}^N T_n$  where  $T_n$  increments (decrements, if  $n < 0$ ) the number of energy quanta by  $n$ .

It is now shown that the initially Hamiltonian (Eq. 6.1.1) fulfills these requirements. For this purpose Eq. 6.1.1 is reformulated according to

$$\frac{H(\lambda)}{J} = H_{\text{strong}} + \lambda H_{\text{weak}}; \quad (6.2.2)$$

with  $\lambda = (1 - \delta)/(1 + \delta)$  and  $J = J_0(1 + \delta)$  analogue to Eq. 6.1.22.  $H_{\text{strong}} = \sum_i \mathbf{S}_{2i} \mathbf{S}_{2i+1}$  denotes strong intradimer coupling and  $H_{\text{weak}} = \sum_i [\mathbf{S}_{2i} \mathbf{S}_{2i-1} + \alpha \mathbf{S}_i \mathbf{S}_{i+2}]$  denotes weak interdimer coupling. The coupling  $J$  is assumed to be antiferromagnetic and set to one henceforth. The limit of isolated strong bonds ( $\delta = 1$ ) is the limit for which the perturbative treatment is controlled.

The ground state of the unperturbed part  $H_{\text{strong}}$  is the product state of singlets on the strong bonds. A first excited state is a strong bond excited to a triplet. There are  $3L/2$  such elementary triplet excitations if  $L$  is the number of spins because there are three  $S^z$ -values for a triplet. The next energetically higher state is given by two triplets and so on. The operator  $H_{\text{strong}}$  counts the number of triplets and therefore condition (A) is fulfilled.

Due to the latter property  $H_{\text{strong}}$  is identified with  $Q$ , i.e. the elementary excitations of the unperturbed part (triplets on strong bonds) serve as quasi-particles in the following treatment of the dimerized and frustrated spin-chain. These excitations are called triplons. These ‘‘triplons’’ shall be the elementary excitations of the system. They have total spin  $S = 1$  and appear with three different flavours (z-components  $-1, 0, 1$ ). The triplon should not be confounded with a magnon which has only two flavours  $\Delta S_x = \pm 1$  and is the elementary excitation of an ordered magnet in contrast to the triplon whose construction originates from the spin liquid picture.

The system consists locally of four states  $\{s, t^{-1}, t^0, t^1\}$ . It is therefore also possible to define local operators  $\hat{t}^i$  in second quantization which obey bosonic commutation relations  $[\hat{t}^i, \hat{t}^j] = \delta_{i,j}$ . Due to the fact that there can only be one excitation on one dimer, there is an additional constraint on the bosonic operators  $\hat{s}^\dagger \hat{s} + \sum_i \hat{t}^{\dagger i} \hat{t}^i = 1$ . These bosons are then called hardcore bosons [253].

As soon as the interaction between strong bonds  $\lambda \neq 0$  is turned on, the local triplons become dressed. The central idea of the particle conserving CUT is to map the initial problem onto an effective Hamiltonian for which the simple triplon-states, originally defined for the unperturbed part, can be used to calculate all energetic properties of the system.

The action of the perturbing part  $H_{\text{weak}}$  on the triplon states is analyzed next in order to check condition (B).

The first step is to classify the change of the triplon-number in the various local processes of Hamiltonian Eq. 6.1.22. Let  $|n\rangle$  denote a  $n$ -triplon state, i.e.  $H_{\text{strong}}|n\rangle = n|n\rangle$ . The perturbing part is then written as

$$H_{\text{weak}} = \sum_{n=-2}^{n=2} T_n \quad (6.2.3)$$

where the subscript  $n$  denotes the change of the triplet number  $T_i|n\rangle \propto |n+i\rangle$ . In order to determine the operators  $T_n$  one has to calculate the local expectation values  $\langle x_i, x_j | H_{\text{weak}} | x_i, x_j \rangle$  for  $x_i, x_j \in \{s, t^{-1}, t^0, t^1\}$ . As can be seen in Eq. 6.1.22, the Hamiltonian for the dimerized and frustrated spin-chain contains only nearest-neighbour dimer-dimer processes (nearest neighbour and next-nearest neighbour spin processes). All matrix elements of interest can be expressed as

$$\langle x_{i-1} x_i | H_{\text{weak}} | x_{i-1} x_i \rangle \quad (6.2.4)$$

The maximum change in the number of local triplets is therefore restricted to  $n = 2$  in Eq. 6.2.3, simply because there are only processes which connect at maximum two dimers.

First the nearest-neighbour spin-products  $\mathbf{S}_{2i}\mathbf{S}_{2i+1}$  originating from the dimerization are investigated. The spin-product can be written locally

$$\mathbf{S}_{2i}\mathbf{S}_{2i-1} = \mathcal{T}_{-2} + \mathcal{T}_{-1} + \mathcal{T}_0 + \mathcal{T}_1 + \mathcal{T}_2 \quad (6.2.5)$$

The subscript of  $\mathcal{T}$  denotes again the change in the number of triplets. In Tab. 6.1 the action of  $\mathcal{T}$  on the states  $\{s, t^{-1}, t^0, t^1\}$  are listed for the nearest-neighbour spin-product  $\mathbf{S}_{2i}\mathbf{S}_{2i+1}$ . All remaining matrix elements can be calculated by using the relation  $\mathcal{T}_n^\dagger = \mathcal{T}_{-n}$ . It is physically convenient to split  $\mathcal{T}_0 = \mathcal{T}_0^a + \mathcal{T}_0^b$ . Processes in  $\mathcal{T}_0^a$  correspond to triplon hopping and processes in  $\mathcal{T}_0^b$  describe triplon-triplon interactions.  $\mathcal{T}_{\pm 1}$  and  $\mathcal{T}_{\pm 2}$  represent the creation (annihilation) of one or two triplons in the system.

In order to include the spin-product induced by the frustration it is not necessary to calculate all matrix elements anew. One can rather deduce the matrix elements by considering the symmetry of the spin states, i.e. one knows that a triplet is symmetric under exchange of spins while a singlet is antisymmetric under spin exchange

$$P_{ij}|t\rangle_{ij} = |t\rangle_{ji} \quad (6.2.6)$$

$$P_{ij}|s\rangle_{ij} = -|s\rangle_{ji}. \quad (6.2.7)$$

Here  $P_{ij}$  is the operator for the exchange of the spins on sites  $i$  and  $j$ .  $\{|t\rangle_{ij}, |s\rangle_{ij}\}$  are triplet/singlet states on sites  $i/j$ . One can therefore decompose the frustration in an analogous manner to the above treatment of the dimerization

$$\alpha S_i S_{i+2} = \sum_{n=-2}^2 \mathcal{T}_n^\alpha. \quad (6.2.8)$$

$4\mathcal{T}_0^a$		
$ t^{0,\pm 1}, s\rangle$	$\rightarrow$	$- s, t^{0,\pm 1}\rangle$
$4\mathcal{T}_0^b$		
$ t^0, t^{0,\pm 1}\rangle$	$\rightarrow$	$ t^{0,\pm 1}, t^0\rangle$
$ t^{\pm 1}, t^{\pm 1}\rangle$	$\rightarrow$	$ t^{\pm 1}, t^{\pm 1}\rangle$
$ t^{\pm 1}, t^{\mp 1}\rangle$	$\rightarrow$	$ t^0, t^0\rangle -  t^{\pm 1}, t^{\mp 1}\rangle$
$ t^0, t^0\rangle$	$\rightarrow$	$ t^1, t^{-1}\rangle +  t^{-1}, t^1\rangle$
$4\mathcal{T}_1$		
$ s, t^1\rangle,  t^1, s\rangle$	$\rightarrow$	$ t^1, t^0\rangle -  t^0, t^1\rangle$
$ s, t^0\rangle,  t^0, s\rangle$	$\rightarrow$	$ t^1, t^{-1}\rangle -  t^{-1}, t^1\rangle$
$ s, t^{-1}\rangle,  t^{-1}, s\rangle$	$\rightarrow$	$ t^0, t^{-1}\rangle -  t^{-1}, t^0\rangle$
$4\mathcal{T}_2$		
$ s, s\rangle$	$\rightarrow$	$ t^1, t^{-1}\rangle -  t^0, t^0\rangle +  t^{-1}, t^1\rangle$

Table 6.1: Action of the local operators  $\mathcal{T}_j$ .

It is now possible to determine the  $\mathcal{T}_n^\alpha$  from the above given  $\mathcal{T}_n$  by spin exchange symmetry. This is illustrated for the state  $|s, t\rangle$  denoting a singlet on sites 0/1 and a triplet on sites 2/3

$$\begin{aligned}
\alpha (\mathbf{S}_0\mathbf{S}_2 + \mathbf{S}_1\mathbf{S}_3) |s, t\rangle &= \alpha (\mathbf{S}_0\mathbf{S}_2 |s, t\rangle + \mathbf{S}_1\mathbf{S}_3 |s, t\rangle) \\
&= \alpha (-\mathbf{S}_1\mathbf{S}_2 |s, t\rangle + \mathbf{S}_1\mathbf{S}_2 |s, t\rangle) \\
&= 0 \quad .
\end{aligned}$$

Therefore one finds for the  $\mathcal{T}_n^\alpha$

$$\begin{aligned}
\mathcal{T}_{\pm 2}^\alpha &= -2\alpha \mathcal{T}_{\pm 2} \\
\mathcal{T}_{\pm 1}^\alpha &= 0 \\
\mathcal{T}_0^{\alpha,a} &= -2\alpha \mathcal{T}_{\pm 2}^a \\
\mathcal{T}_0^{\alpha,b} &= 2\alpha \mathcal{T}_{\pm 2}^b \quad .
\end{aligned} \tag{6.2.9}$$

The operators  $\mathcal{T}_n$  can then be written as

$$\begin{aligned}
\mathcal{T}_{\pm 2} &= \sum_{i=0}^{\frac{L}{2}-1} (1 - 2\alpha) \mathcal{T}_{\pm 2} \\
\mathcal{T}_{\pm 1} &= \sum_{i=0}^{\frac{L}{2}-1} \mathcal{T}_{\pm 1} \\
\mathcal{T}_0 &= \sum_{i=0}^{\frac{L}{2}-1} [(1 - 2\alpha) \mathcal{T}_0^a + (1 + 2\alpha) \mathcal{T}_0^b] \quad .
\end{aligned} \tag{6.2.10}$$

Physically the effect of the frustration is a decrease of the hopping amplitude and an increase in the interaction amplitude [251]. Additionally, the frustration enhances the pair creation and

annihilation of the triplons. These findings correspond to the first order results described in Sect. 6.1. Condition (B) is therefore fulfilled.

### 6.2.1 Perturbative CUT

The perturbative CUT is formulated by introducing an auxiliary flow parameter  $l \in [0, \infty[$ . The CUT gives rise to the flow equation

$$\frac{\partial H(\lambda; l)}{\partial l} = [\eta(\lambda; l), H(\lambda; l)] , \quad (6.2.11)$$

which controls the flow of the Hamiltonian in the transformation process. The starting Hamiltonian is fixed to be  $H(\lambda; l = 0) = H(\lambda)$  and the effective Hamiltonian is defined as  $H_{\text{eff}}(\lambda) = H(\lambda; l = \infty)$ .

As discussed in Chapt. 3, the choice for the infinitesimal unitary generator  $\eta$  which conserves the number of triplons during the flow is

$$\eta_{i,j}(\lambda; l) = \text{sgn}(Q_i - Q_j) H_{i,j}(\lambda; l) . \quad (6.2.12)$$

Here  $\eta_{i,j}$  and  $H_{i,j}$  are matrix elements in the eigen basis  $\{|n\rangle\}$  of  $Q = H_{\text{strong}}$ . In the limit  $l \rightarrow \infty$  the generator (6.2.12) eliminates all parts of  $H(\lambda; l)$  changing the number of triplons, i.e.  $[H_{\text{eff}}, H_{\text{strong}}] = 0$ . The vanishing commutator expresses the fact that the effective Hamiltonian  $H_{\text{eff}}$  is block-diagonal with respect to the number of triplons.

A perturbative realization of the transformation yields the effective Hamiltonian as an operator series expansion [143]

$$H_{\text{eff}}(\lambda) = H_{\text{strong}} + \sum_{k=1}^{\infty} \sum_{|\underline{m}|=k, M(\underline{m})=0} C(\underline{m}) T_{\underline{m}} . \quad (6.2.13)$$

Here  $\underline{m}$  is a vector of dimension  $|\underline{m}| = k$  of which the components are elements of  $\{\pm N, \pm(N-1), \dots, \pm 1, 0\}$ . In the case of the dimerized and frustrated spin-chain  $N = 2$  holds. The operator products  $T_{\underline{m}}$  are monomials  $T_{\underline{m}} = T_{m_1} T_{m_2} \dots T_{m_k}$ , with  $T_{m_i}$  as given in Eq. 6.2.3. The perturbative order of a given process is  $k$ . The conservation of the triplon number is reflected by the condition that the sum of the indices vanishes for every process ( $M(\underline{m}) := \sum_i m_i = 0$ ).

The effective Hamiltonian is calculated up to order 10 in  $\lambda$  for the zero-, one- and two-triplon sector. Therefore processes up to a range  $\approx 20$  spins are captured by the calculation. A linked cluster expansion yield results up to order 23 in  $\lambda$  for the zero- and one-triplon sector [186]. In the two-triplon sector order 7 in  $\lambda$  for the singlet states and order 11 in  $\lambda$  for the triplet and quintet states has been computed for the dimerized chain. On the disordered line  $\alpha = 1/2$ , order 19 in  $\lambda$  for two-triplon singlet, triplet and quintet states has been evaluated [184].

### 6.2.2 Observables

In this part the evaluation of the effective observables for the dimerized and frustrated spin-chain are described. The effective observables are calculated up to order 7 in the one-, two- and three-triplon



sector. The four-triplon sector is calculated up to order 6. Note that in the case of frustration  $\alpha = 1/2$ , the so-called Majumdar-Gosh point, the decomposition of the Hamiltonian in terms of the operators  $T_n$  is rather simple.  $T_{\pm 2}$  and  $T_0^a$  vanish and one is only left with  $T_{\pm 1}$  and  $T_0^b$ . The effective observables are determined up to order 10 in the one-, two- and three-triplon sector and up to order 9 in the four-triplon sector for this case. One distinguishes between observables creating a state with total spin one and those creating states with total spin zero. A linked cluster calculation yields results for the unfrustrated case up to order 13 in  $\lambda$  for the one-triplon sector and up to order 12 in  $\lambda$  for the two-triplon sector [282].

### 6.2.2.1 $S=1$

The physical observable for  $S = 1$  excitations which is studied in this work is locally

$$\mathcal{O}_{\text{loc}}^{S=1}(r) = S_r^z = \mathcal{T}_{-1}^{S=1} + \mathcal{T}_0^{S=1} + \mathcal{T}_1^{S=1} , \quad (6.2.14)$$

where  $r$  denotes a site of the chain. In the following  $L$  and  $R$  denote the left and the right site on a strong bond, cf. Fig. 6.8. The decomposition for the  $\mathcal{T}^{S=1}$  is given in Tab. 6.2 for  $\mathcal{O}^{S=1} = S_L^z$  and  $\mathcal{O}^{S=1} = S_R^z$ .

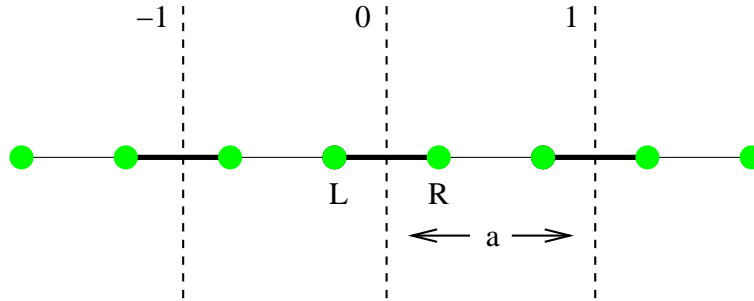


Fig. 6.8: Sketch of the local observable for  $S = 1$  excitations. Bold lines denote strong bonds and thin lines weak bonds. The observable is the left (L) or the right (R) spin of a strong bond.

### One-triplon Sector

In the one-triplon channel the action of the full observable  $\mathcal{O}^{S=1}|_{1\text{trp}}$  on the ground state is decomposed for fixed one-triplon momentum  $k$  by writing

$$\mathcal{O}^{S=1}|_{1\text{trp}}|0\rangle = A_{1\text{trp}}^{S=1}(k)|k\rangle, \quad (6.2.15)$$

$\mathcal{O}_{\text{loc}}^{S=1} = S_L^z$			$\mathcal{O}_{\text{loc}}^{S=1} = S_R^z$		
$2\mathcal{T}_0^{l,S=1}$			$2\mathcal{T}_0^{l,S=1}$		
$ t^{-1}\rangle$	$\rightarrow$	$- t^{-1}\rangle$	$ t^{-1}\rangle$	$\rightarrow$	$- t^{-1}\rangle$
$ t^1\rangle$	$\rightarrow$	$ t^1\rangle$	$ t^1\rangle$	$\rightarrow$	$ t^1\rangle$
$2\mathcal{T}_1^{l,S=1}$			$2\mathcal{T}_1^{l,S=1}$		
$ s\rangle$	$\rightarrow$	$ t^0\rangle$	$ s\rangle$	$\rightarrow$	$- t^0\rangle$
$ t^0\rangle$	$\rightarrow$	$ s\rangle$	$ t^0\rangle$	$\rightarrow$	$- s\rangle$

Table 6.2: Action of the local operators  $\mathcal{T}_j^l$  for the observables  $\mathcal{O}^{S=1} = S_L^z$  (left panel) and  $\mathcal{O}^{S=1} = S_R^z$  (right panel).

where the amplitudes  $A_{\text{1trp}}^{S=1}$  are given by

$$\begin{aligned}
 A_{\text{1trp}}^{S=1} &= \frac{1}{\sqrt{2}} \sum_l \left[ a_l^L e^{-ik(2l+\frac{1}{2})} + a_l^R e^{-ik(2l-\frac{1}{2})} \right] \\
 &= -\sqrt{2}i \sum_l a_l^l \sin \left( k(2l + \frac{1}{2}) \right). \tag{6.2.16}
 \end{aligned}$$

The sum runs over all dimers  $l$ . The coefficient  $a_l^L$  is the amplitude for the creation of one triplon at site  $l$  by  $S_L^z$ . The amplitudes of  $S_R^z$  do not need to be calculated separately because one can use the inversion symmetry of the chain. The latter gives  $a_l^R = -a_{-l}^L$ . The basic unit length  $a/2$  is the distance between two neighboring sites. In the figures momenta between 0 and 1 are given in units of  $\pi/(a/2)$ . So the comparison of our results to the conventional notation for undimerized chains using the distance  $a' = a/2$  between two neighboring spins as unit length is simplified.

### Two-triplon Sector

In the two-triplon channel one decomposes the action of the full observable  $\mathcal{O}^{S=1}|_{2\text{trp}}$  on the ground state for fixed two-triplon momentum  $k$

$$\mathcal{O}^{S=1}|_{2\text{trp}}|0\rangle = \sum_d A_{2\text{trp}}^{S=1}(k, d)|k, d\rangle. \tag{6.2.17}$$

Here  $d$  denotes the relative distance between the two triplons and

$$A_{2\text{trp}}^{S=1}(k, d) = -\sqrt{2}i \sum_l a_{l,l+d}^{L,S=1} \sin \left( k(2l + \frac{1}{2} + d) \right). \tag{6.2.18}$$

The sum runs over all strong bonds  $l$  and  $a_{l,l+d}^{L,S=1}$  is the amplitude for the creation of two triplons on dimers  $l$  and  $l+d$  by  $S_L^z$ . Here it is convenient to use a mixed representation in which the center-of-mass coordinate is Fourier transformed and the relative coordinate is dealt with in real space. The action of  $S_R^z$  does not need to be calculated. The inversion symmetry of the chain gives the relation  $a_{l,l+d}^{R,S=1} = -a_{-l-d,-l}^{L,S=1}$ . The basic unit length  $a/2$  is again the distance between two neighboring sites.

6.2.2.2  $S=0$ 

The physical observable  $R^{S=0}$  for  $S = 0$  excitations locally reads

$$\mathcal{O}_{\text{loc}}^{S=0} = \mathcal{O}_{\text{loc,NN}}^{S=0} + \beta \mathcal{O}_{\text{loc,NNN}}^{S=0}, \quad (6.2.19)$$

i.e., it is a sum over nearest neighbor (NN) and next-nearest neighbor coupling (NNN). The coefficient  $\beta$  is a measure for the relative strength between the two couplings. It depends on the underlying microscopic physics and will not be discussed in this work. As illustrated in Fig. 6.9 these observables are given by

$$\mathcal{O}_{\text{loc,NN}}^{S=0} = (1 + \gamma) \mathbf{S}_{0,L} \mathbf{S}_{0,R} + (1 - \gamma) \mathbf{S}_{0,R} \mathbf{S}_{1,L} \quad (6.2.20)$$

for nearest neighbor (NN) coupling and

$$\mathcal{O}_{\text{loc,NNN}}^{S=0} = \mathbf{S}_{0,L} \mathbf{S}_{1,L} + \mathbf{S}_{0,R} \mathbf{S}_{1,R} \quad (6.2.21)$$

for next-nearest neighbor (NNN) coupling where  $\gamma$  is proportional to the dimerization  $\delta$ .  $\mathcal{O}_{\text{loc,NN}}^{S=0}$  is a sum over couplings on weak and strong bonds. In this work the discussion is restricted to the case

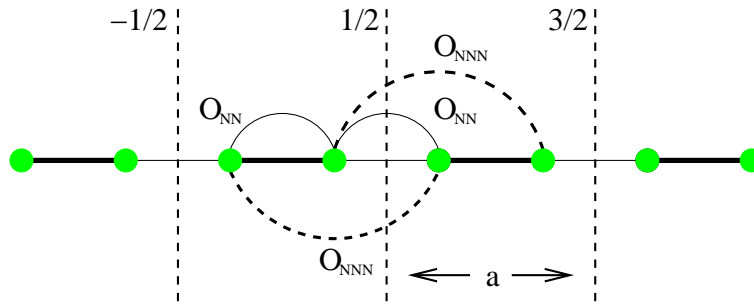


Fig. 6.9: Sketch of the local observables for  $S=0$  excitations.  $\mathcal{O}_{\text{NN}}^{S=0}$  is a sum of couplings on strong bonds (thick lines) and weak bonds (thin line).  $\mathcal{O}_{\text{NNN}}^{S=0}$  couples next-nearest-neighbor spins.

of nearest-neighbor coupling on the weak bonds and on the next-nearest-neighbor coupling. This choice is motivated by the relevance of various observables for Raman spectroscopy and infrared absorption in the limit of vanishing dimerization. Raman spectroscopy measures excitations with total momentum zero while infrared absorption is governed by the response at large momenta [277, 278].

Locally one has

$$\mathcal{O}_{\text{loc}}^{\text{NN}}(r) = \mathbf{S}_{r,L} \mathbf{S}_{r+1,R} = \mathcal{T}_{-2}^{\text{NN}} + \mathcal{T}_{-1}^{\text{NN}} + \mathcal{T}_0^{\text{NN}} + \mathcal{T}_1^{\text{NN}} + \mathcal{T}_2^{\text{NN}} \quad (6.22a)$$

$$\mathcal{O}_{\text{loc}}^{\text{NNN}}(r) = \mathbf{S}_{r,L} \mathbf{S}_{r+1,L} + \mathbf{S}_{r,R} \mathbf{S}_{r+1,R} = \mathcal{T}_{-2}^{\text{NNN}} + \mathcal{T}_{-1}^{\text{NNN}} + \mathcal{T}_0^{\text{NNN}} + \mathcal{T}_1^{\text{NNN}} + \mathcal{T}_2^{\text{NNN}} \quad (6.22b)$$

The action of the operators  $\mathcal{T}^{\text{NN}}$  and  $\mathcal{T}^{\text{NNN}}$  is listed in Tab. 6.3 and Tab. 6.4.

The action of the full observable on the ground state is decomposed again for fixed total momen-

$\mathcal{O}^{S=0,NN}$		
$4\mathcal{T}_0^{i,NN}$		
$ t^{0,\pm 1}, s\rangle$	$\rightarrow$	$- s, t^{0,\pm 1}\rangle$
$ t^0, t^{0,\pm 1}\rangle$	$\rightarrow$	$ t^{0,\pm 1}, t^0\rangle$
$ t^{\pm 1}, t^{\pm 1}\rangle$	$\rightarrow$	$ t^{\pm 1}, t^{\pm 1}\rangle$
$ t^{\pm 1}, t^{\mp 1}\rangle$	$\rightarrow$	$ t^0, t^0\rangle -  t^{\pm 1}, t^{\mp 1}\rangle$
$ t^0, t^0\rangle$	$\rightarrow$	$ t^1, t^{-1}\rangle -  t^{-1}, t^1\rangle$
$4\mathcal{T}_1^{i,NN}$		
$ s, t^1\rangle,  t^1, s\rangle$	$\rightarrow$	$ t^1, t^0\rangle -  t^0, t^1\rangle$
$ s, t^0\rangle,  t^0, s\rangle$	$\rightarrow$	$ t^1, t^{-1}\rangle -  t^{-1}, t^1\rangle$
$ s, t^{-1}\rangle,  t^{-1}, s\rangle$	$\rightarrow$	$ t^0, t^{-1}\rangle -  t^{-1}, t^0\rangle$
$4\mathcal{T}_2^{i,NN}$		
$ s, s\rangle$	$\rightarrow$	$ t^1, t^{-1}\rangle -  t^0, t^0\rangle +  t^{-1}, t^1\rangle$

Table 6.3: Action of the local operators  $\mathcal{T}_j^i$  for the observable  $\mathcal{O}^{NN}$ .

tum  $k$  in the two-triplon sector according to

$$\mathcal{O}_{NN,weak}^{S=0}(k)|0\rangle = \sum_d A_{2trp,NN,weak}^{S=0}(k, d)|k, d\rangle \quad (6.2.23a)$$

$$\mathcal{O}_{NNN}^{S=0}(k)|0\rangle = \sum_d A_{2trp,NNN}^{S=0}(k, d)|k, d\rangle, \quad (6.2.23b)$$

where

$$A_{2trp,NN,weak}^{S=0}(k, d) = \sqrt{2} \sum_l a_{l,l+d}^{weak,NN} \cos(k(2l + d)) \quad (6.2.24a)$$

$$A_{2trp,NNN}^{S=0}(k, d) = \sqrt{2} \sum_l a_{l,l+d}^{L,NNN} \cos(k(2l + 1/2 + d)). \quad (6.2.24b)$$

Here  $d$  is the distance between the two triplons,  $a_{l,l+d}^{weak,NN}$  is the amplitude for the creation of two triplons on the dimers  $l$  and  $l + d$  by  $\mathbf{S}_{0,R}\mathbf{S}_{1,L}$ , and  $a_{l,l+d}^{L,NNN}$  is the amplitude for the creation of two triplons on the dimers  $l$  and  $l + d$  by  $\mathbf{S}_{0,L}\mathbf{S}_{1,L}$ . In analogy to the  $S = 1$  case, it is not necessary to calculate  $a_{l,l+d}^{R,NNN}$  because it can be determined by  $a_{l,l+d}^{R,NNN} = a_{-l-d,-l}^{L,NNN}$  which is a consequence of the inversion symmetry of the chain. The basic unit length  $a/2$  is again the distance between two neighboring sites. The momentum is measured in units of  $\pi/(a/2)$ .

First, the symmetries of the two observables are discussed.  $\mathcal{O}_{NN,weak}^{S=0}$  possesses a reflection symmetry about  $k = \pi/2$  for the same reasons as the Hamiltonian. For any mode at momentum  $k$  which is created by  $\mathcal{O}_{NN,weak}^{S=0}$  there is also an identical mode at  $k + \pi$  which is created. In addition, each mode at  $k$  is degenerate with the reflected mode at  $-k$ . Therefore, the whole spectral density will be symmetric about  $k = \pi/2$ . This symmetry is absent for  $\mathcal{O}_{NNN}^{S=0}$ . For  $\mathcal{O}_{NNN}^{S=0}$  the spectral weight is mainly concentrated at small and intermediate momenta while it vanishes exactly at  $k = \pi$ . The

$\mathcal{O}^{S=0, \text{NNN}}$		
$4\mathcal{T}'_0^{\text{NNN}}$		
$ t^{0, \pm 1}, s\rangle$	$\rightarrow$	$ s, t^{0, \pm 1}\rangle$
$ t^0, t^{0, \pm 1}\rangle$	$\rightarrow$	$ t^{0, \pm 1}, t^0\rangle$
$ t^{\pm 1}, t^{\pm 1}\rangle$	$\rightarrow$	$ t^{\pm 1}, t^{\pm 1}\rangle$
$ t^{\pm 1}, t^{\mp 1}\rangle$	$\rightarrow$	$ t^0, t^0\rangle -  t^{\pm 1}, t^{\mp 1}\rangle$
$ t^0, t^0\rangle$	$\rightarrow$	$ t^1, t^{-1}\rangle -  t^{-1}, t^1\rangle$
$4\mathcal{T}'_1^{\text{NNN}}$		
$ s, t^1\rangle$	$\rightarrow$	$- t^1, t^0\rangle +  t^0, t^1\rangle$
$ t^1, s\rangle$	$\rightarrow$	$ t^1, t^0\rangle -  t^0, t^1\rangle$
$ s, t^0\rangle$	$\rightarrow$	$- t^1, t^{-1}\rangle +  t^{-1}, t^1\rangle$
$ t^0, s\rangle$	$\rightarrow$	$ t^1, t^{-1}\rangle -  t^{-1}, t^1\rangle$
$ s, t^{-1}\rangle$	$\rightarrow$	$- t^0, t^{-1}\rangle +  t^{-1}, t^0\rangle$
$ t^{-1}, s\rangle$	$\rightarrow$	$ t^0, t^{-1}\rangle -  t^{-1}, t^0\rangle$
$4\mathcal{T}'_2^{\text{NNN}}$		
$ s, s\rangle$	$\rightarrow$	$- t^1, t^{-1}\rangle +  t^0, t^0\rangle -  t^{-1}, t^1\rangle$

Table 6.4: Action of the local operators  $\mathcal{T}'_j$  for the observable  $\mathcal{O}^{\text{NNN}}$ .

latter follows from the fact that at  $k = \pi$  the observable creates an odd state with respect to reflection about the axis  $1/2$  (see Fig. 6.9) while a singlet made from two triplets is always an even state with respect to particle exchange.

### 6.2.3 Extrapolation

In the following spectral weights and spectral densities of the dimerized and frustrated spin-chain are analyzed. The spectral weights are positive. They are local in real space, i.e. they correspond to the frequency and momentum integrated spectral densities. The positivity makes it possible to analyze the spectral weights in the complete parameter range down to vanishing dimerization using dlog-Padé extrapolants as described in Sect. 5.2. The explicit extrapolations are discussed in the next section.

Concerning the extrapolation, the case of the spectral densities is more complicated. Here one can observe that longer range processes become more and more important when reducing the dimerization. It follows that no extrapolation is possible in this situation. One therefore has to restrict the analysis of the full spectral density to large and intermediate values of the dimerization. The following extrapolation technique is used which is explained in detail in Sect. 5.4 [208, 209]. After fixing the frustration  $\alpha$  to the desired value the plain series in  $\lambda$  is converted into a series in  $1 - \Delta$  invoking the one-triplon gap. The one-triplon gap is the natural internal energy scale of the problem. Since in this work the interest is only in strong and intermediate dimerization, no further extrapolation techniques like standard Padé extrapolants are used. There is no uncertainty

in the obtained spectral densities for strong dimerization  $\lambda = 0.3$ . The uncertainty is about 2% for intermediate dimerization ( $\lambda = 0.6$ ). In order to investigate the cases of weak or vanishing dimerization it would be important to use further extrapolation tools and to treat processes with longer or infinite range explicitly.

### 6.3 Spectral weights

In this section, it is investigated to which extent a triplon-based description is possible by computing spectral weights of multi-triplon contributions for the dimerized and frustrated spin-chain. Two scenarios are conceivable for  $\delta \rightarrow 0$ :

(i) The spectral weight is distributed rather evenly over the multi-triplon channels implying that the weight of a particular channel is small and that a large number of channels must be taken into account, see the discussion in Ref. [251]. This scenario would make an approach in terms of triplons difficult and hence inappropriate.

(ii) The spectral weight is found mainly in the channels with a *small* number of triplons, implying that a triplon approach is very useful and appropriate because spectral properties can be computed from the dynamics of a small number of excitations in a small number of channels.

The discussion is split in two. First, the focus is laid on the case of vanishing frustration, i.e.  $\delta = 0$  corresponds to the isotropic one-dimensional Heisenberg model. Here the extrapolations of the spectral weights are safer than in the frustrated case. Second, results for  $S = 1$  and  $S = 0$  excitations are presented. In the case of finite frustration the extrapolation becomes very complicated. Here most attention is concentrated on the case  $\alpha = 0.5$  where it is possible to determine higher orders of the perturbation expansion due to the above mentioned simpler structure of the Hamiltonian. The findings and implications of the analysis of the spectral weights are summarized in an intermediate conclusion at the end of this section.

#### 6.3.1 The dimerized chain ( $\alpha = 0$ )

The most interesting case to study is the case of  $S = 1$  excitations because  $S_i^z$  is the most basic observable. In this situation there is a one-triplon contribution for all  $\delta \neq 0$ . It is therefore possible to investigate the decrease of spectral weight in the one-triplon sector and at the same time the evolution of the multi-triplon channels. In the case of  $S = 0$  excitations, there is no one-triplon sector because at least two triplons are needed to create an excitation with total spin zero.

##### 6.3.1.1 S=1

In the following arguments are listed which favor scenario (i) or (ii) for the dimerized spin-chain approaching the limit  $\delta \rightarrow 0$ .

**Scenario (i)** A field theoretic description gives some indications for this scenario. Using abelian bosonization [82, 232, 250, 252, 279, 280] the low-lying states of an anisotropic spin-chain are described by the Hamiltonian Eq. 6.1.14. The interaction parameter  $K$  is  $K = 1$  for the XY-model, equivalent to free fermions, and  $K = 1/2$  for the isotropic case. A local operator is

$$S_j^z \approx (2\pi)^{-1} \partial_x \Phi(j) + A(-1)^j \cos(2\Phi(j)) \quad (6.3.1)$$

where the lattice constant is unity, and  $A$  a non-universal constant. The undimerized Hamiltonian (Eq. 6.1.22 for  $\alpha = 0$ ) corresponds essentially to free bosons (6.1.14). A finite dimerization is accounted for by an additional term proportional to  $\delta \int_{-\infty}^{\infty} \cos(2\Phi(x)) dx$  leading to a sine-Gordon model (see also the model introduced in Sect. 6.1). For  $K < 2$  the system is massive with a gap  $\Delta \propto \delta^{1/(2-K)}$  ( $= \delta^{2/3}$  for the isotropic chain). A single bosonic mode of (6.1.14) is created by

$$b_k^\dagger = 1/\sqrt{2} (\tilde{\Phi}(k)/N_k - iN_k \tilde{\Pi}(k)) \quad (6.3.2)$$

where  $N_k = \sqrt{\pi K/|k|}$ . The quantities with tilde are the Fourier transforms of the real-space fields. The excited state  $S_j^z|0\rangle$  is expanded in states of various number of bosons with focus on the vicinity of momentum  $\pi$  where most of the weight in the dynamic structure factor is found:  $S_j^z \propto \cos(2\Phi(j))$ . The coefficients of one- and two-boson states are

$$c_k = \langle 0|b_k \cos(2\Phi)|0\rangle = \langle 0|[b_k, \cos(2\Phi)]|0\rangle \quad (6.3.3)$$

$$c_{k,q} = \langle 0|b_k b_q \cos(2\Phi)|0\rangle = \langle 0|[b_k[b_q, \cos(2\Phi)]]|0\rangle. \quad (6.3.4)$$

By making use of

$$[b_k, 2\Phi(j)] = \sqrt{K/|k|} \sqrt{2\pi/L} \exp(ikj) \quad (6.3.5)$$

where the momenta are discretized by introducing a finite system size  $L$  to ensure normalizability. This yields  $c_k = 0$  and

$$c_{k,q} \propto \frac{K}{\sqrt{|k||q|}} \frac{2\pi}{L} \exp(i(k+q)j) \Delta^K \quad (6.3.6)$$

where  $\langle \sin(2\Phi) \rangle = 0$  and  $\langle \cos(2\Phi) \rangle \propto \Delta^K$  is used. So the total weight  $W_1^z$  in the one-boson channel vanishes for  $\Delta \rightarrow 0$ . The total weight  $W_2^z$  in the two-boson channel is

$$\begin{aligned} W_2^z &\propto \sum_{k,q} |c_{k,q}|^2 \propto \Delta^{2K} \int_{\nu|k|, \nu|q| \Delta} \frac{K^2}{|k||q|} dk dq \\ &\propto \Delta^{2K} \ln(\Delta)^2 \\ &\propto \delta^{2K/(2-K)} \ln(\delta)^2 \end{aligned} \quad (6.3.7)$$

in leading order in  $\ln(\delta)$ . Generally, all channels with an odd number of bosons carry no weight (at momentum  $\pi$ ) whereas channels with  $2n$  bosons behave like

$$W_{2n}^z \propto \delta^{2K/(2-K)} \ln(\delta)^{2n}. \quad (6.3.8)$$

whence one can conclude that *any* single channel becomes *unimportant* on  $\delta \rightarrow 0$ . Only the consideration of an infinite number allows to treat the case vanishing dimerization correctly. This appears to be sound evidence for scenario (i).

**Scenario (ii)** The main argument for scenario (ii) is an explicit calculation of spectral weights for the first triplon channels. First, however, the *general* validity of the previous argument is discussed by four basic considerations.

(a) Considering free fermions ( $K = 1$ ) it is known that the operator  $S_j^z = n_j - 1/2$  excites a particle-hole continuum at all wave-vectors. So the dynamic correlations of this operator are exhaustively described by *two* elementary excitations, a particle and a hole, independent of the dimerization  $\delta$ .

(b) Considering the isotropic spin-chain ( $K = 1/2$ ) it was shown that 72.89 % of the total weight (sum over all wave vectors) of the dynamic structure factor is described by the *two*-spinon continuum [272].

(c) It is undisputed that the dimerized isotropic spin-chain displays a *single*-mode peak with finite spectral weight at all wave vectors as long as  $\delta \neq 0$  [251, 252].

(d) By construction, the bosonic modes of the field theory (6.3.2) exist at *small* momenta  $k \approx 0$  [232, 280, 281]. The dynamics at momenta close to  $\pi$  is captured by the superposition of an infinite number of these modes as becomes evident from Eq. 6.3.1 and from Eq. 6.3.8.

The above arguments prove that there can be several, rather different looking descriptions for the *same* physics. One may *not* conclude from the validity of a particular description, e.g. in terms of a multitude of modes, that another description, e.g. in terms of only a few modes, is not valid. This is an absolutely crucial observation for the interpretation and comparison of different results.

In the following the spectral weight will be analyzed explicitly. The total weight  $I_{\text{tot}} = \sum_{n=0}^{\infty} I_n$  is given by the sum rule  $I_{\text{tot}} = \langle R^\dagger R \rangle = \langle (S_j^z)^2 \rangle = 1/4$  which serves as sensitive check for the validity of the results. In the following the relative weights  $I_{n,\text{rel}} = I_n/I_{\text{tot}} = 4I_n$  are discussed.

dlogPadé	a) Zero $\lambda_0$	b) $\gamma _{\lambda=\lambda_0}$	c) $\gamma _{\lambda=1}$
[4, 2]			0.32524
[3, 3]	1.02503	0.36798	0.32891
[2, 4]	1.09817	0.58184	0.34110
[1, 5]	1.09817	0.58184	0.31457
[0, 6]			0.31458

Table 6.5: Relative weight  $I_{1,\text{rel}}$  of the one-triplon channel. a) position of the singularity from unbiased extrapolants; b) exponent at the unbiased positions; c) exponents in the biased extrapolants. (blanks: extrapolants without singularity).

For isolated dimers ( $\lambda = 0$ ), the total spectral weight lies in the one-triplon channel  $I_{1,\text{rel}} = 1$ . As  $\lambda$  increases  $I_{1,\text{rel}}$  decreases and the weight is transferred to the multi-triplon sectors. In Tab. 6.5, the results for unbiased dlogPadé extrapolants indicate a singularity at  $\lambda \approx 1$ . From the physics of the Hamiltonian (6.1.22 for  $\alpha = 0$ ) it is known that the singularity is located at  $\lambda = 1$  where the system becomes critical. Thus it is advised to investigate extrapolants biased to display the singularity at unity:  $I_1 \propto (1 - \lambda)^\gamma$  (last column in Tab. 6.5). The exponent is found to be  $\gamma = 0.325 \pm 0.016$ . which leads one to conjecture that it takes exactly the value  $\gamma = 1/3$ . More generally, it is presumed that any single mode, which vanishes due to mixing with a continuum with



square-root singularities at the band edges, loses its weight like  $I_{\text{mode}} \propto \sqrt{\Delta\omega}$ , where  $\Delta\omega$  is the distance of the mode to the band edge of the continuum. The weight in the continuum is assumed to be constant.

This presumption is supported by considering a generic resolvent  $I(\omega) = 1/(\omega - a - \Sigma(\omega))$  with  $\Sigma(\omega) = [\omega + \sqrt{\omega^2 - 4}]/2$  for  $\omega \leq -2$ . Such a resolvent appears for instance in the dynamics of two hard-core particles hopping from site to site in one dimension at given total momentum [251]. The constant  $a$  allows to tune a nearest-neighbor interaction ( $a < 0$ : attraction,  $a > 0$ : repulsion) whereas  $\Sigma(\omega)$  incorporates the kinetic energy of the relative motion. For  $a \leq -1$  a bound state emerges from the continuum. It is separated from the continuum by the energy  $\Delta\omega = -(2 + a + 1/a)$ . Its weight  $I_{\text{mode}}$  is

$$I_{\text{mode}} = \frac{1}{(1 - \partial_\omega \Sigma(-2 - \Delta\omega))} \quad (6.3.9)$$

The derivative of  $\Sigma(-2 - \Delta\omega)$  is given as

$$\begin{aligned} (\partial_\omega \Sigma(\omega)) \Big|_{\omega=-(2+\Delta\omega)} &= \left( \frac{1}{2} + \frac{\omega}{2\sqrt{\omega^2 - 4}} \right) \Big|_{\omega=-(2+\Delta\omega)} \\ &= \frac{1}{2} \left( 1 - \frac{2 + \Delta\omega}{\sqrt{4\Delta\omega + (\Delta\omega)^2}} \right) \end{aligned}$$

The latter implies for  $I_{\text{mode}}$  in the limit  $\Delta\omega \rightarrow 0$

$$I_{\text{mode}} \propto \sqrt{\Delta\omega} \quad (6.3.10)$$

For dimerized spin-chains, the single triplon mode is separated from the continuum by an energy  $\Delta\omega$  of the order of the energy gap  $\Delta$  [251]. Using  $I_{\text{mode}} \propto \sqrt{\Delta\omega}$  for each total momentum and integrating then over all momenta to obtain the local weights one finds that the single mode loses its weight as  $\sqrt{\Delta} \propto \delta^{1/3}$  [266] which agrees excellently with the extrapolations.

dlogPadé	a) Zero $\lambda_0$	b) $\gamma_2 _{\lambda=\lambda_0}$	c) $\gamma_2 _{\lambda=1}$	d) $I_{2,\text{rel}}$
[5, 0]			*	1.0618
[4, 1]			*	0.9818
[3, 2]			-0.7601	0.9976
[2, 3]	0.9908	-0.7323	-0.7603	*
[1, 4]			*	0.9895

Table 6.6: Relative weight  $I_{2,\text{rel}}$  of the two-triplon channel. a) position of the singularity from unbiased extrapolants for  $\partial_\lambda I_{2,\text{rel}}$ ; b) exponent at the unbiased positions; c) exponents in the biased extrapolants; d)  $I_{2,\text{rel}}|_{\lambda=1}$  integrated from the biased (position  $\lambda = 1$  and exponent  $-2/3$ ) extrapolants (extrapolants without singularity: blanks; with spurious poles: stars).

Fig. 6.10 shows the final results for  $I_{1,\text{rel}}$ ,  $I_{2,\text{rel}}$  and  $I_{3,\text{rel}}$ ; the tiny four- and more triplon contributions are neglected. The sum rule is excellently fulfilled to within  $\approx 0.003$  for all values of  $\lambda$  supporting the above analysis.

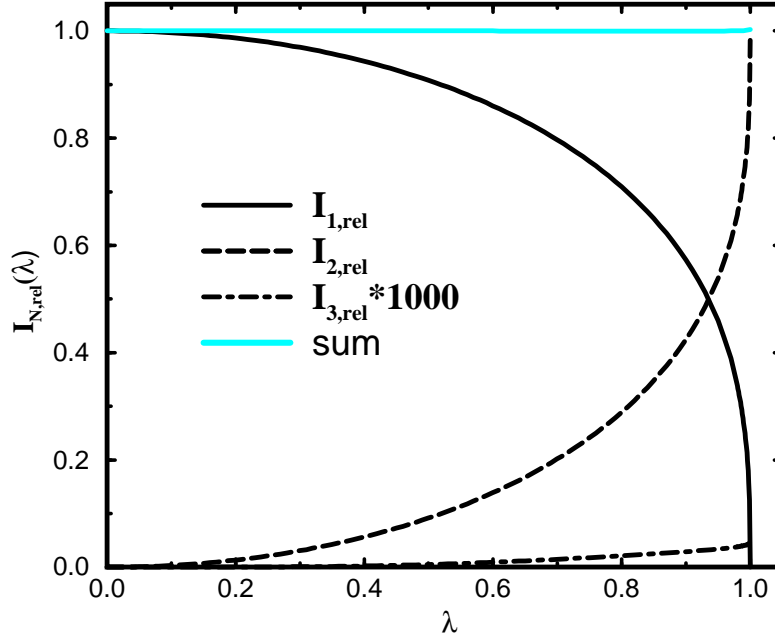


Fig. 6.10: Relative spectral weights  $I_{N,\text{rel}}(\lambda)$  of the dynamic structure factor in the dimerized chain. Depicted are biased extrapolants with singularity at  $\lambda = 1$  and exponent  $1/3$  for  $I_{1,\text{rel}}$  ( $[4,2]$ , black solid line); exponent  $-2/3$  in the derivative of  $I_{2,\text{rel}}$  ( $[3,2]$ , dashed line) and similarly for  $1000 \cdot I_{3,\text{rel}}$  ( $[2,2]$ , dashed-dotted line). The grey line is the sum  $\sum_{N=1}^3 I_{N,\text{rel}}$ .

In the two-triplon channel, there is no indication for a zero of  $I_2$  at  $\lambda = 1$ . On the contrary, Padé extrapolants indicate significant weight at criticality. The weight in the two-triplon channel is the weight transferred from the one-triplon channel minus the weight transferred further to channels with three and more triplons. Hence it is natural to assume the existence of a singularity with exponent  $1/3$  in  $I_2$ . But if this singularity is not linked to a zero, dlogPadé extrapolants cannot detect it. Hence the derivative  $\partial_\lambda I_2$  is investigated which should be governed by a divergence with exponent  $-2/3$ . Indeed, Padé (not shown) and dlogPadé extrapolants (see Tab. 6.6) indicate a singularity at  $\lambda \approx 1$ . Extrapolants biased to a singularity of  $\partial_\lambda I_2$  at  $\lambda = 1$  yield exponents  $\gamma_2 \approx -0.76$ . The corresponding value of  $I_{2,\text{rel}}$  found from integrating  $\partial_\lambda I_2$  is 1.25. Since this value overestimates the sum rule by at least 25%, one concludes that the exponent  $\gamma_2 \approx -0.76$  is too large in absolute value. Thus, the extrapolants are biased to the expected behavior  $\partial_\lambda I_2 \propto (1-\lambda)^{-2/3}$ . In the last column of Tab. 6.6 the ensuing values for  $I_{2,\text{rel}}$  are given. Quite unexpectedly, the results conclusively point to a spectral weight very close to unity! Since diagonal extrapolants usually yield the most reliable results one retains the value  $I_{2,\text{rel}} \approx 0.998$ , keeping a possible error of a few percent in mind.

The sum rule corroborates the above result strongly. Padé and unbiased dlogPadé extrapolants

consistently show that  $I_{3,\text{rel}}$  is not larger than about  $3 \cdot 10^{-4}$  which agrees perfectly with the value close to unity for  $I_{2,\text{rel}}$ . The inclusion of a singularity does not enhance  $I_{3,\text{rel}}$ . The biased extrapolants for  $\partial_\lambda I_3$  (position  $\lambda = 1$  and exponent  $-2/3$ ) also yield only a contribution of about  $2 \cdot 10^{-4}$  ([2,2]). Finally, the Padé and dlogPadé extrapolants for the four-triplon contribution  $I_{4,\text{rel}}$  consistently indicate values well below  $10^{-4}$ . The biased approximant for  $\partial_\lambda I_4$  (position  $\lambda = 1$  and exponent  $-2/3$ ) even yield values below  $10^{-5}$ . Therefore, one concludes that the contributions of channels with four and more triplons can be safely neglected.

Fig. 6.10 shows the final results for  $I_{1,\text{rel}}$ ,  $I_{2,\text{rel}}$  and  $I_{3,\text{rel}}$ ; the tiny four- and more triplon contributions are neglected. The sum rule is excellently fulfilled to within  $\approx 0.003$  for all values of  $\lambda$  supporting the above analysis.

In conclusion, it is found that even the dynamic structure factor of the critical uniform spin-chain can be described to about 99% by taking only the two-triplon contribution. This shows that scenario (ii) is correct for spin-chains with vanishing frustration.

This result is confirmed by a recent work of Hamer and coworkers [187, 282]. They calculate the one- and two-triplon spectral weight up to order 13/12 using a linked cluster expansion. The one-triplon weight vanishes with  $(1 - \lambda)^{1/3}$  approaching  $\lambda = 1$  consistent with the above findings. In addition, the two-triplon weight accounts for 99.8% of the spectral weight at  $\lambda = 1$  which is almost exactly the value obtained by the continuous unitary transformations [82]. Note that the two-triplon spectral weight even accounts for 90% of the total spectral weight even if no singularity at  $\lambda = 1$  is included. They find an exponent of  $\eta \approx -0.6$  for  $dI_2/d\lambda$  instead of  $\eta = -2/3$ . This is explained by the influence of logarithmic corrections.

Hamer and coworkers also analyzed the momentum distribution of the spectral weights [282]. They find that the one-triplon weight vanishes in the limit  $\lambda \rightarrow 1$  for all momenta except in the limit  $k \rightarrow 0$ . But at  $k \rightarrow 0$  the dynamical structure factor vanishes itself. The two-triplon spectral weights are more subtle. They clearly dominate at large and intermediate momenta where most of the spectral weight is located, but they only play a subdominant role for small momenta where the total weight itself is small.

### 6.3.1.2 S=0

In this part the same analysis as in the last section is done for the case of spectral weights for excitations with spin zero. The first quantity to focus on is the total intensity  $I_{\text{tot}}$ . The direct extrapolation of  $I_{\text{tot}}$  turns out to be very complicated because the extrapolants show poles in the denominator which lie close to the critical point  $\lambda = 1$ . But in contrast to the extrapolation in the last section, in most cases there are two poles near  $\lambda = 1$ . The same features appear when analyzing the first derivative of  $I_{\text{tot}}$ . But the total intensity can be determined from the ground state energy  $E_0$

$$I_{\text{tot}}(\lambda) = \frac{3}{16} - \frac{1}{2} \frac{d}{d\lambda} E_0(\lambda) - \left( \frac{d}{d\lambda} E_0(\lambda) \right)^2. \quad (6.3.11)$$

The ground state energy  $E_0$  is known up to order 10 by continuous unitary transformations and up to order 15 by linked cluster expansions. Therefore the total intensity  $I_{\text{tot}}$  is known up to order 14 since it depends on the first derivative of  $E_0$ . The appearance of two poles in the extrapolation of

the total intensity can be understood from the structure of Eq. 6.3.11 and the asymptotic behavior of the ground state energy.  $I_{\text{tot}}$  constitutes of two structural different terms. From the fact that two different singularities are present at the same time it is therefore plausible that the extrapolation of  $I_{\text{tot}}$  is complicated. In the following the total intensity is computed not directly but indirectly from an extrapolation of the ground state energy.

The extrapolation of the ground state energy is simpler because the asymptotic behavior of  $E_0$  is simpler [266, 267]. The asymptotic behavior of the ground state energy for small dimerization is

$$E_0(\lambda) = E_{0,0} + E_{0,1}(1 - \lambda) + E_{0,2}(1 - \lambda)^{\frac{4}{3}} \quad , \quad (6.3.12)$$

i.e. also the ground state energy is a sum of two different asymptotic terms. In order to separate out a single singularity the derivatives of  $E_0$  are investigated. The first and the second derivative of  $E_0$  are

$$\begin{aligned} \frac{d}{d\lambda} E_0(\lambda) &= -E_{0,1} - \frac{4}{3} E_{0,2} (1 - \lambda)^{\frac{1}{3}} \\ \frac{d^2}{d\lambda^2} E_0(\lambda) &= +\frac{4}{9} E_{0,2} (1 - \lambda)^{-\frac{2}{3}} \quad . \end{aligned} \quad (6.3.13)$$

The determination of  $dE_0/d\lambda$  is therefore similar to the determination of  $I_2$  in the case of  $S = 1$  excitations in the last section as far as the singularities are concerned.  $d^2E_0/d\lambda^2$  shows asymptotically a power-law behavior  $\partial_\lambda^2 E_0 \propto (1 - \lambda)^{\gamma_E}$  (with  $\gamma_E = -2/3$ ). In analogy to the latter case the second derivative  $d^2E_0/d\lambda^2$  is extrapolated and then integrated in order to obtain the total intensity  $I_{\text{tot}}$ .

dlogPadé	a) Zero $\lambda_0$	b) $\gamma_E _{\lambda=\lambda_0}$	c) $\gamma_E _{\lambda=1}$	d) $\frac{dE_0}{d\lambda} _{\lambda=1}$	e) $I_{\text{tot}} _{\lambda=1}$
[10, 2]	1.0029	-0.5483	-0.5301	-0.4424	0.2130
[8, 4]	1.0024	-0.5447	-0.5269	-0.4416	0.2130
[6, 6]	1.0039	-0.5539	-0.5259	-0.4414	0.2134
[5, 7]	1.0051	-0.5589	-0.5211	-0.4404	0.2138
[4, 8]	1.0056	-0.5604	-0.5252	-0.4412	0.2135
[3, 9]	1.0022	-0.5438	-0.5231	-0.4407	0.2136

Table 6.7: Second derivative  $(d^2/d\lambda^2)E_0$  of the ground state energy. a) position of the singularity from unbiased extrapolants; b) exponent at the unbiased positions; c) exponents in the biased extrapolants. d) Value of the first derivative  $(d/d\lambda)E_0$  at  $\lambda = 1$ . e) Value of the total intensity  $I_{\text{tot}}$  at  $\lambda = 1$ .

The results for  $d^2E_0/d\lambda^2$  are summarized in Tab. 6.7. The extrapolants show clear singularities at  $\lambda_0$  close to  $\lambda = 1$ . The exponents are approximately  $\gamma_E \approx -0.55$ . Extrapolants biased to a singularity of  $d^2E_0/d\lambda^2$  at  $\lambda = 1$  yield exponents  $\gamma_E \approx -0.52$ . The determined exponent  $-0.52$  is qualitatively close to the desired value of  $2/3$  so it is reasonable to try to fix the exponent to be  $2/3$  in the extrapolation. Unfortunately the inclusion of the exact exponent fails due to spurious poles in the denominator of the extrapolants. This can be understood by a recent DMRG study finding large logarithmic corrections and an effective exponent  $\gamma_E \approx -0.55$  [283]

It is possible to check the quality of the extrapolants not biased to  $\gamma_E = 2/3$  (using  $\gamma_E \approx -0.52$ ) by comparing to the value for  $dE_0/d\lambda$  at  $\lambda = 1$  to the one exactly known from Bethe ansatz

$$\frac{d}{d\lambda}E_0(\lambda)|_{\lambda=1} = \frac{E_0}{L} = \frac{1}{4} - \ln 2 \approx -0.4431 \quad . \quad (6.3.14)$$

The results for this value obtained by integrating the not biased extrapolants ( $\gamma_E \approx -0.52$ ) are given in Tab. 6.7 d). The values differ only in the third digit. The exact total intensity as obtained by inserting Eq. 6.3.14 in Eq. 6.3.11 is

$$I_{\text{tot}}|_{\lambda=1} = \ln 2 - (\ln 2)^2 \approx -0.2127 \quad . \quad (6.3.15)$$

The corresponding results for this value is shown in column e) of Tab. 6.7. It can be concluded that the extrapolation of  $I_{\text{tot}}$  is well justified up to  $\lambda = 1$ . The difference to the exact results for the undimerized case is determined to be about  $10^{-3}$  in absolute scale. The discrepancy between the extrapolated and the exact exponent can be explained by large logarithmic corrections which are usually strong in this system [267, 293]. The resulting total intensity is shown in Fig. 6.12 as the grey solid line.

In the following the extrapolation of the two-triplon spectral weight is discussed. Similar to the case of the total intensity the direct extrapolation of  $I_2$  is rather complicated. The reason is the same as in the case before. The structure of the singularities will be the same for  $I_2$  and  $I_{\text{tot}}$ . It is therefore reasonable to argue that  $I_2$  depends on a function  $\mathbb{E}(\lambda)$  in the same way as  $I_{\text{tot}}$  depends on  $dE_0/d\lambda$ . One defines

$$I_2(\lambda) = \frac{3}{16} - \frac{1}{2}\mathbb{E}(\lambda) - (\mathbb{E}(\lambda))^2 \quad . \quad (6.3.16)$$

Inverting this equation gives

$$\mathbb{E}_2 = -\frac{1}{4} + \sqrt{\frac{1}{4} - I_2} \quad . \quad (6.3.17)$$

In analogy to  $dE_0/d\lambda$  the first derivative  $\partial_\lambda \mathbb{E}_2$  will be extrapolated having in mind that the singularities of  $dE_0/d\lambda$  and  $\mathbb{E}_2$  are the same. The quantity  $\partial_\lambda \mathbb{E}_2$  is known up to order 6. DlogPadé extrapolation gives no sign for a singularity at  $\lambda = 1$  which may be due to the low order available. In a next step the extrapolants can be forced to have a singularity at  $\lambda = 1$ . Determining the corresponding exponent  $\gamma_2$  yields no clear picture. In a last step it is reasonable to bias the extrapolants to have the same exponent  $\gamma_E \approx -0.523$  as the first derivative of the ground state energy. It is found that this stabilizes the extrapolation which can be viewed as support for this extrapolation scheme. The results for the latter extrapolants are summarized in Tab. 6.8. It can be concluded that the two-triplon spectral weight governs more than 90% of the total spectral weight even at  $\lambda = 1$ . The resulting two-triplon intensity is shown in Fig. 6.12 as the black solid line.

In the last part of this section the three- and four-triplon contributions to the spectral weight are discussed. Guided by the previous paragraphs the functions

$$\mathbb{E}_{3/4} = -\frac{1}{4} + \sqrt{\frac{1}{4} - I_{3/4}} \quad (6.3.18)$$

are defined. Unfortunately  $\mathbb{E}_3$  is governed by a sign change at small  $\lambda$  prohibiting an analysis in terms of dlogPadé extrapolants.  $I_3$  is therefore extrapolated directly without having the opportunity

dlogPadé	a) $\mathbb{E}_2 _{\lambda=1}$	b) $I_2 _{\lambda=1}$	c) $I_{2,rel} _{\lambda=1} = I_2 _{\lambda=1}/I_{tot} _{\lambda=1}$
[4, 2]	-0.45859	0.2065	0.9709
[3, 3]	-0.47596	0.1989	0.9351
[2, 4]	-0.47442	0.1996	0.9384

Table 6.8: Results for two-triplon spectral weight  $I_2$  at  $\lambda = 1$ . a) Value of  $\mathbb{E}_2$  at  $\lambda = 1$ ; b) Value of the two-triplon spectral weight at  $\lambda = 1$ . c) Value of the relative two-triplon intensity  $I_{2,rel} = I_2/I_{tot}$  at  $\lambda = 1$ .

to include the same singularities as in the latter cases. The results of various dlogPadé extrapolants are shown in Fig. 6.11. Note that the absolute scale is much smaller than in the case of the two-triplon spectral weight. In addition, a clear tendency can be seen that the three-triplon spectral weight is reduced more and more approaching  $\lambda = 1$ . It can be concluded that the three-triplon spectral weight is very small.

The four-triplon contribution to the spectral weight is determined indirectly over the function  $\mathbb{E}_4$

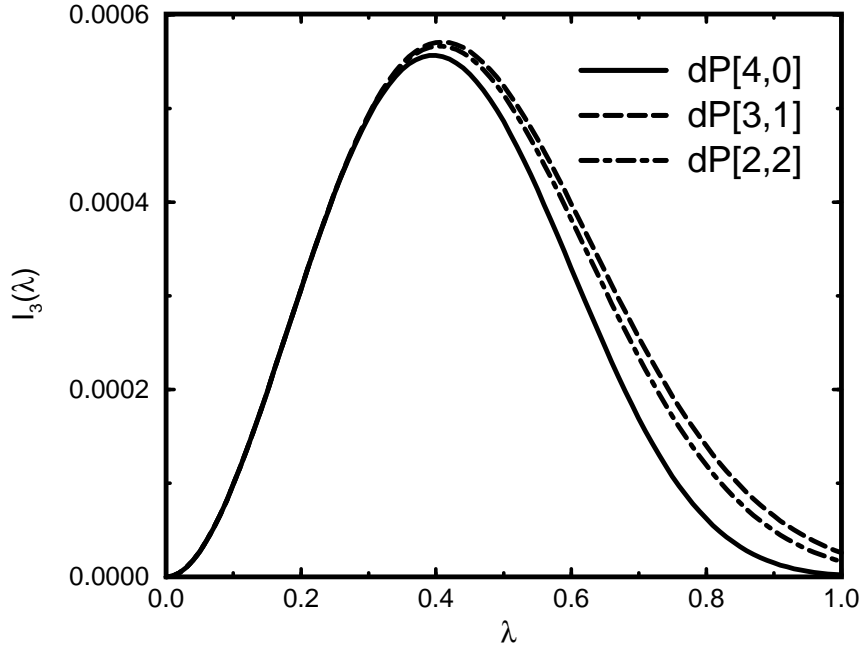


Fig. 6.11: DlogPadé extrapolants for three-triplon spectral weights  $I_3(\lambda)$  for  $S = 0$ . Solid black line denotes a [4, 0]-dlogPadé, long dashed line a [3, 1]-dlogPadé and dot-dashed line a [2, 2]-dlogPadé.

similar to the two-triplon case, i.e. the function  $\mathbb{E}_4$  is biased to have the same singularity as the function  $dE_0/d\lambda$  which determined the total intensity. The results at  $\lambda = 1$  are summarized in Tab. 6.9. It can be clearly seen that the four-triplon contribution is very small, i.e. about  $10^{-4}$  of the total intensity. The resulting four-triplon intensity is shown in Fig. 6.12 as the dashed black

line.

The overall picture for the spectral weights with total spin zero for the unfrustrated case is depicted

dlogPadé	a) $\mathbb{E}_4 _{\lambda=1}$	b) $I_4 _{\lambda=1}$	c) $I_{4,rel} _{\lambda=1} = I_4 _{\lambda=1}/I_{tot} _{\lambda=1}$
[4, 0]	0.24997	0.0000298	0.000140
[3, 1]	0.24999	0.0000064	0.000030
[2, 2]	0.24998	0.0000180	0.000084

Table 6.9: Results for two-triplon spectral weight  $I_4$  at  $\lambda = 1$ . a) Value of  $\mathbb{E}_4|$  at  $\lambda = 1$ ; b) Value of the four-triplon spectral weight at  $\lambda = 1$ . c) Value of the relative two-triplon intensity  $R I_4 = I_4/I_{tot}$  at  $\lambda = 1$ .

in Fig. 6.12. The two-triplon contribution dominates the physics for all values of the dimerization including the case of the zero dimerization ( $\lambda = 1$ ). These findings are in agreement with the results for the  $S = 1$  spectral weights analyzed in the last section.

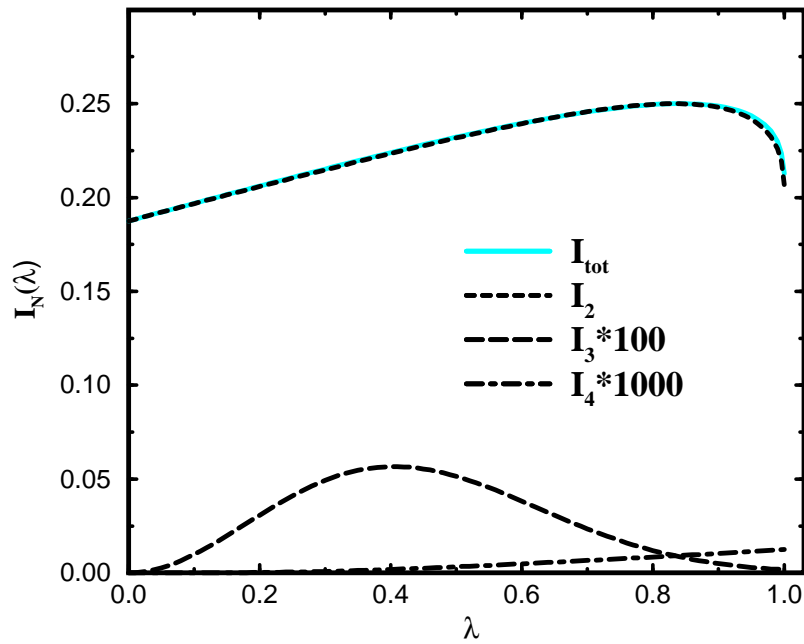


Fig. 6.12: Spectral weights  $I_N(\lambda)$  for  $S = 0$ . The dashed black line displays  $I_2$  (biased [4,2] dlogPadé used), the long dashed line shows  $I_3$  ([2,2] dlogPadé used) and the dot-dashed line corresponds to  $I_4$  ([2,2] dlogPadé used). The grey solid line is the total intensity  $I_{tot}$ .

### 6.3.2 Finite frustration

In this section the influence of frustration on the spectral weights is discussed. It will turn out that the extrapolation is even harder than in the unfrustrated case. The discussion is therefore restricted to spectral weights of excitations with total spin one.

As discussed in Sect. 6.1, the system undergoes a phase transition at critical frustration  $\alpha_{0,c} \approx 0.24$  from a gapless phase for  $\alpha_0 < \alpha_{0,c}$  to a gapped phase for  $\alpha_0 > \alpha_{0,c}$ . It is therefore reasonable to expect that the results for vanishing frustration hold at least up to the critical frustration. The main physical question is therefore whether the triplon picture even survives in the massive phase at zero dimerization, which occurs at larger frustration.

The straightforward extension of the analysis for zero frustration is to take the extrapolants for  $\alpha = 0$  and to turn on the frustration. Here the focus is on the behavior of the two-triplon contribution to the spectral weight at  $\lambda = 1$ . In Fig. 6.13 the results for the relative spectral weight  $I_{2,\text{rel}}|_{\lambda=1}(\alpha)$  at  $\lambda = 1$  are shown as a function of frustration. It can be seen clearly that the extrapolations become quite involved. The dlogPadé extrapolants [1,4] and [4,1] are influenced by poles in the denominator spoiling the extrapolation at some value of the frustration ( $\alpha \approx 0.1$  for [4,1] and  $\alpha \approx 0.4$  for [1,4]). Generically, the results fit to the above expectations. The spectral weight of two triplons stays on a high level for small values of  $\alpha$ . The extrapolation in the massive phase is complicated and the spectral weight in the two-triplon sector is reduced. It is of course hard to make a definite conclusion from these results.

In order to strengthen the results, in the following the focus is laid on the Majumdar-Gosh point ( $\alpha = 0.5$ ). Here the system is in the massive phase. The Hamiltonian simplifies and it is possible to obtain higher order series for the spectral weights. It is expected that the qualitative behavior at  $\alpha = 1/2$  applies everywhere in the phase of asymptotically free and massive spinons. The crucial question is whether or not the triplon description breaks down.

#### 6.3.2.1 Majumdar-Gosh point ( $\alpha_0 = 0.5$ )

At the Majumdar-Gosh point, i.e.  $\alpha_0 = 1/2$  and  $\lambda = 1$  in Eq. 6.1.1, the ground state is known exactly as discussed in Sect. 6.1. The ground state is a short range resonating valence bond state (RVB) which breaks translational symmetry. The system is always gapped and the usual description is formulated in terms of massive spinons.

As before, the total spectral weight for  $\lambda = 0$  lies in the one-triplet channel. For finite  $\lambda$  the intensity in  $I_{1,\text{rel}}$  decreases and the spectral weight of the multi-triplon channels are finite. First the spectral weight  $I_{1,\text{rel}}$  for one-triplon creation will be analyzed. Note that it is not clear whether  $I_1$  has a vanishing or a finite spectral weight in the limit  $\lambda \rightarrow 1$ . The one-triplon state with momentum  $k = \pi/2$  is an exact eigenstate of the system. Therefore it is plausible that a finite one-triplon spectral weight is present at  $\lambda = 1$  originating from one-triplon states with momentum  $k \approx \pi/2$ . All extrapolation techniques clearly yield a singularity at  $\lambda = 1$  (see Tab. 6.10). However, the determination of the exponent  $\gamma^{\text{Maj}}$  for  $I_1 \propto |1 - \lambda|^{\gamma^{\text{Maj}}}$  is rather difficult. Standard dlogPadé extrapolants yield  $\gamma^{\text{Maj}} = 0.15 \pm 0.05$ . The result changes if one uses biased dlogPadé



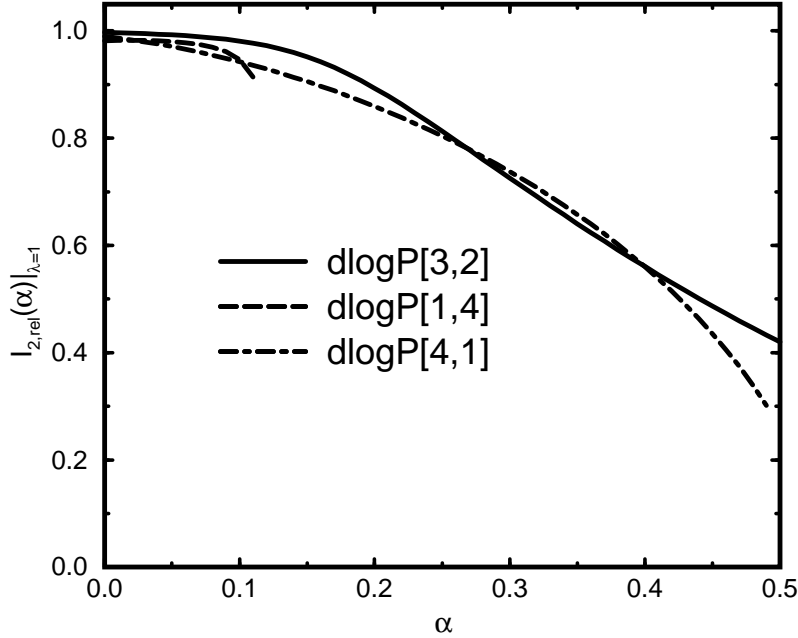


Fig. 6.13: Two-triplon spectral weight  $l_{2,\text{rel}}|_{\lambda=1}(\alpha)$  for  $S = 1$  excitations at  $\lambda = 1$  as a function of frustration  $\alpha$ . The same biased dlogPadé extrapolation scheme is used as in the case of vanishing frustration.

extrapolants. One finds  $\gamma^{\text{Maj}} = 0.34 \pm 0.005$ . One can conclude that the exponent is equal  $1/3$  which is consistent with earlier results [186]. However, one is not able to decide whether  $l_1$  turns to zero for  $\lambda \rightarrow 1$  or stays at a finite but small value. As discussed below it is claimed that the latter scenario is true. Using  $\gamma^{\text{Maj}} = 1/3$  and extrapolating for the derivative  $dl_{1,\text{rel}}/d\lambda$  the value  $l_{1,\text{rel}} \approx 0.14$  is found. The resulting curve is shown as the black solid line in Fig. 6.14.

The direct extrapolation of  $l_{2,\text{rel}}$  is very complicated and yields no indications for a singularity at  $\lambda = 1$  due to spurious poles in the extrapolation scheme. If one biases the extrapolation to have the same exponent as  $l_{1,\text{rel}}$ , i.e.  $dl_{2,\text{rel}}/d\lambda \propto |1 - \lambda|^{-2/3}$ , one finds an improvement in the convergence of the extrapolation schemes. These findings support the way of extrapolating  $l_{2,\text{rel}}$ .  $l_{2,\text{rel}}$  is determined to be  $0.74 \pm 0.2$ . The dashed curve in Fig. 6.14 corresponds to dlogPadé[3,7] for  $l_{2,\text{rel}}$ . The investigation of  $l_{3,\text{rel}}$ ,  $l_{4,\text{rel}}$ ,  $l_{5,\text{rel}}$  and  $l_{6,\text{rel}}$  consistently shows that the spectral weight is of orders of magnitude smaller than  $l_{1,\text{rel}}$  and  $l_{2,\text{rel}}$ .

In Fig. 6.14 the spectral weights  $l_{1,\text{rel}}$ ,  $l_{2,\text{rel}}$  and  $l_{3,\text{rel}}$  are shown. Here  $l_{1,\text{rel}}$  rests at a finite spectral weight for  $\lambda = 1$ . Looking at the sum of the three spectral weights (see grey solid line), the sum rule  $\sum_n l_{n,\text{rel}} = 1$  is fulfilled almost perfectly using  $l_{1,\text{rel}}|_{\lambda=1} \neq 0$  which is an indication to use this extrapolation for  $l_1$ .

The interpretation of the results in the limit of vanishing dimerization ( $\lambda = 1$ ) is the following. At the Majumdar-Gosh point, the lowest excitation energy is equal  $2\Delta_{\text{spinon}}$  where  $\Delta_{\text{spinon}}$  is the mass

dlogPadé	NS	$\gamma^{\text{Maj}} _{\lambda=NS}$	$\gamma^{\text{Maj}}_{\lambda=1}$
[7, 2]			0.196
[6, 3]	0.903	0.093	0.181
[5, 4]	0.946	0.129	
[4, 5]	0.946	0.129	0.191
[3, 6]	0.951	0.134	
BdlogPadé	NS	$\gamma^{\text{Maj}} _{\lambda=NS}$	$\gamma^{\text{Maj}} _{\lambda=1}$
[7, 3]	0.993	0.302	0.335
[6, 4]	0.969	0.207	0.337
[5, 5]	0.968	0.202	0.344
[4, 6]	0.968	0.202	0.344
[3, 7]	0.971	0.214	0.335
[2, 8]	1.008	0.377	0.336

Table 6.10: shows relevant results of the analysis of  $I_{1,\text{rel}}$  at the Majumdar-Gosh point. The notation is equivalent to Tab. 6.5.

of a single spinon. This energy is the lower edge of the two-spinon continuum. In the triplon-picture the lowest excitation is the creation of a single triplon ( $I_{1,\text{rel}}|_{\lambda=1} \neq 0$ ) which has the energy  $\Delta_{\text{triplon}} = 2\Delta_{\text{spinon}}$ . At higher energies at  $2\Delta_{\text{triplon}}$  there is a two-triplon continuum. From the result for  $I_{2,\text{rel}}$  it follows that the triplon-triplon interaction becomes very long ranged in the limit  $\lambda \rightarrow 1$  so that more and more bound states emerge out of the two-triplon continuum. At the point  $\lambda = 1$  an infinite number of bound states exists which form a continuum in the range  $]\Delta_{\text{triplon}}, 2\Delta_{\text{triplon}}[$ .

### 6.3.3 Intermediate conclusion

Since the unfrustrated spin-chain ( $\delta = 0, \alpha = 0$ ) is the archetype of a gapless critical model described by spinons one has to conclude that neither the occurrence of fractional excitations nor the vanishing of the gap precludes the applicability of an approach in terms of integer triplons. For the case of zero frustration even a larger part of the spectral weight is covered by two-triplon states than is covered by two-spinon states (72.89%) [272]. This result calls for further investigations of the relation between spinon and transformed triplon states. The latter does not mean that a description in terms of spinons is wrong or bad but that the triplon and the spinon picture can both be used to describe the physics.

The case of finite frustration is harder to analyze. Therefore the final conclusions are harder to pinpoint. There are strong indications that the above result also holds in the whole gapless phase ( $\alpha_0 < \alpha_{0,c}$ ). No definite conclusion can be made in the phase of massive spinons ( $\alpha_0 > \alpha_{0,c}$ ). But an analysis of the system at the Majumdar-Gosh point gives indications that the two-triplon contribution to the spectral weight is also dominant in the massive phase. Physically, the main problem of a triplon description in the phase of massive spinons are the implications on the triplon-

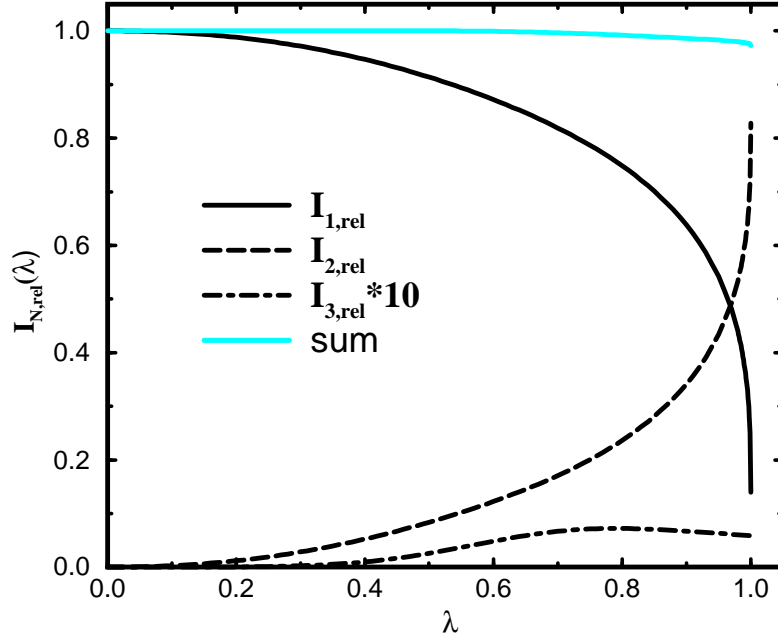


Fig. 6.14: Spectral Weights for  $S = 1$  excitations at the Majumdar-Gosh point. The black solid line denotes the one-triplon spectral weight  $I_{1,rel}$ , the dashed line  $I_{2,rel}$  and the dotted line  $I_{3,rel}$ .  $I_{3,rel}$  is multiplied by a factor 10. The grey line is the sum  $\sum_N = 1..3 I_{N,rel}$ .

triplon interaction. The two-spinon continuum has the lowest energy at  $2\Delta_{\text{spinon}} = \Delta_{\text{triplon}}$  but the two-triplon continuum has the lowest energy at  $2\Delta_{\text{triplon}} = 4\Delta_{\text{spinon}}$ . This implies that the triplon-triplon interaction has to be a constant  $-\Delta_{\text{triplon}}$  in real space (at least at large distances) in order to give an infinite number of bound states producing a two-triplon continuum which starts at  $\Delta_{\text{triplon}} = 2\Delta_{\text{spinon}}$ .

In the following the one- and two-triplon contributions to the the momentum- and energy-resolved spectral densities are discussed. Results are presented for large and intermediate dimerization. Features of the zero dimerization case obtained by different methods (see Sect. 6.1) are compared with the the two-triplon contribution at finite dimerization. Due to the above results the two-triplon spectral density at finite dimerization has to evolve continuously into the two-triplon spectral density at zero dimerization covering all essential physics of the system.

## 6.4 S=1 excitations

This part of the thesis contains results for the dynamical structure factor of the dimerized and frustrated spin-chain. In the following results are shown for the one-triplon and the two-triplon

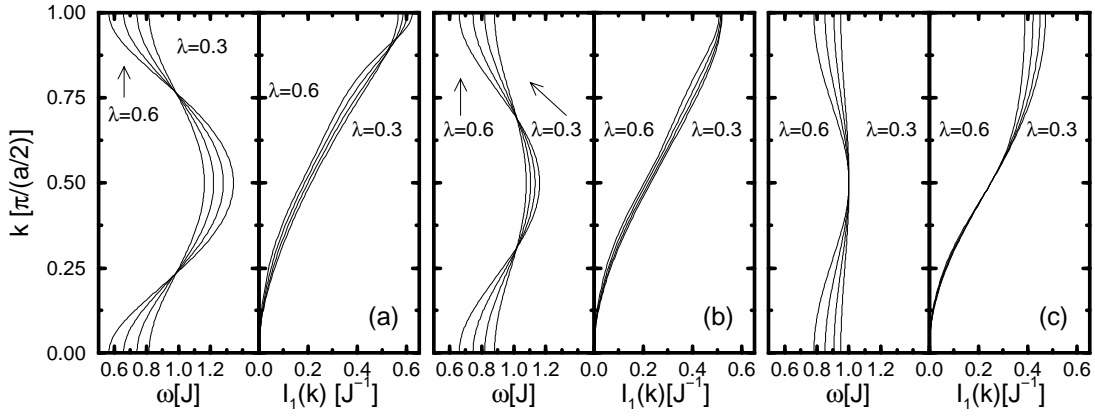


Fig. 6.15: One-triplon dispersion  $\omega(k)$  (left panels) and one-triplon spectral weight  $I_1(k)$  (right panels) for  $\lambda \in \{0.3; 0.4; 0.5; 0.6\}$ . The value for the frustration is  $\alpha = 0.0$  in (a),  $\alpha = 0.25$  in (b) and  $\alpha = 0.5$  in (c).

contribution to the spectral density. The one-triplon contribution contains most of the spectral weight at strong and intermediate dimerization. In the limit of small dimerization it is strongly reduced and becomes unimportant for zero dimerization. From the discussion of the last section it is expected that the two-triplon contribution is the only relevant contribution in the limit of zero dimerization.

A discussion of the one-triplon contribution to the dynamic susceptibility of a dimerized chain without frustration can be found in a work by Müller and Mikeska [284]. Recently Zheng et al. published results for the one- and two-triplon contribution of a strongly dimerized spin chain without frustration [187]. The results at zero frustration obtained in this work agree with the findings of Zheng et al..

Here the generic features of the two-triplon contribution for various values of the dimerization and of the frustration are extracted in order to gain insight in the evolution of these contributions in the limit of vanishing dimerization. Therefore it is interesting to compare the obtained results with results for the dynamical structure factor at zero dimerization.

At  $\alpha = 0$  an exact calculation of the two-spinon contribution to the dynamical structure factor using Bethe-ansatz is possible [272]. The two-spinon contribution exhausts 72.89% of the total spectral weight and it displays a singular divergent behavior at the lower edge of the two-spinon continuum. At finite frustration only numerical results using exact diagonalization at finite temperatures including frustration are available [285]. In addition, there exist also results using Abelian bosonization where the universal features of the dynamical structure factor at low energies for small dimerization are extracted [252]. In the following the major features of these studies are identified in our triplonic description at finite dimerization.

### 6.4.1 One-triplon contribution

In Fig. 6.15 the results for the one-triplon dispersion  $\omega(k)$  (left panels) and for the one-triplon spectral weight  $I_1(k)$  (right panels) are shown. Results for  $\lambda \in \{0.3; 0.4; 0.5; 0.6\}$  and  $\alpha = 0$  (Fig. 6.15a),  $\alpha = 0.25$  (Fig. 6.15b) and  $\alpha = 0.5$  (Fig. 6.15c) are presented.

The case of vanishing frustration ( $\alpha = 0$ ) is discussed first. At  $\lambda = 0$  the system consists of isolated dimers and the one-triplon dispersion is flat. Turning on  $\lambda$  the triplon starts to hop from dimer to dimer and it acquires a finite dispersion (Fig. 6.15a, left panel). The dispersion has minima at  $k = 0$  and  $k = \pi$  (in units of  $1/(a/2)$ ) which represent the one-triplon gap  $\Delta$ . In the limit of zero dimerization the one-triplon gap closes and it is expected that the one-triplon dispersion equals the well known des Cloizeaux-Pearson [229] dispersion relation  $\omega_{CP}(k) = \pi/2|\sin(k)|$ .

The one-triplon spectral weight  $I_1(k)$  is shown in the right panel of Fig. 6.15a. The leading term of  $I_1(k)$  is proportional to  $\sin^2(k/2)$ . It is called the dimer structure factor [284] (note again that the momentum  $k$  is measured in units of  $1/(a/2)$ ). The one-triplon spectral weight is concentrated at  $k = \pi$ . At finite dimerization the reduction of  $I_1$  due to the inter-dimer exchange occurs mainly for momenta  $k < 0.9\pi$ . The spectral weight increases in a small interval around  $k = \pi$  for increasing  $\lambda$  [284]. For even smaller dimerizations the one-triplon spectral weight becomes more concentrated about  $k = \pi$ . Recall that the weight, integrated over momentum and frequency, vanishes for vanishing dimerization.

In Fig. 6.15b the corresponding results for  $\alpha = 0.25$  are shown. The one-triplon dispersion is similar in shape to the case of zero frustration. Due to the finite frustration the excitations become more local and the triplon is less dispersive. The gap values are slightly larger and the maximum values of the one-triplon dispersion are slightly lower at the same values of  $\lambda$  than for the unfrustrated case (Fig. 6.15a and Fig. 6.15b, left parts).

The one-triplon spectral weight at  $\alpha = 0.25$  differs from the one at  $\alpha = 0$  for momenta close to  $k = \pi$  (Fig. 6.15b, right part). The spectral weight is reduced for all momenta at  $\alpha = 0.25$  on increasing  $\lambda$ . But the reduction is smallest for  $k = \pi$ . In the limit of zero dimerization the one-triplon spectral weight  $I_1(k)$  vanishes for all momenta.

The one-triplon dispersion  $\omega(k)$  for  $\alpha = 0.5$  is shown in the left part of Fig. 6.15c. The dispersion is highly reduced due to the increased locality of the triplon. At  $k = \pi/2$ , the one-triplon state is an eigen-state of the system [286, 287] and it has an energy  $J$  independent of  $\lambda$ . It is an interesting question whether there is a finite interval around  $\pi/2$  in which the triplon state retains a finite weight in the limit  $\lambda \rightarrow 1$ . In the limit of zero dimerization the system remains in a gapped state of asymptotically free spinons [239–241, 245, 246].

The one-triplon spectral weight  $I_1(k)$  for  $\alpha = 0.5$  is shown in the right part of Fig. 6.15c. The spectral weight is reduced for increasing  $\lambda$  for all momenta except for  $k = \pi/2$ . Since the one-triplon state at  $k = \pi/2$  is an eigen-state independent of  $\lambda$  its spectral weight is also constant [186]. In contrast to the previous cases, there is also a one-triplon contribution for zero dimerization, at least for  $k = \pi/2$ , but most probably also in the vicinity of this momentum.

### 6.4.2 Two-triplon contribution

In this section the two-triplon contribution to the dynamical structure factor is discussed. The two-triplon contribution displays additional physics in comparison to the one-triplon part. The reason is that besides the kinetic part of the excitations also the triplon-triplon interaction is important and has to be included. An attractive interaction can lead to bound states of two triplons. Furthermore, the total momentum of two triplons does not fix the state of the system. There is also a relative momentum between the triplons which is not fixed. Thus there is a continuum of two-triplon states for each given total momentum. In the following the spectral properties of the two-triplon continuum and the two-triplon bound states are focused on.

In Figs. 6.16-6.19 the results for the two-triplon continua, the dispersions of the two-triplon bound states and their spectral weights are shown.

The spectral density of the two-triplon continuum as function of frequency and momentum is displayed in Fig. 6.16 and in Fig. 6.18. The spectrum for fixed momentum  $k$  is shifted by  $k$  in  $y$ -direction in order to provide a three dimensional view on the spectral densities. The lower and upper band edges are marked by solid grey lines. If there are any two-triplon bound states, their dispersion is also displayed as a black line. The  $S = 1$  two-triplon bound states are denoted as  $T_n$ , and the  $S = 0$  two-triplon bound states are denoted as  $S_n$  where the counting label  $n \in \{1, 2, \dots\}$ .

Detailed information about the bound states is given in Fig. 6.17 and in Fig. 6.19 which consists of two parts for each parameter set. The left part shows an enlargement of the dispersion of the bound state and the lower edge of the two-triplon continuum. In the right part the corresponding spectral weight of the bound states is shown. The spectral weight is multiplied by the given factors for clarity.

What are the general features of the obtained spectra? Due to the conservation of the total  $S^z$ -component there is no spectral weight at zero momentum. The energies of the system possess a reflection symmetry about  $k = \pi/2$  which is a consequence of the inversion symmetry  $k \leftrightarrow -k$  and of the coupling of the momenta  $k$  and  $k + \pi$  [251]. This symmetry can be clearly seen in the bound state energies and in the lower and the upper band edges of the continuum. It does *not* hold for the spectral weights [251].

In Fig. 6.16a the spectral density for  $\lambda = 0.3$  and  $\alpha = 0.0$  is shown. The spectral weight is mostly concentrated at the lower band edge of the continuum. There are two bound states centered about  $k = \pi/2$  emerging from the continuum at some finite momentum. The dispersions and the spectral weights of the bound states are plotted in Fig. 6.17a. The points where the bound states are leaving the continuum can also be discerned in the singular behavior at the lower band edge of the continuum. The spectral weight is mainly concentrated in the first bound state  $T_1$ . The spectral weight of the second bound state  $T_2$  is highly reduced compared to  $T_1$ .

The binding energy of the bound states has its maximum at  $k = \pi/2$ . It vanishes quadratically  $\propto (k - k_c)^2$  when the bound state enters the continuum [282]. Correspondingly their spectral weight vanishes linearly  $\propto |k - k_c|$  in accordance to the exemplary calculation provided in Ref. [82]. There it was shown for square root type continua that the binding energy as a function of an external parameter vanishes quadratically while the spectral weight of the bound state vanishes linearly. The external parameter was the attraction strength. In the present case it is the total

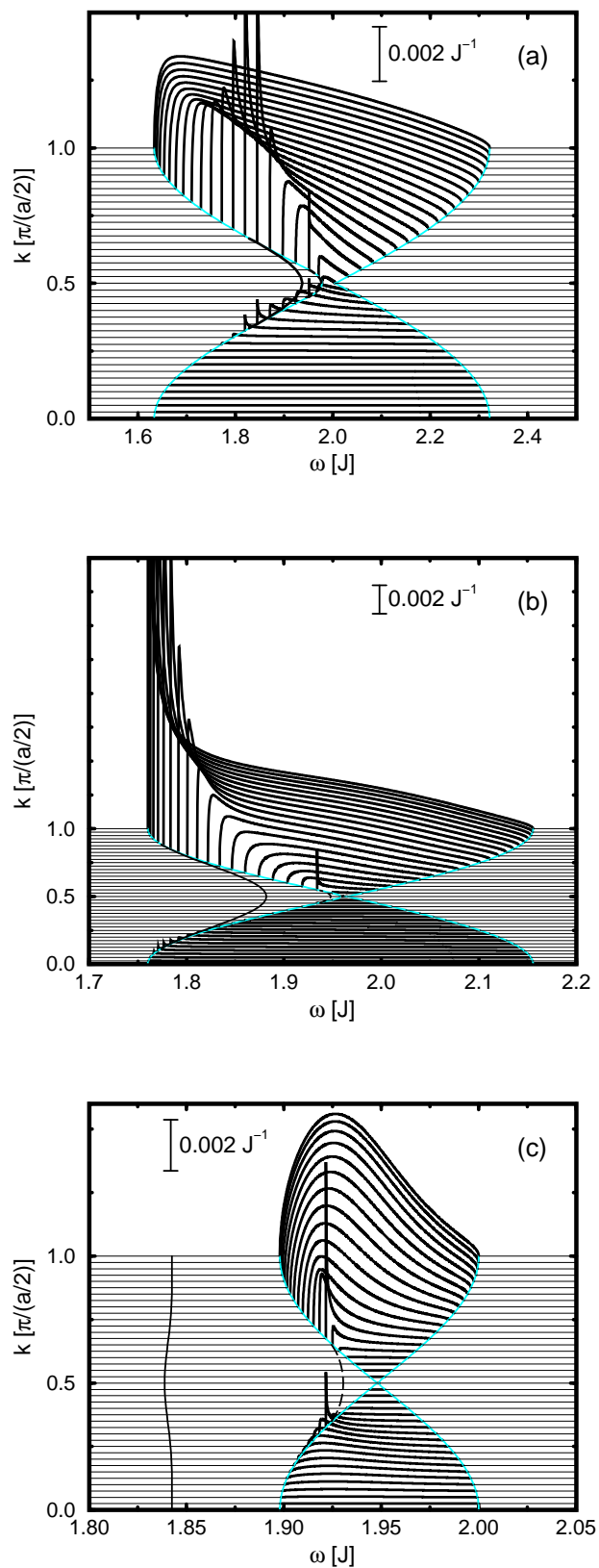


Fig. 6.16: Two-triplon spectral density  $I_2(k, \omega)$  for  $R^{S=1}$  with  $\lambda = 0.3$  and  $\alpha = 0.0$  (a),  $\alpha = 0.25$  (b) and  $\alpha = 0.5$  (c). Grey lines denote the lower and upper edge of the continuum. The black lines indicate the dispersion of two-triplon bound states.

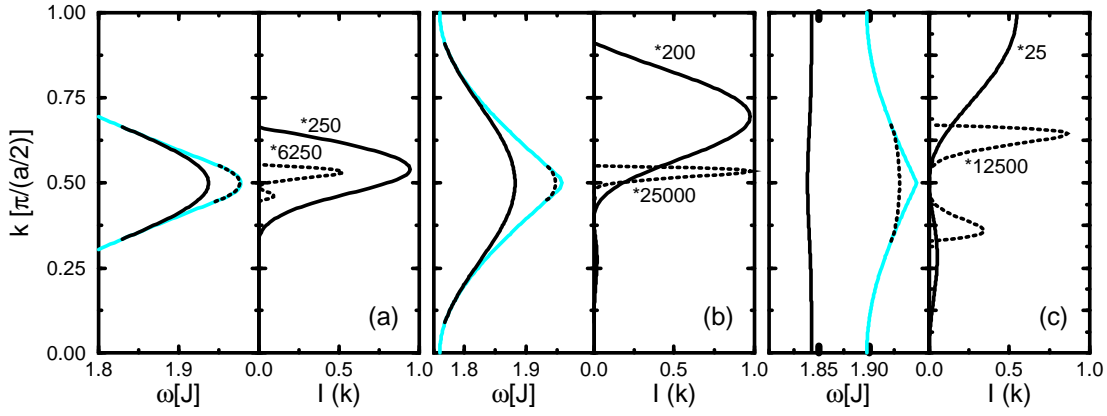


Fig. 6.17: Two-triplon bound states for  $R^{S=1}$  with  $\lambda = 0.3$  and  $\alpha = 0.0$  (a),  $\alpha = 0.25$  (b) and  $\alpha = 0.5$  (c). The dispersion of the bound states is shown in the left panels. The spectral weight of the bound states multiplied by the indicated factors is shown in the right panels. Grey lines denote the lower edge of the continuum.

momentum which controls the relative strength of the interaction and the kinetic energy.

Decreasing the dimerization to intermediate values ( $\lambda = 0.6$ , see Figs. 6.18a and 6.19a), there are no qualitative changes in the spectrum. The spectral weight is mainly concentrated at low energies. The range of energies where the bound states exist is slightly enhanced while the binding energy is slightly reduced. We expect that this tendency continues to lower values of the dimerization. For exactly zero dimerization, but *not* for an arbitrarily small but finite one, the first bound state  $T_1$  coincides with the lower edge of the continuum leading to a square root divergence at the lower edge of the continuum for all momenta. This expectation is strongly corroborated by the exact results for the spectral densities in the sine-Gordon model [252, 288]. The generic behavior is a square root behavior at the band edges. Only if a breather becomes degenerate with the multiparticle band edge the square root behavior switches to a square root divergence. Exactly the same characteristic appears naturally in the triplonic description. Recall also that for the uniform spin-chain at zero dimerization the square root divergence is well-known from the exact two-spinon contribution to the dynamical structure factor [272].

In Figs. 6.16b and 6.16c the spectra for strong dimerization and finite frustrations  $\alpha = 0.25$  and  $\alpha = 0.5$  are shown. The corresponding information about the two-triplon bound states is plotted in Figs. 6.17b and 6.17c. The frustration makes the excitations more local and less dispersive which leads to a narrowing of the two-triplon continuum. At the same time the triplon-triplon interaction is enhanced causing an increase of the binding energy of the bound states. It can be clearly seen that for  $\alpha = 0.25$  the first bound state extends over a wide range in momentum space lying for small and large momenta very close to the lower band edge inside the continuum while for  $\alpha = 0.5$  the bound state  $T_1$  exists for all momenta well separated from the continuum.

Due to the existence of the bound states only in a finite interval of the momentum for both values  $\alpha = 0$  and  $\alpha = 0.25$  the qualitative distribution of their spectral weight is similar. This will be true for all values of frustration between 0 and 0.25. The same holds for the bound state  $T_2$



for  $\alpha = 0.5$ . In contrast, the spectral weight of the first bound state  $T_1$ , which is well separated from the continuum for  $\alpha = 0.5$ , has its maximum at  $k = \pi$ .

The whole two-triplon contribution, i.e. the two-triplon bound states and the two-triplon continuum, vanishes for  $k = \pi/2$  at  $\alpha = 0.5$ . Here the one-triplon excitation is an exact eigen-state of the spectrum and therefore comprises the total spectral weight [286, 287] (see also the preceding section).

Next the influence of the frustration on the shape of the two-triplon continuum is analyzed. In the case of vanishing frustration the spectral weight is mainly distributed close to the lower band edge for strong and intermediate dimerization. The spectral weight decreases monotonically for higher energies. Turning on the frustration a shift of spectral weight towards higher energies is observed. In the case of strong dimerization this tendency is weak (Figs. 6.16b and 6.16c) while for intermediate dimerization one observes a huge transfer of spectral weight (Figs. 6.18b and 6.18c). This transfer produces a non-monotonic shape for intermediate dimerization and  $\alpha = 0.25$  having a minimum of spectral weight inside the continuum (Fig. 6.18b). Increasing the frustration ( $\alpha = 0.5$ ) shifts the minimum to the lower band edge. The spectral weight is mainly at the upper band edge (Fig. 6.18c).

These observations are very similar to the results obtained by exact diagonalization at finite temperatures for the dynamical structure factor of a homogeneous spin-chain including frustration [285]. There a decrease of spectral weight at  $k = \pi$  inside the continuum is observed on increasing the frustration. This results in a high-energy maximum for large frustration and a minimum inside the continuum, i.e., a trough-like shape. From this comparison one concludes that the above findings represent the generic features which are probably also valid in the limit of vanishing dimerization.

### 6.4.3 Comparison with field theory results

The first part of this section concentrates on the  $S = 1$  breather and the corresponding behavior of the lower band edge of the two-triplon continuum. In the second part a closer look at the energy of the  $S = 0$  breather and at the one-triplon gap is taken. Finally, the importance of marginal terms (in the renormalization group sense) for the quantitative shape of spectral densities is discussed. A detailed analysis of the  $S = 0$  channel which contains also a discussion of the singlet two-triplon bound states is presented in the next section.

The  $S = 1$  response function displays a square root divergence  $\propto (\omega - \omega_0)^{-1/2}$  at the lower band edge. Here the energy of the  $S = 1$  breather  $\omega_{br,S=1}$  is exactly degenerate with the lower band edge ( $\omega_{br,S=1} = 2\Delta$ ). This is in agreement with what is found at  $\alpha = 0.25$ , cf. Figs. 6.16b and 6.18b. Without any frustration, however, a square root behavior  $\propto (\omega - \omega_0)^{1/2}$  is found, cf. Figs. 6.16a and 6.18a. Hence one concludes that the sine-Gordon model does not exhaustively describe the unfrustrated, dimerized spin-chain at strong and intermediate dimerization. But the sine-Gordon model applies much better to the spin-chain at critical frustration where the higher cosine-term  $\cos(4\Phi)$  vanishes. It is interesting to note that one finds a square root divergence for  $\alpha \approx \alpha_{0,c}$  and not for  $\alpha_0 \approx \alpha_{0,c}$ .

The conclusion about the applicability of the sine-Gordon model to the unfrustrated and dimerized

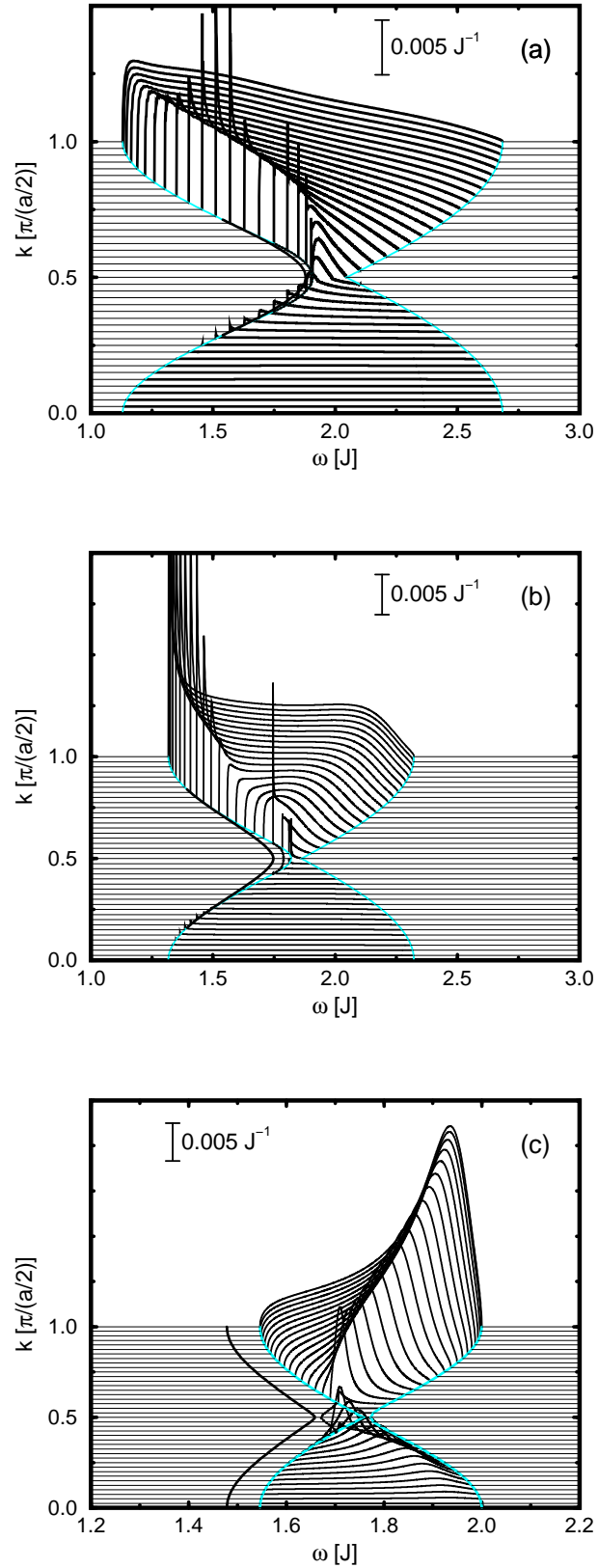


Fig. 6.18: Two-triplon spectral density  $I_2(k, \omega)$  for  $R^{S=1}$  with  $\lambda = 0.6$  and  $\alpha = 0.0$  (a),  $\alpha = 0.25$  (b) and  $\alpha = 0.5$  (c). Grey lines denote the lower and the upper edge of the continuum. Black lines indicate the dispersion of two-triplon bound states.

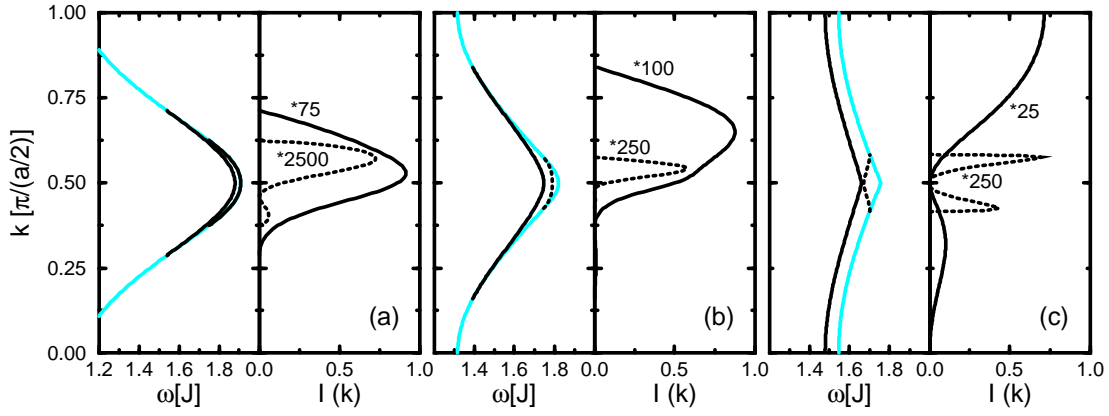


Fig. 6.19: Two-triplon bound states for  $R^{S=1}$  with  $\lambda = 0.6$  and  $\alpha = 0.0$  (a),  $\alpha = 0.25$  (b) and  $\alpha = 0.5$  (c). The dispersion of the bound states is shown in the left panels. The spectral weights of the bound states multiplied by the indicated factors is shown in the right panels. Grey lines denote the lower edge of the continuum.

spin-chain is in agreement with the results of the numerical investigation of the bound states [257]. It is known that the elementary excitations of the  $SU(2)$  symmetric sine-Gordon model consist of soliton and antisoliton excitations and two breathers, which represent bound states, as well as a breather which is degenerate with the lower band edge [245, 251, 289]. The lowest-lying breather is degenerate with the soliton and antisoliton excitations and corresponds to the  $S^z = 0$  triplet state in spin language. This fixes the interaction parameter to  $K = 1/2$ . The second breather is assigned to a spin singlet excitation, since there is no counter part in the soliton or antisoliton sector. The ratio between the energy of the  $S = 0$  breather  $\omega_{br,S=0}$  and the one-triplon gap  $\Delta$  is exactly  $\sqrt{3}$  at  $K = 1/2$  [250, 251].

In Fig. 6.20 this ratio is shown for various values of  $\lambda \in \{0.3; 0.4; 0.5; 0.6\}$  versus the bare frustration  $\alpha_0$ . Padé extrapolants are used for  $\lambda = 0.6$ . It can be clearly seen that almost all points (except for the case of strong dimerization  $\lambda = 0.3$ ) fall onto one curve. The values for  $\alpha_{0,c}$  and  $\sqrt{3}$  are included as solid lines. The point where these two lines cross lies on the calculated curve and corresponds to the prediction of the  $SU(2)$  symmetric sine-Gordon model. In all other cases ( $\alpha_0 \neq \alpha_{0,c}$ ) the ratio  $\omega_{br,S=0}/\Delta$  differs from  $\sqrt{3}$ . This is due to corrections resulting from the marginal term  $\cos(4\Phi)$ . These calculations agree perfectly with previous numerical results [257].

The relative importance of the two cosine-terms in Eq. 6.1.18 at finite dimerization is a subtle issue which is discussed in the following.

In the self-consistent harmonic approximation one replaces [290, 291]  $\Phi \rightarrow \Phi_{\text{class}} + \hat{\Phi}_{\text{fluct}}$  where only the fluctuation part is of operator character. The cosine-terms can then be approximated by

$$\begin{aligned} \cos(n\Phi) &\rightarrow \\ \exp(-\langle n^2/2 \rangle \sigma(x)) \cos(n\Phi_{\text{class}}(x)) &\left(1 - \frac{n^2}{2} \hat{\Phi}_{\text{fluct}}^2\right) \end{aligned} \quad (6.4.1)$$

where  $\sigma(x) := \langle \hat{\Phi}_{\text{fluct}}^2(x) \rangle$ . This kind of approach corresponds to renormalization in first order. In

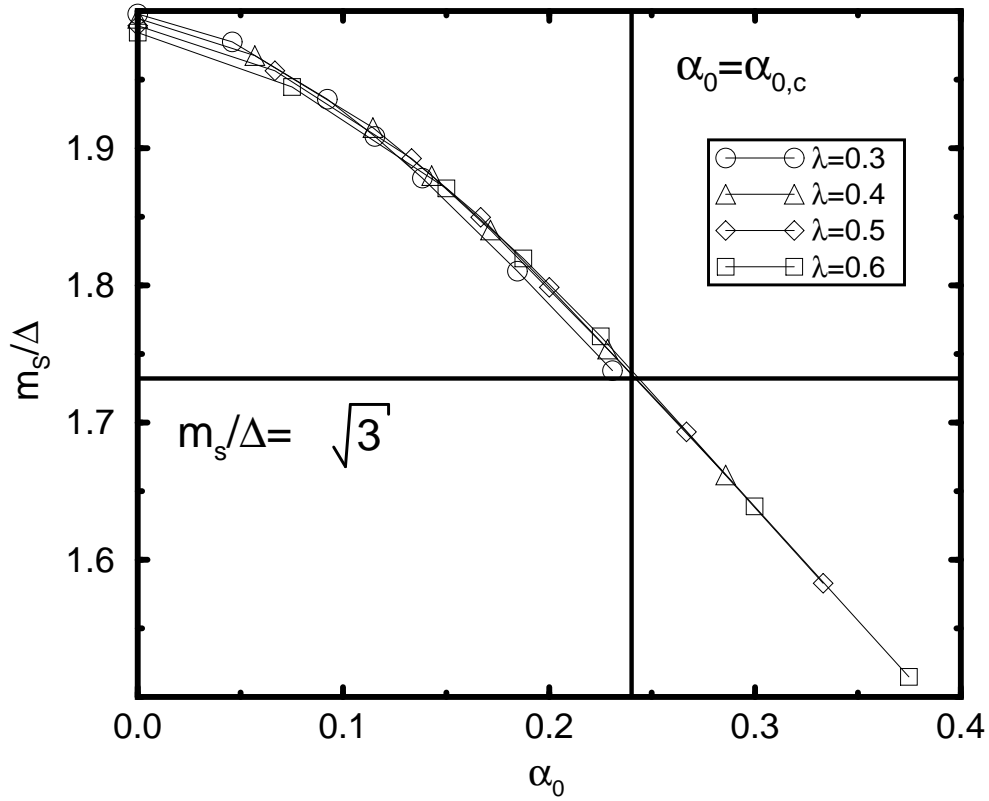


Fig. 6.20: Ratio of the singlet two-triplon bound state energy  $m_s$  and the one-triplon gap  $\Delta$  for  $\lambda \in \{0.3; 0.4; 0.5; 0.6\}$  depending on the frustration  $\alpha_0$ . The horizontal black solid line denotes  $\sqrt{3}$  and the vertical black solid line shows the critical frustration  $\alpha_{0,c}$ .

the ground state (without solitons) one has  $\Phi_{\text{class}} = 0$ . In the ungapped phase the fluctuations diverge, hence  $\sigma \rightarrow \infty$ . But in the gapped phase, the fluctuations are cut off at low energies so that  $\sigma = -(K/2) \ln(\Delta/\Delta_0)$  where  $\Delta$  is the gap and  $\Delta_0$  is proportional to the ultraviolet cutoff.

Since the square of the gap  $\Delta^2$  is proportional to the coefficient of  $\hat{\Phi}(x)^2$  which one obtains from the term  $\delta \cos(2\Phi)$  the self-consistency equation

$$\begin{aligned} \Delta^2 &\propto \delta \exp(-2\sigma) \\ \Delta &\propto \delta^{1/(2-K)} \end{aligned} \quad (6.4.2)$$

yielding the well-known result  $\Delta \propto \delta^{2/3}$  obtained first by Cross and Fisher [266]. Hence the total contribution of this cosine-term is proportional to  $\Delta^2$  or  $\delta^{4/3}$ . The crucial point to note is that the amplitude of the second cosine-term  $\cos(4\Phi)$  is of the same magnitude  $\exp(-8\sigma) \propto \Delta^{4K}$  which also yields  $\Delta^2$  or  $\delta^{4/3}$  for  $K = 1/2$  [292]. Hence it follows from the self-consistent harmonic approximation that even in the regime where the frustration is marginal for  $\alpha < \alpha_c$  it influences

the low-energy physics on the quantitative level.

Considering, however, the renormalization to second order the marginal term is reduced logarithmically, hence the name “marginally irrelevant” [252, 293]. The flow is valid down to the infrared cutoff which is the energy gap due to the dimerization here. Note that one is working in the thermodynamic limit  $L = \infty$ . Hence the suppression of the marginally irrelevant cosine term compared to the relevant one is logarithmical in  $\delta$  and thus very slow. Hence it is possible that the scales which are discussed in this chapter ( $\delta$  down to 0.25) are still too large to see the emergence of the physics of a pure sine-Gordon model with one cosine only. But it is at least puzzling that no precursors of the convergence to the predictions of the pure sine-Gordon model can be seen. The ratio of the energy gaps shown in Fig. 6.20 (or those obtained in Ref. [257]) appears almost independent of  $\delta$  as far as is investigated here.

Note that the vanishing of the  $\cos(4\Phi)$  term at the end of the flow of  $l$  is *not* identical to the question whether this term is present at the beginning of the flow. It is presumed that this difference explains the puzzling finding that the bare coefficient of the Umklapp term  $\cos(4\Phi)$  vanishes [245] at  $\alpha_0 = 1/6$ , that means relatively far from the quantum critical point  $\alpha_0 = 0.241$ .

The results shown in Figs. 6.16-6.18(a-b) show that the square root divergence known from the sine-Gordon model [252, 288] is changed to normal square root behavior. So the quantitative changes of the low-energy Hamiltonian influence the shape of the spectral densities qualitatively. Hence for spectral densities one must know whether the effective low-energy model is a (simple) sine-Gordon model or a double sine-Gordon model with two cosine terms. The answer depends on the energy scale considered, i.e. the value of  $\delta$ .

For strong frustration  $\alpha = 0.5$ , cf. Figs. 6.16c and 6.18c, the physics is dominated by bound states. Their number proliferates for decreasing dimerization [292, 294]. At  $\delta = 0$  there are infinitely many bound states densely distributed between  $\Delta$  and  $2\Delta$ . They form the continuum which can be understood as two-spinon continuum [246, 292, 294]. The values of  $\lambda$  for which the spectral densities in Figs. 6.16c and 6.18c are displayed are still too small, i.e., too far in the dimerized regime to see more than a small number of bound states. This was also observed by Zheng *et al.* [184]. In a series expansion up to order  $\lambda^{19}$  they found three singlet and three triplet bound states.

The fact, that only a small number of bound states could be found so far, is attributed to the limited range of the effective interaction. In the perturbative approaches for  $\alpha = 0.5$  an order of  $\lambda^n$  corresponds to a maximum range of  $[n/2]$ . So even calculations at  $n = 19$  provide only a potential of a small finite range which does not allow for many bound states. The alternative presumption [184] that the lacking bound states are found in the channels with more than two triplons would require that the spectral weight is passed to channels with more and more triplons. No channel with only a finite number of bound states may retain a finite spectral weight at zero dimerization since at zero dimerization only a continuum is found [246]. None of the above results are in favor of the scenario that the missing bound states appear in the multi-triplon channels, so that one can be convinced that the range of the interaction is the crucial point [247]. But the precise description of the deconfinement transition for vanishing dimerization is still an open issue. Future developments like self-similar realizations of the continuous unitary transformations will help

to release this constraint on the range of the interaction [161, 171].

## 6.5 $S=0$ excitations

In this section the two-triplon contribution to the spectral density with total spin zero is discussed. It is relevant for optical experiments. For  $S = 0$  one needs at least two triplons which form a state with vanishing total spin. For the case of isolated dimers ( $\lambda = 0$ ) the total spectral weight is in the two-triplon contribution. At finite  $\lambda$ , the spectral weight in the two-triplon channel is reduced and spectral weight is also found in channels with more than two triplons.

In the limit of vanishing dimerization and for zero frustration it was shown in Subsect. 6.3.1.2 in a similar analysis as for the dynamical structure factor that the two-triplon contribution possesses almost the total spectral weight [82, 209]. The two-triplon contribution is therefore the only sizable contribution for the whole range of dimerizations for the unfrustrated case. In the presence of frustration the analogous analysis is quantitatively more difficult as stated before. But again there are indications (see Sect. 6.3) that only a small number of triplons dominates the spectral properties. Therefore the leading two-triplon contribution for the  $S = 0$  channel is investigated. For the dimerizations treated in this work there is no doubt that the two-triplon contribution is the only sizable term. The crucial point, however, is to which extent one can obtain the generic features which govern also the limit of vanishing dimerization. All results obtained so far show that the one- and two-triplon contributions indeed capture the relevant physics.

In the case of a uniform spin-chain without frustration the nearest neighbor Raman operator commutes with the Hamiltonian and one obtains a vanishing Raman response. Therefore the next-nearest-neighbor Raman operator is the leading contribution in terms of a Loudon-Fleury scattering theory [295, 296]. In contrast to the case of zero momentum,  $R_{NN}$  does not commute with the Hamiltonian for finite momenta and it will be the most important contribution to the infrared absorption. For simplicity,  $R_{NN}$  is not treated completely but only its weak-bond part. This is no major restriction because one is interested in the generic properties of these quantities. In addition, the weak-bond part dominates for strong dimerization.

The two observables  $R_{NN}$  and  $R_{NNN}$  will be discussed separately. For a direct comparison with experimental data one should take the sum over all contributing parts of  $R^{S=0}$  to account for possible interference effects. The necessary superposition, however, strongly depends on the details of the system and cannot be discussed generally.

In Figs. 6.21-6.24 the spectral densities for  $R_{NN,weak}^{S=0}$  are shown and in Figs. 6.25-6.28 the corresponding densities for  $R_{NNN}^{S=0}$ . First, the results for the nearest neighbor (NN) coupling  $R_{NN,weak}^{S=0}$  are discussed passing then to the results for next-nearest-neighbor coupling  $R_{NNN}^{S=0}$ . Finally, the implications for Raman spectroscopy and infrared absorption will be assessed.

### 6.5.1 Case $R_{NN,weak}^{S=0}$

In Fig. 6.21a the spectral density for strong dimerization ( $\lambda = 0.3$ ) and vanishing frustration is depicted. The corresponding information about the dispersion and the spectral weight of the two-triplon bound states is shown in Fig. 6.22a. The same notation as in the section for  $S = 1$

excitations is used. The spectrum is symmetric about  $k = \pi/2$  due to the inversion symmetry  $k \leftrightarrow -k$  and  $R_{\text{NN,weak}}^{S=0}(k + \pi) = R_{\text{NN,weak}}^{S=0}(k)$  (see Sect. 6.2).

Two  $S = 0$  two-triplon bound states  $S_1$  and  $S_2$  are found. In the total  $S = 0$  channel the triplon-triplon interaction is larger than it was in the total  $S = 1$  channel. Therefore the binding energy of the bound states is enhanced and the first bound state  $S_1$  exists for all momenta in contrast to the  $S = 1$  case. In general, the  $S = 0$  channel is dominated by the bound states which carry most of the spectral weight. This statement applies also to the experimental relevance, see below.

The dispersion of the two-triplon bound state  $S_1$  is roughly sinusoidal having three extrema at momenta  $k = \{0; \pi/2; \pi\}$ . The binding energy is largest for  $k = \pi/2$  while it becomes small near momentum zero and  $\pi$ . The spectral weight of  $S_1$  is roughly proportional to the square root of the binding energy similar the above used argument that the one-triplon spectral weight  $I_1$  behaves like  $I_1 \propto \sqrt{\omega} \propto \delta^{1/2}$ . The second singlet two-triplon bound state  $S_2$  exists only in a finite interval about  $k = \pi/2$ . The spectral weight of  $S_2$  vanishes at  $k = \pi/2$  and possesses two maxima below and above  $k = \pi/2$ .

The spectral weight of the two-triplon continuum is concentrated at small frequencies. At small and large momenta this effect is enhanced due to the vicinity of  $S_1$ . Lowering the dimerization one sees no qualitative changes in comparison to the case of strong dimerization (Fig. 6.23a and Fig. 6.24a). So it is expected that the dispersion of the bound state  $S_1$  is degenerate with the lower band edge of the two-triplon continuum for  $\lambda \rightarrow 1$  inducing a square root divergence. This expectation is supported also by numerical results for the second breather [257].

For clarity, it is emphasized again that one must clearly distinguish the case of zero dimerization and the case of small, but finite, dimerization. For zero dimerization bosonization predicts a  $1/\omega$  divergence at  $k = \pi$  which becomes  $(\omega - \omega_0)^{-1/2}$  close to  $k = \pi$  [245, 266]. This has been used for instance in the empirical calculation of Lorenzana and Eder [297]. For small, but finite, dimerization the sine-Gordon model prediction of a square root behavior without divergence applies to the critical frustration and in the region around this value. For other values of the frustration a breather may coincide with the lower band edge implying a square root divergence.

In Figs. 6.21b-c the spectral density at finite frustration for strong dimerization is shown. At  $\alpha = 0.25$  three bound states  $S_1$ ,  $S_2$  and  $S_3$  are found. The binding energy of  $S_1$  increases drastically when turning on the frustration, especially at small and large momenta. The spectral weight increases in a similar fashion for these momenta. The third two-triplon bound state  $S_3$  exists merely in a very small region about  $k = \pi/2$ . The binding energy and the spectral weight are tiny. The spectral weight has a maximum at  $k = \pi/2$ .

The two-triplon continuum for  $\alpha = 0.25$  does not show a lot of structure. This is a consequence of the fact that at almost all momenta no bound state is close to the lower band edge of the continuum. Upon decreasing the dimerization no qualitative changes are seen (see Fig. 6.23b).

At  $\alpha = 0.5$  two bound states are detected. The dispersion of  $S_1$  becomes flatter which again also holds for the spectral weight distribution. The biggest change can be seen in  $S_2$ . This bound state exists for almost all momenta in contrast to the cases  $\alpha \in \{0; 0.25\}$ . In the regions close to  $k = 0$  and symmetrically close to  $k = \pi$ , the bound state  $S_2$  does not exist, but it can be thought

to lie just above the lower band edge implying an almost divergent behavior of the two-triplon continuum.

Smirnov [252, 288] showed that the corresponding spectral density of the sine-Gordon model displays a square root behavior at the lower band edge. This applies to the  $S = 0$  channel of the frustrated spin-chain for  $\alpha \leq \alpha_{0,c}$  if the marginal term  $D \cos(4\Phi)$  of Eq. 6.1.18 is neglected. This neglect is quantitatively justified for  $\alpha = \alpha_{0,c}$ . Indeed, the results for  $\alpha = 0.25$  clearly show a square root behavior. As for the  $S = 1$  case, one finds that the predictions of the sine-Gordon model for the physics of the spin chain are verified for  $\alpha = \alpha_{0,c}$ . For other values, notably  $\alpha = 0$  and  $\alpha = 0.5$ , one finds square root divergences or strong tendencies towards square root divergences. Again such divergent behavior results from the vicinity of bound states, here in the  $S = 0$  sector.

### 6.5.2 Case $R_{\text{NNN}}^{S=0}$

In Figs. 6.25 and 6.27 the spectral densities of the observable  $R_{\text{NNN}}^{S=0}$  for various values of the dimerization and the frustration are shown. The information on the singlet two-triplon bound states is plotted in Figs. 6.26 and 6.28. All considerations concerning the energetic properties of the  $S = 0$  channel are the same as for  $R_{\text{NNN}}^{S=0}$  and need not be discussed again in this section.

The concentration is laid on the spectral differences between the two observables. The spectral weight is suppressed for large momenta due to symmetry reasons. This can be clearly seen for the two-triplon continuum and the spectral weight of the two-triplon bound states. Therefore only momenta  $k \in [0, \pi/2]$  carry significant spectral weight. In this region no qualitative differences to the results for  $R_{\text{NN,weak}}^{S=0}$  are found.

The most important difference is a change of the spectral weight distribution of  $S_1$ . At  $\alpha = 0$  the spectral weight has a maximum at  $k = \pi/2$  which is similar to the case of  $R_{\text{NN,weak}}^{S=0}$ . Finite frustration shifts the maximum to  $k = 0$ . Close to the critical frustration the spectral weight is almost constant for  $k \in [0, \pi/2]$ . At  $\alpha = 0.5$  the spectral weight is a monotonically decreasing function (from  $k = 0$  to  $k = \pi$ ).

### 6.5.3 Raman spectroscopy

The dominant observable for magnetic light scattering (Raman response) using the standard Fleury-Loudon scattering theory [295, 296] is

$$R_{\text{Raman}} = \sum_i (R_{\text{loc,NN}}^{S=0}(i) + \beta R_{\text{loc,NNN}}^{S=0}(i)), \quad (6.5.1)$$

where the sum runs over all spins. The Raman response is therefore the  $k = 0$  contribution to the spectral density which is discussed in the last section. Here it is focused on the case of next-nearest-neighbor coupling which is the leading process in the case of a uniform Heisenberg chain without frustration.

In Fig. 6.29 the Raman response for next-nearest coupling is shown at zero frustration (a), close to critical frustration  $\alpha = 0.25$  (b) and for  $\alpha = 0.5$  (c). In each graph the spectrum is shown for  $\lambda \in \{0.3; 0.4; 0.5; 0.6\}$ . In these figures, a broadening of  $\Gamma = 0.01$  is used and the spectra are shifted in  $y$ -direction for clarity. The spectral densities for  $\alpha = 0$  are multiplied by 6.



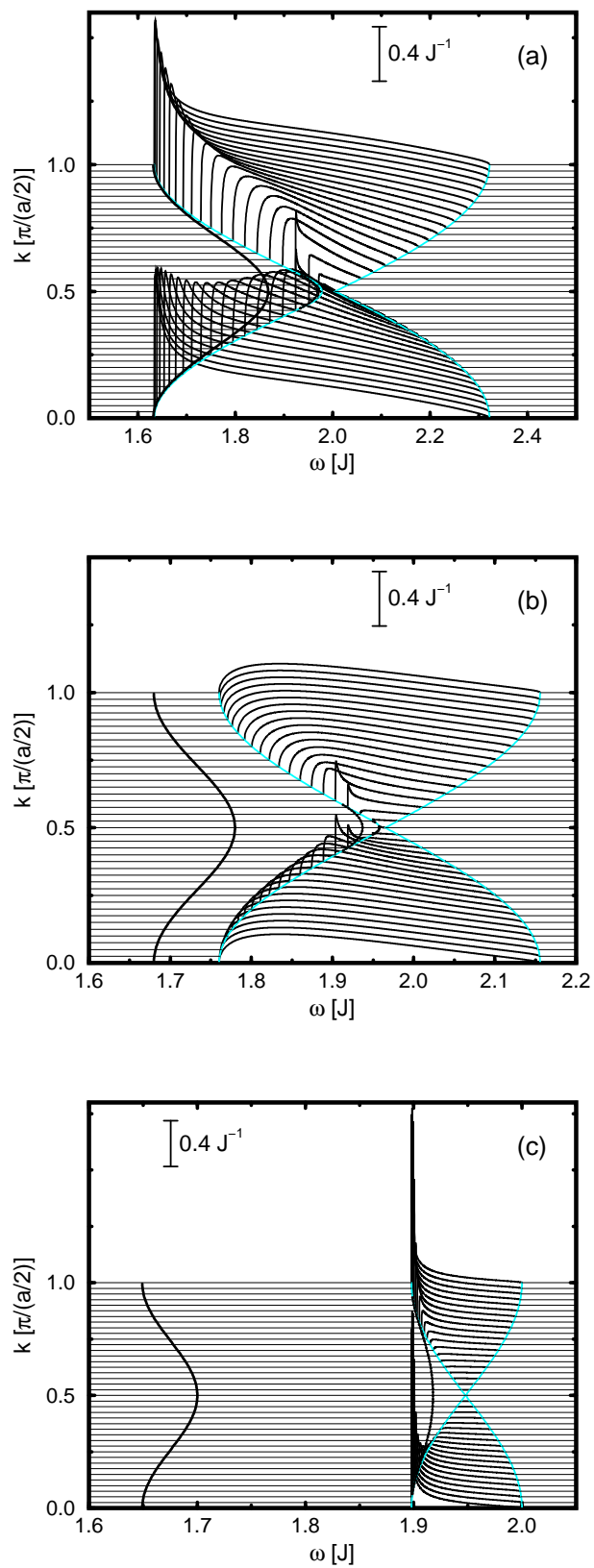


Fig. 6.21: Two-triplon spectral density  $I_2(k, \omega)$  for  $R_{NN,weak}^{S=0}$  with  $\lambda = 0.3$  and  $\alpha = 0.0$  (a),  $\alpha = 0.25$  (b) and  $\alpha = 0.5$  (c). Grey lines denote the lower and the upper edge of the continuum. The black lines indicate the dispersion of two-triplon bound states.

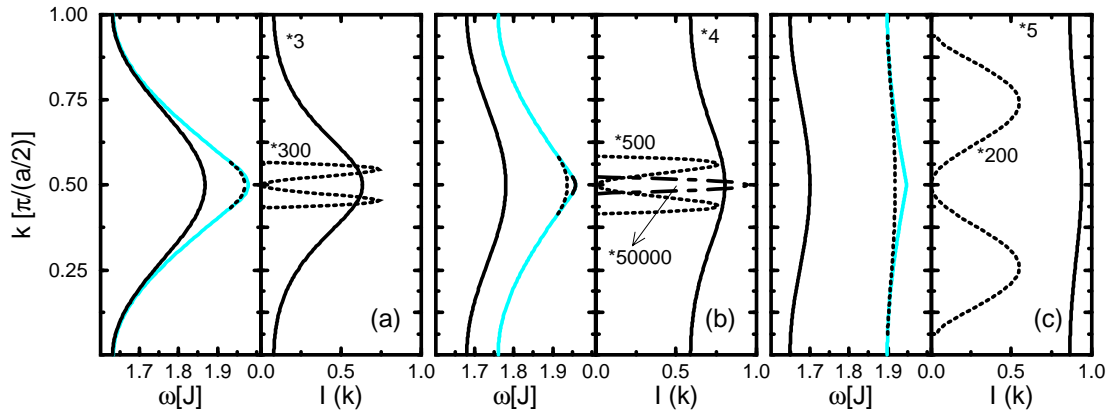


Fig. 6.22: Two-triplon bound states for  $R_{NN,weak}^{S=0}$  with  $\lambda = 0.3$  and  $\alpha = 0.0$  (a),  $\alpha = 0.25$  (b) and  $\alpha = 0.5$  (c). The dispersion of the bound states is shown in the left panels. The spectral weights of the bound states multiplied by the indicated factors is shown in the right panels. Grey lines denote the lower edge of the continuum.

For the values of the dimerizations considered here, the spectra are dominated by the first  $S = 0$  two-triplon bound state  $S_1$ . This dominance is enhanced by the frustration. In Fig. 6.29a the case of vanishing dimerization is shown. Due to the finite broadening and the small binding energy of the bound state there is no separation of the two-triplon bound state and the two-triplon continuum. An increase of  $\lambda$  reduces the weight of the bound state and gives rise to a broad featureless continuum.

In Fig. 6.29b and 6.29c the results for finite frustration are plotted. The binding energy of the bound state  $S_1$  is enhanced and one can clearly separate the contribution of the bound state  $S_1$  and of the continuum. The spectral weight of the two-triplon continuum is very small.

### 6.5.4 IR-absorption

In this section the results are applied to phonon-assisted infrared absorption of magnetic excitations [277, 278]. This experimental technique allows to study the spin-spin correlation function by measuring the optical conductivity. The direct absorption of two magnetic excitations is generically not allowed due to inversion symmetry. However, this selection rule can be broken by simultaneously exciting a phonon. The leading infrared-active magnetic absorption is a two-triplon-plus-phonon process [277, 278]. Due to the momentum of the excited phonon, the magnetic spectra  $I(k, \omega)$  have to be integrated over all momenta weighted with a phonon-specific form factor.

The absorption spectra are sensitive to the  $S = 0$  two-triplon bound states. Especially the extrema yield prominent van-Hove singularities in the density of states which can be identified in the experiment. In this way, the first experimental evidence for the two-triplon bound state in cuprate spin ladder systems [298] was possible. One therefore expects interesting line shapes in the optical absorption also for dimerized and frustrated spin-chain systems.

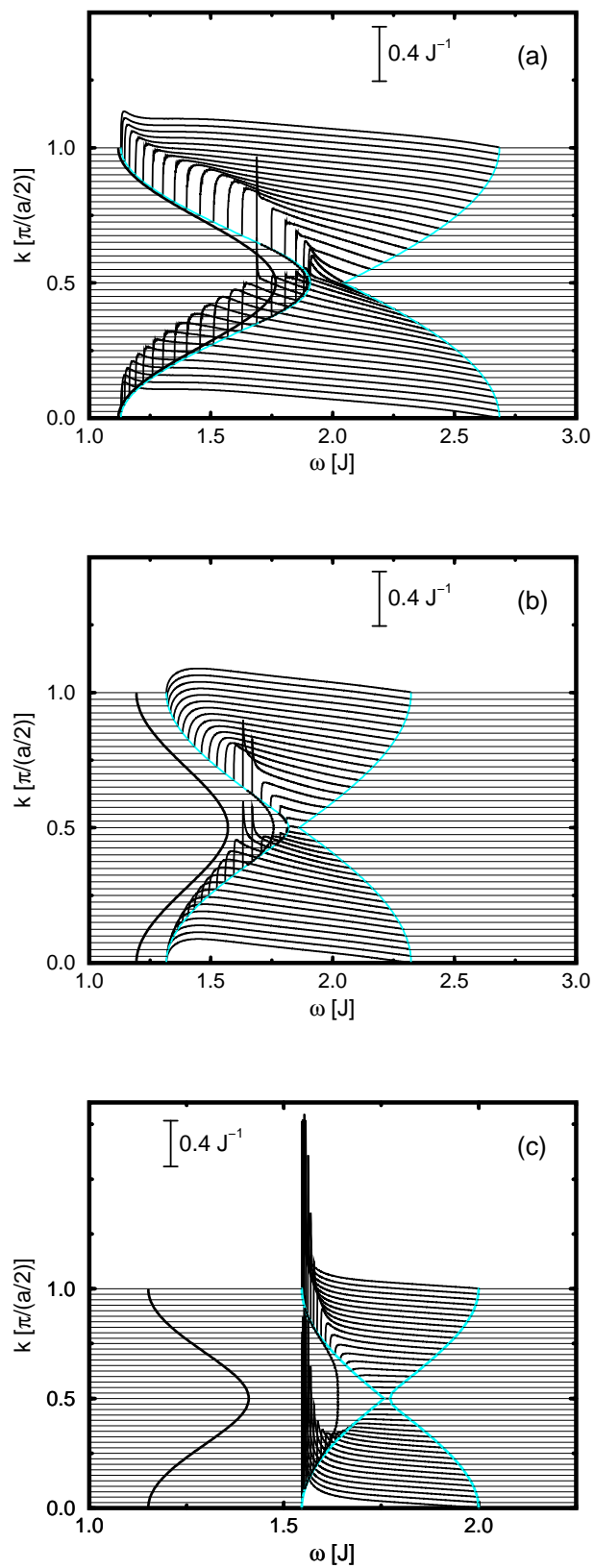


Fig. 6.23: Two-triplon spectral density  $I_2(k, \omega)$  for  $R_{NN,weak}^{S=0}$  with  $\lambda = 0.6$  and  $\alpha = 0.0$  (a),  $\alpha = 0.25$  (b) and  $\alpha = 0.5$  (c). Grey lines denote the lower and the upper edge of the continuum. Black lines indicate the dispersion of two-triplon bound states.

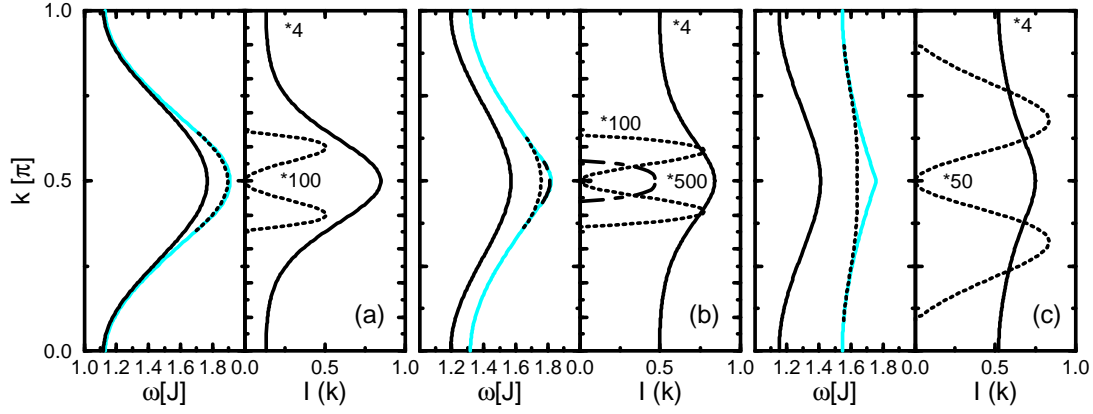


Fig. 6.24: Two-triplon bound states for  $R_{NN,weak}^{S=0}$  with  $\lambda = 0.6$  and  $\alpha = 0.0$  (a),  $\alpha = 0.25$  (b) and  $\alpha = 0.5$  (c). The dispersion of the bound states is shown in the left panels. The spectral weights of the bound states multiplied by the indicated factors is shown in the right panels. Grey lines denote the lower edge of the continuum.

The absorption coefficient is given by [297]

$$a(\omega) = a_0 \omega I^{\text{IR}}(\omega - \omega_0). \quad (6.5.2)$$

Here  $a_0$  is a constant depending on the material and  $\omega_0$  is the phonon frequency. The phonon is considered to be local and without dispersion (Einstein phonon). The function  $I^{\text{IR}}$  is given by

$$I^{\text{IR}}(\omega) = 16\pi \sum_k \sin^4(k/2) I(k, \omega). \quad (6.5.3)$$

The specific form factor given is valid strictly only for a uniform Heisenberg chain. It was successfully used to explain the optical absorption in uniform cuprate spin-chains [297, 299]. The same form factor is also used for the dimerized and frustrated chain in order to explore the general features of the optical conductivity and to compare the line shapes at finite dimerization with the line shapes at zero dimerization. In a detailed analysis of experimental data one must analyze which phonons are involved and which specific form factors matter.

In Fig. 6.30a-c and Fig. 6.31a-c the optical absorption  $a(\omega)$  for various values of the dimerization and of the frustration is shown for  $R_{NNN}^{S=0}$  and  $R_{NN,weak}^{S=0}$ . Here  $a_0$  is set to one and  $\omega_0$  is set to zero. The spectra comprise a broadening of  $\Gamma = 0.01$  which is a reasonable value in the view of experimental resolutions. In the insets the contribution of the two-triplon continuum without the broadening is shown to highlight the shape of the continuum contributions and to distinguish it from contributions of the bound states.

The phonon form factor favors large momenta while it reduces the contribution of small momenta. Hence the discussion of the spectral densities implies that  $R_{NN,weak}^{S=0}$  is more relevant than  $R_{NNN}^{S=0}$  for  $a(\omega)$ . This can also be seen in the absolute heights of the spectra in Fig. 6.30 and Fig. 6.31. In addition, one expects that the nearest-neighbor coupling is stronger than the next-nearest neighbor one because exchange processes of longer range will generically be less important.

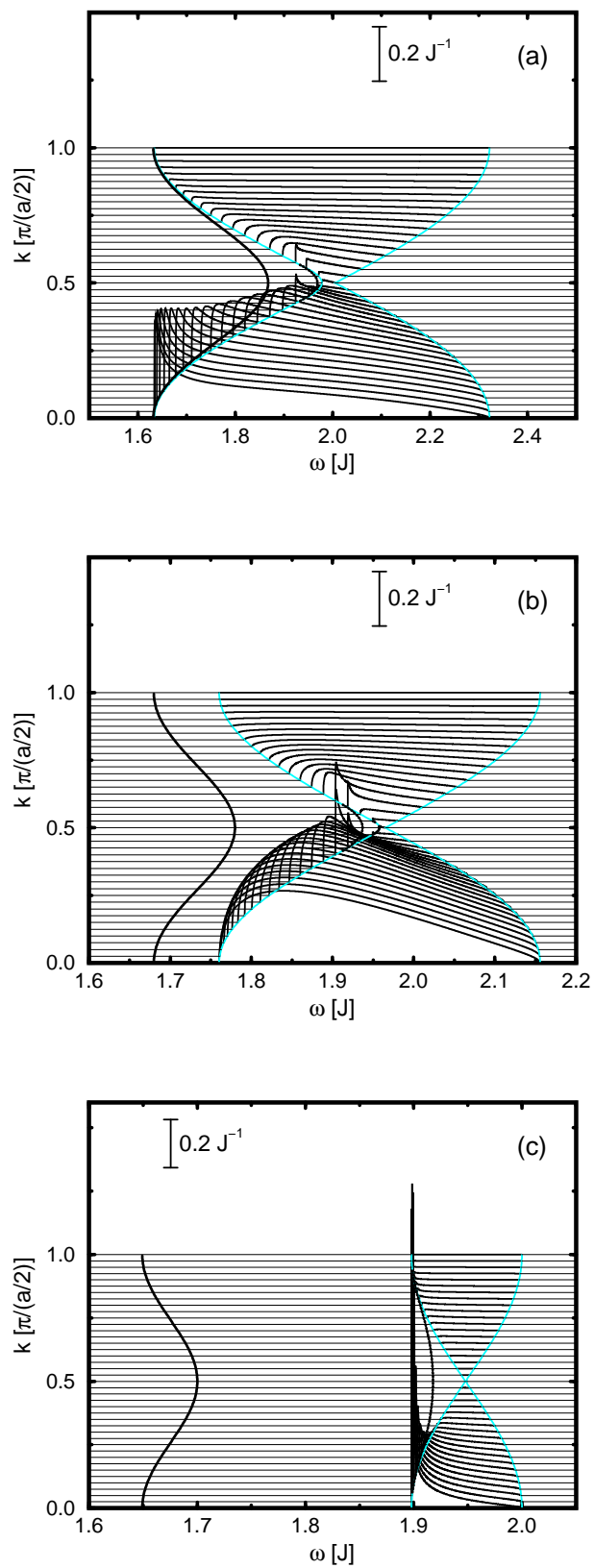


Fig. 6.25: Two-triplon spectral density  $I_2(k, \omega)$  for  $R_{NNN}^{S=0}$  with  $\lambda = 0.3$  and  $\alpha = 0.0$  (a),  $\alpha = 0.25$  (b) and  $\alpha = 0.5$  (c). Grey lines denote the lower and the upper edge of the continuum. Black lines indicate the dispersion of two-triplon bound states.

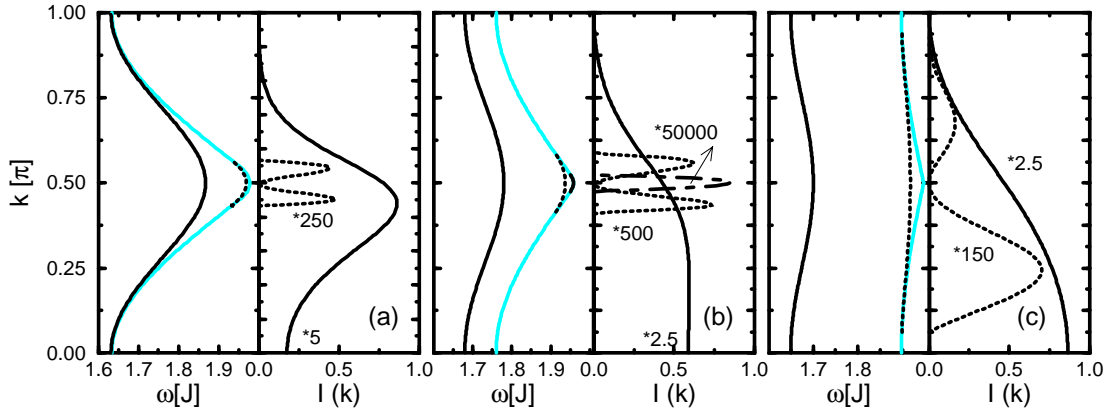


Fig. 6.26: Two-triplon bound states for  $R_{\text{NNN}}^{S=0}$  with  $\lambda = 0.3$  and  $\alpha = 0.0$  (a),  $\alpha = 0.25$  (b) and  $\alpha = 0.5$  (c). The dispersion of the bound states is shown in the left panels. The spectral weights of the bound states multiplied by the indicated factors is shown in the right panels. Grey lines denote the lower edge of the continuum.

The starting point of the discussion is the case of  $R_{\text{NN,weak}}^{S=0}$ . As stated above the first  $S = 0$  two-triplon bound state  $S_1$  carries most of the spectral weight for all momenta. Hence, it is of crucial importance for the optical absorption. In Figs. 6.22 and 6.24, it is shown that the dispersion  $\omega_{\text{bound}}(k)$  of the bound state  $S_1$  possesses three extrema at  $k \in \{0, \pi/2, \pi\}$ . Therefore one obtains three van-Hove singularities in  $I^{\text{IR}}(\omega)$ . The spectral density is symmetric about  $k = \pi/2$  so that two van-Hove singularities coincide and there are two peaks resulting from the bound state  $S_1$  in the optical conductivity. The weight of the minimum at  $k = 0$  is suppressed by the phonon form factor. This implies that the regions about  $k = \pi/2$  and  $k = \pi$  dominate.

In Fig. 6.30a the optical absorption for a dimerized chain ( $\lambda \in \{0.3, 0.4, 0.5, 0.6\}$ ) without frustration is depicted. The spectra are shifted in  $y$ -direction for clarity. The line shape is dominated by a small peak at low energies, a sharp peak at intermediate energies and a broad structure at high energies. The first two features are mainly produced by the above mentioned van-Hove singularities resulting from the extrema of the bound state dispersion of  $S_1$ . The second peak is dominant because the spectral weight has a maximum at  $k = \pi/2$ , see Fig. 6.22a and 6.24a. For increasing  $\lambda$  this peak loses intensity while the first peak becomes more pronounced. The latter effect is due to the increasing binding energy of  $S_1$  at  $k = \pi$ .

For strong dimerization the feature at low energies, which is more like a shoulder than like a peak, is an effect of the two-triplon continuum (inset Fig. 6.30a). The second bound state  $S_2$  is of no greater relevance for the optical absorption because it has zero spectral weight for  $k = \pi/2$  which is the only extremum of the bound state dispersion. In addition, the binding energy is very small without frustration and so is the corresponding spectral weight.

Lorenzana and Eder [297] calculated the two-spinon-plus-phonon contribution to the optical absorption for a uniform Heisenberg chain. The line shape consists mainly of three parts: a concave uprise at low energies which vanishes for zero frequency, a singularity at intermediate energies and a convex tail for higher frequencies. It is very interesting to see that all these features have precursors

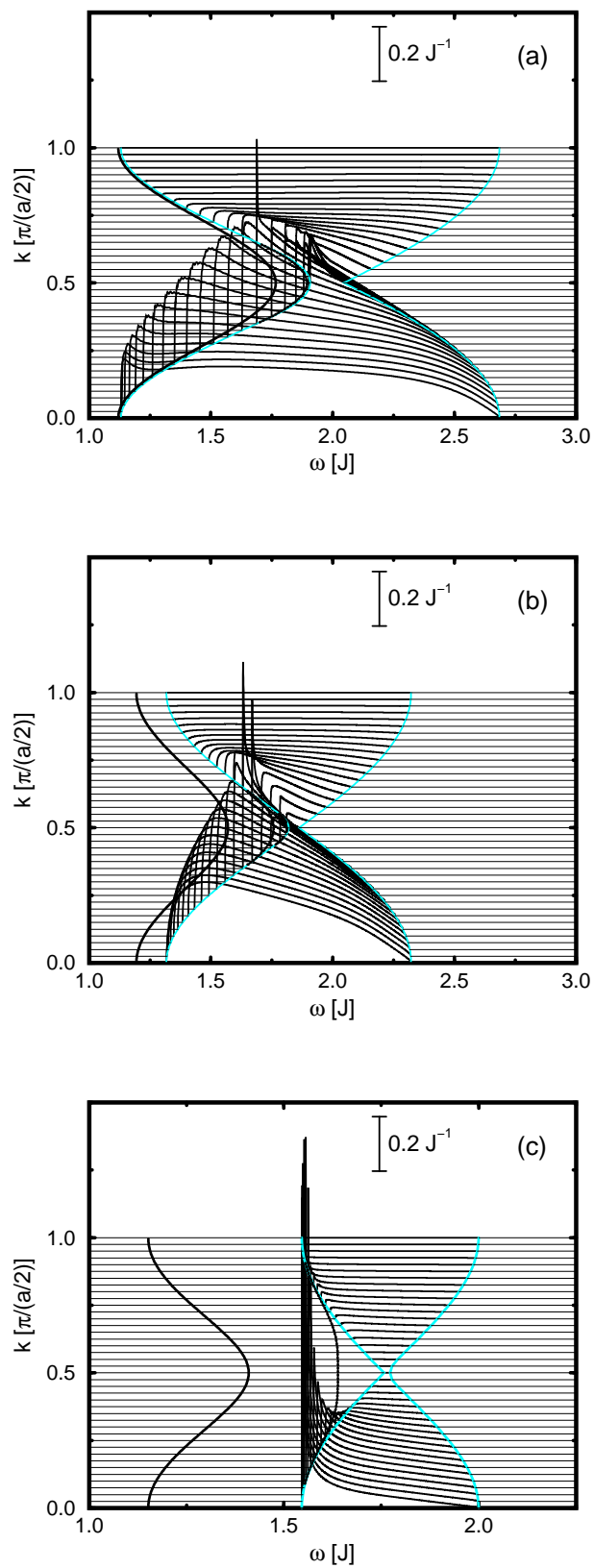


Fig. 6.27: Two-triplon spectral density  $I_2(k, \omega)$  for  $R_{NNN}^{S=0}$  with  $\lambda = 0.6$  and  $\alpha = 0.0$  (a),  $\alpha = 0.25$  (b) and  $\alpha = 0.5$  (c). Grey lines denote the lower and the upper edge of the continuum. Black lines indicate the dispersion of two-triplon bound states.

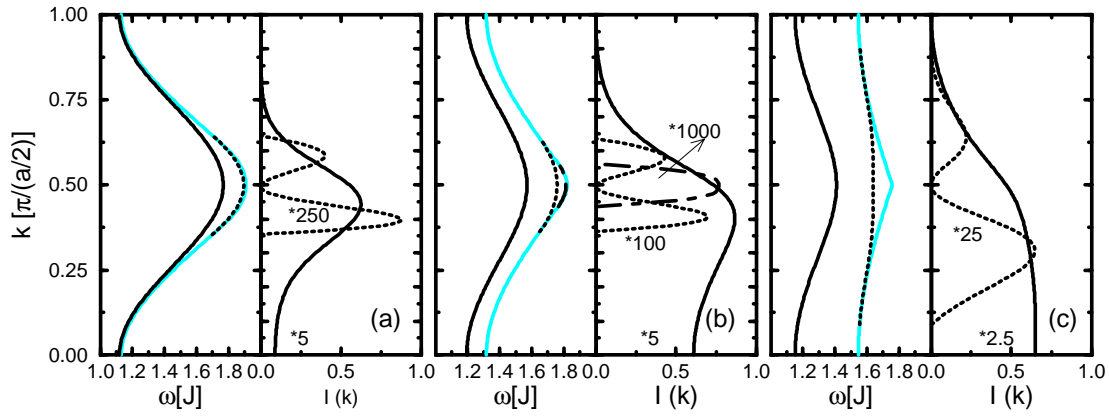


Fig. 6.28: Two-triplon bound states for  $R_{\text{NNN}}^{S=0}$  with  $\lambda = 0.6$  and  $\alpha = 0.0$  (a),  $\alpha = 0.25$  (b) and  $\alpha = 0.5$  (c). The dispersion of the bound states is shown in the left panels. The spectral weights of the bound states multiplied by the indicated factors is shown in the right panels. Grey lines denote the lower edge of the continuum.

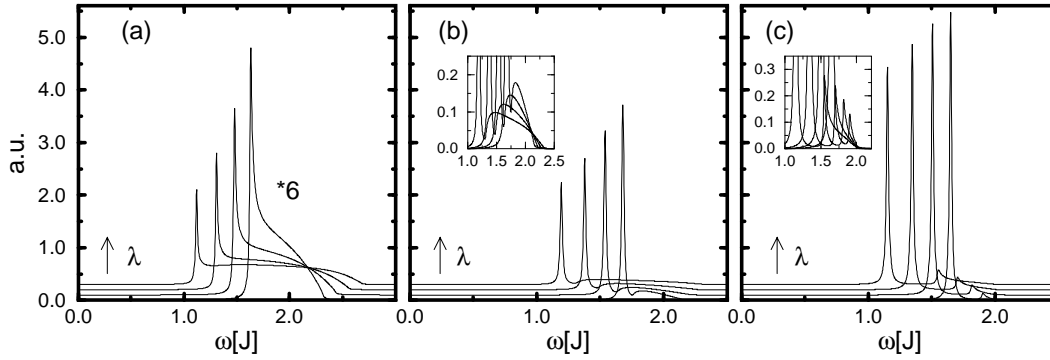


Fig. 6.29: Raman line shape for  $R_{\text{NNN}}^{S=0}$  with additional broadening  $\Gamma = 0.01$  is shown for  $\alpha = 0$  (a),  $\alpha = 0.25$  (b) and  $\alpha = 0.5$  (c). In each picture, curves for  $\lambda \in \{0.3; 0.4; 0.5; 0.6\}$  are shown, shifted in  $y$ -direction for increasing  $\lambda$ . The Raman response for  $\alpha = 0$  is multiplied by 6. The insets in (b) and (c) zoom on the continua.

at finite dimerization which are captured in the triplon picture.

In the limit of vanishing dimerization the system becomes gapless and the spectra therefore start at zero energy. As long as there is some finite dimerization the bound state  $S_1$  exists and produces the concave uprise at small energies and the singularity at intermediate energies resulting from the maximum of the dispersion of  $S_1$  at  $k = \pi/2$ . It is expected that for vanishing dimerization ( $\lambda = 1$ ) the dispersion of  $S_1$  coincides with the lower band edge of the two-triplon continuum leading to a square root divergence at the lower band edge for all momenta. Since the dispersions and the band edges display an extremum at  $k = \pi/2$  this divergence leads to the singularity discernible at intermediate energies. The convex tail at the upper band edge is equally present even for strongly dimerized chains, see inset in Fig. 6.30a. It is a consequence of the convex square root behavior



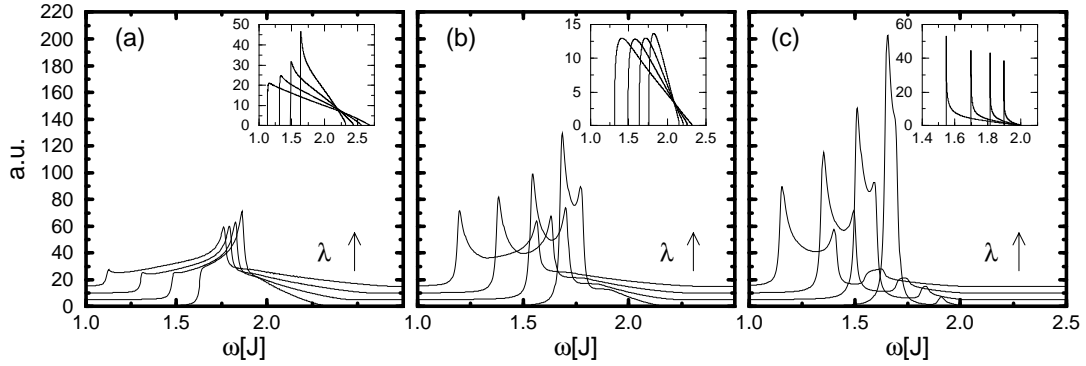


Fig. 6.30: Optical absorption for  $R_{NN,weak}^{S=0}$  with additional broadening  $\Gamma = 0.01$  is shown for  $\alpha = 0$  (a),  $\alpha = 0.25$  (b) and  $\alpha = 0.5$  (c). In each picture, curves for  $\lambda \in \{0.3; 0.4; 0.5; 0.6\}$  are shown. Insets: Contribution of the two-triplon continuum without broadening.

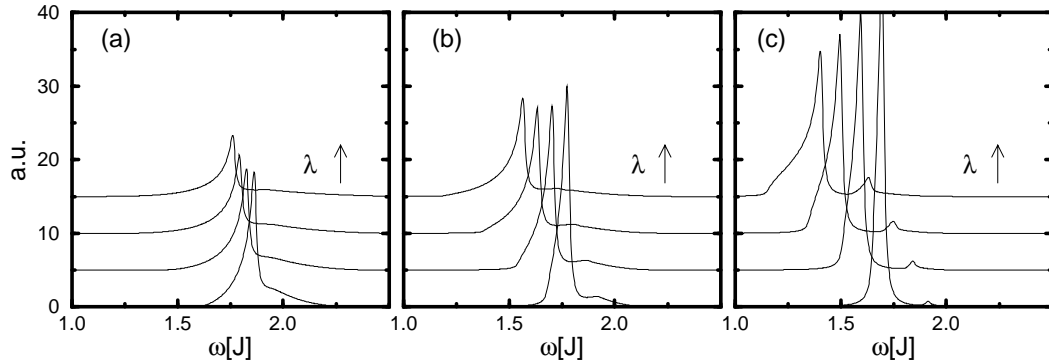


Fig. 6.31: Optical absorption for  $R_{NNN}^{S=0}$  with additional broadening is shown for  $\alpha = 0$  (a),  $\alpha = 0.25$  (b) and  $\alpha = 0.5$  (c). In each picture, curves for  $\lambda \in \{0.3; 0.4; 0.5; 0.6\}$  are shown.

at the upper edge of the two-triplon continuum.

In Figs. 6.30b and 6.30c the optical absorption at finite frustration  $\alpha = 0.25$  and  $\alpha = 0.5$  for the same values of the dimerization is shown. As discussed earlier, the frustration enhances the triplon-triplon interaction and increases the binding energy of the two-triplon bound states. As can be clearly seen in Figs. 6.22b-c and Figs. 6.24b-c, the spectral weight of  $S_1$  at  $k = \pi$  increases compared to the weight at  $k = \pi/2$ . Therefore, the first peak in the optical absorption becomes more and more prominent on increasing frustration. This leads to the most important features at large frustration. At  $\alpha = 0.5$ , the spectral weight of  $S_2$  is also sizable. Besides the contribution of the two-triplon continuum (inset of Fig. 6.30c) an additional peak appearing for decreasing dimerization can be discerned. This peak originates from the dispersion of the bound state  $S_2$  which displays two energetically degenerate maxima.

The optical absorption for  $R_{NNN}^{S=0}$  is plotted in Fig. 6.31. The main difference to the discussion of the optical absorption produced by  $R_{NN,weak}$  are the consequences of the different symmetries of the observables.  $R_{NNN}$  suppresses the spectral weight for large momenta. Thus the optical response

is weak due to the phonon form factor which stresses large momenta. In addition, the van-Hove singularity resulting from  $k = \pi$  of  $S_1$  is suppressed completely so that only a weak shoulder can be observed at low energies, independent of frustration and dimerization. At  $\alpha = 0.25$  the additional side structures are produced by the bound states  $S_2$  and  $S_3$ .

## 6.6 Chapter summary

In this chapter results for the spectral weights and the spectral densities of the dimerized and frustrated Heisenberg chain are presented. A perturbative realization of the continuous unitary transformations is used starting from the limit of isolated dimers. By means of the transformations an effective model is obtained which conserves the number of triplons.

The first part of the chapter deals with the analysis of the obtained spectral weights for  $S = 1$  and  $S = 0$  excitations. It has been shown [82] that for unfrustrated chains a description in terms of two triplons is sufficient even in the limit of zero dimerization. The triplon may also serve as an elementary excitation of the uniform Heisenberg chain besides the well-established spinon excitation. The situation at finite frustration is more subtle. Nevertheless indications are found that the situation is similar also in this case.

The second part presents results for the one-triplon and the two-triplon contribution to the spectral density for strong ( $\lambda = 0.3$ ) and intermediate ( $\lambda = 0.6$ ) dimerization and for various values of the frustration ( $\alpha = 0; 0.25; 0.5$ ) and for total spin one and zero.

In Sect. 6.4 of this chapter the dynamical structure factor is examined which is relevant for inelastic neutron scattering experiments. The one-triplon contribution contains most of the spectral weight at strong and intermediate dimerization. Results are provided for the one-triplon dispersion  $\omega(k)$  and the  $k$ -resolved spectral weight  $I_1(k)$ . The one-triplon dispersion becomes larger on lowering the dimerization while it becomes flatter on increasing the frustration. The spectral weight  $I_1(k)$  is mainly concentrated at  $k = \pi$ . In the limit  $\lambda \rightarrow 1$  the one-triplon contribution vanishes except for  $\alpha = 0.5$  around  $k = \pi/2$ .

Subsequently the two-triplon contribution to the dynamical structure factor is discussed. Results are provided for the spectral density of the two-triplon continuum and for the dispersion and for the spectral weight of the two-triplon bound states.

For the unfrustrated spin-chain, the spectral weight is concentrated at the lower band edge at larger momenta. Two-triplon bound states only exist in a finite region about  $k = \pi/2$ . Increasing the frustration leads to a shift of spectral weight to higher energies. At  $\lambda = 0.6$  and  $\alpha = 0.5$ , the spectral weight is shifted almost totally to the upper band edge at  $k = \pi$ . This transfer of spectral weight is also found for  $\lambda = 1$  by exact diagonalization at finite temperatures [285].

The behavior of the lower band edge changes strongly when varying of the frustration. Generically, one finds a square root behavior of the lower band edge. It is a consequence of the hardcore interaction between the triplons which makes it difficult for them to pass each other. In contrast to this finding, a square root divergence is found at the lower band edge for  $\alpha = 0.25$ . Here the energy of a two-triplon bound state is degenerate (to the precision of our analysis of about 2% of  $J$ ) with the lower band edge of the two-triplon continuum.

The latter finding is compared to the results obtained from field theory [252]. In contrast to the above findings for the unfrustrated spin-chain, field theory predicts a square root divergence for the lower band edge of the dynamical structure factor of the sine-Gordon model. Thus the commonly used reduction of the spin-chain to a sine-Gordon model by neglecting the marginal operator cannot be justified quantitatively for the values of dimerization considered here.

It is shown that in the self-consistent harmonic approximation (corresponding to renormalization in first order) the marginal operator  $D \cos(4\Phi)$  is as important as the mass operator  $\delta \cos(2\Phi)$  at any finite dimerization. Renormalization in second order, however, predicts a slow logarithmic suppression of the marginal term [293] below critical frustration.

It is found that square root behavior represents the generic behavior of the spectral density of the band edges. A square root divergence occurs if a two-triplon bound state is degenerate with the lower band edge of the continuum. In the field theoretic language this degenerate bound state, which has not yet emerged from the continuum, is the third breather. One finds the concomitant square root divergence for  $\alpha \approx \alpha_{0,c}$ .

The applicability of the sine-Gordon model to the unfrustrated, but significantly dimerized spin-chain is further questioned by the study of the excitation energies of the bound states. The ratio of the excitation energies of the  $S = 0$  two-triplon bound state and of the one-triplon gap is exactly  $\sqrt{3}$  in the SU(2)-symmetric sine-Gordon model. This ratio is found only for  $\alpha_0 = \alpha_{0,c}$  in agreement with a previous numerical study [257]. At present, one does not know why  $\alpha_0 = \alpha_{0,c}$  is required to retrieve the field theory result for the second breather, but  $\alpha \approx \alpha_{0,c}$  to retrieve the field theory result for the third breather. It is expected that one has to go to very much lower values of the dimerization, i.e. closer to  $\lambda = 1$ , to retrieve the behavior of a pure sine-Gordon model. But as long as the dimerization is *not* extremely small the marginal operator cannot be neglected for a quantitative description. Thus, the effective low-energy model to be considered is the double sine-Gordon model for which the SU(2) symmetry condition will be different from  $K = 1/2$  and hence also the ratios of the breather energies will differ from the ratios known for the sine-Gordon model [289].

In Sect. 6.5, the spectral properties of the dimerized and frustrated spin-chain for excitations with total spin zero are discussed which are relevant for optical experiments. Results for the two-triplon contribution are presented which contains most of the spectral weight.

Two different observables are examined: a nearest-neighbor (NN) coupling on the weak bonds  $R_{\text{NN,weak}}^{S=0}$  and a next-nearest-neighbor (NNN) coupling  $R_{\text{NNN}}^{S=0}$ . The observables obey different symmetries. The nearest-neighbor coupling possesses a reflection symmetry about  $k = \pi/2$ . The next-nearest-neighbor coupling does not have any reflection symmetry except for  $k = \pi$  where it is odd so that no even  $S = 0$  two-triplon state can be excited. The spectral densities for both observables are dominated by the two-triplon bound state  $S_1$  which contains most of the spectral weight. This bound state exists for all momenta, independent of dimerization and frustration. The binding energy increases when turning on the frustration.

The spectral weight of the two-triplon continuum is concentrated at the lower band edge for all considered values of the dimerization and the frustration. For finite dimerization, the lower band edge displays a square root behavior for  $\alpha = 0.25$  in accordance with the results of the sine-Gordon

model. Divergences may occur only at exactly zero dimerization. The behavior changes similarly to the  $S = 1$  case if a two-triplon bound state is almost degenerate with the lower band edge of the two-triplon continuum. Such a degeneracy appears in our data for  $\alpha \approx 0$  and for  $\alpha \approx 0.5$ .

Finally, results for the Raman response and the infrared absorption are presented. Both experiments are dominated by the bound state  $S_1$  for the values of the dimerization considered. This bound state produces two van-Hove singularities in the infrared absorption resulting from  $k = \pi/2$  and from  $k = \pi$ . The van-Hove singularity at lower energies becomes more important for larger values of the frustration.

## 6.7 Chapter conclusion

It is shown that triplon-based conserving continuous unitary transformations are an effective tool to calculate quantitatively spectral densities for the dimerized and frustrated spin-chain at strong and intermediate dimerization. All relevant quantities can be calculated in this parameter regime. Longer range processes become important for small dimerizations. Here the perturbative realization of the continuous unitary transformation is not useful anymore.

It is shown that only one or two triplons are necessary to capture the essential physics at significant dimerization. In addition, an analysis of the spectral weight shows that even in the limit of vanishing dimerization most of the spectral weight seems to remain in the one- and two-triplon channel.

Since undimerized spin-chains are the archetypes of models described by spinons it seems that neither the occurrence of fractional excitations nor the vanishing of the gap (for  $\alpha < \alpha_c$ ) precludes the applicability of an approach in terms of integer triplons. This calls for further investigations of the relation between spinon and transformed triplon states. Since these results hold in spin-chains, it is plausible that a large class of low-dimensional quantum antiferromagnets is accessible by calculations based on integer excitations.

Further strong support for this result is found in the analysis of the two-triplon spectral density. The two-triplon spectral densities computed at finite dimerization display well-developed precursors of the results for the uniform chain based on spinons, e.g. the dynamical structure factor probing the  $S = 1$  sector [272] or the optical absorption [297] probing the  $S = 0$  sector.

In the case of finite frustration the extrapolations become hard to control in the limit of vanishing dimerization but nevertheless indications are found that the two-triplon contribution is the dominant contribution in the whole phase diagram of the dimerized and frustrated spin-chain. Especially the gapped phase ( $\alpha_0 > \alpha_{0,c}$ ) requires that the two-spinon continuum between  $\Delta$  and  $2\Delta$  can be described by a dense distribution of bound two-triplon states. For this to occur an infinite-range effective interaction is necessary which is beyond the scope of the perturbative CUTs. But the nice agreement between the shifts of spectral weight obtained by complete exact diagonalization at finite temperatures [285] for the undimerized frustrated chain with the above results at finite dimerization is taken as further indication that the triplon description can also be extended to the undimerized frustrated chain.

The comparison of the results to those obtained by mapping the spin-chain to a sine-Gordon model lead to a number of insights. Both approaches agree in that the generic singularity at the lower

band edge is a square root, either a divergence or a zero. The divergence occurs if and only if a bound state is degenerate with the band edge. It turns out that the predictions of the single sine-Gordon model hold for critical frustration only which agrees with previous conclusions based on numerical results [257]. The general spin-chain at significant dimerization requires to go beyond the single sine-Gordon model.

## 7 The antiferromagnetic two-leg ladder

In this chapter the energetic and especially the spectral properties of the antiferromagnetic two-leg Heisenberg ladder are analyzed. The Heisenberg model on a two-leg ladder can be viewed as the natural intermediate system between the one-dimensional Heisenberg model as studied in the last chapter and the two-dimensional Heisenberg model on a square lattice.

The nature of the elementary excitations of the two-leg ladder system is a key issue in studying this system. The two-leg ladder can be viewed either in a chain-like picture (two-coupled chains) or in a rung-like picture (coupled rungs). The first approach usually favors a description in terms of fractional spinons as elementary excitations while the latter approach offers a possible description in terms of integer excitation, namely rung-triplons. In this chapter it will be shown that a description in terms of rung-triplons is possible even if the coupling between the rungs is of the same order as the coupling in the rungs.

In addition, there are a number of materials which are realizations of two-leg ladder systems. This offers the possibility to directly compare the obtained spectral densities with experiments, namely inelastic neutron scattering, Raman spectroscopy and infrared absorption.

It will be found that a quantitative understanding of the magnetic properties of experimentally realized two-leg ladder systems is not possible in a pure Heisenberg model. One has to include additional four-spin interactions in the model Hamiltonian. This extended two-leg ladder system will be discussed in the subsequent chapter.

### 7.1 Model

In this section the nature of the ground state and the corresponding elementary excitations of the antiferromagnetic two-leg Heisenberg ladder are presented [300, 304]. The Hamiltonian of the two-leg Heisenberg ladder reads

$$\begin{aligned} H(J_{\perp}, J_{\parallel}) &= J_{\perp} H_{\perp} + J_{\parallel} H_{\parallel} \\ &= \sum_i [J_{\perp} \mathbf{s}_{1,i} \mathbf{s}_{2,i} + J_{\parallel} (\mathbf{s}_{1,i} \mathbf{s}_{1,i+1} + \mathbf{s}_{2,i} \mathbf{s}_{2,i+1})] , \end{aligned} \quad (7.1.1)$$

where  $i$  denotes the rung and 1, 2 the leg. This is illustrated in Fig. 7.1.

The two-leg ladder can be tackled starting from two different limits. On the one hand, the system can be thought of as to consist of two weakly coupled chains ( $J_{\parallel} \ll J_{\perp}$ ) or, on the other hand, of weakly interacting rungs ( $J_{\parallel} \ll J_{\perp}$ ). The latter approach was first to find evidence for a finite spin gap in two-leg ladder systems [301–303], i.e. a finite energy is needed to create an excitation with  $S = 1$ .

In the case of isolated rungs ( $J_{\parallel} = 0$ ), the ground state of the system is the product-state of singlets on each rung. An excitation of the system corresponds to converting one singlet in one

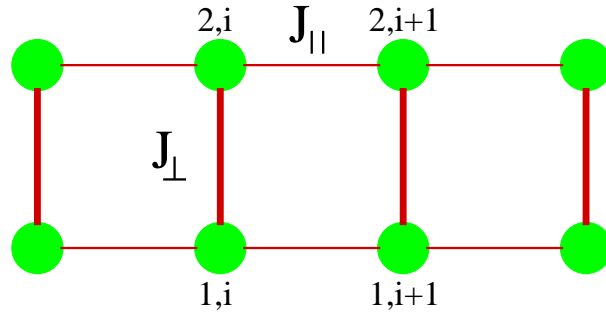


Fig. 7.1: Illustration of the antiferromagnetic two-leg Heisenberg system.

triplet. The energy for this process is exactly  $J_{\perp}$ . Turning on a finite but small coupling  $J_{\parallel}$ , a band of  $S = 1$  excitations with dispersion  $\omega(k) = J_{\perp} + J_{\parallel} \cos(k)$  is generated. These excitations will be referred to as rung-triplets. The ground state remains in a phase dominated by rung-singlets. The spin gap  $\Delta$  is the minimum excitation energy, i.e.  $\Delta = \omega(\pi) = J_{\perp} - J_{\parallel}$  in this limit. The two-leg ladder is therefore a gapped system with a gap  $\Delta$  of the order  $J_{\perp}$  for small  $J_{\parallel}$ .

In the other limit the two-leg ladder decouples into two isolated spin-chains. The starting point of this limit is therefore a gapless and critical system as discussed in the last chapter. In analogy to the transition of the gapless spin-chain to the gapful dimerized spin-chain, the coupling  $J_{\perp}$  is relevant and opens a gap of the order  $J_{\perp}$  for any finite value of  $J_{\perp}$  [304, 305]. The spin-ladder can be mapped via bosonization onto a free massive Thirring model (Eq. 6.1.6). There are two kinds of excitations. A threefold degenerate excitation with mass  $\Delta$  corresponding to one-triplet and a excitation with mass  $\approx 3\Delta$  corresponding to a singlet excitation [305]. The antiferromagnetic two-leg ladder system is always in a spin-liquid state, in contrast to the one-dimensional and the two-dimensional Heisenberg model.

## 7.2 Materials

In this section experimental realizations of two-leg ladder systems are introduced. The focus is laid on the structure of these materials. The direct comparison between experimental data and theoretical results will be done later in the application sections.

Realizations of two-leg ladders are recognized in  $\text{CaV}_2\text{O}_5$  [306],  $\text{SrCu}_2\text{O}_3$  [307, 308] and  $\text{A}_{14}\text{Cu}_{24}\text{O}_{41}$  with  $\text{A}=\{\text{Sr}, \text{Ca}, \text{La}\}$  [311, 312] compounds. The vanadium based compound  $\text{CaV}_2\text{O}_5$  is a quasi two-dimensional layered material, where  $S = 1/2 \text{ V}^{4+}$  vanadium ions forming the sites of weakly coupled two-leg ladders, a so-called trellis lattice. The spin gap is determined to be about 600 K [313, 314] and magnetic susceptibility measurements predict a  $S = 1/2$  Heisenberg model with weakly interacting rungs ( $J_{\parallel} \approx 0.1J_{\perp}$ ) [314, 315].

The other two compounds belong to the class of low-dimensional materials which are based on copper-oxide structures. Therefore they are also interesting concerning the understanding of two-dimensional copper-oxide planes which are the basic building blocks of the high- $T_c$ -superconductors.  $\text{Sr}_{0.4}\text{Ca}_{13.6}\text{Cu}_{24}\text{O}_{41}$  is even superconducting under high pressure [308], enhancing in particular the

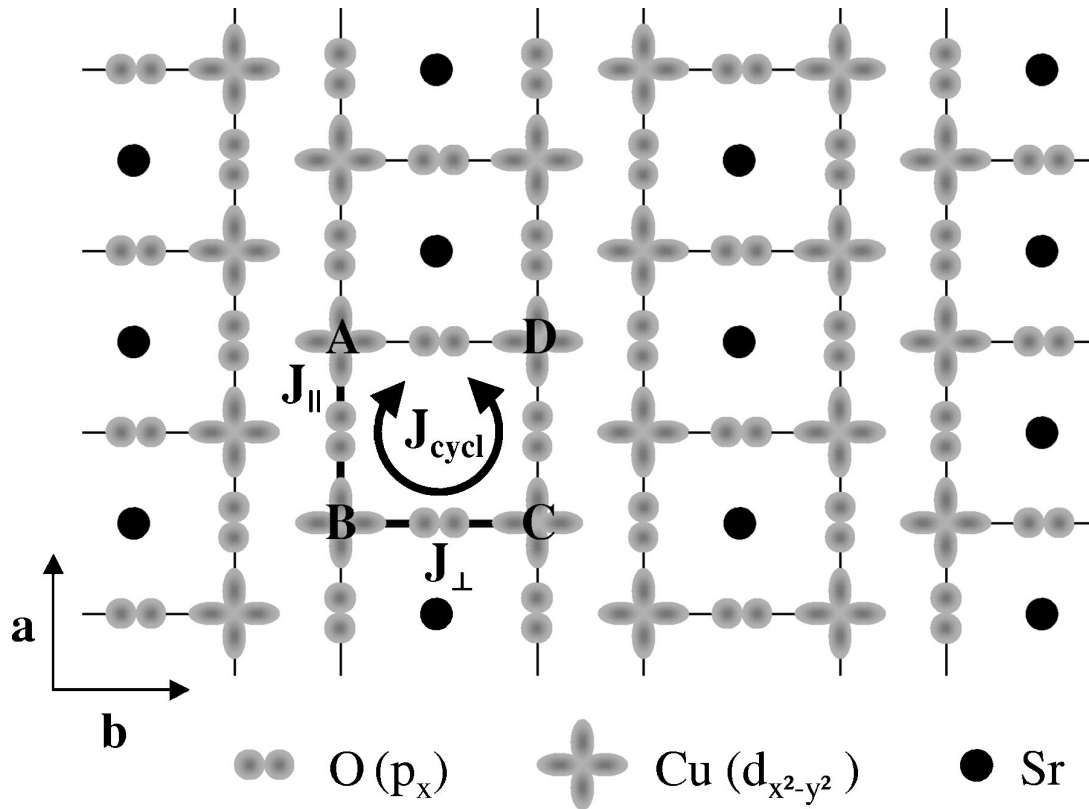


Fig. 7.2: Schematic view of the two-leg ladder  $\text{SrCu}_2\text{O}_3$  projected on the  $ab$  plane. The Sr atoms are located between the planes containing the  $\text{Cu}_2\text{O}_3$  units.

interest in this class of compounds (see below).

$\text{SrCu}_2\text{O}_3$  is the prototype of weakly coupled  $\text{Cu}_2\text{O}_3$  spin-ladders. A schematic view of this compound is shown in Fig. 7.2. The copper atoms are represented by  $d$ -orbitals. They couple via an intermediate oxygen  $p$ -orbital by superexchange [13]. The interladder coupling is small because the superexchange via a  $\text{Cu-O-Cu}$  path with a  $90^\circ$  bond angle has a smaller overlap than with a bond angle of  $180^\circ$  [13, 309, 310]. The disadvantage of this system is that it has to be grown under high pressure so that only small single crystals/polycrystals are available (e.g. [316]). The latter point complicates scattering experiments on this compound. A detailed discussion of Raman scattering results will be done later in Chapt. 8 [317].

The last class of compounds to be introduced are the so-called telephone number compounds  $\text{A}_{14}\text{Cu}_{24}\text{O}_{41}$  with  $\text{A}=\{\text{Sr}, \text{Ca}, \text{La}\}$ . The main advantage of this system is the possibility to grow large single crystals which renders inelastic neutron scattering and optical experiments possible. A disadvantage is the complex structure of this system. It consists of two-leg  $\text{Cu}_2\text{O}_3$  ladders as described in the last paragraph, but also on the other hand of  $\text{CuO}_2$  chains. Both structures are



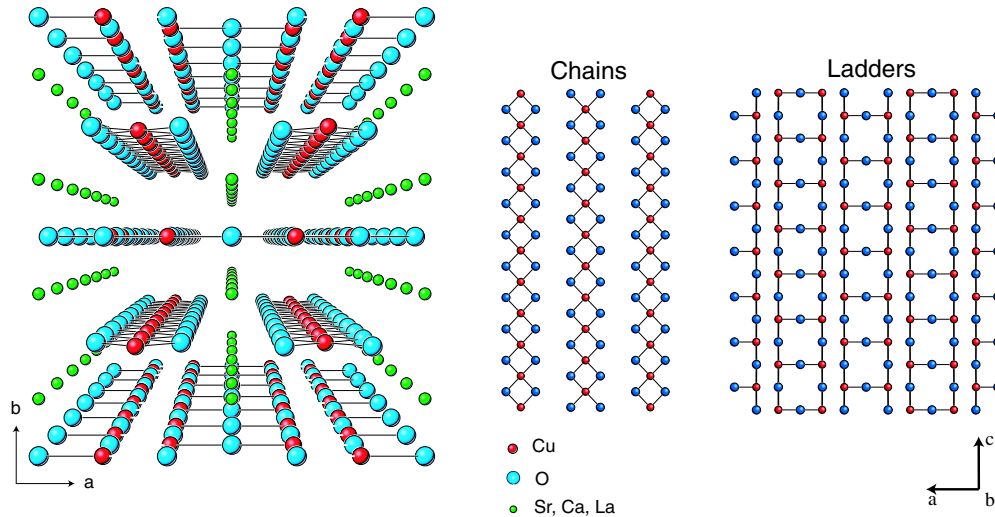


Fig. 7.3: Schematic view of the telephone number compound  $\text{Sr}_{14}\text{Cu}_{24}\text{O}_{41}$ . The left part shows a three-dimensional view on the layered material. There are planes of ladder structures, chain structures and Sr atoms. The basic ladder ( $\text{Cu}_2\text{O}_3$ ) and chain ( $\text{CuO}_2$ ) building blocks are shown on the right part.

oriented along the  $c$ -axis. These two structures are illustrated on the right hand side of Fig. 7.3. It is instructive to write  $\text{A}_{14}\text{Cu}_{24}\text{O}_{41} = (\text{A}_2\text{Cu}_2\text{O}_3)_7(\text{CuO}_2)_{10}$  in order to stress both structures. Ladders and chains form two-dimensional layers which are stacked in  $b$ -direction alternating with Sr layers. This is shown in the left part of Fig. 7.3.

The magnetic couplings due to superexchange in the ladder structure are expected to be almost isotropic. The distance between two copper atoms is roughly the same in rung and in leg direction. Both superexchanges go via a  $180^\circ$  Cu-O-Cu bond. The coupling between two copper atoms on neighboring ladders is weakly ferromagnetic. A typical magnetic coupling  $J$  is of the order of 1000 K which is similar to the two-dimensional cuprates. The nearest-neighbor exchange in the chains is mediated via two symmetric Cu-O-Cu bonds with about  $90^\circ$  bonding angle leading to weakly ferromagnetic exchange. A typical  $J$  in the chains is about one order of magnitude smaller than in the ladders. The magnetic scattering events of chains and ladders occur therefore on two different energy scales making it possible to study the physics of both structures separately in experiments.

Two members of this class of compounds, namely  $\text{Sr}_{14}\text{Cu}_{24}\text{O}_{41}$  and  $\text{La}_6\text{Ca}_8\text{Cu}_{24}\text{O}_{41}$  are the focus in this work. The system  $\text{Sr}_{14}\text{Cu}_{24}\text{O}_{41}$  is intrinsically doped with 6 holes per unit cell. Using X-ray absorption spectroscopy, it is possible to conclude that there are on average 0.8 holes in the ladders and 5.2 holes in the chains [318] which can be explained by a higher electronegativity in the chains [319].

It is possible to substitute  $\text{Sr}^{2+}$  by isovalent  $\text{Ca}^{2+}$  or by  $\text{La}^{3+}$  (and  $\text{Y}^{3+}$ ). The substitution by  $\text{La}^{3+}$  reduces the number of holes in the system. The limiting case of an undoped sample is the formal compound  $\text{La}_6\text{Ca}_8\text{Cu}_{24}\text{O}_{41}$ . Experimentally it is not possible to realize this limiting case. But there exist realizations up to  $\text{La}_{5.2}\text{Ca}_{8.8}\text{Cu}_{24}\text{O}_{41}$  which can be viewed as almost undoped samples [298].

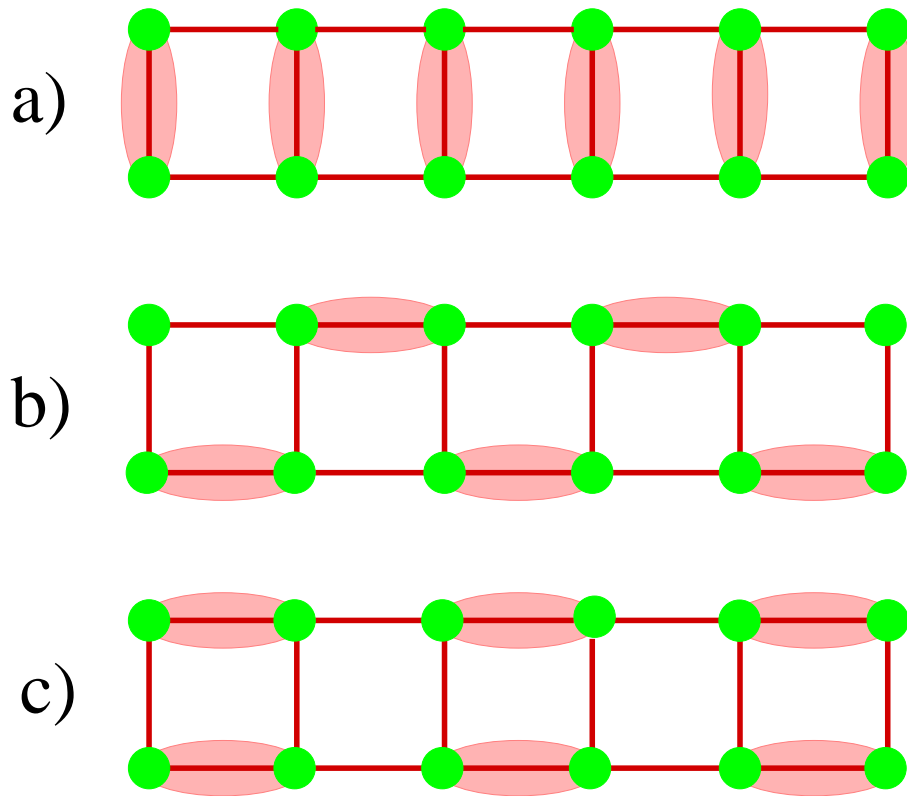


Fig. 7.4: Possible dimerization pattern for the two-leg ladder: a) Dimerization on the rungs, b) meander-like dimerization and c) symmetric dimerizations on the legs.

This will also be seen later in the application sections.

### 7.3 Method

This section presents the aspects concerning the method in the ladder case. As there are a lot of similarities between the dimerized chain and the spin-ladder, this section will focus on the points special for the ladder system.

In order to set up a triplon description of the system it is necessary to specify the dimerization pattern. This was canonical in the case of the dimerized chain because there is only one way of dimerization possible (up to an exchange of strong and weak bonds). In the ladder system there are three different ways of dimerization pattern which are distinct from each other. These are illustrated in Fig. 7.4. The first starting point is the already mentioned pattern with dimers on the rungs of the ladder. The associated ground state is the rung-singlet phase and the excitations are rung triplons. The other two starting points put the dimers in a symmetric and in a staggered way on the legs of the ladder (case b/c in Fig. 7.4). Choice (a) is the only choice which does not break a symmetry of the original model. The meander-like pattern is not continuously connected to

the rung-singlet phase. But it might be necessary to use the third configuration if the physics is dominated by the legs of the ladder.

In the following the starting point of isolated rungs is used to set up the perturbative continuous unitary transformation. The ladder Hamiltonian is reformulated according to

$$\frac{H(x)}{J_{\perp}} = H_{\perp} + xH_{\parallel}, \quad (7.3.1)$$

with  $x = J_{\parallel}/J_{\perp}$  as perturbation parameter,  $H_{\perp} = H(1,0)$  and  $H_{\parallel} = H(0,1)$ . The exchange coupling  $J_{\perp}$  is antiferromagnetic and is set to unity henceforth. The limit of isolated rungs is the limit for which the perturbative treatment is controlled.

The ground state of the unperturbed part  $H_{\perp}$  is the product state with singlets on all rungs. A first excited state is a single rung excited to a triplet. There are  $3L/2$  such elementary triplet excitations if  $L$  is the number of spins. The energetically next higher state is given by two rung-triplets and so on. The operator  $H_{\perp}$  simply counts the number of rung-triplets.

For the rest of the discussion of the two-leg ladder  $Q$  is identified with  $H_{\perp}$ , i.e., the elementary excitations of the unperturbed part (rung-triplets) serve as (quasi-)particles in the treatment of the ladder system. These excitations are called *rung triplons* [208]. In the following the prefix *rung* is skipped and the excitations will be just called *triplons*. But one has always to keep in mind which underlying topology is associated with the word triplon.

Now the action of the perturbing part  $H_{\parallel}$  on the triplon-states is analyzed in analogy to the case of the dimerized chain. Let  $|n\rangle$  denote a state with  $n$  rungs excited to triplets ( $n$ -triplon state), i.e.,  $H_{\perp}|n\rangle = n|n\rangle$ . Then

$$H_{\parallel} = T_{-2} + T_0 + T_2, \quad \text{with} \quad (7.3.2)$$

$$T_i|n\rangle \sim |n+i\rangle \quad \text{and}$$

$$T_{0,\pm 2} = \sum_{\nu} \mathcal{T}_{0,\pm 2}(\nu), \quad (7.3.3)$$

where  $\nu$  denotes pairs of adjacent rungs. The index  $\nu$  can also be viewed to count the bonds connecting adjacent rungs. The action of the local operators  $\mathcal{T}_{0,\pm 2}(\nu)$  on neighboring rungs is given in Tab. 7.1. There are no  $T_{\pm 1}$  in  $H_{\parallel}$  because the two-leg ladder conserves the parity concerning the reflection about the centerline of the ladder.

### 7.3.1 Observables for the two-leg ladder

Next, the evaluation of the observables of interest in the ladder system is focused on. The observables differ from the chain system due to the different topology of the ladder. The four *local*

$2\mathcal{T}_0$	
$ t^{0,\pm 1}, s\rangle \longrightarrow$	$ s, t^{0,\pm 1}\rangle$
$ t^0, t^{\pm 1}\rangle \longrightarrow$	$ t^{\pm 1}, t^0\rangle$
$ t^{\pm 1}, t^{\pm 1}\rangle \longrightarrow$	$ t^{\pm 1}, t^{\pm 1}\rangle$
$ t^{\pm 1}, t^{\mp 1}\rangle \longrightarrow$	$ t^0, t^0\rangle -  t^{\pm 1}, t^{\mp 1}\rangle$
$ t^0, t^0\rangle \longrightarrow$	$ t^1, t^{-1}\rangle +  t^{-1}, t^1\rangle$
$2\mathcal{T}_2$	
$ s, s\rangle \longrightarrow$	$ t^0, t^0\rangle -  t^1, t^{-1}\rangle -  t^{-1}, t^1\rangle$

Table 7.1: Action of the operators  $\mathcal{T}_i$  as defined by Eq. 7.3.3 on product states of adjacent rungs. Singlets are denoted by  $s$  and triplons by  $t^i$  where the superscript indicates the magnetic quantum number. The remaining matrix elements can be found by using  $\mathcal{T}_n^\dagger = \mathcal{T}_{-n}$ .

operators considered are

$$\mathcal{O}^I(r) = \mathbf{S}_{1,r} \mathbf{S}_{2,r} = \mathcal{T}_0^I \quad (7.3.4a)$$

$$\begin{aligned} \mathcal{O}^{II}(r) &= \mathbf{S}_{l,r} \mathbf{S}_{l,r+1} \quad (7.3.4b) \\ &= \frac{1}{4} (\mathcal{T}_{-2} + \mathcal{T}_0 + \mathcal{T}_2 + \mathcal{T}_{-1}^{II} + \mathcal{T}_1^{II}) \end{aligned}$$

$$\mathcal{O}^{III}(r) = \mathbf{S}_{1,r}^z - \mathbf{S}_{2,r}^z = \mathcal{T}_{-1}^{III} + \mathcal{T}_1^{III} \quad (7.3.4c)$$

$$\mathcal{O}^{IV}(r) = \mathbf{S}_{1,r}^z + \mathbf{S}_{2,r}^z = \mathcal{T}_0^{IV}, \quad (7.3.4d)$$

where the decompositions are either given in Tab. 7.1 for the  $\mathcal{T}$  or in Tab. 7.2 for the  $\mathcal{T}^\mu$ , with  $\mu \in \{I, II, III, IV\}$ . The index  $l = 1, 2$  in Eq. 7.3.4b denotes the leg on which the observable operates. The discussion is started with a simple but important symmetry property. Let  $\mathcal{P}$  denote the operator of reflection about the center-line of the ladder as depicted in Fig. 7.5. If  $|n\rangle$  denotes

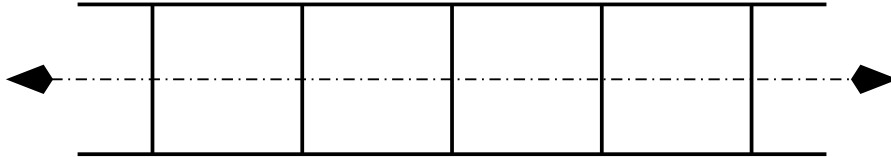


Fig. 7.5: The operator  $\mathcal{P}$  reflects about the depicted axis. A *single rung-singlet* (-triplon) has odd (even) parity with respect to  $\mathcal{P}$ . The action of  $\mathcal{P}$  on the rung-singlet ground state is defined to be of even parity  $\mathcal{P}|0\rangle = |0\rangle$ . If in  $|0\rangle$  one singlet is substituted by a triplon one obtains the state  $|1\rangle$  and  $\mathcal{P}|1\rangle = -|1\rangle$ . Generally, one has  $\mathcal{P}|n\rangle = (-1)^n |n\rangle$ .

a state with  $n$  rungs excited to triplons while all other rungs are in the singlet state one finds  $\mathcal{P}|n\rangle = (-1)^n |n\rangle$ , see caption of Fig. 7.5. The state  $|n\rangle$  might be a linear combination of many  $n$ -triplon states so no generality is lost in writing

$$\mathcal{O}_{\text{eff}}|0\rangle = \sum_{n \geq 0} |n\rangle. \quad (7.3.5)$$

$4\mathcal{T}_0^I$		
$ s\rangle$	$\rightarrow$	$-3 s\rangle$
$ t^i\rangle$	$\rightarrow$	$ t^i\rangle$
$4\mathcal{T}_1^{II}$		
$ s, t^1\rangle$	$\rightarrow$	$ t^1, t^0\rangle -  t^0, t^1\rangle$
$ t^1, s\rangle$	$\rightarrow$	$- t^1, t^0\rangle +  t^0, t^1\rangle$
$ s, t^0\rangle$	$\rightarrow$	$ t^1, t^{-1}\rangle +  t^{-1}, t^1\rangle$
$ t^0, s\rangle$	$\rightarrow$	$- t^1, t^{-1}\rangle +  t^{-1}, t^1\rangle$
$ s, t^{-1}\rangle$	$\rightarrow$	$ t^0, t^{-1}\rangle -  t^{-1}, t^0\rangle$
$ t^{-1}, s\rangle$	$\rightarrow$	$- t^0, t^{-1}\rangle +  t^{-1}, t^0\rangle$
$\mathcal{T}_1^{III}$		
$ s\rangle$	$\rightarrow$	$ t^0\rangle$
$ t^{\pm 1}\rangle$	$\rightarrow$	$0$
$\mathcal{T}_0^{IV}$		
$ s\rangle$	$\rightarrow$	$0$
$ t^i\rangle$	$\rightarrow$	$i t^i\rangle$

Table 7.2: Action of the local operators  $\mathcal{T}_i^\mu$  appearing in Eqs. 7.3.4. The notation is the same as in Tab. 7.1.

The parity of the ladder observables introduced in Eqs. 7.3.4 with respect to  $\mathcal{P}$  is clear from their definition:  $\mathcal{O}^{III}$  is odd while  $\mathcal{O}^I$  and  $\mathcal{O}^{IV}$  are even with respect to  $\mathcal{P}$ , just as the symmetrized observable  $\mathcal{O}^{II} = (\mathcal{O}_1^{II} + \mathcal{O}_2^{II})/2$ . These parities are conserved under the CUT so that  $\mathcal{P}$  applied on both sides of Eq. 7.3.5 yields

$$\mathcal{O}_{\text{eff}}|0\rangle = \begin{cases} \sum_n |2n\rangle, & \mathcal{O}_{\text{eff}} \text{ even} \\ \sum_n |2n+1\rangle, & \mathcal{O}_{\text{eff}} \text{ odd} \end{cases}. \quad (7.3.6)$$

It is thus found that an even (odd) parity of  $\mathcal{O}_{\text{eff}}$  implies that  $\mathcal{O}_{\text{eff}}$  can inject an even (odd) number of triplons into the system.

The coefficients  $c$  in Eq. 3.7.14 have been calculated for the one- and two-triplon case on a computer in a similar fashion as the coefficients  $t$  for the effective Hamiltonian. The implementation of  $\mathcal{O}_{\text{eff}}$  acting on the ground state  $|0\rangle$  follows the same line as described in detail for  $H_{\text{eff}}$  in Ref. [143]. The minimum clusters necessary for some fixed order arise from the same considerations as in Sect. 3.6. Again, the coefficients  $c$  are rational numbers which are computed up to  $k_{\text{max}} = 10^{\text{th}}$  order for the observables in Eqs. 7.3.4. This corresponds to processes which extend over up to ten rungs.

## 7.4 Spectral weights

In this section the spectral weights of the two-leg ladder are analyzed. As explained above there is no phase transition except for  $x \rightarrow \infty$ , i.e. the extrapolation of the spectral weights should work reliably in a broad range of  $x$ . On the other hand, it is clear that the physics involving the legs of the ladder becomes more and more important for  $x > 1$  meaning that more and more rung triplons are needed to describe the system.

### 7.4.1 $S = 1$

First, the spectral weights for excitations with total spin  $S = 1$  are discussed. The local observable considered is the symmetric combination of Eq. 7.3.4c and Eq. 7.3.4d

$$\mathcal{O}^{S=1}(r) = \frac{1}{2}(\mathcal{O}^{\text{III}}(r) + \mathcal{O}^{\text{IV}}(r)) \quad . \quad (7.4.1)$$

This observable injects an odd and an even number of triplons in the system and it is therefore predestinated for analysing the spectral weights. The spectral weights were calculated up to order 10 in the one- and two-triplon channel, up to order 9 in the three-triplon channel and up to order 10 in the four-triplon channel. The total spectral weight  $I_{\text{tot}}$  is equal to 1/4 for  $S = 1$ .

In Fig. 7.6 the relative spectral weights  $I_{N,\text{rel}} = I_N/I_{\text{tot}}$  are shown. In all extrapolants standard dlogPadé is used. At  $x = 0$ , the total spectral weight is in the one-triplon channel. Turning on  $x$ , the spectral weight in the one-triplon channel reduces but stays dominant in the whole range up to  $x = 1.5$ . The two-triplon spectral weight grows faster than the other multi-triplon channels for increasing  $x$  and contains 20% of the spectral weight for the isotropic ladder. The three-triplon contribution stays small up to  $x \approx 1$  and grows then very fast for larger  $x$ . Note that the extrapolation for the three-triplon channel is not reliable anymore for  $x \geq 1$ . This can also be seen at the sum rule which differs from 1 in the same way as the three-triplon spectral weight shoots up. The extrapolations for the one- and two-triplon channels are very stable in this range. The contribution of four triplons is at least one order of magnitude smaller than the three-triplon contribution and therefore would not change the Fig. 7.6.

It can be concluded that the one- and two-triplon contribution capture the dominant part of the total spectral weight for  $x < 1.5$ .

### 7.4.2 $S = 0$

The local observable  $\mathcal{O}_{\text{eff}}^{\text{II}}$  in Eq. 7.3.4b is considered for the  $S = 0$  case. Here the total spectral weight  $I_{\text{tot}}(x)$  can be obtained in analogy to the case of the dimerized chain from the ground state energy per spin  $\epsilon_0(x)$ . Since  $2\mathcal{O}_{\text{eff}}^{\text{II}}(x) = \partial/\partial x H_{\text{eff}}(x)$  the sum rule can be expressed in terms of

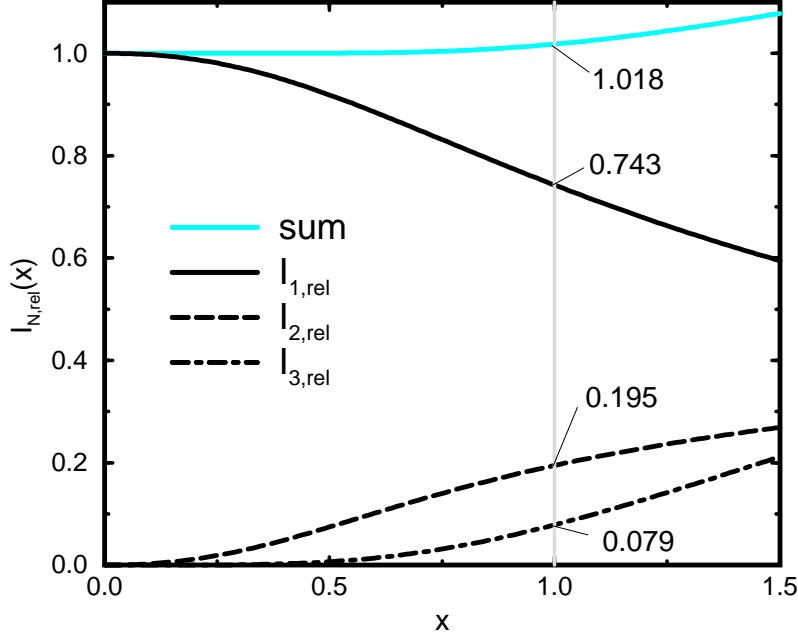


Fig. 7.6: Relative weights for the  $S=1$  operator  $\frac{1}{2}(\mathcal{O}^{III}(r) + \mathcal{O}^{IV}(r))$  (Eq. 7.3.4c and Eq. 7.3.4d). The  $I_N$  are calculated according to Eq. 3.7.15 up to and including order 10, 10 and 9 in  $x$  for  $N = 1, 2$  and  $3$  respectively. The total intensity  $I_{tot}$  is equal to  $1/4$ .

the effective Hamiltonian, giving rise to

$$\begin{aligned}
 I_{tot} &= \sum_{N=0}^{\infty} I_N = \langle 0 | \mathcal{O}^2 | 0 \rangle - \langle 0 | \mathcal{O} | 0 \rangle^2 \\
 &= \frac{3}{16} - \frac{Y}{2} - \frac{Y^2}{2}, \tag{7.4.2}
 \end{aligned}$$

with  $Y := \partial \epsilon_0 / \partial x$ . Therefore one can calculate the corresponding relative spectral weights  $I_N / I_{tot}$  as functions of  $x$  by extrapolating  $y$ . Fig. 7.7 shows the resulting relative weights for the observable  $\mathcal{O}_{eff}^{II}$  for the first four triplon sectors.

Since one cannot form an  $S = 0$  object from a single rung-triplon there is no  $I_1$  for this observable. The contribution of  $I_{5,rel}$  is of order  $10^{-3}$  leading to no visible changes in Fig. 7.7. Contributions of higher triplon channels are expected to be even smaller. All relative weights add up to unity. As can be seen in Fig. 7.7 the first four relative weights fulfill this requirement with great precision. For  $x = 0$  the singlet made from two isolated-rung triplons contains the full weight of the considered operator. As  $x$  increases the triplons start to polarize their environment, the two-triplon weight decreases and multi-triplon states gain weight.

From the results shown for the  $S = 1$  and  $S = 0$  cases it can be concluded that the *rung* triplon is an excellent choice for a quasi-particle description in the ladder system. For  $x$  not too large most

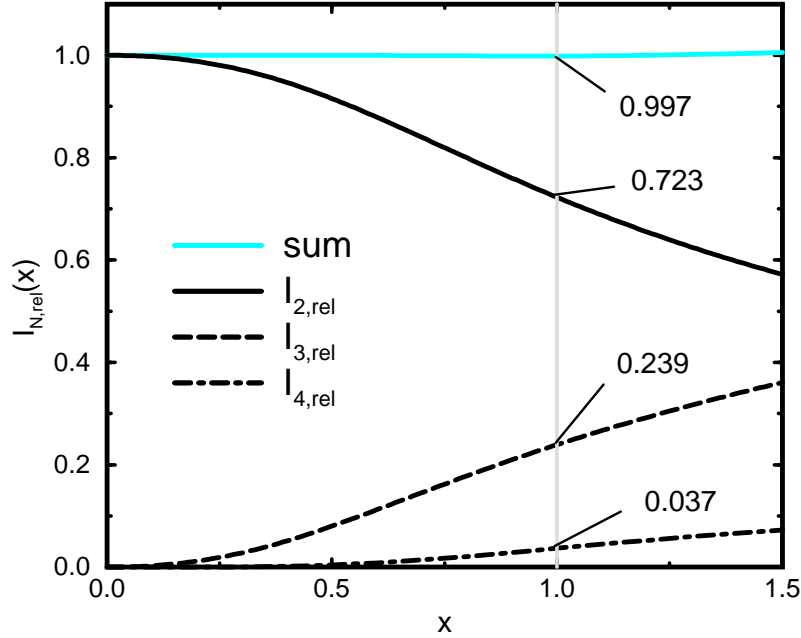


Fig. 7.7: Relative weights for the  $S=0$  operator  $S_{1,i}S_{1,i+1}$  (Eq. 7.3.4b). The  $l_N$  are calculated according to Eq. 3.7.15 up to and including order 10, 8 and 7 in  $x$  for  $N=2, 3$  and 4 respectively. The total intensity  $l_{tot}$  has been extracted from the 14<sup>th</sup> order result for the ground state energy per spin according to Eq. 3.7.16.

of the spectral weight is captured by a few triplons. Therefore calculations containing only a few triplons suffice to explain most of the physics for  $x \lesssim 1.0$ .

## 7.5 Energy properties

In this section the energy properties of the two-leg ladder system are discussed. The focus is laid on typical aspects which have the strongest influence on the one-triplon and the two-triplon spectral properties and on the relative positions of multi-triplon continua to each other.

### 7.5.1 Ground state energy

The action of  $H_{eff}$  on  $|0\rangle$  was calculated up to 14<sup>th</sup> order on a cluster of 15 rungs to find the ground state energy. The result is a 14<sup>th</sup> order polynomial in  $x$ . It is the exact energy of the infinite system to the given order. The coefficients are fractions of integers and therefore free from rounding errors. The series agree with the numerical results given by Zheng et al. [320].

The plain polynomial is depicted as dashed line in Fig. 7.8. The solid lines correspond to four differ-



ent dlog-Padé extrapolants (see Chapt. 5) of this quantity and constitute a reliable extrapolation. The truncated series result can be trusted up to  $x \approx 0.7$ .

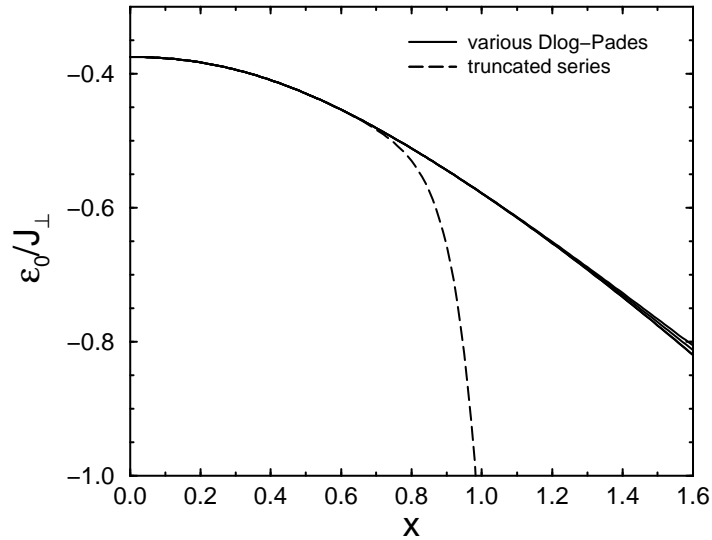


Fig. 7.8: Ground state energy per spin as function of  $x$ . The plain series result is depicted as dashed line. Four different Dlog-Padé approximants ( $[7,6]$ ,  $[8,5]$ ,  $[5,8]$  and  $[6,7]$ ) are shown as solid lines.

### 7.5.2 One-triplon dispersion

The effective Hamiltonian  $H^{\text{eff}}$  is calculated in the one-triplon channel up to order 14 in  $x := J_{\parallel}/J_{\perp}$ . Thereby the one-triplon dispersion  $\omega(k) = \langle k | H_{\text{eff}} | k \rangle - E_0$  is obtained. The one-triplon dispersion has a global minimum for  $k = \pi$ , the one-triplon gap  $\Delta(x)$ . In Fig. 7.9 the truncated series for  $\Delta(x)$  is shown as a dashed line. The truncated series for  $\Delta(x)$  and  $t_n(x)$  is reliable up to  $x \sim 0.6$ .

The solid and dotted lines in Fig. 7.9 depict biased dlogPadé extrapolants (see Sect. 5.2) for the one-triplon gap  $\Delta(x)/J_{\perp}$ . The bias used is that the one-triplon gap  $\Delta$  when measured in the rung coupling  $J_{\perp}$  have to approach a constant for  $x \rightarrow \infty$ . The latter follows from the fact that the one-triplon gap  $\Delta/J_{\parallel}$  scales as  $1/x$  if two Heisenberg chains are coupled by a small  $J_{\perp}$  [321, 345]. The extrapolation is very stable for the one-triplon gap. The one-triplon gap for the isotropic ladder ( $x = 1$ ) is  $\Delta/J_{\perp} \sim 0.504$ . Increasing the coupling to  $x > 1$  only leads to a small additional reduction of  $\Delta/J_{\perp}$ . A more detailed discussion of the one-triplon gap, especially of the asymptotics  $x \rightarrow \infty$ , will be given in the next chapter.

The one-triplon dispersion  $\omega(k)/J_{\perp}$  is shown in Fig. 7.10. The truncated series is valid up to  $x \approx 0.6$  similar to the case of the one-triplon gap. For larger values of  $x$  additional extrapolation is needed. The results depicted in Fig. 7.10 were obtained by using the method of internal parameters as explained in Sect. 5.4. The black curves are the truncated series in the internal parameter without

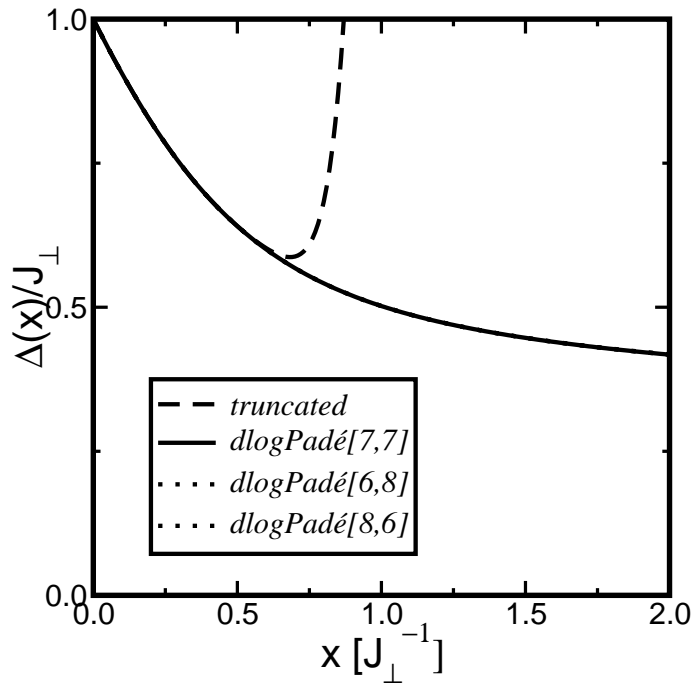


Fig. 7.9: One-triplon gap  $\Delta(x) = \omega(\pi)$  depending on the parameter  $x$ . The dashed line shows the one-triplon gap as obtained from the truncated series. The other three curves show the biased dlogPadé extrapolants [8,6], [7,7] and [6,8].

using any further extrapolation. The grey curves show results where an additional [11,2] dlogPadé extrapolation is used. The small differences between the black and the grey curve for the isotropic ( $x = 1$ ) case demonstrate that even the truncated series in the internal parameter gives quantitative results up to these values of  $x$ .

At  $x = 0$  the system is completely local resulting in a flat dispersion  $\omega(k)/J_{\perp} = 1$ . The dispersion is cosine-like for finite  $x \leq 0.6$ . For larger values of  $x$  the one-triplon dispersion shows a local minimum at  $k = 0$  shifting the global maximum away from  $k = 0$  to  $k = \pi/2$ . This development can be understood in two ways: in the limit of isolated chains and in the rung-triplon picture. The dispersion of an isolated Heisenberg chain is symmetric about  $k = \pi/2$  and it is gapless for  $k = 0$  and  $k = \pi$  (see Chapt. 6). The dip at  $k = 0$  of the one-triplon dispersion for the spin-ladder is therefore a precursor of the spin-chain physics. On the other hand, the dip can be understood as a consequence of the closeness of the three-triplon continuum. It will be shown in Subsect. 7.5.4 that the three-triplon continuum comes close to the one-triplon dispersion, especially at  $k = 0$ , pushing the one-triplon dispersion downward.

The latter also explains that difficulties in the extrapolation of the one-triplon dispersion arise mainly near  $k = 0$  while the extrapolation for larger values of  $k$  is safe even for very large values of  $x$ . The results shown in Fig. 7.10 are in quantitative agreement with other series expansion results [322], exact diagonalization [323] and DMRG results [324].

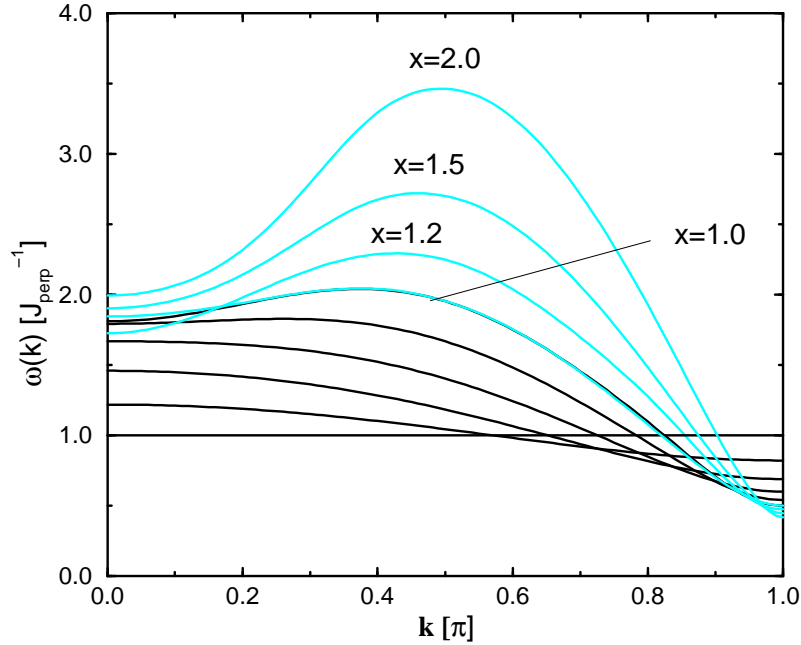


Fig. 7.10: One-triplon dispersion  $\omega(k)$  for different values of  $x \in \{0.0; 0.2; 0.4; 0.6; 0.8; 1.0; 1.2; 1.5; 2.0\}$ . The results were obtained by using the method of internal parameters as explained in Sect. 5.4. The black curves are the truncated series in the internal parameter without any further extrapolation. The grey curves show results where an additional [11,2] dlogPadé extrapolation is used. For the case of the isotropic ladder  $x = 1$  extrapolants for both extrapolation schemes are plotted showing that even the plain series gives quantitative results for these values of  $x$ .

### 7.5.3 Two-triplon continuum and bound states

In this section the two-triplon energy properties are described. As illustrated for the one-triplon dispersion one should distinguish between  $x \leq 0.6$  where the physics of the spin-ladder is dominated purely by rung physics and  $x > 0.6$  where the crossover from ladder to chain physics begins. In the following results for  $x = 0.5$  and  $x = 1.0$  are shown illustrating these two cases.

In analogy to the spin-chain case discussed in Chapt. 6, two triplons form a two-triplon continuum. Additionally, two-triplon bound or antibound states are formed depending on the total spin of the two triplons [177, 179, 181, 197, 198, 251, 298, 325]. In Fig. 7.11 the two-triplon continuum and the two-triplon bound states are depicted for a)  $x = 0.5$  and b)  $x = 1.0$ . Note that the total spin  $S = 2$  case where an antibound exists [177] is not discussed here.

The structures at  $x = 0.5$  are quite featureless due to the cosine-form of the one-triplon dispersion (see Fig. 7.11a). The continuum has the largest width at  $k = 0$  and becomes monotonically smaller for finite momentum reaching a very small width for  $k = \pi$ . At about  $k = 0.4\pi$ , a  $S = 1$  and a  $S = 0$  two-triplon bound state emerge from the continuum. The binding energy of the  $S = 1$

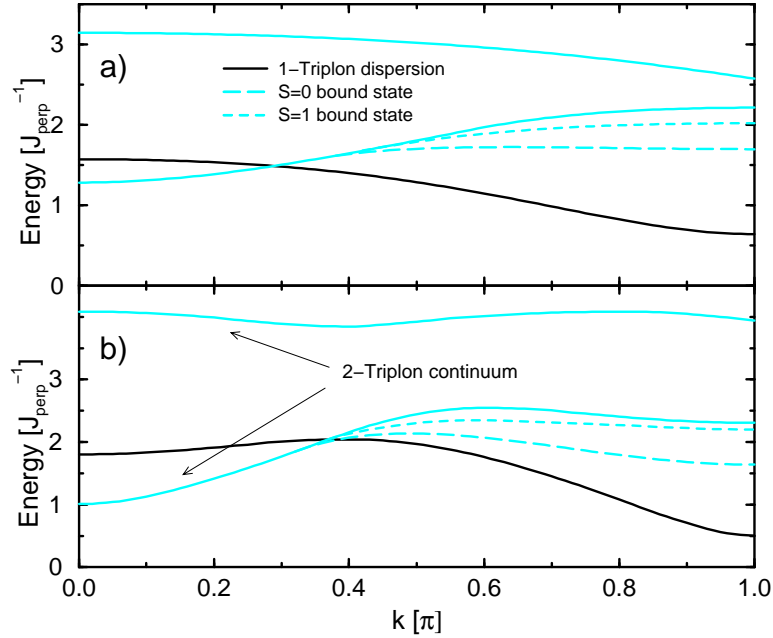


Fig. 7.11: One-triplon and two-triplon energies of the two-leg ladder for  $x = 0.5$  (a) and  $x = 1$  (b). The thick solid black line denotes the one-triplon dispersion  $\omega(k)$ . The grey solid lines correspond to the lower and the upper edge of the two-triplon continuum. The dashed grey lines denote the  $S = 1$  two-triplon bound states and the long dashed grey lines correspond to the  $S = 0$  two-triplon bound states.

bound state is smaller than the  $S = 0$  bound state. The dispersion of the  $S = 1$  bound state is monotonic approaching  $k = \pi$  while the dispersion of the  $S = 0$  bound state is almost flat showing a maximum at about  $k \approx 0.6\pi$  and a minimum at  $k = \pi$ .

The situation at  $x = 1$  shows more pronounced features (see Fig. 7.11b). The form of the two-triplon continuum has changed due to the local minimum of the one-triplon dispersion at  $k = 0$ . The minimum width of the continuum has shifted from  $k = \pi$  at  $x = 0.5$  to  $k \approx \pi/2$ . This results in a change of the dispersion of the two-triplon bound states. Both bound states show a maximum at  $k \approx \pi/2$  and a minimum at  $k = \pi$ . The binding energy of the  $S = 1$  bound state is small for almost all  $k$ -values while the  $S = 0$  bound state lies well below the two-triplon continuum and has a fairly large dispersion.

#### 7.5.4 Multi-triplon continua

This part presents information about the relative position of multi-triplon continua (three- and four-triplon) to one- and two-triplon energies depending on the parameter  $x$ . This information is extremely important for the interpretation of the results which will be shown in following sections. In the spin-ladder, only channels with both odd or both even number of triplons are connected

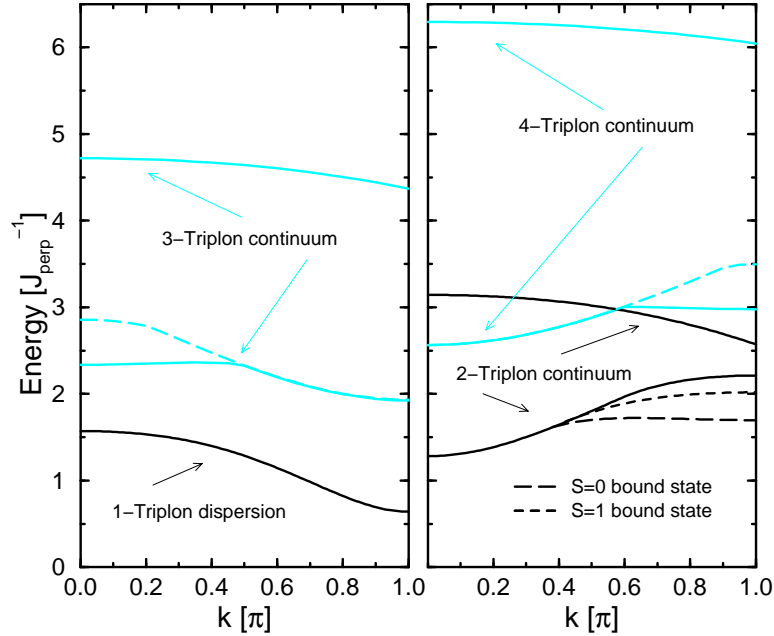


Fig. 7.12: Multi-triplon continua of the two-leg ladder for  $x = 0.5$  are shown. One- and three-triplon energies are shown in the left panel while two- and four-triplon energies are depicted in the right panel. Left panel: the solid black line denotes the one-triplon dispersion  $\omega(k)$ . The grey solid lines correspond to the lower and the upper edge of the three-triplon continuum including binding effects. The dashed grey lines denote the lower band edge of the three-triplon continuum neglecting binding effects. Right panel: the solid black lines correspond to the lower and the upper edge of the two-triplon continuum. The dashed black line corresponds to the two-triplon bound states. The solid grey lines denote the lower and the upper band edge of the four-triplon continuum. The dashed grey line depicts the lower band edge of the four-triplon continuum neglecting binding effects.

directly, i.e. the one- and three-triplon channel or the two- and four-triplon channel. It is clear that for small values of  $x$  all triplon channels are energetically separated; the energy difference is of order  $J_{\perp}$ . It will turn out that this changes gradually upon increasing  $x$ . Note that a wrong order of triplon channels, meaning the energy of more triplons is smaller than the energy of less triplons, results in a breakdown of the particle conserving continuous unitary transformation as described in this thesis [326]. Nevertheless it is even in these situations possible to find extrapolations of the well defined perturbative series. The extrapolations neglect possible life-time effects due to the decay in channels with higher triplon number. Such life-time effects are small as long as the overlap between the continua is small because the spectral densities for three and four triplons are strongly suppressed at the band edges [327].

In Fig. 7.12 and Fig. 7.13 multi-triplon continua of the spin-ladder are depicted. In Fig. 7.12 results for  $x = 0.5$  are shown while Fig. 7.13 presents the same data for the isotropic case  $x = 1$ .

As discussed above, only channels with odd or even number of triplons are connected directly. It was shown in Sect. 7.4 that only channels up to four triplons contain a sizable spectral weight. Therefore it is important to study the relative position of the one-triplon dispersion and the three-triplon continuum (left panels in Fig. 7.12 and in Fig. 7.13) and the relative position of the two- and four-triplon continua (right panels in Fig. 7.12 and in Fig. 7.13).

It can be seen that the one-triplon dispersion is located below the three-triplon continuum for  $x = 0.5$  and  $x = 1.0$ . It is important to note that one has to include binding effects to calculate the lower band edge of the three-triplon continuum. One has to distinguish between the energy of three independent triplons and the energy of two triplons forming a two-triplon bound state plus the energy of one triplon. The grey dashed line in the left panels corresponds to the lower band edge of three triplons neglecting the triplon-triplon interaction. The solid grey line in the left panels takes binding effects into account. This means that one can lower the total energy of three triplons near  $k \approx 0$  by binding two triplons to one two-triplon bound state and combining this particle with the one which is left over. Note that in principal multi-triplon interactions can result in multi-triplon bound states which would change the picture. But it has been investigated that the three-triplon interaction is weak for all parameters considered in this work [327]. It can be expected that interaction with more than three triplons involved are even less important.

The minimal energy difference between both triplon channels is at  $k = 0$ . The lowest energy of the three-triplon continuum is the sum of the  $S = 0$  two-triplon bound state at  $k = \pi$  and the one-triplon gap  $\Delta$ . This difference is lowered by increasing  $x$  due to the enhancement of triplon-triplon interactions for growing  $x$ . The dip for  $x \geq 0.6$  of the one-triplon dispersion at  $k = 0$  can therefore be understood as a consequence of the closeness of the three-triplon continuum pushing the one-triplon energy downward<sup>1</sup>.

The relative position of the two- and four-triplon continua is a more subtle issue. The solid black lines denote the lower and upper band edge of the two-triplon continuum and the solid grey lines depict the lower and upper band edge of the four-triplon continuum. Here again the effect of binding is included in the calculation (combination of two two-triplon bound states to a four-triplon state). The dashed grey lines denote the lower band edge of the four-triplon continuum neglecting triplon-triplon interactions.

It can be seen that the four-triplon continuum lies (at least partially for  $x = 0.5$ ) below the upper edge of the two-triplon continuum, i.e. these two contribution intersect each other. A strict separation of energies due to the continuous unitary transformation is therefore not possible [326]. Nevertheless it is possible to extrapolate the well defined plain series in this regime. The spectral weight near the lower band edge of the four-triplon continuum increases slowly like  $I_4(\omega) \propto \omega^{13/2}$  [327]. Therefore the error is expected to be very small. But at higher energies life-time effects may give rise to more important deviations<sup>2</sup>.

---

<sup>1</sup>The generator of the particle conserving continuous unitary transformation represents the states in increasing order of  $Q$ . [141, 143].

<sup>2</sup>The intersection of the two- and four-triplon continuum is larger in the  $S = 0$  case than in the  $S = 1$  case due to the larger binding energy of the  $S = 0$  two-triplon bound state. Therefore life-time effects are expected to be smaller in the  $S = 1$  case.

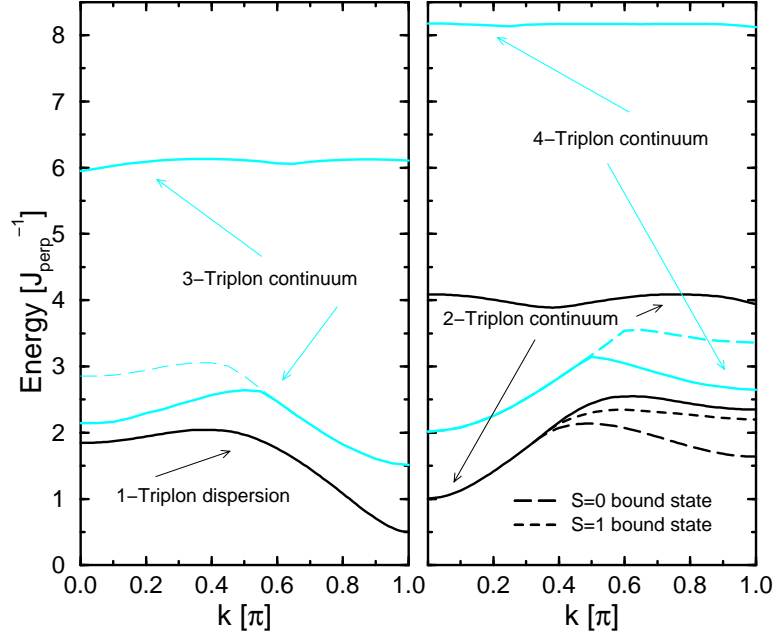


Fig. 7.13: Multi-triplon continua of the two-leg ladder for  $x = 1$ . One- and three-triplon energies are shown in the left panel while two- and four-triplon energies are depicted in the right panel. The notation is the same as in Fig. 7.12.

## 7.6 $S = 1$ excitations

This part shows results for the dynamical structure factor of the spin-ladder. In the following results are shown for the one-triplon and the two-triplon contribution to the spectral density analogue to the case of the dimerized and frustrated spin-chain (see Sect. 6.4). These two contributions are the most relevant ones for the exchange couplings considered (see Sect. 7.4).

### 7.6.1 One-triplon contribution

The action of the full observable  $\mathcal{O}^{\text{III}}|_{1\text{trp}}$  is decomposed in the one-triplon channel on the ground state for fixed one-triplon momentum  $k$  by writing

$$\mathcal{O}^{\text{III}}|_{1\text{trp}}|0\rangle = A_{1\text{trp}}^{\text{III}}(k)|k\rangle, \quad (7.6.1)$$

where the amplitudes  $A_{1\text{trp}}^{\text{III}}$  are given by

$$A_{1\text{trp}}^{\text{III}} = a_0^1 + 2 \sum_{l>0} a_l^1 \cos(kl) \quad . \quad (7.6.2)$$

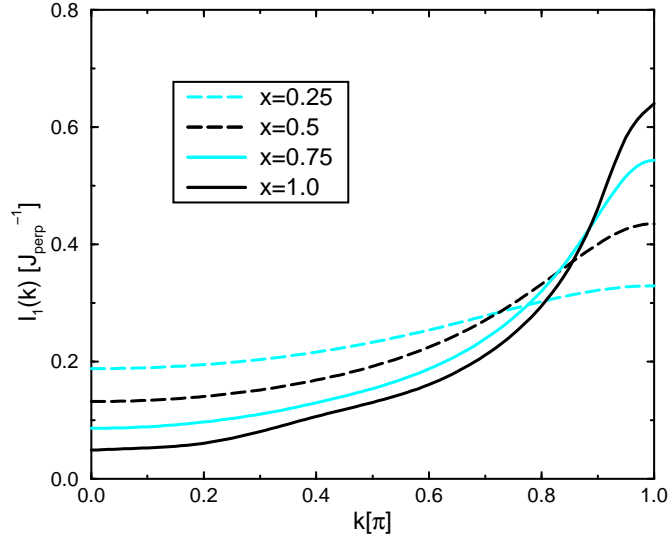


Fig. 7.14: One-triplon spectral density  $I_1(k)$  for  $\mathcal{O}^{\text{III}}$ . Dashed grey line corresponds to  $x = 0.25$ , dashed black depicts  $x = 0.5$ , solid grey line represents  $x = 0.75$  and solid black line denotes  $x = 1.0$ .

The sum runs over all rungs  $l \geq 0$ . The amplitudes  $a_l^1$  correspond to the operator  $S_{1,r}^z$ . The amplitudes  $a_l^2$  of  $\mathbf{S}_{2,r}^z$  do not need to be calculated separately because it can be determined by using the inversion symmetry of the ladder plus the symmetry concerning the reflection about the centerline of the ladder. One obtains  $a_l^2 = -a_l^1$  and  $a_{-l}^1 = a_l^1$  so that only amplitudes  $a_l^1$  with non-negative  $l$  have to be determined.

The one-triplon contribution to the dynamical structure factor is dominant for the couplings considered here for all momenta. The  $k$ -resolved spectral weight  $I_1(k)$  is shown in Fig. 7.14 for  $x = 0.25$ ,  $x = 0.5$ ,  $x = 0.75$  and  $x = 1$ . The result for  $x = 1$  is in agreement with exact diagonalization data [328].

At  $x = 0$ , the total spectral weight is in the one-triplon channel. Therefore the  $k$ -resolved spectral weight for  $x = 0$  is  $I_1(k) = 1/4$ . Turning on  $x$ , the one-triplon spectral weight decreases for small momenta while it increases for momenta near  $k = \pi$ . In the next subsection it will be shown that the two-triplon contribution of the dynamical structure factor vanishes at  $k = 0$ . Therefore the spectral weight of the one-triplon channel near this momentum is shifted mostly to the three-triplon channel. It can be concluded from Fig. 7.14 that the spectral weight in the one-triplon channel is concentrated about  $k = \pi$  for increasing  $x$ . This agrees with findings from bosonization where the case of weakly interacting chains is studied. One finds a  $\delta$ -peak in the dynamical structure factor in the surrounding of the momentum  $k = \pi$  corresponding to the excitation of one triplon [321].



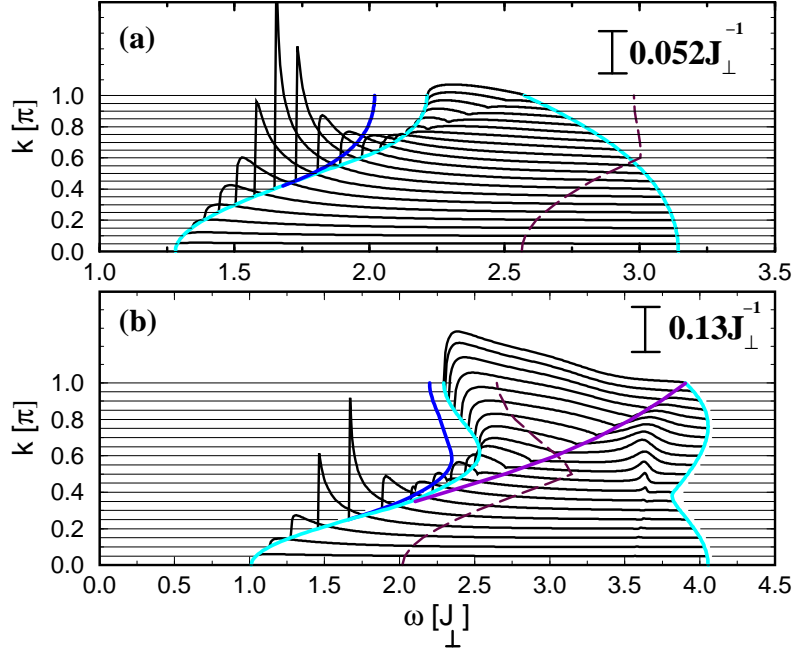


Fig. 7.15: Two-triplon spectral density  $I_2(k, \omega)$  for  $\mathcal{O}^{\text{IV}}$ : (a)  $x = 0.5$  and (b)  $x = 1.0$ . The grey solid lines mark the lower and the upper edge of the two-triplon continuum. The black solid lines denote the two-triplon bound states. The dark grey dashed line denotes the lower band edge of the four-triplon continuum. In (b) an additional dark grey solid line is included which is a guide to the eye linking the midband square-root singularities.

## 7.6.2 Two-triplon contribution

The two-triplon contribution to the dynamical structure factor represents the only sizable contribution besides the one-triplon part discussed in the last subsection (see Sect. 7.4). Nevertheless its overall spectral weight is quite small ( $I_{2,\text{rel}} < 0.3$  for  $x < 1.5$ ). Fortunately the two-triplon contribution is protected by its parity. As discussed in Sect. 7.3, all contributions can be classified concerning the parity  $\mathcal{P}$  denoting the operator of reflection about the center-line of the ladder as depicted in Fig. 7.5. Channels excited by  $\mathcal{O}^{\text{III}}$  have odd parity and channels excited by  $\mathcal{O}^{\text{IV}}$  have even parity as is seen from Eq. 7.3.6. The two-triplon contribution is therefore the dominant contribution with even symmetry and so of possible experimental relevance inspite of its overall spectral weight is small.

One decomposes the action of the full observable  $\mathcal{O}^{\text{IV}}|_{2\text{trp}}$  in the two-triplon channel on the ground state for fixed two-triplon momentum  $k$

$$\mathcal{O}^{\text{IV}}|_{2\text{trp}}|0\rangle = \sum_d A_{2\text{trp}}^{S=1}(k, d)|k, d\rangle. \quad (7.6.3)$$

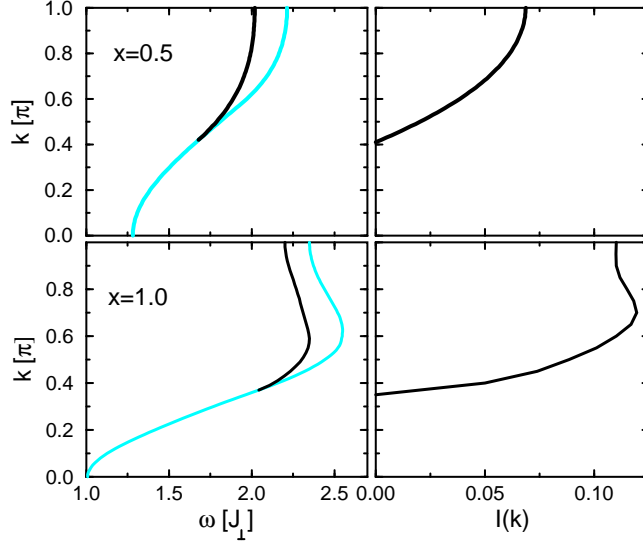


Fig. 7.16: The two-triplon  $S = 1$  bound state energy and the spectral weight for  $x = 0.5$  (upper panels) and for  $x = 1.0$  is shown (lower panels). Left panels: The solid grey line denotes the lower edge of the two-triplon continuum and the solid black line depicts the dispersion of the  $S = 1$  two-triplon bound state. Right panels: The  $k$ -resolved spectral weight of the  $S = 1$  two-triplon bound state is depicted.

Here  $d$  denotes the relative distance between the two triplons and

$$A_{2\text{trp}}^{\text{IV}}(k, d) = \sum_l a_{l, l+d}^1 \sin\left(k\left(l + \frac{d}{2}\right)\right). \quad (7.6.4)$$

The sum runs over all rungs  $l$  and  $a_{l, l+d}^1$  is the amplitude for the creation of two triplons on rungs  $l$  and  $l + d$  by  $S_1^z$ .

Here in analogy to the case of the dimerized and frustrated chain it is convenient to use a mixed representation in which the center-of-mass coordinate is Fourier transformed and the relative coordinate is dealt with in real space. The action of  $S_2^z$  does not need to be calculated. In analogy to the one-triplon case the relations  $a_{l, l+d}^2 = a_{l, l+d}^1$  and  $a_{l, l+d}^1 = -a_{-l-d, -l}^1$  hold. These two relations follow from inversion symmetry and the reflexion about the centerline of the two-leg ladder.

In Fig. 7.15 and Fig. 7.16 the results for the two-triplon contribution to the dynamical structure factor are shown for  $x = 0.5$  and  $x = 1.0$ . First the two-triplon continuum is described. The lower and upper band edge of the two-triplon continuum is indicated in Fig. 7.15 as solid grey lines. The spectral density shows square root behavior  $\sim \sqrt{\omega}$  near the band edge reflecting again the hard-core property of the triplons. The spectral weight is distributed mainly close to the lower band edge of the continuum for  $x = 0.5$  and  $x = 1.0$ . So the distribution of spectral weight shows already properties of the chains which was discussed in the last chapter. The latter point is strengthened by the observation that a mid-band singularity occurs in both spectral densities which can be interpreted as a precursor of the upper band edge of the two-spinon continuum for

the isolated spin-chain. In Fig. 7.15b the dark grey line is a guide to the eye linking the midband square-root singularities [179].

The dark dashed grey line in Fig. 7.15 signals the lower band-edge of the four-triplon continuum. As discussed in Subsect. 7.5.4, the two-triplon and four-triplon continua intersect each other so that life-time effects change the obtained extrapolated results. It is expected that these effects are small in the  $S = 1$  sector because the spectral weight is very small in the four-triplon sector (at least up to  $x \approx 1$ ). Nevertheless some effects can be expected for large momenta for the isotropic case.

The dispersion of the  $S = 1$  two-triplon bound state is depicted as a solid black line in Fig. 7.15 and in the left panels of Fig. 7.16. The spectral weight of the two-triplon bound state is depicted in the right panels of Fig. 7.16. The emergence of the bound state from the continuum can also be nicely seen in the singular behavior of the spectral density at the lower band edge. The spectral weight of the bound state is largest for the largest binding energy. Therefore the maximum of the spectral weight is shifted from  $k = \pi$  at  $x = 0.5$  to  $k \approx 0.7\pi$  for  $x = 1$ .

## 7.7 $S = 0$ excitations

In this section the two-triplon contribution of the observables  $\mathcal{O}^I$  and  $\mathcal{O}^{II}$  is discussed. The two-triplon contribution is the leading and the most important contribution to the spectral density with total spin zero in the coupling regime under study. The  $S = 0$  case is relevant for optical experiments like Raman spectroscopy and infrared absorption. This will be discussed in more detail in the next chapter.

The action of the full observable  $\mathcal{O}^I|_{2\text{trp}}$  and  $\mathcal{O}^{II}|_{2\text{trp}}$  in the two-triplon channel on the ground state is decomposed for fixed two-triplon momentum  $k$

$$\mathcal{O}^{I/II}|_{2\text{trp}}|0\rangle = \sum_d A_{2\text{trp}}^{I/II}(k, d)|k, d\rangle. \quad (7.7.1)$$

Here  $d$  denotes again the relative distance between the two triplons and

$$A_{2\text{trp}}^{I/II}(k, d) = \sum_l a_{l, l+d}^{I/II} \sin\left(k\left(l + \frac{d}{2}\right)\right). \quad (7.7.2)$$

The sum runs over all rungs  $l$  for  $\mathcal{O}^I$  and over all bonds on the leg for  $\mathcal{O}^{II}$ . The amplitudes  $a_{l, l+d}^{I/II}$  denote the creation of two triplons on rungs  $l$  and  $l + d$ .

In Fig. 7.17 and Fig. 7.18 the results for the two-triplon continuum are shown for  $x = 0.5$  and  $x = 1$ . The dispersion and the spectral weight of the  $S = 0$  two-triplon bound state is depicted for both values of  $x$  in Fig. 7.19. Spectral densities for  $x \in \{0.2, 0.4, 0.6, 0.8\}$  can be found in Ref. [189].

The energy situation in the  $S = 0$  case is very similar to the  $S = 1$  case. The support of the continuum is the same and there is also one  $S = 0$  two-triplon bound state. The binding energy of the bound state is larger compared to the case  $S = 1$ . But the spectral properties are different in some respects.

The main difference occurs for small momenta where the two-triplon contribution in the  $S = 1$  case

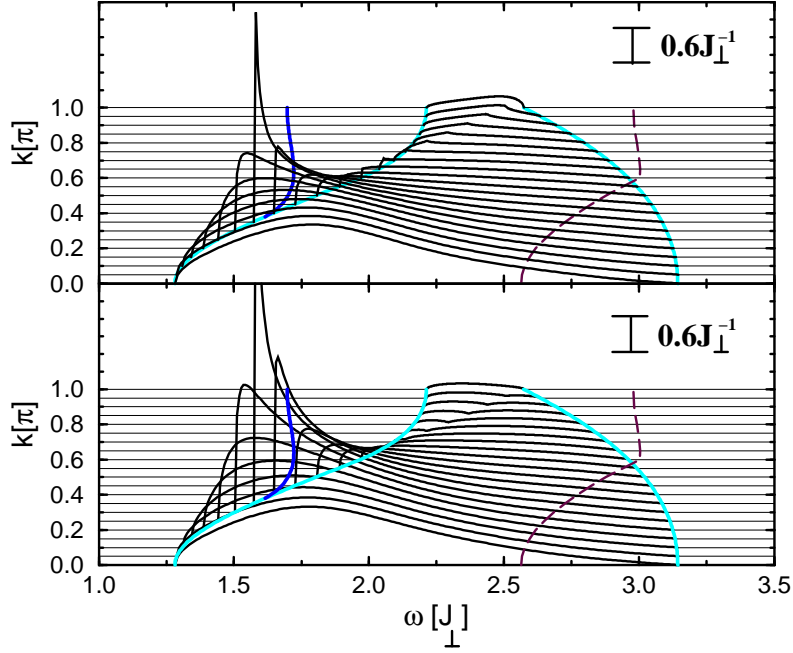


Fig. 7.17: Two-triplon spectral density  $I_2(k, \omega)$  for total spin zero at  $x = 0.5$ . The upper panel shows results for observable  $\mathcal{O}^I$  and the lower panel depicts results for  $\mathcal{O}^{II}$ . The grey solid lines represent the lower and the upper band edge of the two-triplon continuum. The black solid line denotes the  $S = 0$  two-triplon bound state. The dashed dark grey line marks the position of the lower band edge of the four-triplon continuum.

is reduced by symmetry while a large continuum exists in the  $S = 0$  channel. The  $k = 0$  two-triplon spectral density represents the leading contribution to the Raman response in spin-ladders [180]. The Raman line-shape is the same for  $\mathcal{O}^I$  and  $\mathcal{O}^{II}$  [180]. This can clearly be seen in Fig. 7.17 and Fig. 7.18. It follows that the three-triplon contribution of  $\mathcal{O}^{II}$  has to vanish for  $k = 0$ . The Raman operator has an even parity [295] so that it does only couple to spin observables with even parity. Therefore the Raman response comprises only of channels with an even number of triplons.

The line shape at  $k = 0$  is dominated by the two-triplon peak which becomes sharper upon increasing  $x$ . In addition, a characteristic zero emerges for  $x \geq 0.6$  inside the continuum producing a second peak at higher energies clearly visible at  $x = 1$  (see Fig. 7.18) [180, 188]. The dashed dark grey line in Fig. 7.17 and Fig. 7.18 denotes the lower band edge of the four-triplon continuum. It can be expected that the characteristic zero inside the band and the second peak at higher energies are modified by life-time effects [326]. The implications for the experimental Raman line-shape will be discussed in more detail in the next chapter.

The two observables  $\mathcal{O}^I$  and  $\mathcal{O}^{II}$  show different spectral properties for finite momentum, especially for large momenta near  $k = \pi$ . The spectral density of  $\mathcal{O}^I$  at  $k = \pi$  displays an almost anti-bound

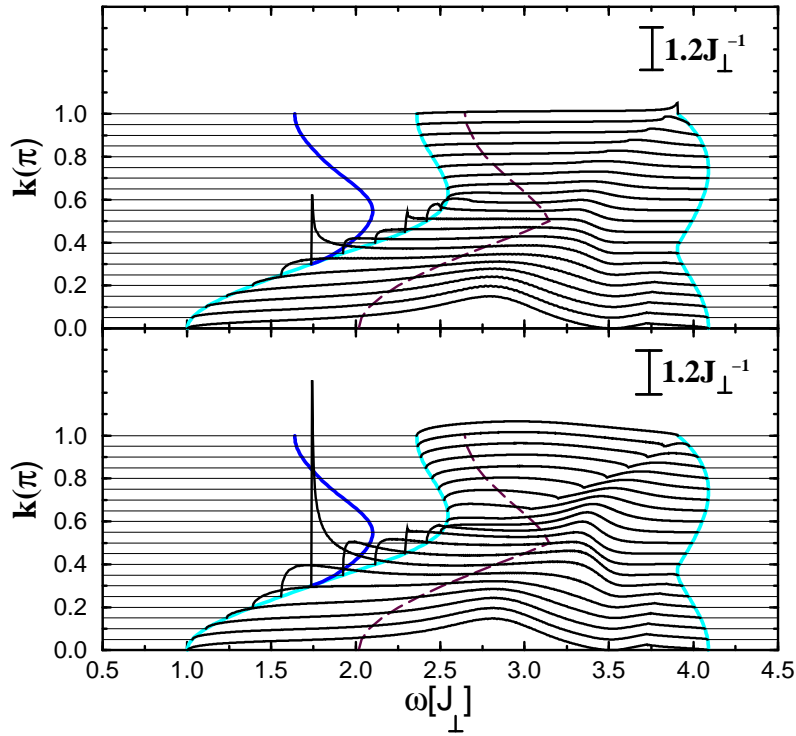


Fig. 7.18: Two-triplon spectral density  $I_2(k, \omega)$  for total spin zero at  $x = 1.0$ . Results for observable  $\mathcal{O}^I$  is shown in the upper panel and results for  $\mathcal{O}^{II}$  are depicted in the lower panel. The grey solid line represents the lower and the upper band edge of the two-triplon continuum. The black solid line denotes the  $S = 0$  two-triplon bound state. The dashed dark grey line marks the position of the lower band edge of the four-triplon continuum.

state while the observable  $\mathcal{O}^{II}$  shows a broad hump centered in the middle of the band. The mid-band square-root singularities present in the  $S = 1$  case are also present for  $\mathcal{O}^{II}$  and for  $\mathcal{O}^I$ . Both observables show sharp structures inside the continuum near  $k = \pi/2$  at high energies. It can be expected that these structures are broadened due to life-time effects.

The distribution of spectral weight for the  $S = 0$  two-triplon bound state is different for both observables as can be nicely seen in the right panels of Fig. 7.19. The spectral weight of the bound state at  $k = \pi$  vanishes for  $\mathcal{O}^I$  while it is maximal for  $\mathcal{O}^{II}$ . This fact and the two extrema of the dispersion of the two-triplon bound state at  $k = \pi/2$  and  $k = \pi$  are crucial for the experimental determination of the  $S = 0$  two-triplon bound state in cuprate ladder systems by infrared absorption [298]. The infrared absorption will be discussed in more detail in the next chapter. Note that the intersection of the two-triplon continuum and the four-triplon continuum is not important for the two-triplon bound state.

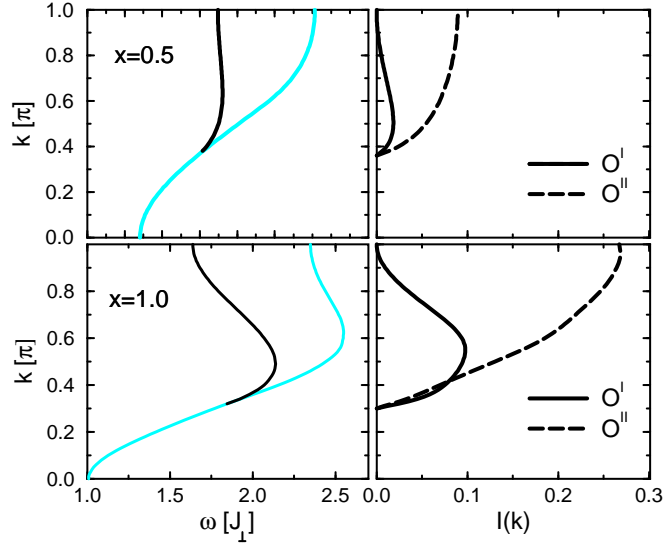


Fig. 7.19: Two-triplon  $S = 0$  bound state energy and spectral weight for  $x = 0.5$  (upper panel) and  $x = 1.0$  (lower panel). Left panels: The solid grey line denotes the lower edge of the two-triplon continuum and the solid black line depicts the dispersion of the  $S = 0$  two-triplon bound state. Right panels: The  $k$ -resolved spectral weight of the  $S = 0$  two-triplon bound state is shown as measured by  $\mathcal{O}^I$  (solid line) and by  $\mathcal{O}^{II}$  (dashed line).

## 7.8 Chapter summary

This chapter deals with the energy and the spectral properties of the two-leg Heisenberg spin-ladder. The perturbative continuous unitary transformation is implemented about the limit of vanishing leg coupling. Therefore the basic quasi-particle is the rung-triplon.

It is shown that the leading channels, namely one- and two-triplon, contain most of the spectral weight up to  $x \approx 1.5$ . Nevertheless three- and four-triplon channels contribute a sizable part to the total spectral weight in comparison to the case of the dimerized and frustrated spin-chain discussed in the last chapter. Hence the rung-triplon quasi-particle picture is less effective for  $J_{||} > J_{\perp}$  but still works and a leg-triplon picture might be more useful there.

Energy properties like the one-triplon dispersion, the bandedges of the two-triplon continuum and the dispersion of the two-triplon bound states but also the position of the three- and four-triplon continua are presented. The one-triplon dispersion changes from a cosine-like form at small coupling to a shape including a characteristic dip feature at  $k = 0$  for larger coupling signaling the crossover to spin-chain physics. There are two two-triplon bound states, one with total  $S = 1$  and one with  $S = 0$ . It has been shown that the one-triplon dispersion lies below the three-triplon continuum while two- and four-triplon continua intersect already at small ratios of the exchange couplings. As a consequence the results for the two-triplon properties in this regime neglect possible life-time effects, namely the decay of two triplons into four triplons.

One- and two-triplon spectral densities for total spin one and total spin zero are presented. The dynamical structure factor is dominated by the leading one-triplon channel. The maximum of its spectral weight is at  $k = \pi$ , where the one-triplon gap is located. It is shown that the subleading two-triplon contribution is the leading contribution with even parity concerning the reflection about the centerline of the ladder. Therefore it is protected due to its parity meaning that it is possibly relevant for experiments in spite of its overall small spectral weight. Spectral densities with total spin zero can be realized either by coupling to the rungs or to the legs of the ladder. It is shown that the spectral properties are identical for zero momentum and therefore similar at small momenta. But both observables differ essentially at large momenta, both in the line shape of the two-triplon continuum and in the spectral weight distribution of the two-triplon bound state.

## 8 The antiferromagnetic two-leg ladder with four-spin interactions

In this chapter the antiferromagnetic two-leg ladder with additional four-spin interaction is discussed. It has become clear in the last years that the minimal magnetic model of cuprate systems (ladders and planes) has to include four-spin interactions in order to obtain a quantitative description of the materials.

The size of the four-spin exchange in cuprate ladders is shown to be about 10% of the leading nearest-neighbour Heisenberg exchange. It is demonstrated that the cuprate ladders remain in the so-called rung-singlet phase. The major part of this chapter deals therefore with the spectral properties of the rung-singlet phase.

The structure of the chapter is analogous to the previous one. The concentration is laid on the effect of the four-spin interactions on the spectral weights, the energy properties like the dispersion of the two-triplon bound states and the band edges of the multi-triplon continua as well as the spectral densities for total spin one and total spin zero. The last part of this chapter is concerned with the description of magnetic properties of ladder systems as realized in the cuprates.

### 8.1 Model

Usually only Heisenberg-like exchanges are considered in the description of magnetic properties of many-body systems. It has been realized early by Dirac [329] and later was introduced in condensed matter physics by Thouless [330] that the general expression for the exchange Hamiltonian reads

$$H_{\text{ex}} = \sum_{n=2}^{\infty} \sum_{\alpha_n} J_{\alpha_n} (-1)^{P_{\alpha_n}} P_{\alpha_n} \quad , \quad (8.1.1)$$

where  $P_{\alpha_n}$  denotes a spin permutation operator and the sum runs over all permutations  $\alpha_n$  of  $n$  spins.  $P_{\alpha_n}$  represents the parity of the permutation  $\alpha_n$ . Physically all these contributions correspond to the exchange of  $n$  spins. The first term represents the usual two-particle exchange which is usually the dominant contribution.

The importance of the exchanges with more than two particles was realized first in the description of the magnetism of solid  $^3\text{He}$  [331]. Here the two-particle exchange is small and higher exchange processes, especially the four-spin exchange, are even the dominant exchange processes.

The situation in cuprate systems is different compared to solid  $^3\text{He}$ . Here the dominant exchange is the nearest-neighbor Heisenberg exchange. Nevertheless, it has turned out by the derivation of effective low-energy Heisenberg models from realistic three-band [61, 332–334] and one-band [63, 64, 326] Hubbard models that the four-spin ring exchange is the dominant correction to the usual



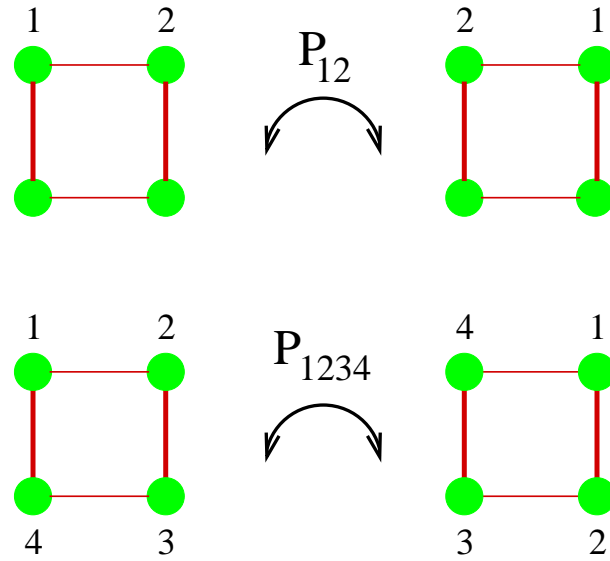


Fig. 8.1: Illustration of the two-particle and the four-particle permutation operators  $P_{i,j}$  and  $P_{i,j,k,l}$

nearest-neighbour Heisenberg exchange. The value of the four-spin ring exchange obtained from these studies is about 10% of the dominant Heisenberg exchange<sup>1</sup>.

The first clear experimental signature of the relevance of four-spin ring exchange in cuprate planes was found by inelastic neutron scattering of  $\text{LaCu}_2\text{O}_4$  in 2001 [57]. It was found that the spin-wave dispersion can only be explained by the inclusion of four-spin interactions [57, 67, 68, 74].

The first hint of four-spin interactions in cuprate ladders was found in 1999 by inelastic neutron scattering [335–337]. The fitting of the experimentally measured one-triplon dispersion with the standard Heisenberg model results in  $J_{\parallel}/J_{\perp} \approx 2$  which seems unphysical considering the geometrical structure of the cuprate ladders suggesting  $J_{\parallel} \approx J_{\perp}$ . The inclusion of four-spin interactions can resolve this discrepancy. The ratio  $J_{\parallel}/J_{\perp} \approx 2$  was later shown to be inconsistent with infrared absorption [298] and Raman spectroscopy [180] which both favored an isotropic exchange  $J_{\parallel} \approx J_{\perp}$ . The first quantitative determination of the exchange constants in cuprate ladders was possible by a DMRG calculation analyzing infrared absorption data [324] which results in  $J_{\parallel}/J_{\perp} \approx 1.2 - 1.3$  and additional four-spin interaction  $J_{\text{cyc}}/J_{\perp} \approx 0.1 - 0.125$ . These parameters were further confirmed by the description of Raman data of cuprate ladders [317, 338].

The Hamiltonian of the two-leg ladder with additional four-spin ring exchange term reads

$$H^{\text{P}} = J_{\perp}^{\text{P}} \sum_i P_{i,1} P_{i,2} + J_{\parallel}^{\text{P}} \sum_{i,\tau} P_{i,\tau} P_{i+1,\tau} + H_{\text{cyc}}^{\text{P}} \quad (8.1.2)$$

$$H_{\text{cyc}}^{\text{P}} = \frac{J_{\text{cyc}}^{\text{P}}}{2} \sum_{\langle ijkl \rangle} (P_{ijkl} + P_{ijkl}^{-1}) .$$

Here  $P_{i,j}$  is the permutation operator of two-particles,  $i$  the rungs and  $\tau \in \{1, 2\}$  the legs. The

<sup>1</sup>Note that the absolute value of the four-spin interaction depends on the way this term is written in the Hamiltonian. In the literature the value 20% is also often used which corresponds to the value discussed in this thesis.

permutation operator of four particles is  $P_{ijkl}$  (see Fig. 8.1) where  $\langle ijkl \rangle$  restricts the sum to permutations of four spins on a plaquette. It is convenient to introduce spin-operators and rewrite (8.1.2) as a Heisenberg model plus additional four-spin interactions

$$H = J_{\perp} \sum_i \mathbf{S}_{i,1} \mathbf{S}_{i,2} + J_{\parallel} \sum_{i,\tau} \mathbf{S}_{i,\tau} \mathbf{S}_{i+1,\tau} + H_{\text{cyc}} \quad (8.1.3)$$

where  $i$  denotes again the rungs and  $\tau \in \{1, 2\}$  the legs, and

$$H_{\text{cyc}} = 2J_{\text{cyc}} \sum_{\text{plaquettes}} [(\mathbf{S}_{1,i} \mathbf{S}_{1,i+1})(\mathbf{S}_{2,i} \mathbf{S}_{2,i+1}) + (\mathbf{S}_{1,i} \mathbf{S}_{2,i})(\mathbf{S}_{1,i+1} \mathbf{S}_{2,i+1}) - (\mathbf{S}_{1,i} \mathbf{S}_{2,i+1})(\mathbf{S}_{1,i+1} \mathbf{S}_{2,i})] \quad (8.1.4)$$

Both Hamiltonians (Eq. 8.1.2 and Eq. 8.1.3) are the same up to two-spin interactions along the diagonal of the spin-ladder. It is known that these couplings are small (of the order  $0.03J_{\perp}$ ) [333] so that the discussion in the following is restricted to the Hamiltonian in Eq. 8.1.3. Note that both expressions are in use in the literature. The relation between the exchange parameters of both Hamiltonians reads

$$J_{\perp} = J_{\perp}^{\text{p}} + J_{\text{cyc}}^{\text{p}} \quad (8.1.5)$$

$$J_{\parallel} = J_{\parallel}^{\text{p}} + \frac{1}{2} J_{\text{cyc}}^{\text{p}} \quad (8.1.6)$$

$$J_{\text{cyc}} = J_{\text{cyc}}^{\text{p}} \quad (8.1.7)$$

## 8.2 Method

In this part, the specific points of the method are discussed. In analogy to the previous chapter, the starting point of isolated rungs is used to set up the perturbative continuous unitary transformation. The ladder Hamiltonian plus additional four-spin interaction (Eq. 8.1.3) is reformulated according to

$$\frac{H(x)}{J_{\perp}} = H_{\perp} + xH_{\parallel} + x_{\text{cyc}}H_{\text{cyc}}, \quad (8.2.1)$$

with  $x = J_{\parallel}/J_{\perp}$  and  $x_{\text{cyc}} = J_{\text{cyc}}/J_{\perp}$  as perturbation parameters.

In the following the action of the additional term  $H_{\text{cyc}}$  on the triplon states is described.  $H_{\text{cyc}}$  can be decomposed in

$$H_{\text{cyc}} = T_{-2}^{\text{cyc}} + T_0^{\text{cyc}} + T_2^{\text{cyc}}, \quad \text{with} \quad (8.2.2)$$

$$T_i^{\text{cyc}}|n\rangle \sim |n+i\rangle \quad \text{and}$$

$$T_{0,\pm 2}^{\text{cyc}} = \sum_{\nu} \mathcal{T}_{0,\pm 2}^{\text{cyc}}(\nu), \quad (8.2.3)$$

where  $\nu$  denotes pairs of adjacent rungs. The action of the local operators  $\mathcal{T}_{0,\pm 2}^{\text{cyc}}(\nu)$  on neighbouring rungs is given in Table 8.1. Looking at Table 8.1, it is obvious that there are two additional matrix elements, namely  $|s, s\rangle \rightarrow |s, s\rangle$  and  $|s, t\rangle \rightarrow |s, t\rangle$ . These processes change only the local energy of the rungs and do not change the state. Therefore they belong formally to  $H_{\perp}$ . It is

$2\mathcal{T}_0^{\text{cyc}}$	
$ t^{0,\pm 1}, s\rangle$	$\longrightarrow$ $ s, t^{0,\pm 1}\rangle - \frac{3}{4} t^{0,\pm 1}, s\rangle$
$ s, s\rangle$	$\longrightarrow$ $\frac{9}{4} s, s\rangle$
$ t^0, t^{\pm 1}\rangle$	$\longrightarrow$ $\frac{1}{4} t^0, t^{\pm 1}\rangle$
$ t^{\pm 1}, t^{\pm 1}\rangle$	$\longrightarrow$ $\frac{1}{4} t^{\pm 1}, t^{\pm 1}\rangle$
$ t^{\pm 1}, t^{\mp 1}\rangle$	$\longrightarrow$ $\frac{1}{4} t^{\pm 1}, t^{\mp 1}\rangle$
$ t^0, t^0\rangle$	$\longrightarrow$ $\frac{1}{4} t^0, t^0\rangle$
$2\mathcal{T}_2^{\text{cyc}}$	
$ s, s\rangle$	$\longrightarrow$ $- t^0, t^0\rangle +  t^1, t^{-1}\rangle +  t^{-1}, t^1\rangle$

Table 8.1: Action of the operators  $\mathcal{T}_i^{\text{cyc}}$  as defined by Eq. 8.2.3 on product states of adjacent rungs. Singlets are denoted by  $s$  and triplons by  $t^i$  where the superscript indicates the magnetic quantum number. The remaining matrix elements can be found by using  $\mathcal{T}_n^{\text{cyc}} = \mathcal{T}_{-n}^{\text{cyc}}$ .

convenient to introduce a local term  $H^{\text{corr}}$  in the Hamiltonian in order to eliminate these matrix elements. Defining

$$H^{\text{corr}} := J_{\text{cyc}} \sum_i \left( \frac{3}{2} \mathbf{s}_{1,i} \mathbf{s}_{2,i} + \frac{9}{16} \right) \quad (8.2.4)$$

and

$$H(x) = (J_{\perp} H_{\perp} - J_{\text{cyc}} H^{\text{corr}}) + J_{\parallel} H_{\parallel} + (J_{\text{cyc}} H_{\text{cyc}} + J_{\text{cyc}} H^{\text{corr}}) \quad (8.2.5)$$

$$= (J_{\perp} H_{\perp} - J_{\text{cyc}} H^{\text{corr}}) + J_{\parallel} H_{\parallel} + J_{\text{cyc}} \tilde{H}_{\text{cyc}} \quad (8.2.6)$$

with  $\tilde{H}_{\text{cyc}} = H_{\text{cyc}} + H^{\text{corr}}$  and the two above mentioned matrix elements vanish in  $\tilde{H}_{\text{cyc}}$ . The corrected matrix elements of  $\tilde{H}_{\text{cyc}}$  decomposed in  $\tilde{\mathcal{T}}_{0,\pm 2}^{\text{cyc}}(\nu)$ , are presented in Tab. 8.2. The final form of the Hamiltonian then reads

$$\begin{aligned} \frac{H}{J_{\perp}} &= (1 - 3x_{\text{cyc}}) \left[ H_{\perp} + \frac{x}{1 - 3x_{\text{cyc}}} H_{\parallel} + \frac{x_{\text{cyc}}}{1 - 3x_{\text{cyc}}} \tilde{H}_{\text{cyc}} \right] \\ &= (1 - 3x_{\text{cyc}}) [H_{\perp} + \tilde{x} H_{\parallel} + \tilde{x}_{\text{cyc}} \tilde{H}_{\text{cyc}}] \end{aligned} \quad (8.2.7)$$

where  $\tilde{x} = x/(1 - 3x_{\text{cyc}})$  and  $\tilde{x}_{\text{cyc}} = x_{\text{cyc}}/(1 - 3x_{\text{cyc}})$ . The perturbative continuous unitary transformation is performed for the Hamiltonian (8.2.7). One obtains the truncated series in the two expansion parameters  $\tilde{x}$  and  $\tilde{x}_{\text{cyc}}$ . The effective Hamiltonian  $H^{\text{eff}}$  is calculated in the one-triplon sector up to order 11 and up to order 10 in the two-triplon sector.

The relevant observables are the same as in the previous chapter. The series obtained depend on the two expansion parameters  $\tilde{x}$  and  $\tilde{x}_{\text{cyc}}$ . The effective observables  $\mathcal{O}^{\text{eff}}$  are determined up to order 10 in both variables. Note that the series for the effective observables do not have the absolute scaling factor  $(1 - 3x_{\text{cyc}})$

$$\mathcal{O}^{\text{eff}}(\tilde{x}, \tilde{x}_{\text{cyc}}) = \mathcal{O}^{\text{eff}}\left(\frac{x}{1 - 3x_{\text{cyc}}}, \frac{x_{\text{cyc}}}{1 - 3x_{\text{cyc}}}\right) \quad (8.2.8)$$

There are two reasons that the maximum order of the perturbative expansion including four-spin interactions is reduced. Obviously, an expansion in two variables  $x$  and  $x_{\text{cyc}}$  costs more computer

$2\tilde{\mathcal{T}}_0^{cyc}$		
$ t^{0,\pm 1}, s\rangle$	$\rightarrow$	$ s, t^{0,\pm 1}\rangle$
$ t^0, t^{\pm 1}\rangle$	$\rightarrow$	$4 t^0, t^{\pm 1}\rangle$
$ t^{\pm 1}, t^{\pm 1}\rangle$	$\rightarrow$	$4 t^{\pm 1}, t^{\pm 1}\rangle$
$ t^{\pm 1}, t^{\mp 1}\rangle$	$\rightarrow$	$4 t^{\pm 1}, t^{\mp 1}\rangle$
$ t^0, t^0\rangle$	$\rightarrow$	$4 t^0, t^0\rangle$
$2\tilde{\mathcal{T}}_2^{cyc}$		
$ s, s\rangle$	$\rightarrow$	$- t^0, t^0\rangle +  t^1, t^{-1}\rangle +  t^{-1}, t^1\rangle$

Table 8.2: Action of the operators  $\tilde{\mathcal{T}}_i^{cyc}$  on product states of adjacent rungs. Singlets are denoted by  $s$  and triplons by  $t^i$  where the superscript indicates the magnetic quantum number. The remaining matrix elements can be found by using  $\tilde{\mathcal{T}}_n^{1,cyc} = \tilde{\mathcal{T}}_{-n}^{cyc}$ .

memory. But additionally care must be taken in choosing the correct cluster size for the calculation. In contrast to the applications in the previous chapters, the cluster size to calculate order  $k$  in the thermodynamical limit correctly is not just  $k + 1$ . This is illustrated in Fig. 8.2 for a third order process  $T_{-2}T_0T_2$  renormalizing the local hopping amplitude  $t_0$ . Usually (as in the last two chapters) the leftmost triplet does not need to be included in the calculation in order to obtain the correct results in the thermodynamic limit because the overall amplitude is zero for processes including this triplet. This is different in the case of finite four-spin interactions.

It follows that one has to use clusters of size 15 to calculate the one-triplon sector up to order 11 and the two-triplon sector to order 10. The same holds true for the cluster choice to compute the effective observables.

### 8.3 Rung-singlet phase

This section is concerned with the so-called rung-singlet phase. It was discussed in the last chapter that there is no phase transition for  $x_{cyc} = 0$  except at  $x = \infty$ , the case of two isolated spin-chains. The ground state of the system is dominated by rung-singlets which is the origin of the name rung-singlet phase. This phase is characterized by a finite rung-triplon gap. In the following the discussion is restricted to the Hamiltonian (8.1.3). An analogous discussion for the Hamiltonian (8.1.2) can be found in Ref. [209].

For a certain finite  $x_{cyc}$ , the rung-singlet phase is destabilized and breaks down at a finite value of  $x_{cyc}$  depending on  $x$ . There are several new quantum phases possible [321, 339–343]. One obtains a spontaneously dimerized phase where the dimers are located in a meander-like structure on the legs (see Fig. 7.4), scalar and vector chirality phases, a phase of dominant collinear spin correlations and a ferromagnetic phase [339]. However, real two-leg ladder cuprate systems are always in the rung-singlet phase, but relatively close to the quantum phase transition to the spontaneously dimerized phase [321]. Therefore, it is important to understand the properties of this transition. In the following the extension of the rung-singlet phase is calculated.

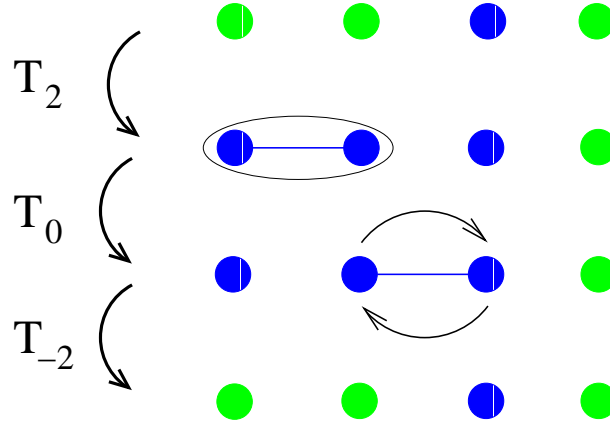


Fig. 8.2: Illustration of the choice of cluster sizes for the two-leg ladder with four-spin interactions. Green (grey) circles denote singlet rungs and blue (dark) circles denote excited triplets on the rungs. The first extended cluster occurs in the depicted third order process  $T_{-2}T_0T_2$  for an on-site hopping process  $t_0$ . In a first step two triplets are created left from the initial triplet by  $T_2$ . The second step is an interaction process  $T_0$  linking all three triplets. In the last step the two triplets left are annihilated by  $T_{-2}$  resulting in a renormalization of the local hopping term  $t_0$ . Note that the amplitude for this process in the two-leg ladder without cyclic exchange is zero. Only for finite four-spin interaction the cluster has to be chosen as indicated in order to obtain the correct results in the thermodynamic limit.

The standard approach to calculate a phase transition line with series expansions is to use dlogPadé extrapolants on  $\Delta(x, x_{cyc})$  as discussed in Sect. 5.2. Applying this approach to the problem under study this yields reliable results only in a very small region about the exactly known phase transition point [ $x = 1/5, x_{cyc} = 1/5$ ] (See grey square in Fig. 8.4). Generally, for  $x = x_{cyc}$  the dispersion and the gap are known exactly [284]

$$\omega(k)/J_{\perp} = 1 + (2 \cos(k) - 3)x \quad (8.1a)$$

$$\Delta(x, x)/J_{\perp} = 1 - 5x. \quad (8.1b)$$

The results extrapolated in  $x$  are reliable for  $x \in [0.1, 0.3]$  where the gap closes linearly in  $x$  and  $x_{cyc}$ .

In the following, an advanced extrapolation techniques [207–209] is used in order to investigate the rung-singlet phase for larger/lower values of  $x$  and  $x_{cyc}$ . The series expansion is expressed not in external parameters like  $x$  and  $x_{cyc}$ , but in an *internal* energy, similar in spirit to an approach for the Ising model [207]. The idea of internal parameters was introduced in a general form in Sect. 5.4. One defines

$$G(x) = 1 - \bar{\Delta}(x) = 1 - \frac{\Delta(x, rx)}{(1+x)J_{\perp}} \quad (8.3.2)$$

where  $r = x_{cyc}/x = J_{cyc}/J_{\parallel}$  will be kept constant for the extrapolation in  $x$ . The function  $G(x)$  behaves like  $G \propto x$  for  $x \rightarrow 0$  so that any expansion in  $x$  can be converted in an expansion in  $G$ . Using the expansion for  $\Delta(x)$  the inverse function  $x = x(G)$  is calculated as a series in  $G$  up to

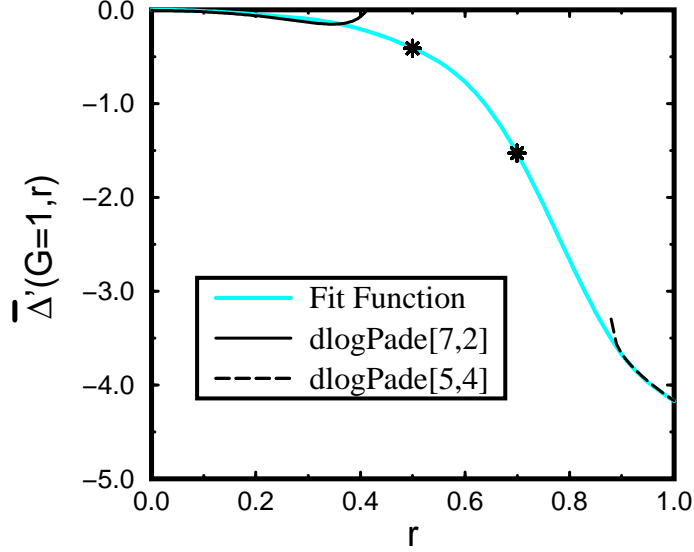


Fig. 8.3: Black lines show the dlogPadé extrapolants for  $d\bar{\Delta}/dx$  at  $G = 1$  as a function of  $r = x_{cyc}/x$ . The grey line is a fitted spline which follows the asymptotic behavior Eq. 8.3.8 with  $\lambda = 0.41$  and  $\lambda' = 0.85$  at small values of  $r$  and approximates the available dlogPadé results. The points marked by stars are set by hand to guide the spline smoothly in the intermediate region. The extrapolation in Fig. 8.4 requires actually only the values  $r \lesssim 0.5$ .

order 11 from Eq. 8.3.2. The quantity  $\bar{\Delta} = \Delta/[(1+x)J_{\perp}]$  measures the gap in units of  $J_{\perp} + J_{\parallel}$  to ensure empirically a monotonic behavior of  $\bar{\Delta}$  as function of  $x$ . Then the existence of the inverse  $x(G)$  is assured. Next the derivative of  $\bar{\Delta}(x)$  is considered

$$\frac{d\bar{\Delta}(x)}{dx} = -\frac{dG}{dx} . \quad (8.3.3)$$

Substituting  $x = x(G)$  in Eq. 8.3.3 one obtains

$$-\frac{dG}{dx} = P(G) , \quad (8.3.4)$$

where  $P(G)$  is the truncated series of order 10 in  $G$ . Note that the empirical convergence of the truncated series  $P(G)$  is significantly better than the convergence of the truncated series  $\Delta'(x)$  in  $x$  [208]. Because the gap is a monotonic decreasing function for  $r = \text{const}$  one can use dlogPadé extrapolants for  $P(G)$  since  $-dG/dx$  is non-negative. Integrating Eq. 8.3.4 yields

$$-\int_0^{G_0} \frac{dG}{P(G)} = \int_0^{x_0} dx = x_0 . \quad (8.3.5)$$

Therefore, integrating the left hand side to  $G_0 = 1$ , i.e.  $\Delta = 0$ , provides the phase transition point  $[x_0, rx_0]$  for a given  $r$ . For any  $G_0 \in [0, 1[$  the gap is  $\Delta(x_0, rx_0)/J_{\perp} = (1+x_0)(1-G_0)$ . In this way,  $\Delta(x, x_{cyc})$  is obtained.

First, the behavior of the gap in the limit of small  $r$  and  $G = 1$  is examined. This corresponds to the situation of two spin-chains which are weakly coupled by the four-spin interaction. Bosonization

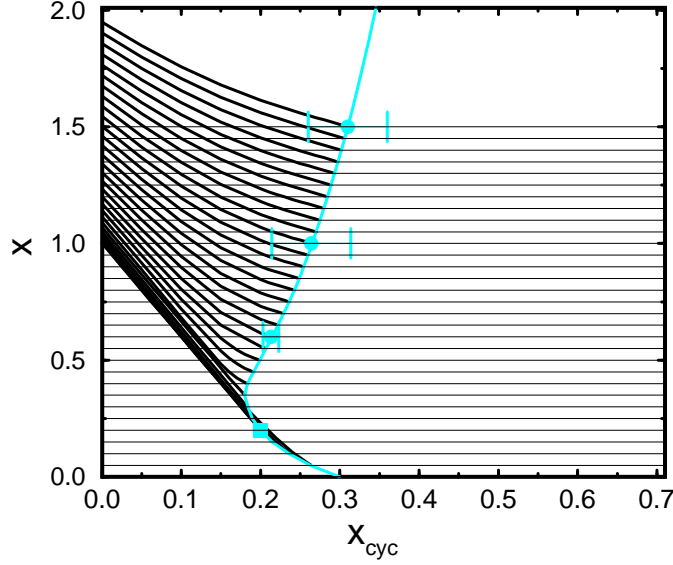


Fig. 8.4: Extrapolated spin gaps for the Hamiltonian Eq. 8.1.3 in the  $[x, x_{cyc}]$ -plane (see main text). The grey line is the obtained phase transition line  $\Delta = 0$  and the grey square is the exactly known transition point  $[x = 1/5, x_{cyc} = 1/5]$ . The points marked by grey circles and error bars indicate the estimated accuracy of the extrapolations. On the left side of the transition line the system is in the rung-singlet phase, on the right side in the spontaneously dimerized phase.

results show that the only relevant operator is the four-spin leg-leg interaction [334]. The triplet gap scales as

$$\Delta = \lambda J_{\perp} - \lambda' J_{cyc} \quad (8.3.6)$$

in leading order in  $J_{\perp}$  and  $J_{cyc}$ . Here  $\lambda$  and  $\lambda'$  are non-universal constants [321]. In our case one has a critical theory with central charge  $c = \frac{3}{2}$  and  $SU(2)$  symmetry which is described by the  $k = 2$  Wess-Zumino-Witten model [321, 344]. Rearranging Eq. 8.3.6 one obtains

$$\frac{\Delta}{J_{\parallel}} = \frac{\lambda}{x_c} \frac{x_c - x}{x} \quad (8.3.7)$$

where  $x_c = \lambda/(\lambda'r)$  is the value of  $x$  where the gap vanishes for given  $r$ . Therefore, the derivative of  $\bar{\Delta}$  for small  $r$  at  $G = 1$ , i.e.  $x = x_c$ , is given by

$$\bar{\Delta}'(G = 1, r) = -\frac{(\lambda'r)^2}{\lambda + \lambda'r} \quad (8.3.8)$$

In the case of  $r \rightarrow 0$   $\bar{\Delta}' = 0$  is expected and  $\bar{\Delta}' = -\lambda/x^2 = -\bar{\Delta}^2/\lambda$  from Eq. 8.3.7. Exploiting  $\bar{\Delta}' = -\bar{\Delta}^2/\lambda$  in a biased dlogPadé approximant one finds  $\lambda = 0.4 \pm 0.03$  in very good agreement with quantum Monte Carlo results  $\lambda_{QMC} = 0.41 \pm 0.01$  from Ref. [345].

In Fig. 8.3 the solid line corresponds to the dlogPadé [7, 2] for  $\bar{\Delta}'(G = 1, r)$ . For  $r < 0.3$  the asymptotic formula (Eq. 8.3.8) is well reproduced by the extrapolant. A minute (not discernible) offset at  $r = 0$  occurs as a natural consequence of the dlogPadé extrapolation which describes a

quantity of a given sign only. Using the value  $\lambda = 0.41 \pm 0.01$  for the second non-universal constant  $\lambda'$  the value

$$\lambda' = 0.85 \pm 0.2 . \quad (8.3.9)$$

is deduced. If one performs the same analysis for the Hamiltonian Eq. 8.1.2 one obtains the same result for  $\lambda'$  [209]. This supports the validity of the analysis and agrees perfectly with Ref. [334] in that the relevant term in the cyclic exchange is the leg-leg coupling so that both Hamiltonians (Eq. 8.1.3 and Eq. 8.1.2) lead to the same result for large leg couplings and small cyclic exchange couplings.

For larger values of  $r$  the interpolation between various extrapolants is used. The uncertainty in the interpolation leads to the error bars in the subsequent extrapolations shown in Fig. 8.4. The extrapolations are done for values  $r \lesssim 0.5$  by subtracting the interpolated values depicted in Fig. 8.4 from the truncated series for  $\overline{\Delta}'(G)$  so that one obtains the series of a function that vanishes at  $G = 1$ . It is found that many in this way biased dlogPadé extrapolants yield reliable results which supports the approach used to include the properties of the weakly coupled chains in the extrapolations. Finally, the subtracted bias is re-added to arrive at the proper result (see also Ref. [209]).

In the limit  $x \rightarrow \infty$ , one concludes from Eq. 8.3.7 that the transition line converges against the asymptotic value

$$x_{\text{cyc}}^{\text{asympt}} = \lambda/\lambda' \approx 0.52 \pm 0.14 \quad (8.3.10)$$

using the values for  $\lambda$  and  $\lambda'$  obtained above. This result holds again for both Hamiltonians (Eq. 8.1.3 and Eq. 8.1.2) [209]. The value of  $x_{\text{cyc}}^{\text{asympt}} = 0.22$  advocated in Ref. [334] cannot be confirmed.

In Fig. 8.4 the extrapolated values of the spin gap of the Hamiltonian Eq. 8.1.3 in the  $[x, x_{\text{cyc}}]$ -plane are presented. The black solid lines denote  $\Delta(x_0, x_{\text{cyc}})$  for a fixed  $x_0$  as a function of  $x_{\text{cyc}}$ . These lines are shifted by  $x_0$  in  $x$ -direction producing a quasi three-dimensional plot. The end-point of a black line corresponds to  $\Delta(x, x_{\text{cyc}}) = 0$  yielding the grey solid line which is the transition line between the rung-singlet phase and the spontaneously dimerized phase. Biased extrapolants are used in the range  $x \in [0.3, \infty[$  for the transition line. In the range  $x \in [0.1, 0.3]$  the unbiased extrapolations are safe due to the good convergence of the series near the exactly known transition point (grey square). In the limit  $x \rightarrow 0$  even the truncated series gives quantitative results. Using Eq. 8.3.5, one finds in addition strong evidence for

$$\frac{d\overline{\Delta}}{dx} \propto (1 - G)^\eta \quad (8.3.11)$$

at  $x = 0$  where  $\eta = 0.3 \pm 0.02$ . The transition point, i.e.  $\Delta = 0$ , for  $x = 0$  is found to be  $[0, 0.3 \pm 0.002]$ .

The smooth connection between the different extrapolations corroborates the reliability of the results found in a wide region in the  $[x, x_{\text{cyc}}]$ -plane. The phase diagram for Hamiltonian Eq. 8.1.2 can be found in Ref. [209]. It is very similar in shape compared to the one for Hamiltonian Eq. 8.1.3.

The exchange parameters discussed for cuprate ladders are  $x \approx 1.2 - 1.3$  and  $x_{\text{cyc}} \approx 0.1$ . It is evident by looking at Fig. 8.4 that the materials are located inside the rung-singlet phase. Therefore



the rung-triplon remains the elementary excitation of the cuprate ladder systems. In the following, the distribution of spectral weight in the various triplon sectors at finite four-spin interaction is discussed.

## 8.4 Spectral weights

In contrast to the case  $x_{\text{cyc}} = 0$ , the rung-singlet phase is unstable for  $x \rightarrow \infty$  in presence of a finite four-spin interaction as shown in the last section. Therefore it is therefore important to analyze the behavior of the spectral weights. The focus is laid here on determining the spectral weights for realistic values of the four-spin interaction. A full analysis of the spectral weights approaching the phase transition is not done. The extrapolation for the spectral weights is performed by using the gap as internal parameter (see Sect. 5.4) and extrapolating the gap as described in the last section [208, 209]. Usually a standard  $[n, 2]$  dlogPadé or  $[n, 2]$  Padé is used for the series expressed in the one-triplon gap.

### 8.4.1 S=1

First, the spectral weights for excitations with total spin one are discussed. The local observable considered is the symmetric combination of Eq. 7.3.4c and Eq. 7.3.4d

$$\mathcal{O}^{S=1}(r) = \frac{1}{2}(\mathcal{O}^{\text{III}}(r) + \mathcal{O}^{\text{IV}}(r)) \quad (8.4.1)$$

in analogy to the discussion of the pure spin-ladder in Sect. 7.4. The spectral weights were calculated up to order 10 in the one- and two-triplon channel, up to order 9 in the three-triplon channel and up to order 10 in the four-triplon channel. The total spectral weight  $I_{\text{tot}}$  is equal to 1/4 for  $S = 1$ .

In Fig. 8.5 the relative spectral weights  $I_n/I_{\text{tot}}$  are shown for  $x_{\text{cyc}} = 0$  (black solid lines),  $x_{\text{cyc}} = 0.05$  (blue dashed lines) and  $x_{\text{cyc}} = 0.1$  (green long-dashed lines) and  $N \in \{1, 2, 3\}$ . In addition, the sum of all plotted relativ weights  $I_{\text{sum}} = (I_1 + I_2 + I_3)/I_{\text{tot}}$  is depicted. Contributions with more than three triplons have negligible weight in the parameter regime displayed.

The general trend is the reduction of the one-triplon weight by switching on the four-spin interactions and an increase of the weights for two and three triplons. Extrapolating the one-triplon spectral weight, one recognizes poles of the denominator near  $G \approx 1$  indicating that the one-triplon weight vanishes at the phase transition. Therefore a pole exactly for  $G = 1$  is included. The extrapolation used in the figure is a  $[7, 2]$  dlogPadé extrapolant. Note that the result for the one-triplon spectral weight is almost independent of the bias at  $G = 1$ .

The two-triplon spectral weight is extrapolated by using a  $[5, 2]$  dlogPadé extrapolant. Here also complex poles near  $G \approx 1$  are seen. So a complete extrapolation requires to treat the derivative of  $I_2$  in analogy to Sect. 6.3. Again, the results for the values do not depend on whether or not the derivated  $I_2$  is biased to  $G = 1$ . The analysis of  $I_2$  closer to the phase transition points in the direction that it stays finite at about 25% at  $G = 1$ . So it seems that, contrary to the case of the one-dimensional Heisenberg chain (see Sect. 6.3), the rung-triplon picture becomes very difficult

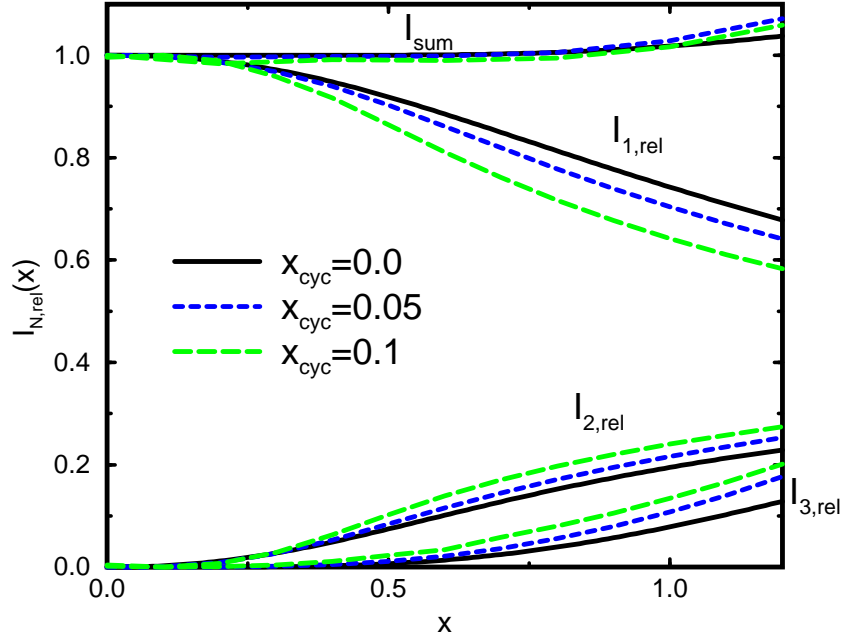


Fig. 8.5: Relative weights for the  $S=1$  operator  $\frac{1}{2}(\mathcal{O}^{\text{III}}(r) + \mathcal{O}^{\text{IV}}(r))$  (Eq. 7.3.4c and Eq. 7.3.4d). The  $I_N$  are calculated according to Eq. 3.7.15 up to and including order 10, 10 and 9 in  $x$  for  $N=1, 2$  and 3 respectively. The total intensity  $I_{\text{tot}}$  is equal to  $1/4$ . Black solid lines corresponds to  $x_{\text{cyc}}=0$ , dashed blue lines to  $x_{\text{cyc}}=0.05$  and long dashed green lines to  $x_{\text{cyc}}=0.1$ .  $I_{\text{sum}} = (I_1 + I_2 + I_3)/I_{\text{tot}}$  denotes the sum of all plotted contributions.

at the phase transition tuned by the four-spin interactions.

The three-triplon sector is extrapolated by a  $[5, 0]$  dlogPadé extrapolant because other extrapolants are spoiled by spurious poles. It can be expected that this results in an overshooting of the three-triplon weight for larger values of  $x$ . The latter conclusion is strengthened by the observation that the sum of all plotted relative weights overshoots in the same fashion as the three-triplon weight increases for larger  $x$ . The extrapolations of the one- and two-triplon sector seem to be very stable so that they are not responsible for the violation of the sum rule in the region of large  $x$ .

The dispersion is known exactly for  $x = x_{\text{cyc}}$  (see Sect. 8.3). It follows that the rung-triplon picture is realized perfectly for these parameters. The total spectral weight is in the one-triplon channel and all other weights are zero. Note that this implies also that the relative one-triplon weight for  $x = 0$  but finite  $x_{\text{cyc}}$  is not equal to one. Therefore the one-triplon spectral weight  $I_1$  increases for  $x < x_{\text{cyc}}$  and decreases for  $x > x_{\text{cyc}}$  as depicted in Fig. 8.5<sup>2</sup>.

It can be concluded from Fig. 8.5 that for realistic values of the four-spin interaction the one- and the two-triplon sector contain by far most of the spectral weight. Therefore the rung-triplon is a

<sup>2</sup>It can be hardly seen in Fig. 8.5 because the deviation from  $I_1 = 1$  at  $x = 0$  are very small for these parameters of the four-spin interaction.

good choice for a quasi-particle description of the two-leg ladder with four-spin interaction.

### 8.4.2 $S=0$

The local observable  $\mathcal{O}_{\text{eff}}^{\parallel}$  in Eq. 7.3.4b is considered for the  $S = 0$  case in analogy to the pure two-leg ladder discussed in Sect. 6.3. The total spectral weight  $I_{\text{tot}}(x)$  can be obtained again from the ground state energy per spin  $\epsilon_0(x)$ . All extrapolations of the spectral weights are done in analogy to the last section using the method of internal parameters [208, 209].

In Fig. 8.6 the relative spectral weights  $I_n/I_{\text{tot}}$  are shown for  $x_{\text{cyc}} = 0$  (black solid lines),  $x_{\text{cyc}} = 0.05$  (blue dashed lines) and  $x_{\text{cyc}} = 0.1$  (green long-dashed lines) and  $N \in \{2, 3, 4\}$ . In addition, the sum  $I_{\text{sum}} = (I_2 + I_3 + I_4)/I_{\text{tot}}$  of all plotted relative weights is depicted.

The extrapolation for the total intensity is done by a [8, 2] Padé for the derivative of the ground state energy. The two-triplon sector is extrapolated by a [7, 2] dlogPadé biased to have a pole at  $G = 1$ . Again, complex poles can be detected near  $G = 1$  which do not change the results depicted in Fig. 8.6. The three- and four-triplon sectors are extrapolated by [8, 2] Padé extrapolants. The sum rule is fulfilled in a quantitative manner for all values of  $x_{\text{cyc}}$  shown in Fig. 8.6.

In analogy to the  $S = 1$  case, the rung-triplon is realized in a perfect way for  $x = x_{\text{cyc}}$ , i.e. the two-triplon weight is exactly one and all other spectral weights are zero for these parameters. The two-triplon spectral weight for  $x < x_{\text{cyc}}$  is slightly smaller than one.

Similar to the  $S = 1$  case, the leading sector, here  $I_2$ , loses spectral weight upon switching on  $x_{\text{cyc}}$  while the triplon sectors with higher numbers of triplons gain spectral weight. The two-triplon sector contains only about 50% of the spectral weight for realistic parameters, i.e. unlike to the  $S = 1$  case one can expect to have sizable contribution especially of three triplons in optical experiments. In addition, the four-triplon sector also is sizable. Possible life-time effects (decay of two triplons into four triplons) may become more important due to a finite four-spin interactions.

## 8.5 Energy properties

In this section the influence of the four-spin interactions on the energy properties is investigated. The focus is laid on the one-triplon dispersion and on the two-triplon bound states. In addition, the relative positions of multi-triplon continua for finite four-spin interaction are illustrated.

### 8.5.1 Ground state energy

The influence of the four-spin interaction on the ground state energy per spin  $\epsilon_0/J_{\perp}$  is shown in Fig. 8.7. The plain series is obtained up to order 11 in  $x$  and  $x_{\text{cyc}}$ . The solid line corresponds to the result already discussed in Sect. 7.5. All curves are extrapolated using the method of internal parameters as explained above. An additional [8, 2] dlogPadé extrapolant is applied.

The ground state energy per spin  $\epsilon_0/J_{\perp}$  increases by turning on  $x_{\text{cyc}}$ .

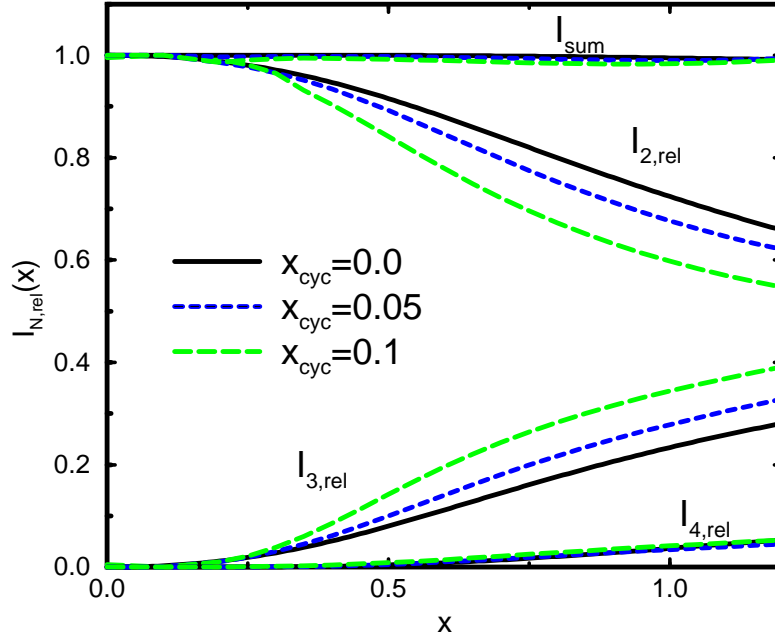


Fig. 8.6: Relative weights for the  $S=0$  operator  $S_{1,i}S_{1,i+1}$  (Eq. 7.3.4b). The  $I_N$  are calculated according to Eq. 3.7.15 up to and including order 10, 8 and 7 in  $x$  for  $N=2, 3$  and 4 respectively. The total intensity  $I_{\text{tot}}$  has been extracted from the 11<sup>th</sup> order result for the ground state energy per spin according to Eq. 3.7.16. Black solid lines corresponds to  $x_{\text{cyc}} = 0$ , dashed blue lines to  $x_{\text{cyc}} = 0.05$  and long dashed green lines to  $x_{\text{cyc}} = 0.1$ .  $I_{\text{sum}} = (I_2 + I_3 + I_4)/I_{\text{tot}}$  denotes the sum of all plotted contributions.

### 8.5.2 One-triplon dispersion

The one-triplon dispersion  $\omega(k)$  is obtained up to order 11 in  $x$  and  $x_{\text{cyc}}$ . Therefore a first important goal is to recover the results obtained from the series up to order 14 for  $x_{\text{cyc}} = 0$ . It turns out that the extrapolation is very stable in the interval  $k \in [0.4\pi, \pi]$  while the extrapolations are very subtle around  $k = 0$  (the dip region for larger  $x$  values). The latter follows from the fact that the three-triplon continuum approaches to the one-triplon dispersion for these small  $k$  values as discussed already in Sect. 7.5. The relative positions of the continua at finite  $x_{\text{cyc}}$  will be shown below.

In order to obtain a good extrapolation for the one-triplon dispersion near  $k = 0$  for  $x_{\text{cyc}} = 0$ , it is necessary to include additional information about the one-triplon dispersion. In the limit of  $x \rightarrow \infty$  approaching separated spin-chains, it is clear that the one-triplon dispersion has to vanish at  $k = 0$  measured in  $J_{\parallel}$ . The closing of a gap at  $k = 0$  is signaled by poles in the complex plane near  $G = 1$ . Therefore it is natural to include this knowledge for the extrapolation at  $k = 0$ . These poles are also present at small but finite  $k$ . Therefore they are no physical poles because the one-triplon dispersion for  $x \rightarrow \infty$  is not zero for these values of the momentum. In the following a biased

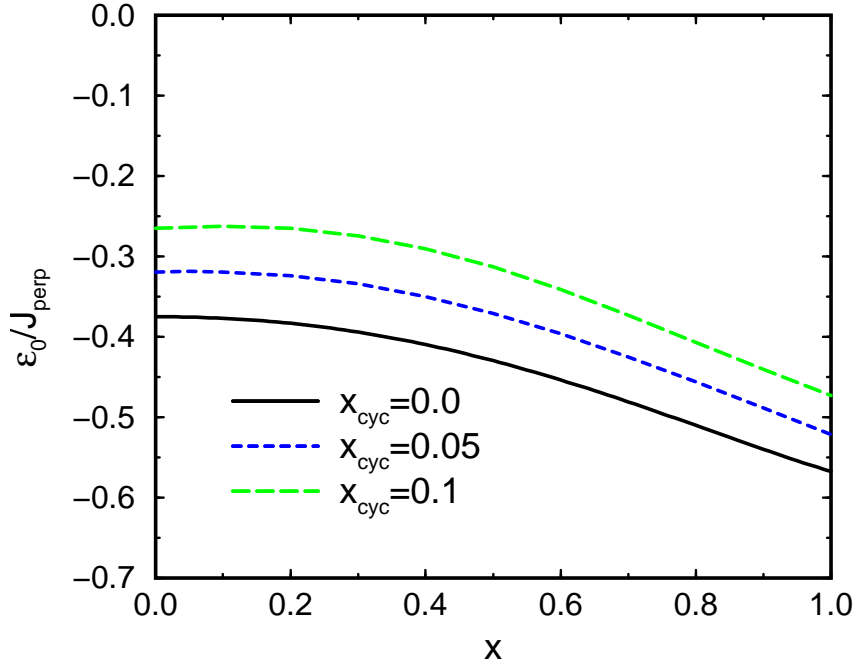


Fig. 8.7: Ground state energy per spin  $\epsilon_0/J_{\perp}$  as function of  $x$  for  $x_{cyc} = 0.0$  (solid black line),  $x_{cyc} = 0.05$  (dashed blue line) and  $x_{cyc} = 0.1$  (green long dashed line).

extrapolation is used in the whole region  $k \in [0; 0.1\pi]$ , i.e. a pole is included at  $G = 1$ . In the region  $k \in [0.4\pi; \pi]$  a standard  $[5, 5]$  dlogPadé extrapolation is used. The results obtained in both regions are connected by a spline interpolation using a Maple package. The same procedure is used for finite four-spin interaction. Therefore one makes two possible systematic approximations. First, for  $x_{cyc} = 0$ , the inclusion of a singularity at finite (but small) momentum induces an error which results in a too low curvature of the dispersion near  $k = 0$ . Second, the inclusion of a singularity also in the case of finite  $x_{cyc}$  results in a pushing down of the dispersion near the phase transition. It can be expected that both errors are small for the realistic values of  $x$  and  $x_{cyc}$  for cuprate ladders as discussed in this chapter.

In Fig. 8.8 the result is shown for  $x = 0.5$  (thin curves) and  $x = 1$  (thick curves) for  $x_{cyc} = 0.0$  (solid black curves),  $x_{cyc} = 0.05$  (dashed blue curves) and  $x_{cyc} = 0.1$  (long-dashed green curves). Note that the smoothness of the curves corroborates the extrapolation procedure. The main effect of the four-spin interactions is a global shift of the one-triplon dispersions to lower energies. The overall shape of the dispersion is almost unchanged. The gap is reduced considerably up to a factor of 2 for  $x_{cyc} = 0.1$ . This explains the importance of the four-spin interaction for a quantitative description of cuprate ladders.

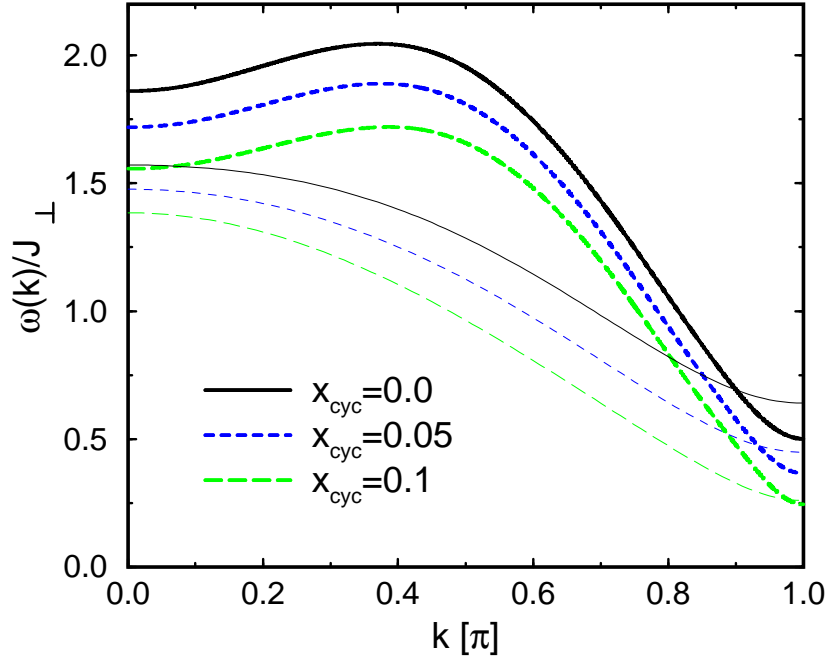


Fig. 8.8: The one-triplon dispersion  $\omega(k)/J_{\perp}$  is shown for  $x = 0.5$  (thin curves) and  $x = 1$  (thick curves) for  $x_{\text{cyc}} = 0.0$  (solid black curves),  $x_{\text{cyc}} = 0.05$  (dashed blue curves) and  $x_{\text{cyc}} = 0.1$  (long-dashed green curves).

### 8.5.3 Two-triplon continuum and bound states

This subsection deals with the determination of energy properties of two triplons. Therefore one needs the one-triplon hopping amplitudes  $t_n$  and the two-triplon interaction amplitudes  $t_{d;n;d'}$  as discussed in Subsect. 3.7.1.

The one-triplon hopping amplitudes are determined in a straightforward way by Fourier transforming the extrapolated one-triplon dispersion  $\omega(k)$  back to real space. The extrapolation of the two-triplon interaction amplitudes is done in an analogous manner. First, the method of internal parameters is used. Second, an additional extrapolation is applied to the matrix elements  $W_{d;d'}(K)$  for  $\{d;d'\} \leq 5$  in momentum space. Note that these are the most local and therefore the most important amplitudes. The extrapolation is done for discrete points in momentum space. The extrapolated values are again connected by a spline interpolation and Fourier transformed back in real space in order to obtain the amplitudes  $t_{d;n;d'}$ .

The extrapolation of the two-triplon interaction amplitudes is quite complicated. This can be understood from the fact that the two-triplon continuum and the four-triplon continuum intersect each other. It turns out that the extrapolation is more stable in the  $S = 1$  case than in the  $S = 0$  case. It follows that two triplons can decay into four triplons which results in poles of the extrapolants of the two-triplon interaction amplitudes (see discussion Subsect. 7.5.4). But the effect is

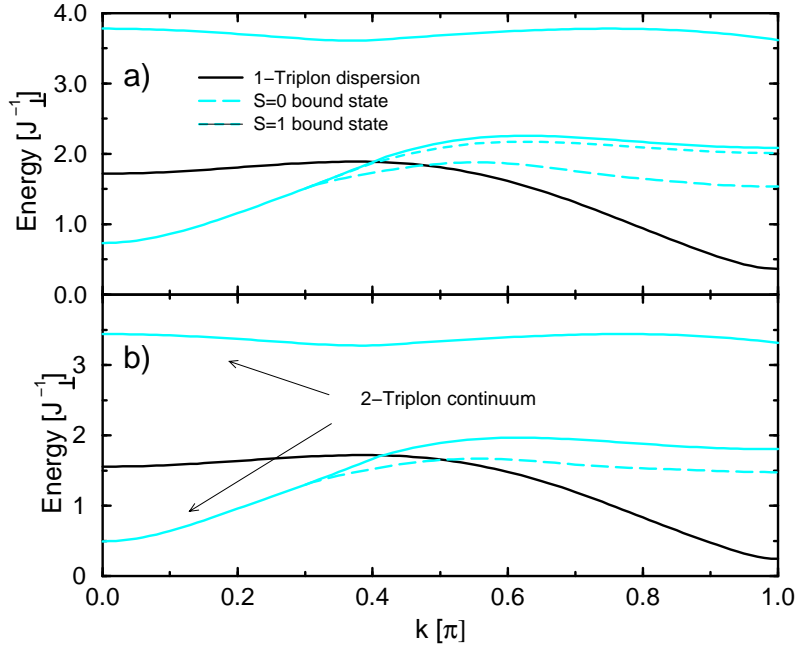


Fig. 8.9: One-triplon and two-triplon energies of the two-leg ladder for  $x = 1$  with  $x_{\text{cyc}} = 0.05$  (a) and  $x_{\text{cyc}} = 0.1$  (b) are shown. The thick solid black line denotes the one-triplon dispersion  $\omega(k)$ . The grey solid lines correspond to the lower and the upper edge of the two-triplon continuum. The dashed grey lines denote the  $S = 1$  two-triplon bound states and the long dashed grey lines corresponds to the  $S = 0$  two-triplon bound states.

stronger in the  $S = 0$  channel because the four-triplon contribution is lower in energy and is of larger size. The extrapolation is therefore more sensitive. In the  $S = 1$  sector a  $[8, 2]$  Padé is applied for all amplitudes. In the  $S = 0$  sector a  $[8, 2]$  Padé is applied in most cases. If there is no extrapolation possible at all, the truncated series in the internal parameter is used.

The extrapolations are quantitative up to  $x \leq 1$  in both spin channels. For  $x > 1$ , the extrapolation in the  $S = 0$  overestimates the two-triplon interaction. This results in too low energies of the two-triplon bound state especially near  $k = \pi/2$ . The results are only semi-quantitative. The extrapolation in the  $S = 1$  case is more stable and the results obtained should be valid also for  $x \approx 1.3$ .

The effect of the four-spin interaction on the two-triplon energies is illustrated in Fig. 8.9 for  $x = 1$  with  $x_{\text{cyc}} = 0.05$  (a) and  $x_{\text{cyc}} = 0.1$  (b). Since the one-triplon dispersion is shifted to lower energies due to  $x_{\text{cyc}}$ , also the two-triplon energies are shifted globally to lower energies. The shape of the lower and the upper edge of the two-triplon continuum is almost unchanged because it is solely determined from the shape of the one-triplon dispersion.

The most interesting effect of the four-spin interaction is on the binding energy of the two-triplon

bound states (grey lines in Fig. 8.9). The four-spin interaction reduces the attractive interaction between the triplons. Thus the binding energy of the bound states is reduced upon increasing  $x_{\text{cyc}}$  (compare also to the case  $x_{\text{cyc}} = 0$  depicted in Fig. 7.11) [324]. This effect is present for total spin zero and total spin one. But the effect is more drastic in the  $S = 1$  case because the  $S = 1$  two-triplon bound state is only weakly bound for  $x_{\text{cyc}} = 0$ . As a consequence, the  $S = 1$  two-triplon bound state is absent for  $x_{\text{cyc}} = 0.1$ . The disappearance of the  $S = 1$  two-triplon bound state has interesting effects on the spectral line-shape of the two-triplon contribution to the dynamical structure factor which will be discussed in the next section.

#### 8.5.4 Multi-triplon continua

Next the relative positions of the multi-triplon continua are investigated. Here the focus is laid on the effect of the four-spin interaction for isotropic coupling  $x = 1$ . But the general trend is the same for all values of  $x$ . The determination of the multi-triplon band edges in combination with the multi-triplon spectral weights (see Sect. 8.4) is important to estimate possible life-time effects neglected in the extrapolation procedure as discussed in Sect. 7.5.4. Note again that  $n$ -triplon interactions with  $n > 2$  are not included in the calculation since they are expected to be very small [327].

In Fig. 8.10 the result for  $x = 1$  and  $x_{\text{cyc}} = 0.1$  is shown. This has to be compared with Fig. 7.13 depicting the same information for  $x = 1$  and  $x_{\text{cyc}} = 0$ . In the left panel the relative position of the one-triplon dispersion and of the three-triplon continuum is presented while the right panel shows the relative position of two-triplon energies and of the four-triplon energies. Note that odd and even triplon channels are not connected due to parity conservation (see Sect. 7.5.4).

The reduction of the one-triplon gap  $\Delta$  by the four-spin interaction results generically in a closer relative position of all multi-triplon continua. It can be seen in Fig. 8.10 that the lower band edge of the three-triplon continuum is very close to the one-triplon dispersion for  $k \in [0, 0.4\pi]$  (left panel). The value for the edge of the three-triplon continuum at  $k = 0$  is the sum of the one-triplon gap and the  $S = 0$  two-triplon bound state energy at  $k = \pi$ . The extrapolation for these two energies is very safe. The determination of the one-triplon dispersion near  $k = 0$  turned out to be very complicated (see Sect. 8.5.2). The closeness of the three-triplon continua explains these complications. Note that the true one-triplon dispersion is even slightly closer to the three-triplon continuum (see systematic errors of the one-triplon dispersion discussed above).

The situation for two and four triplons is depicted in the right panel of Fig. 8.10. Both continua intersect strongly for these parameters similar to the case of  $x = 1$  and  $x_{\text{cyc}} = 0$ . The intersection of the two- and four-triplon continuum is larger in the  $S = 0$  case than in the  $S = 1$  case due to the larger binding energy of the  $S = 0$  two-triplon bound state. Therefore life-time effects are expected to be smaller in the  $S = 1$  case. Moreover, the total spectral weight in the four-triplon channel with  $S = 1$  is very small. Possible effects of the neglected processes are discussed later in the sections dealing with spectral densities and the application to optical experiments.



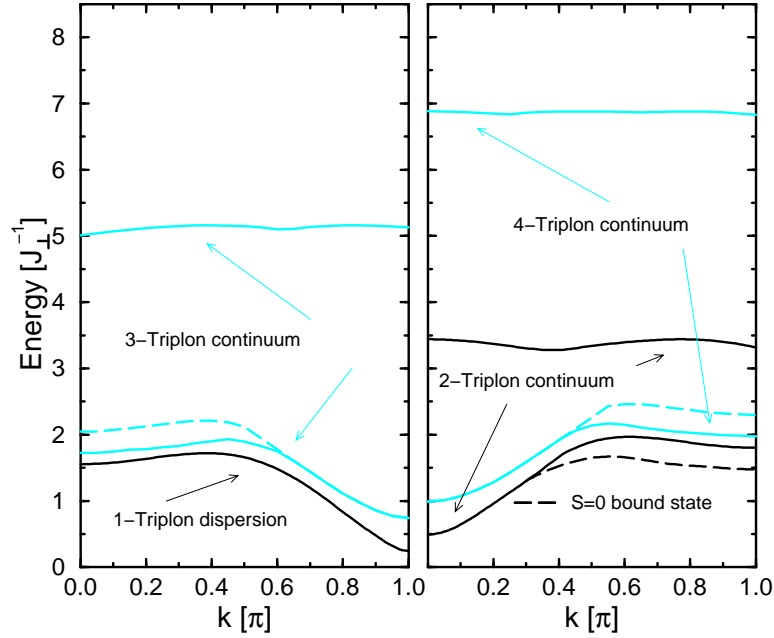


Fig. 8.10: Multi-triplon continua of the two-leg ladder for  $x = 1$  and  $x_{\text{cyc}} = 0.1$  are shown. One- and three-triplon energies are depicted in the left panel while two- and four-triplon energies are plotted in the right panel. Left panel: The solid black line denotes the one-triplon dispersion  $\omega(k)$ . The grey solid lines correspond to the lower and the upper edge of the three-triplon continuum including binding effects. The dashed grey lines denote the lower band edge of the three-triplon continuum neglecting binding effects. Right panel: The solid black lines correspond to the lower and the upper edge of the two-triplon continuum. The dashed black line corresponds to the ( $S = 0$ ) two-triplon bound state. The solid grey lines denote the lower and the upper band edge of the four-triplon continuum. The dashed grey line depicts the lower band edge of the four-triplon continuum neglecting binding effects.

## 8.6 $S = 1$ excitations

This part deals with the dynamical structure factor of the two-leg ladder with four-spin interaction. Results are shown for the one- and the two-triplon contribution which capture most of the spectral weight (see Sect. 8.4).

### 8.6.1 One-triplon contribution

The most important contribution to the dynamical structure factor is the leading one-triplon contribution. The  $k$ -resolved spectral weight for  $x_{\text{cyc}} = 0$  was discussed in Sect. 7.6. The spectral weight is always accumulated around  $k = \pi$ . Upon increasing  $x$ , the spectral weight decreases for small momenta and concentrates more and more at  $k = \pi$  (see Fig. 7.14).

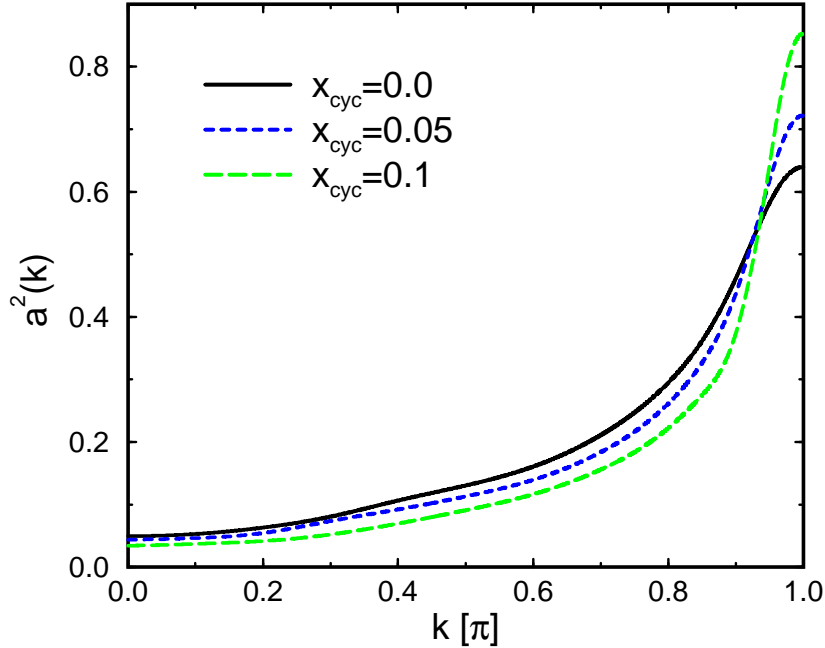


Fig. 8.11: The one-triplon spectral density  $I_1(k)$  for  $\mathcal{O}^{\text{III}}$  at  $x = 1$  is shown. The solid black line denotes  $x_{\text{cyc}} = 0.0$ , the dashed blue line  $x_{\text{cyc}} = 0.05$  and the long-dashed green line  $x_{\text{cyc}} = 0.1$ .

The effect of the four-spin interaction on the one-triplon spectral weight is shown in Fig. 8.11 exemplified for  $x = 1$  with  $x_{\text{cyc}} = 0$  (solid black line),  $x_{\text{cyc}} = 0.05$  (dashed blue line) and  $x_{\text{cyc}} = 0.1$  (long-dashed green line). All extrapolations were done using the method of internal parameters plus additional  $[8, 2]$  Padé extrapolation. It can be seen clearly in Fig. 8.11 that the effect of  $x_{\text{cyc}}$  on the  $k$ -resolved one-triplon spectral weight is similar to the effect of  $x$ . The spectral weight is reduced at small momenta but it increases around  $k = \pi$ . The findings suggest that the one-triplon spectral weight near the phase transition to the meander-like dimerization is governed by only one mode at  $k = \pi$  which has negligible spectral weight. Similar results were also found by exact diagonalisation [328].

### 8.6.2 Two-triplon contribution

The two-triplon contribution to the dynamical structure factor is the leading contribution with even parity as discussed in Sect. 7.6. Its total spectral weight slightly increases by turning on  $x_{\text{cyc}}$  (see Sect. 8.4). The generic relative spectral weight is about 20% to 30% of the leading one-triplon contribution for realistic values of cuprate ladders.

In Fig. 8.12 the result for the two-triplon contribution to the dynamical structure factor is shown for  $x = 1$  and  $x_{\text{cyc}} = 0$  (a),  $x_{\text{cyc}} = 0.05$  (b) and  $x_{\text{cyc}} = 0.1$  (c). It was already discussed in Sect. 8.5.3 that the four-spin interaction has a strong influence on the  $S = 1$  two-triplon bound state

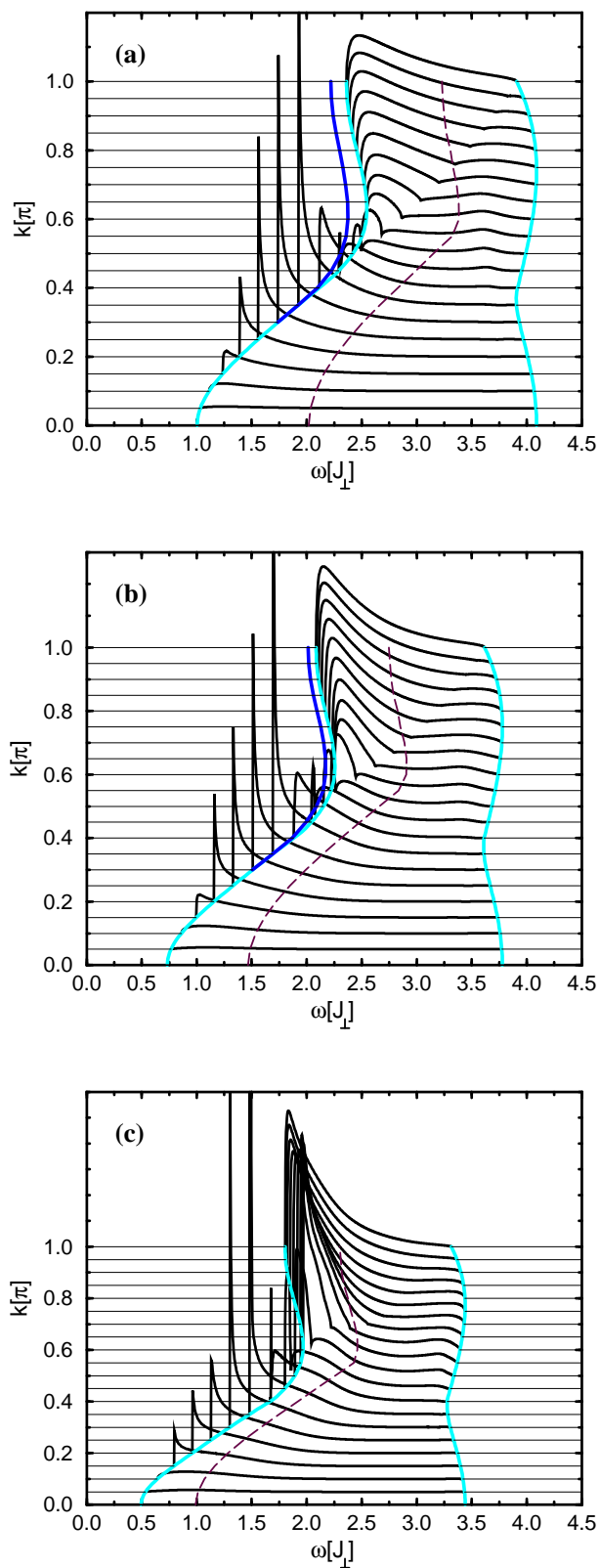


Fig. 8.12: The two-triplon spectral density  $I_2(k, \omega)$  for  $\mathcal{O}^{\text{IV}}$  with  $x = 1.0$  and  $x_{\text{cyc}} = 0.0$  (a),  $x_{\text{cyc}} = 0.05$  (b) and  $x_{\text{cyc}} = 0.1$  (c) is shown. The grey lines denote the lower and the upper edge of the two-triplon continuum. The black lines indicate the dispersion of the  $S = 1$  two-triplon bound state. The long-dashed dark grey lines depict the lower edge of the  $S = 1$  four-triplon continuum.

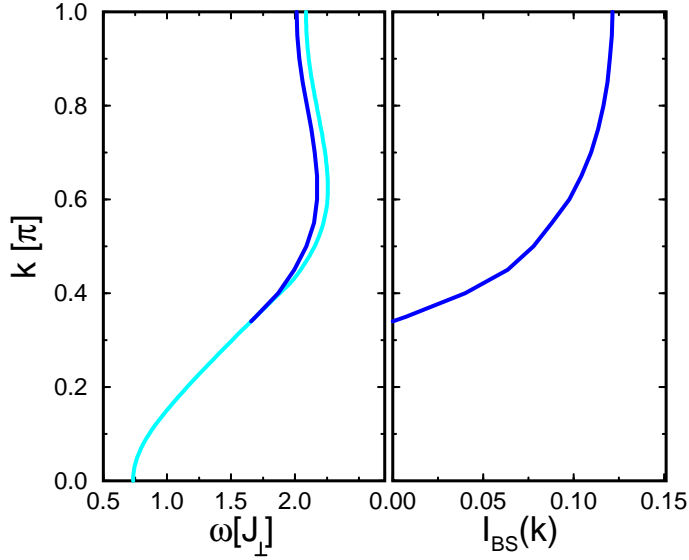


Fig. 8.13: The two-triplon  $S = 1$  bound state energy and the spectral weight for  $x = 1.0$  and  $x_{\text{cyc}} = 0.05$  are shown. Left panel: The solid grey line denotes the lower edge of the two-triplon continuum and solid blue (dark) line depicts the dispersion of the  $S = 1$  two-triplon bound state. Right panel: The  $k$ -resolved spectral weight of the  $S = 1$  two-triplon bound state is plotted.

which gives rise to interesting changes of the line-shape of the two-triplon spectral density.

The dispersion of the  $S = 1$  two-triplon bound state is denoted as a blue solid line in Fig. 8.12 and in the left panel of Figs. 7.16 and 8.13. In the right panel of the latter figures the  $k$ -resolved spectral weight of the bound state is depicted. Upon turning on  $x_{\text{cyc}}$ , the binding energy and the spectral weight of the bound state is reduced. At  $x_{\text{cyc}} = 0.1$ , the  $S = 1$  two-triplon bound state has disappeared.

The reduction of the binding energy of the two-triplon bound state results in a sharpening of the spectral density at the lower band edge. The effect is most drastic near  $k = \pi$ . At the point where the bound state is degenerate with the lower edge of the two-triplon continuum, the spectral density will display a square root singularity. This in analogy to the discussion of the dimerized and frustrated spin-chain for certain values of the exchange couplings. At  $x_{\text{cyc}} = 0.1$ , where the two-triplon bound state has already dissolved in the two-triplon continuum, a signature of this divergence can be seen in the sharp structures near the lower band edge of the two-triplon continuum. The lower band edge of the  $S = 1$  four-triplon continuum is shown as dark grey long dashed lines in Fig. 8.12. It can be seen that the overlap of the two-triplon and the four-triplon continuum increases with increasing four-spin interaction. Nevertheless, possible life-time effects should be of minor importance because most of the two-triplon spectral weight is below the lower band edge of the four-triplon continuum. In addition, the spectral weight of the four-triplon continuum increases only slowly like  $I_4(\omega) \propto (\Delta\omega)^{13/2}$  at the lower band edge [327]. The distance to the band edge is

measured by  $\Delta\omega$ .

## 8.7 $S = 0$ excitations

In this section two-triplon spectral densities with total spin zero are analyzed. The effect of the four-spin interaction on the energy spectrum was already discussed in Sect. 8.5.3. In contrast to the  $S = 1$  case studied in the last section, the  $S = 0$  two-triplon bound state is present also for finite  $x_{\text{cyc}}$ , at least in the range of parameters considered here. Therefore the impact of the four-spin interaction on the line-shape of the two-triplon spectral density is less drastic than in the  $S = 1$  case. In the following, first the complete two-triplon contribution is discussed focusing on  $x = 1$ . The general trends are the same for other values of  $x$  as well. The second and the third part deal with the two-triplon contribution to Raman spectroscopy and infrared absorption. In all parts results are presented for observables  $\mathcal{O}^I$  and  $\mathcal{O}^{II}$  (see Subsect. 7.3.1).

### 8.7.1 Two-triplon contribution

The two-triplon contribution contains most of the spectral weight in the  $S = 0$  sector (see Sect. 8.4). Nevertheless the three- and four-triplon spectral weights are sizable for  $x \geq 1$  and especially for finite  $x_{\text{cyc}}$ . The latter contributions have to be kept in mind in comparing the results to experimental data and in estimating possible neglected life-time effects. Remember that the observable  $\mathcal{O}^I$  has only contributions with an even triplon number of triplons while the observable  $\mathcal{O}^{II}$  includes contributions of odd and even triplon number.

In Fig. 8.14 results for  $x = 1$  with  $x_{\text{cyc}} = 0.05$  (a) and  $x_{\text{cyc}} = 0.1$  (b) are shown. The upper panels depict the findings for  $\mathcal{O}^I$  and the lower panels give the results obtained for  $\mathcal{O}^{II}$ . The effect of the four-spin interaction can be judged by comparing Fig. 8.14 with Fig. 7.18, the case of  $x = 1$  with  $x_{\text{cyc}} = 0$ . Detailed information about the  $S = 0$  two-triplon bound state dispersion and its  $k$ -resolved spectral weight can be found in Fig. 8.15 for finite  $x_{\text{cyc}}$  and in Fig. 7.19 for  $x_{\text{cyc}} = 0$ .

The first effect to note is that the overall line-shape of the two-triplon spectral density is not changed in the  $S = 0$  case. In analogy to the situation in the  $S = 1$  sector, there is a global shift to lower energies at finite  $x_{\text{cyc}}$  resulting from the change of the one-triplon dispersion.

Both observables yield the same line-shape for  $k = 0$  and  $x_{\text{cyc}} = 0$  (see Sect. 7.7). This symmetry at  $k = 0$  is broken for finite  $x_{\text{cyc}}$ . Nevertheless, the global line-shape of both observables is similar for small momenta. A detailed discussion of the  $k = 0$  contribution will be given in the next subsection about Raman spectroscopy.

In analogy to the situation  $x_{\text{cyc}} = 0$ , both observables differ for large momenta. The main effect of the four-spin interaction besides the global shift of the spectrum is the lowering of the binding energy of the bound state near  $k = \pi$ . The loss of binding energy can be seen clearly in Fig. 8.15. The latter effect is accompanied by a reduction of spectral weight of the bound state near  $k = \pi$  (see right panels of Fig. 8.15 and Fig. 7.19). The spectral weight is shifted to the two-triplon continuum which becomes more pronounced for increasing  $x_{\text{cyc}}$ .

The dark long-dashed curve in Fig. 8.14 represents the lower band edge of the  $S = 0$  four-triplon continuum. The intersection of the two- and four-triplon continuum is larger in the  $S = 0$  case

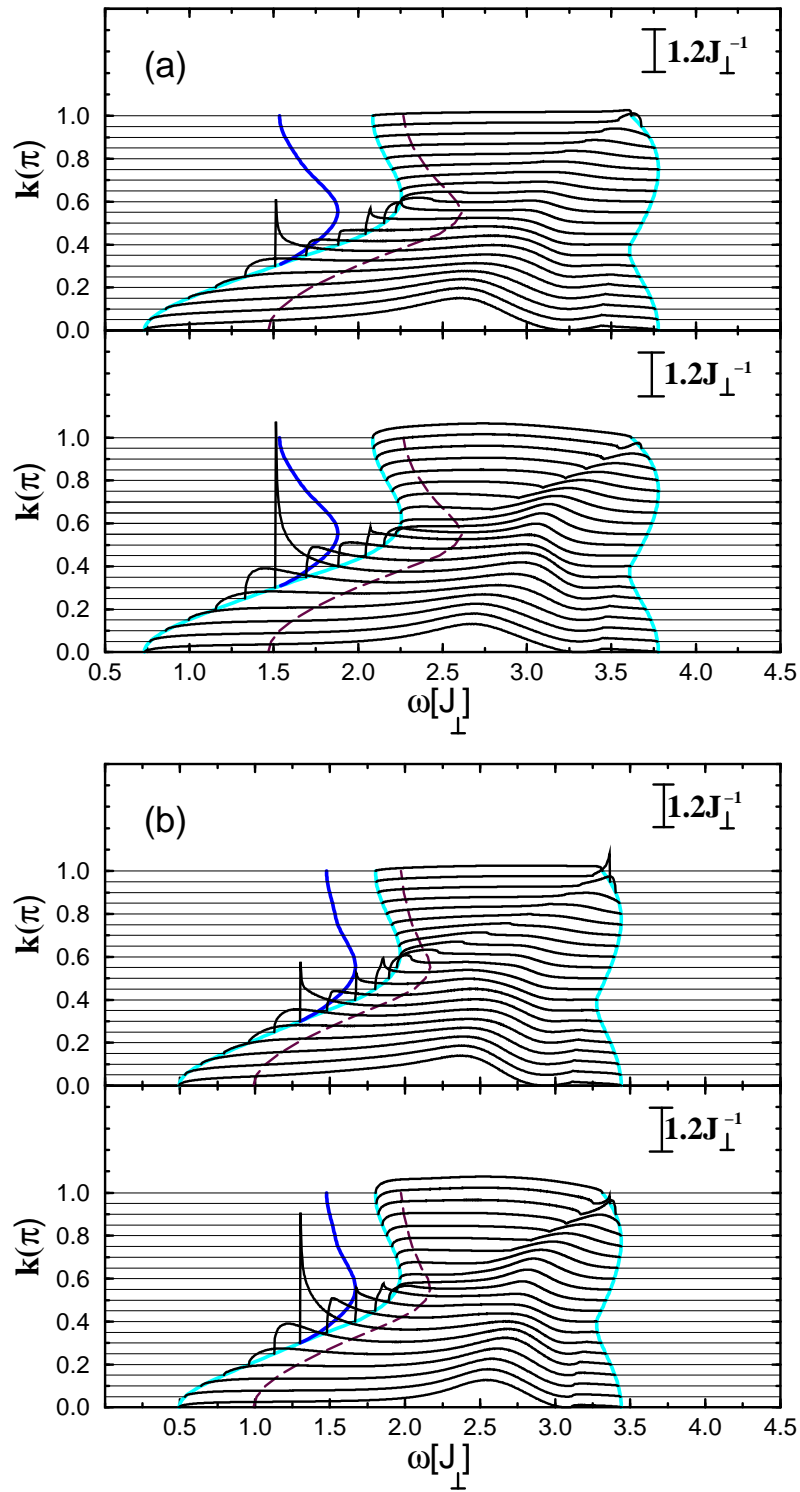


Fig. 8.14: Two-triplon spectral density  $I_2(k, \omega)$  with  $S = 0$  at  $x = 1.0$  with  $x_{\text{cyc}} = 0.05$  (a) and  $x_{\text{cyc}} = 0.1$  (b) is shown. The upper panels correspond to  $\mathcal{O}^I$  and the lower panels to  $\mathcal{O}^{II}$ . The grey lines denote the lower and the upper edge of the two-triplon continuum. The black lines indicate the dispersion of the  $S = 0$  two-triplon bound state. Long-dashed dark grey lines depict the lower edge of the  $S = 1$  four-triplon continuum.

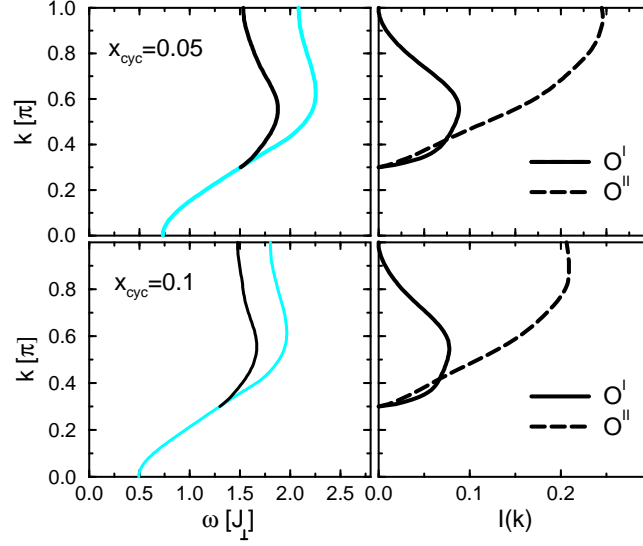


Fig. 8.15: Two-triplon  $S = 0$  bound state energy and spectral weight for  $x = 1.0$  with  $x_{\text{cyc}} = 0.05$  (upper panel) and  $x = 1.0$  with  $x_{\text{cyc}} = 0.1$  (lower panel) is shown. Left panels: The solid grey line denotes the lower edge of the two-triplon continuum and the solid black line depicts the dispersion of the  $S = 0$  two-triplon bound state. Right panels: The  $k$ -resolved spectral weight of the  $S = 0$  two-triplon bound state is plotted as measured by  $\mathcal{O}^I$  (solid line) and by  $\mathcal{O}^{II}$  (dashed line).

than in the  $S = 1$  case due to the larger binding energy of the  $S = 0$  two-triplon bound state. This overlap slightly enhanced by the four-spin interactions. Note that the two-triplon bound state is located below the four-triplon continuum (for all momenta) so that no corrections due to lifetime effects are present for this part of the two-triplon contribution. In addition, the two-triplon contribution displays only broad features for large momenta. Therefore lifetime effects should have only minor effects on this part of the spectrum. This is different for small momenta. Here relatively sharp structures are present in the line-shape which will be affected by including possible decays of two triplons into four triplons. The latter will be discussed in the next subsection.

### 8.7.2 Raman spectroscopy

This subsection deals with the two-triplon contribution to the Raman response. The observables  $R^{\text{rung}}$  ( $R^{\text{leg}}$ ) for magnetic light scattering in rung-rung (leg-leg) polarization are the  $k = 0$  part of  $\mathcal{O}^I$  ( $\mathcal{O}^{II}$ ) [180, 295, 296, 338]

$$R^{\text{leg}} = A_0^{\text{leg}} \sum_i (\mathbf{S}_{1,i} \mathbf{S}_{1,i+1} + \mathbf{S}_{2,i} \mathbf{S}_{2,i+1}) \quad (8.1a)$$

$$R^{\text{rung}} = A_0^{\text{rung}} \sum_i \mathbf{S}_{1,i} \mathbf{S}_{2,i} . \quad (8.1b)$$

The factors  $A_0^{\text{leg}}$  and  $A_0^{\text{rung}}$  depend on the underlying microscopic electronic model. It is beyond the scope of the present work to compute them. Equally, no resonating Raman excitation processes are considered. Results will be given in units of the factors  $[A_0^{\text{leg}}]^2$  and  $[A_0^{\text{rung}}]^2$ .

Channels with odd number of triplons are inaccessible by Raman scattering due to the invariance of the two observables  $R^{\text{leg}}$  and  $R^{\text{rung}}$  with respect to reflection about the centerline of the ladder. Thus only excitations with even number of triplons matter. Therefore the leading contributions to the Raman response come from the 2-triplon and the 4-triplon sector.

In Fig. 8.16(a-c) and in Fig. 8.17(a-c), the result for the two-triplon contribution for both observables with  $x \in \{0.5; 0.75; 1.0; 1.25\}$  and  $x_{\text{cyc}} \in \{0.0; 0.05; 0.1\}$  is shown. All curves are normalized to  $0.4[A_0^2]$  and shifted by  $x$  in order to distinguish between the various curves. The line shape is the same for  $x_{\text{cyc}} = 0$  as mentioned already in Sect. 7.7 (see also [347]) because the Hamiltonian is a weighted sum of the two observables  $H = R^{\text{rung}} + xR^{\text{leg}}$  (for  $A_0 = 1$ ). Thus the excited state  $R^{\text{rung}}|0\rangle$  equals  $-xR^{\text{leg}}|0\rangle$  except for a component proportional to the ground state  $|0\rangle$  which does not matter at finite frequencies.

First the case  $x_{\text{cyc}} = 0$  is considered (Fig. 8.16a and Fig. 8.17a). The spread of the lines on increasing  $x$  indicates clearly the increasing band width. For small  $x$  the Raman intensity shows a strong resonance near the lower band edge [180]. This resonance is a consequence of the 2-triplet attraction on neighboring sites [251, 348]. Since the kinetic energy of the relative motion of the triplons increases for larger  $x$  the influence of the attraction decreases. Therefore, the resonance is rapidly broadened and shifted to the center of the continuum. In view of the analysis of the spin gap [349] one should note that it is not possible to detect the onset of the 2-triplon, non-resonant Raman continuum, i.e. twice the spin gap, reliably for  $x \gtrsim 0.4$  because there is only little weight at the lower band edge [180]. Furthermore, it is found that the non-resonant line shapes do not depend much on the excited state  $R|0\rangle$ . The qualitative features depend more on the kinetics and on the interaction than on the matrix elements.

In Figs. 8.16a and 8.17a for  $x > 0.6$ , a second peak is visible near the upper boundary of the 2-triplon continuum, becoming more pronounced on increasing  $x$  [180, 338]. This feature is the combined effect of 1-triplon kinetics, 2-triplon interaction and matrix elements. First, the occurrence of a dip in the 1-triplon dispersion  $\omega(k)$  at  $k = 0$  leads to an additional van-Hove singularity situated at  $2\omega(0)$  providing additional spectral weight. Second, the additional spectral weight is separated from the main peak by a double zero in the spectral density. This double zero stems from a simple zero in the matrix elements implying that at a certain energy  $\omega$  the state  $R|0\rangle$  is orthogonal to the excited state  $|\omega\rangle$ . This intriguing phenomenon results from destructive interference between several coupling contributions. It is found that the destructive interference is triggered by the 2-triplon interaction since it vanishes when the 2-triplon interaction is switched off by hand [188]. Hence the orthogonality is induced by the interaction. Indeed, an arbitrarily small amount of the interaction suffices to induce at least a very narrow dip with the double zero at its bottom. One is led to the conclusion that the large density of states provided by the additional van-Hove singularity renders the system particularly susceptible to the interaction-induced orthogonality.

The latter point has to be confronted with possible life-time effects originating from the decay of two-triplons into four-triplons as discussed already in the last Section [326]. The four-triplon



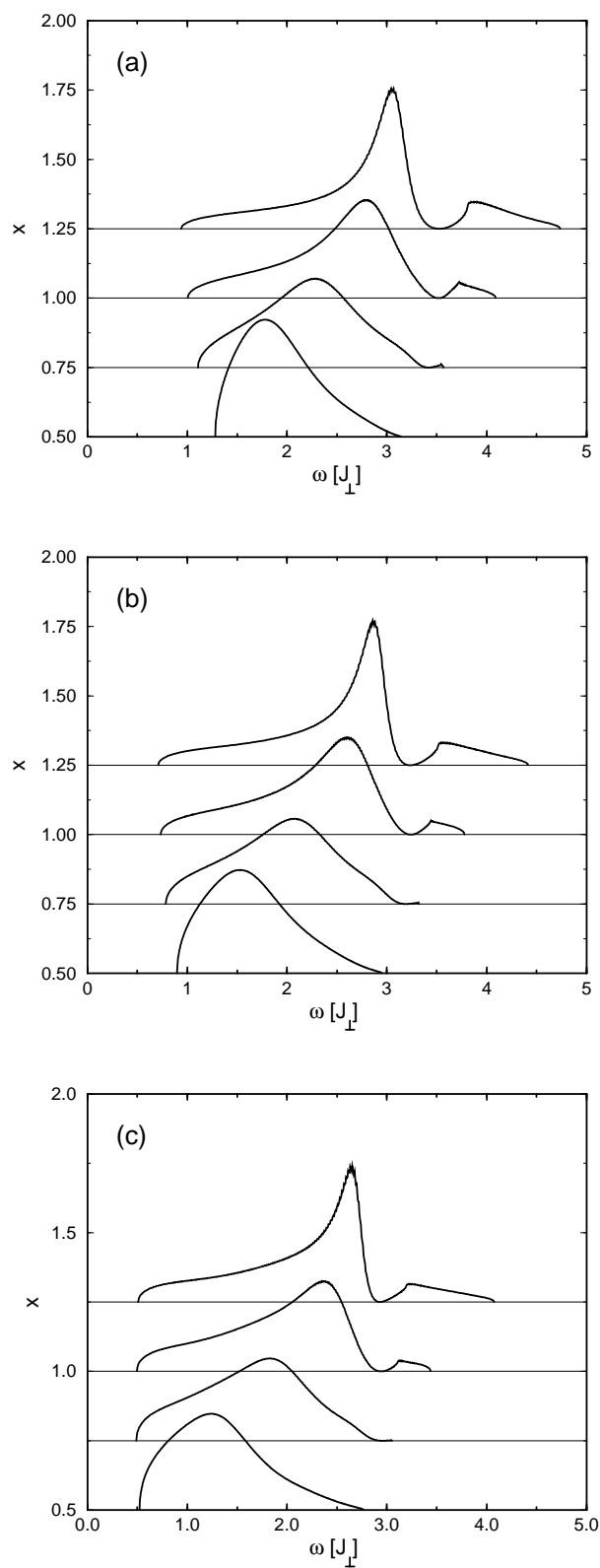


Fig. 8.16: Two-triplon contribution to the Raman response is shown as measured by  $\mathcal{O}^{\parallel}$  with (a)  $x_{\text{cyc}} = 0$ , (b)  $x_{\text{cyc}} = 0.05$  and (c)  $x_{\text{cyc}} = 0.1$ . All curves are normalized to  $0.4[A_0^2]$ .

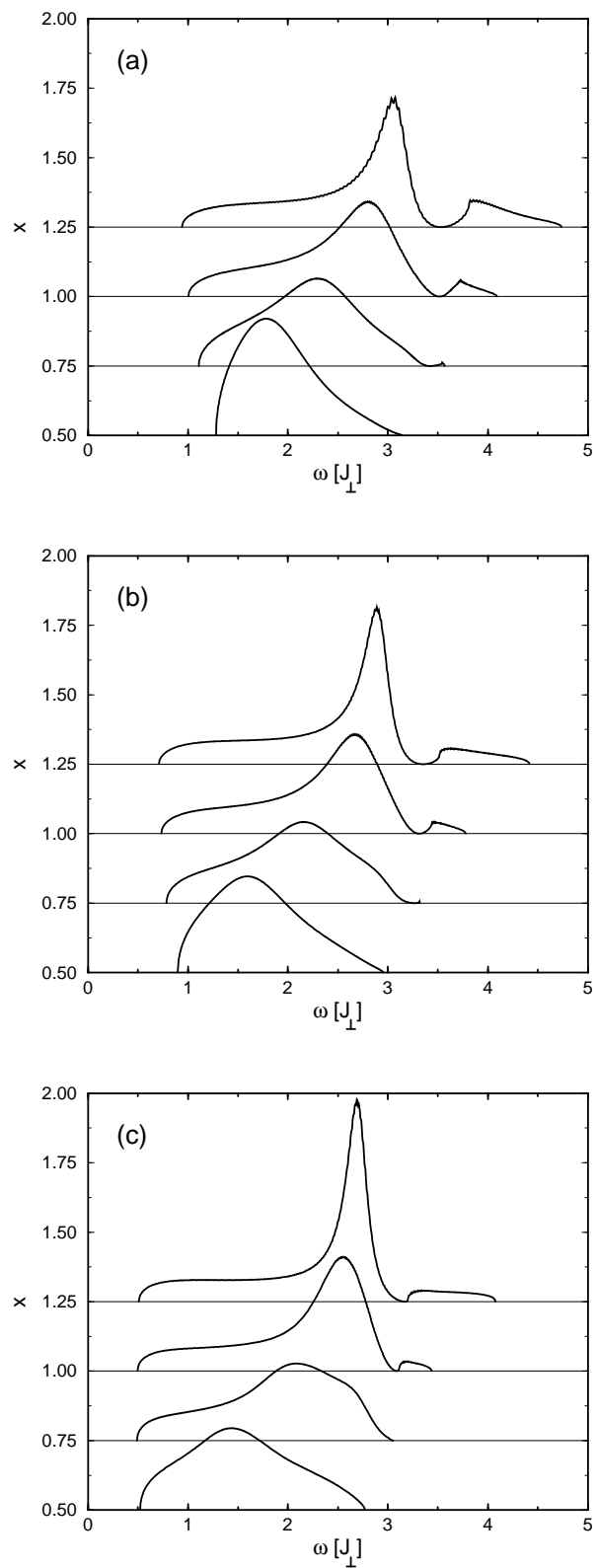


Fig. 8.17: Two-triplon contribution to the Raman response is shown as measured by  $\mathcal{O}^{\parallel}$  with (a)  $x_{cyc} = 0$ , (b)  $x_{cyc} = 0.05$  and (c)  $x_{cyc} = 0.1$ . All curves are normalized to  $0.4[A_0^2]$ .

continuum intersects significantly with the two-triplon continuum. In addition, the four-triplon contribution becomes sizable especially for  $x \geq 1$  [180]. Therefore it is probable that the appearance of the double zero in the Raman response is a consequence of the neglect of life-time effects. The latter processes should produce a high energy shoulder rather than a zero plus second peak at high frequencies.

Note that the results shown in this work differ from those in Ref. [180] for  $x \geq 1$ . In the older work the optimized perturbation theory is used which is not reliable for  $x \geq 1$ . Here the method of internal parameters is used as explained in the previous sections which gives more reliable results (see also [338]).

The influence of the four-spin interaction is illustrated in Figs. 8.16b-c and 8.17b-c. The line shape of  $R^{\text{rung}}$  and  $R^{\text{leg}}$  for finite  $x_{\text{cyc}}$  does not need to be the same anymore for  $x_{\text{cyc}} > 0$ . It can be seen clearly that the line-shape of  $R^{\text{rung}}$  is almost unchanged by turning on  $x_{\text{cyc}}$  while the line-shape of  $R^{\text{leg}}$  does change. Nevertheless, the overall difference between the line-shapes in both polarizations stays small for the parameters discussed in this chapter. The main effect of the four-spin interaction besides the global shift to lower frequencies of all spectra is a sharpening of the two-triplon peak if measured by  $R^{\text{leg}}$ . In addition, an almost constant plateau is produced for frequencies smaller than the two-triplon peak in this polarization.

### 8.7.3 IR-absorption

In this section the results obtained for the two-triplon spectral density are compared to phonon-assisted infrared absorption of magnetic excitations similar to the discussion for the dimerized and frustrated spin-chain in Sect. 6.5. The leading infrared-active magnetic absorption is a two-triplon-plus-phonon process [277, 278]. Note that also three- and four-triplon processes can give a sizable contribution to the infrared absorption depending on the exchange couplings of the ladder (see Fig. 8.6).

The two-triplon spectral density  $I_2(k, \omega)$  has to be integrated over all momenta weighted with a phonon-specific form factor  $|f_{\text{ph}}(k)|^2$  in order to obtain the two-triplon part of the infrared absorption  $I_{2\text{trp}}^{\text{IR}}$

$$I_{2\text{trp}}^{\text{IR}}(\omega) = \omega \int_0^\pi dk |f_{\text{ph}}(k)|^2 I_2(k, \omega) \quad . \quad (8.7.2)$$

The precise form of the phonon form factor  $|f_{\text{ph}}(k)|^2$  depends on the specific phonon which is involved in the process. It will be seen in the next section that in realistic cases often more than one phonon is active. Different phonons have usually different form factors and so the superposition of several contributions has to be considered. First, the general properties of  $I_{2\text{trp}}^{\text{IR}}$  are discussed for the commonly used form factor

$$|f_{\text{ph}}(k)|^2 = \sin^4(k/2) \quad . \quad (8.7.3)$$

The latter corresponds to the stretching modes of the oxygen in the legs of cuprate ladders [351]. In Figs. 8.19 and 8.18, results are shown for rung and for leg polarization. The spectra comprise an additional broadening of  $\Gamma = 0.02J_{\text{perp}}$  which is reasonable in view of the comparison with

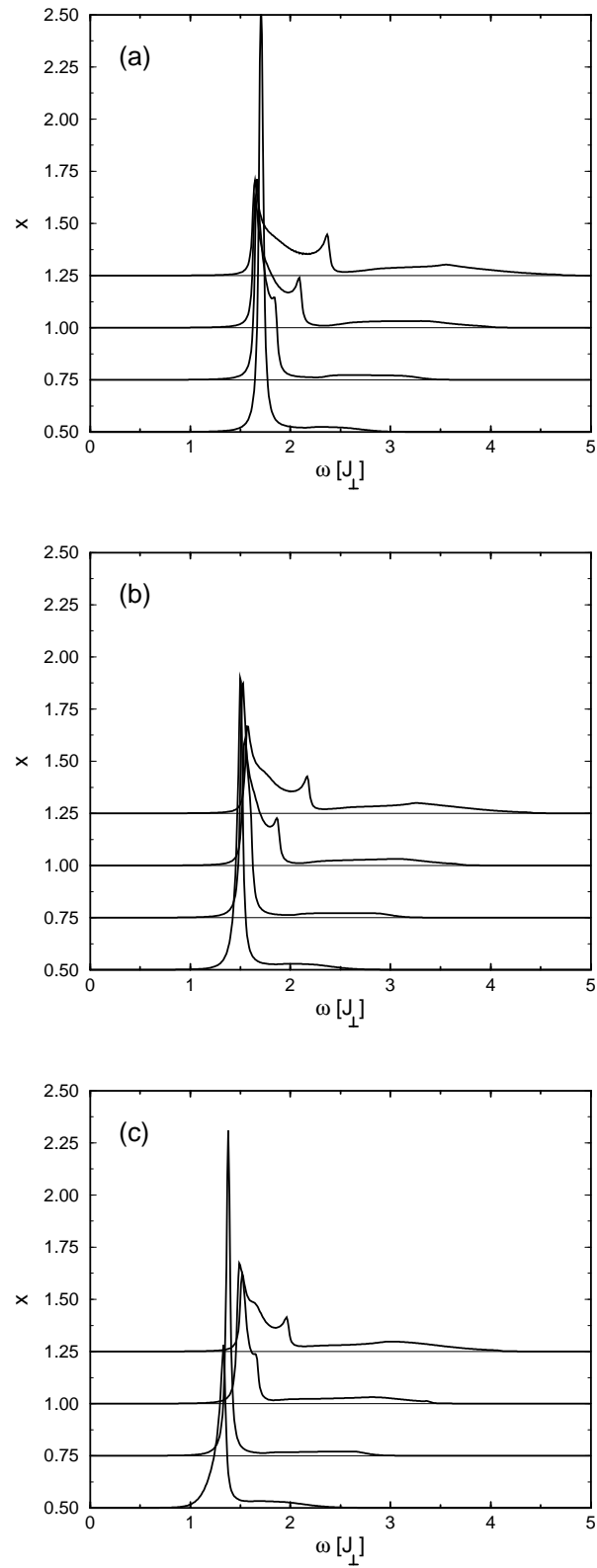


Fig. 8.18: Two-triplon contribution to the infrared absorption  $I_{2\text{trp}}^{\text{R}}$  in leg polarization is shown as measured by  $\mathcal{O}^{\parallel}$  with (a)  $x_{\text{cyc}} = 0$ , (b)  $x_{\text{cyc}} = 0.05$  and (c)  $x_{\text{cyc}} = 0.1$  and a broadening of  $\Gamma = 0.02J_{\perp}$ .  $|f_{\text{ph}}(k)|^2 = \sin^4(k/2)$  is used as the phonon form factor. All curves are divided by 100.

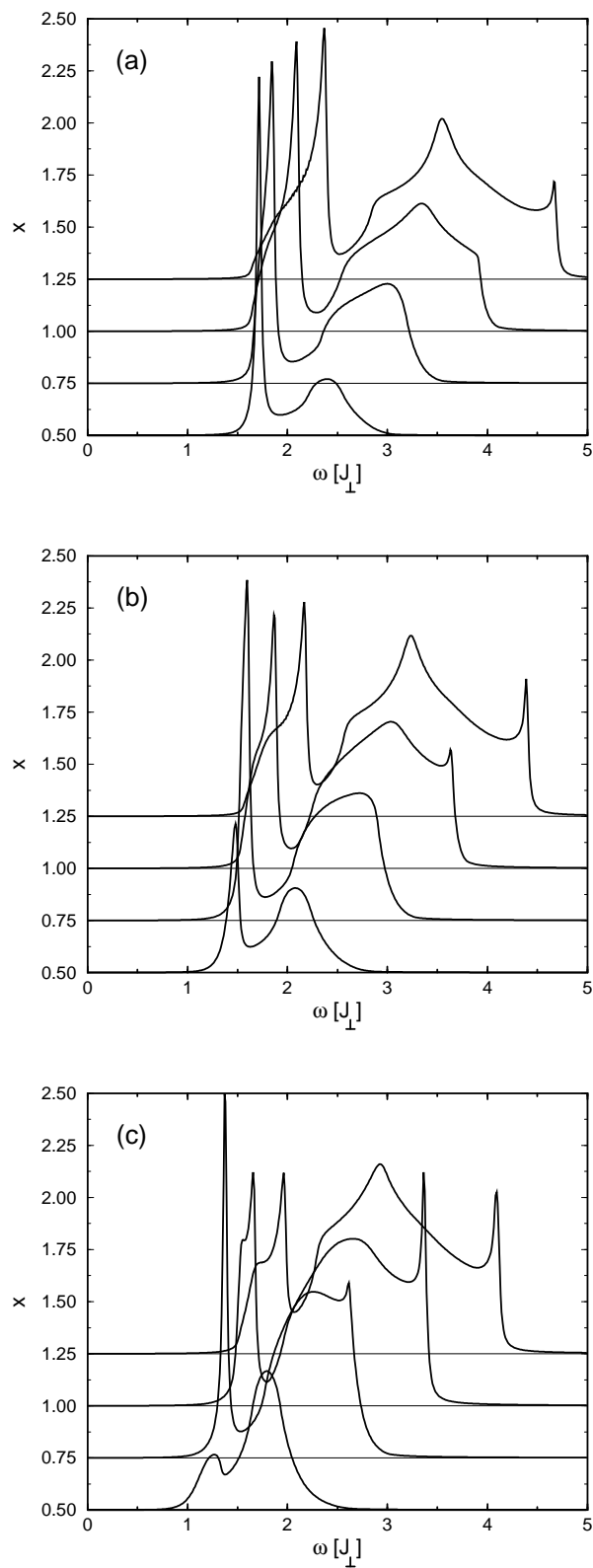


Fig. 8.19: Two-tripion contribution to the infrared absorption  $I_{2\text{trp}}^{\text{R}}$  in rung polarization is shown as measured by  $\mathcal{O}^{\text{I}}$  for with (a)  $x_{\text{cyc}} = 0$ , (b)  $x_{\text{cyc}} = 0.05$  and (c)  $x_{\text{cyc}} = 0.1$  and a broadening of  $\Gamma = 0.02J_{\perp}$ .  $|\tilde{f}_{\text{ph}}(k)|^2 = \sin^4(k/2)$  is used as the phonon form factor. All curves are divided by 10.

experiment<sup>3</sup>. All curves are shifted by their  $x$ -value for clarity.

First the case  $x_{\text{cyc}} = 0$  is discussed (Fig. 8.19a and Fig. 8.18a). Results are shown for  $x \in \{0.5; 0.75; 1.0; 1.25\}$ . The phonon form factor Eq. 8.7.3 strongly favors large momenta while small momenta almost do not contribute to  $I_{2\text{trp}}^{\text{IR}}$ . In leg polarization (Fig. 8.18a) three features are present in the spectra: two peaks at lower energies and a broad hump at higher energies. At lower energy the spectrum is dominated by the two-triplon  $S = 0$  bound state which was predicted for small values of  $x$  [350]. The bound state dispersion displays a maximum at  $k \approx \pi/2$  and a minimum at  $k = \pi$  (see Sect. 8.5.3). Both give rise to van Hove singularities in the density of states which cause peaks in  $I_{2\text{trp}}^{\text{IR}}$ . The spectral weight of the bound state has a maximum at  $k = \pi$  for  $\mathcal{O}^{\text{II}}$  (Fig. 8.15). The two-triplon contribution in leg polarization shows therefore two peaks originating from the extrema of the dispersion of the two-triplon bound state. The intensity of the first peak is larger. The peaks are more clearly seen for larger values of  $x$  because the difference between maximum and minimum of the two-triplon bound state dispersion increases with increasing  $x$ . The third broad peak originates from the two-triplon continuum. This phonon form factor focuses mainly on the spectral density near  $k = \pi$ . The spectral density of the two-triplon continuum is a large hump for large momentum. Therefore it displays almost no structure for this phonon form factor.

In rung polarization the three features are also present but the intensity is distributed differently (see Fig. 8.19). Here the spectral weight of the two-triplon bound state has a minimum at  $k = \pi$  (Fig. 8.15). Therefore the first low-energy peak is only a low-energy shoulder which becomes more pronounced for larger  $x$  values. The dominant peak results from the van Hove singularity at  $k \approx \pi/2$ . The contribution of the two-triplon continuum is more important in this polarization. The sharp structure at high energies is most probably an artefact of the extrapolation. Possible life time effects will smear out this feature.

Next the influence of the four-spin interaction on the two-triplon contribution to the infrared absorption is discussed (Fig. 8.19b-c and Fig. 8.18b-c). First, the largest effect is again a redshift of the entire spectra due to the shift of the one-triplon dispersion to lower energies by turning on  $x_{\text{cyc}}$ . Second, the reduced attractive interaction introduced by  $x_{\text{cyc}}$  results in a lower binding energy of the two-triplon bound state. Thus the distance of the first two low-energy peaks in the infrared absorption spectra is reduced by a finite value of  $x_{\text{cyc}}$ . In addition, spectral weight is shifted from the two-triplon bound state to the two-triplon continuum.

The effect of different phonon form factors on  $I_{2\text{trp}}^{\text{IR}}$  is shown in Fig. 8.20 for both polarizations with  $x = 1$  and  $x_{\text{cyc}} = 0$ . The relevant form factors are  $|f_{\text{ph}}(k)|^2 = \sin^2(k/2) + 1/2$ ,  $|f_{\text{ph}}(k)|^2 = \sin^2(k/2)$  and  $|f_{\text{ph}}(k)|^2 = 1$  [351]. In contrast to the case considered first, these form factors do not focus entirely on large momenta around  $k = \pi$ . So changing the form factor will result in a different intensity distribution.

This can be seen clearly in the relative spectral weight of the first two peaks originating from the two-triplon bound state. Changing the form factor from  $|f_{\text{ph}}(k)|^2 = \sin^4(k/2)$  to  $|f_{\text{ph}}(k)|^2 = 1$ , the spectral weight of the first peak is reduced while the spectral weight of the second peak increases.

<sup>3</sup>Note that the experimental resolution is higher. The chosen  $\Gamma$  corresponds is a typical value for the infrared absorption on spin ladders. Here the effect of a finite phonon dispersion or disorder in the compound is included.

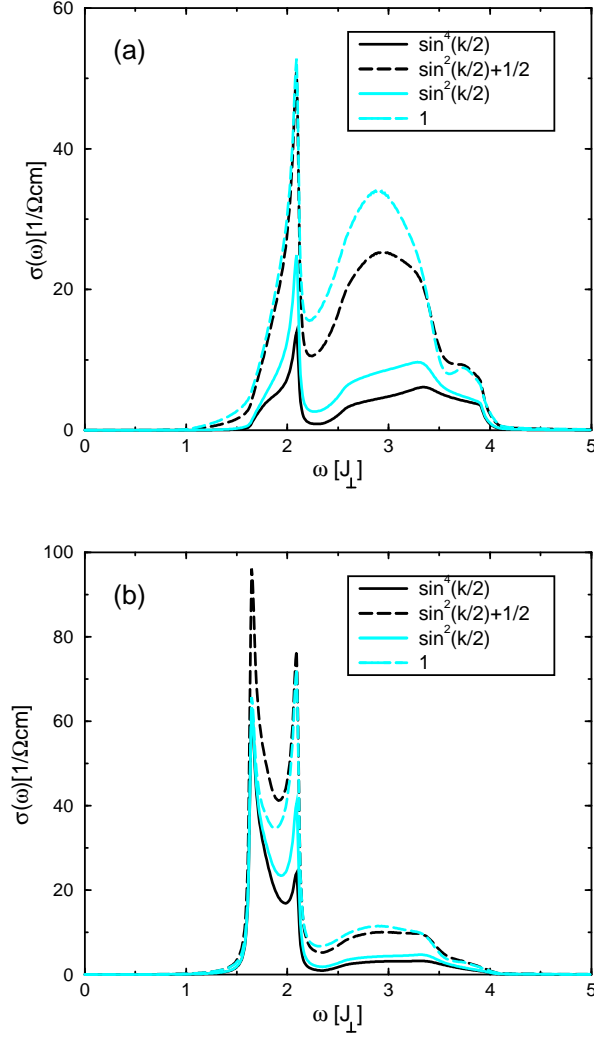


Fig. 8.20: The two-tripion contribution to the infrared absorption is shown as measured by  $\mathcal{O}^I$  (a) and  $\mathcal{O}^{II}$  (b) for  $x = 1$  and  $x_{\text{cyc}} = 0$  and various phonon form factors  $|f_{\text{ph}}(k)|^2$ . A broadening of  $\Gamma = 0.02J_{\perp}$  is used.

The line-shape of the third broad peak is changing from a plateau-like shape to a round shape for the form factors not containing a constant part. The spectral weight of the two-tripion continuum is concentrated for  $k \in \{0; \pi/2\}$  almost constantly at the energy of the  $k = 0$  two-tripion peak. This property produces the round shape in the infrared absorption. This is absent for  $|f_{\text{ph}}(k)|^2 = \sin^4(k/2)$  and  $|f_{\text{ph}}(k)|^2 = \sin^2(k/2)$ .

The contribution in leg polarization is a sum of odd and even triplon channels. The analysis of the spectral weights showed that a sizable contribution of the three-tripion channel to the infrared absorption can be expected (see Sect. 8.4). A sizable contribution with odd symmetry in leg polarization was already found with DMRG [324]. This can be almost completely identified with the three-tripion contribution because the contribution of five triplons or more should be negligible.

The three-triplon contribution (not shown here) is a broad hump with its spectral weight located at the low-energy part of the three-triplon continuum due to the strong two-triplon interaction [327]. The contributions with odd parity are absent in rung polarization. Therefore the next correction is the four-triplon contribution which can be expected to be a rather featureless and broad structure. The two-triplon spectra presented should contain the essential physics in this energy range. Possible discrepancies to the experimental data originate most probably from neglecting of life-time effects and from related extrapolation uncertainties.

## 8.8 Cuprate Ladders

This section provides information about the current theoretical understanding of the spectroscopic properties of magnetic excitations in cuprate two-leg ladder systems. The obtained theoretical results presented so far are related to experiments.

The prototype of a two-leg cuprate ladder is the  $\text{SrCu}_2\text{O}_3$  system. Unfortunately, no large single crystals of this compound are available. There is only a Raman spectroscopy study [317] of this material. Large single crystals can be grown of the telephone number compounds  $\text{A}_{14}\text{Cu}_{24}\text{O}_{41}$  so that the majority of experimental data was collected for these compounds [298, 337, 349].

### 8.8.1 Undoped telephone number compound

The nominally undoped sample containing only  $\text{Cu}^{2+}$  is  $\text{La}_x\text{Ca}_{14-x}\text{Cu}_{24}\text{O}_{41}$  with  $x = 6$ . Single-phase crystals could only be synthesized for  $x \leq 5.2$  [352]. Polarized x-ray absorption data [318] show that at least for  $x > 2$  the holes are located within the second structural unit of these compounds, the  $\text{CuO}_2$  chains, so that the two-leg ladders can be considered as undoped for  $x > 2$  [189, 298]. The exchange coupling in the  $\text{CuO}_2$  chains is much weaker than in the ladders since it is mediated via Cu-O-Cu bonds with an angle close to  $90^\circ$ . Therefore the spectroscopic contribution of the chains and of the ladders is separated energetically.

The need of four-spin interaction in the magnetic model arose in the simultaneous description of inelastic neutron scattering data [337] and infrared absorption data [298]. The first quantitative determination of the exchange couplings  $J_\perp$ ,  $J_\parallel$  and  $J_{\text{cyc}}$  was performed in Ref. [324]. There the one-triplon gap from inelastic neutron scattering data and the two low-energy peak energies of the infrared absorption originating from the  $S = 0$  two-triplon bound state (see last section) are used to fix the three exchange constants to

$$\begin{aligned} J_\perp &= 1150 \pm 150 \text{cm}^{-1} \\ x &= 1.22 \pm 0.05 \\ x_{\text{cyc}} &= 0.105 \pm 0.015 \end{aligned} .$$

In Fig. 8.21 the result for  $x = 1.25$  and  $x_{\text{cyc}} = 0.09$  obtained by the continuous unitary transformation is displayed. The phonon form factors used are [324]

$$f_{\text{ph}}^{\text{leg}} = 8 \sin^4\left(\frac{k}{2}\right) \quad \text{and} \quad f_{\text{ph}}^{\text{rung}} = 8 \sin^2\left(\frac{k}{2}\right) + 4 \quad . \quad (8.8.1)$$



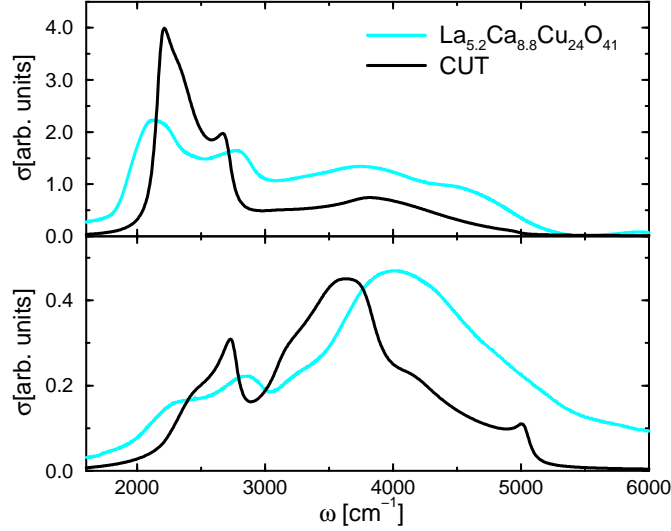


Fig. 8.21: Comparison of the infrared absorption of  $\text{La}_{5.2}\text{Ca}_{8.8}\text{Cu}_{24}\text{O}_{41}$  (grey lines) at  $T=4$  K with the two-triplon contribution calculated by CUT (black lines) for  $J_{\parallel}/J_{\perp} = 1.25$ ,  $J_{cy}/J_{\perp} = 0.09$ ,  $J_{\perp} = 1060 \text{ cm}^{-1}$ ,  $\omega_{ph}^{\text{leg}} = 570 \text{ cm}^{-1}$ ,  $\omega_{ph}^{\text{rung}} = 620 \text{ cm}^{-1}$  and a finite broadening of  $\Gamma = 0.05J_{\perp}$ . (**Top panel**) Polarization parallel to the legs. The missing weight is mainly due to the sizeable three-triplon contribution. (**Bottom panel**) Rung polarization. Here, the leading omitted correction is the small four-triplon part

Note that the exchange parameters are quite challenging for the extrapolation. Nevertheless a semi-quantitative agreement can be reached. It seems that the extrapolation overestimates the two-triplon interaction amplitudes for these parameters so that the spectral weight is shifted to lower energies. In comparison to the DMRG results [324], the CUT is able to resolve the two low-energy peaks better due to the smaller broadening. Clearly, a sizable contribution is missing in leg polarization. The theoretical spectrum in Fig. 8.21 is scaled such that the spectral weight for  $\omega < 3000 \text{ cm}^{-1}$  is equal in experiment and theory. This part originates from the two-triplon bound state. It contains in leg polarization about 45% of the total weight. The contribution of the two-triplon continuum in this polarization contains about 25% of the total weight. The missing 30% spectral weight can be identified with the three-triplon contribution [327]. This is in agreement with the analysis of the spectral weights in Sect. 8.4 and with DMRG results [324]. In contrast, the total spectral weight is already correct in rung polarization. Here the next correction is the four-triplon contribution which is small.

A direct probe of the magnetic excitations is obtained by INS experiments. Especially the one-triplon properties are accessible. Unfortunately, the only INS data published on this compound have only a poor momentum resolution [337, 353] as shown in Fig. 8.22 (left panel). No decisive quantitative

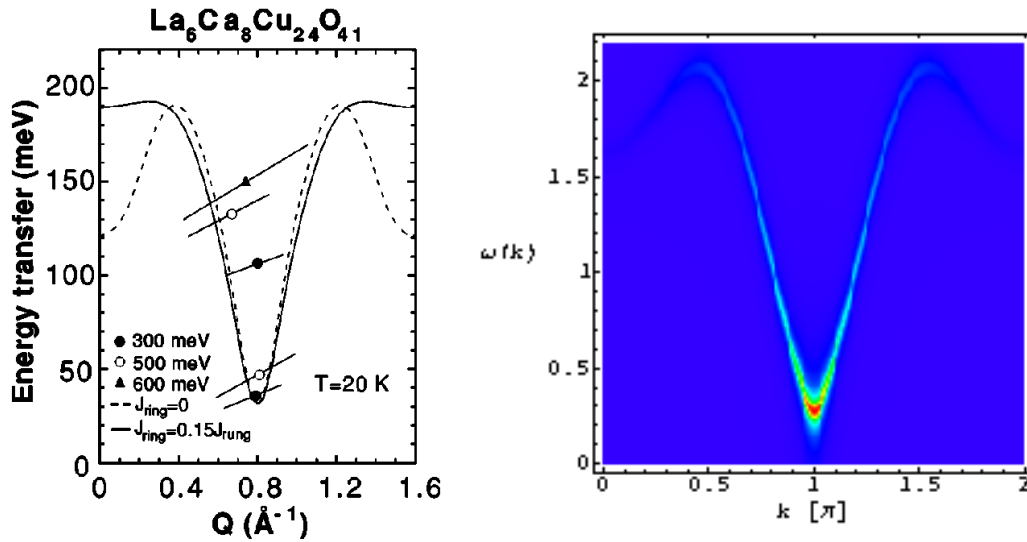


Fig. 8.22: **(Left panel)** Experimentally deduced one-triplon dispersion relation  $\omega(Q)$  reduced to a single Brillouin zone for the two-leg spin-ladder in  $\text{La}_6\text{Ca}_8\text{Cu}_{24}\text{O}_{41}$  [353] obtained by inelastic neutron scattering. Black curves represent theoretical results obtained by exact diagonalisation of 12 rungs (for details see [353]). **(Right panel)** Calculated one-triplon contribution to the dynamical structure factor for  $x = 1.25$  and  $x_{\text{cyc}} = 0.09$ . An additional broadening of  $\Gamma = 0.05J_{\perp}$  is used.

conclusion can be drawn from this experimental data concerning the exchange couplings. So a new experimental INS study with high momentum resolution is desirable to study the full one-triplon dispersion and the full one-triplon spectral weight. In addition, the study of two-triplon properties with total spin one would come into reach in such an experiment.

The one-triplon contribution to the dynamical structure factor for  $x = 1.25$  and  $x_{\text{cyc}} = 0.09$  is shown in Fig. 8.22 (right panel) with a broadening of  $\Gamma = 0.05$ . The extrapolation is reliable in this regime so that the results should be quantitatively correct. The intensity is concentrated at the one-triplon gap  $\Delta$ . It is reduced strongly at momenta far away from  $k = \pi$ . It can be expected that an additional structure occurs in experiment at  $k = \pi$  corresponding to the lower-band edge of the two-triplon continuum situated at  $\omega \approx 1.9J_{\perp}$ . Note that the two-triplon bound state with total spin one is absent in this parameter regime because  $J_{\text{cyc}}$  is too large. The right panel represents a clear theoretical prediction<sup>4</sup> which can guide future experimental work.

Raman spectroscopy is the third spectroscopic tool to analyze magnetic excitations. It probes  $S = 0$  excitations with momentum zero. The Raman observable couples to the even part concerning the parity with respect to reflection at the centerline of the ladder as discussed in Sect. 8.7. The Raman response consists therefore of a dominant two-triplon contribution plus a four-triplon part. It was discussed in Sect. 8.7 that the line shape of both polarization is identical for  $x_{\text{cyc}} = 0$  in both polarization. Differences are introduced by turning on the four-spin interactions. The result for  $x = 1.25$  and  $x_{\text{cyc}} = 0.09$  is shown in Fig. 8.23 with a broadening of  $\Gamma = 0.02$ . The experimental

<sup>4</sup>Note that the right panel of Fig. 8.22 displays only the one-triplon contribution to the dynamical structure factor. The two-triplon contribution will give rise to additional high-energy features.

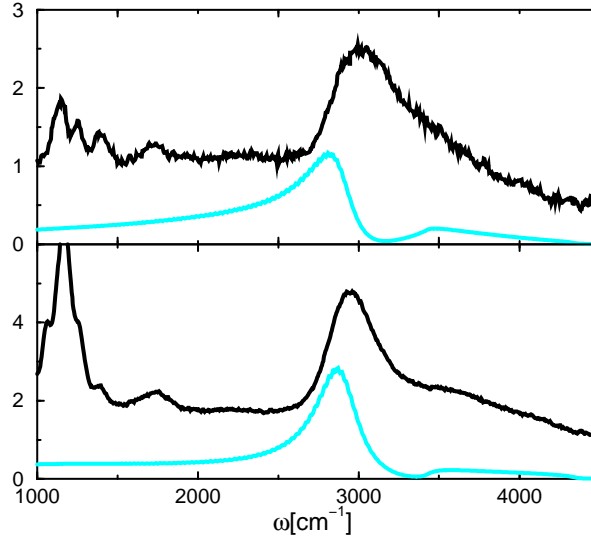


Fig. 8.23: Comparison of the Raman response of  $\text{La}_6\text{Ca}_8\text{Cu}_{24}\text{O}_{41}$  (black lines) [349] with the two-triplon contribution calculated by CUT (red lines) for  $J_{\parallel}/J_{\perp} = 1.25$ ,  $J_{cyc}/J_{\perp} = 0.09$ ,  $J_{\perp} = 1060 \text{ cm}^{-1}$ , and a finite broadening of  $\Gamma = 0.02J_{\perp}$ . (**Top panel**) Polarization parallel to the legs. (**Bottom panel**) Rung polarization.

data display a similar line-shape in both polarizations. It is dominated by the two-triplon peak at about  $3000 \text{ cm}^{-1}$  accompanied by a shoulder at the high energy side. At energies lower than the two-triplon peak the spectra show a plateau with some additional small substructures which are probably not of magnetic origin (see also discussion below on modulation effects). The position and the width of the two-triplon peaks can be fairly well described by the theoretical curves. Note that the exchange couplings used are optimized to fit *all* presented experimental data in order to use only one set of parameters. So the Raman data is not fitted.

Theory and experiment differ at high energies. The theoretical two-triplon contribution displays a zero in the spectrum and an additional high energy peak. Possible life-time effects are most probably responsible for this difference. The latter is corroborated by the fact that the four-triplon density of states is large in the region of the zero because the zero is located approximately at twice the  $S = 0$  two-triplon bound state energy at  $k = \pi$ . So it is expected that a decay of two triplons into four triplons is especially large in this region and leads to a filling of the zero resulting in a shoulder at high energy as seen in the experiment.

### 8.8.2 Structural modulations

Up to this point the spectroscopic properties of the telephone number compounds were explained by an isolated two-leg ladder neglecting the presence of the CuO chains. In spite of the fact that a direct contribution of the spin-chains is small, an indirect influence of the chain subsystem can

result in a sizable modulation of the magnetic exchange constants of the ladder. These modulations can be caused by the differing periodicity of the chains and the ladders in one unit cell and by a charge ordering of holes which also leads to a modulation of the exchange constants [338]. In this subsection a brief discussion is given how these modulation can affect the energy and the spectral properties of the ladder. Here the focus is laid on the modulation which originates from the different periodicities of chains and ladders.

There are ten sites of the chain and seven sites of the ladder in one unit cell. The presence of the chains makes the rungs in the ladder inequivalent. Therefore seven inequivalent ladder rungs per formula unit (f.u.) are present. Hence it is plausible to assume that the ladder is modulated. This modulation is characterized by the wave vector  $Q_S = 10/7 = 3/7 + 1$  in reciprocal lattice units (r.l.u.) of the ladder. In the magnetic subsystem of the spins on the Cu sites of the ladder, wave vectors are only meaningful modulo unity so that  $Q_S = 10/7$  and  $Q_S = 3/7$  are equivalent (see also Ref. [338]).

These modulations can be estimated from the modulated positions of the atoms at room temperature [338] to be

$$J_{\parallel,i} = J_{\parallel} [1 + 0.05 \cos(2\pi \frac{3}{7}(i + \frac{1}{2}))] \quad (8.8.2a)$$

$$J_{\perp,i} = J_{\perp} [1 - 0.10 \sin(2\pi \frac{3}{7}i) + 0.05 \cos(2\pi \frac{6}{7}(i+3))] \quad (8.8.2b)$$

with phase accuracy  $|\Delta i| \lesssim 0.1^5$  where  $i$  counts the leg- or the rung-bonds. The term with  $2Q_S = 6/7$  denotes the second harmonic; overtones with amplitude  $\lesssim 1\%$  are omitted. The amplitudes in Eq. 8.8.2 show that the induced modulation of the couplings is indeed sizeable.

The modulation can be included on the level of the effective model, i.e. *after* the continuous unitary transformation [338]. This is no serious caveat since a microscopic calculation is not available. The leading-order effect of  $J_{\parallel}$  is to enable the triplon to hop from rung to rung by a nearest-neighbor hopping element  $t_1 \propto J_{\parallel}$  and to induce a nearest-neighbor interaction  $w_1 \propto J_{\parallel}$ . So the most straightforward way to account for the modulation of  $J_{\parallel}$  as given in Eq. 8.8.2 and is to modulate  $t_1$  and  $w_1$ ,

$$t_1 \propto w_1 \propto J_{\parallel} \cdot [1 + \sum_{Q=3/7, 6/7} \alpha_Q \cos(2\pi Q i)] . \quad (8.8.3)$$

Here only the effect of a modulation of  $J_{\parallel}$  is discussed in order to describe the general effects of modulations on the spectral properties of two-leg ladders.

The main effect of the modulations is the opening of gaps in the one-triplon dispersion wherever the wave vector  $Q$  links equal energies  $\omega(k) = \omega(k+Q)$  of the unmodulated ladder. Smaller gaps open for higher-order processes, e.g. for  $\omega(k) = \omega(k+2Q)$ . The energies at which gaps open depend decisively on the wave vector of the modulation.

The resulting one-triplon dispersions including the modulations of the coupling given in Eq. 8.8.2 are shown in Fig. 8.25. The different modulation gaps are clearly visible. As there are no high resolution INS data available at the moment, a direct observation of the effects of the modulations

<sup>5</sup>Fig. 8.24 shows the periodicity; the modulation *phases* of the couplings cannot be read off because (i) Cu sites in the chains and ladders are not in line; (ii) each ladder is influenced by the four chains close by which are shifted by different amounts; (iii) the important oxygens are not depicted. For details see Ref. [354].

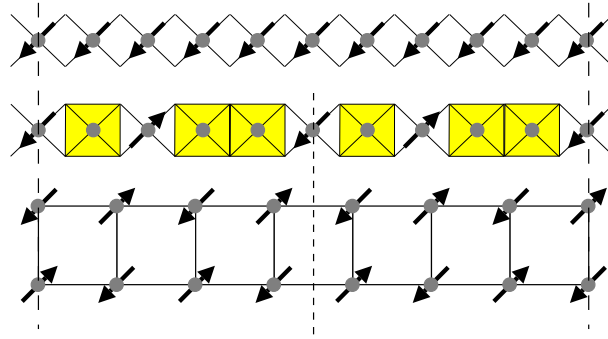


Fig. 8.24: Scheme of the superstructure along the chains and the ladders ( $c$  axis). 10 chain units (top row) match 7 ladder units (bottom row) inducing a modulation in the ladders with wave vector  $Q_S = Q_{\text{ladder}}/c_{\text{chain}} = 10/7 = 3/7 + 1$  (in r.l.u. of the ladder) [354]. In  $\text{Sr}_{14}\text{Cu}_{24}\text{O}_{41}$  the charge order (CO) implies an additional superstructure with  $Q_{\text{CO}} = 2/10$  (in r.l.u. of the *chain*) [355–358], corresponding to a periodicity of  $5 \cdot c_{\text{chain}}$ . It is visualized (middle row) as two units of “spin-hole-spin-hole-hole” per 7 rungs (grey squares denote the six holes per f.u.). This superstructure induces an additional modulation in the ladder with  $Q_{\text{CO}} = Q_{\text{ladder}}/(5 \cdot c_{\text{chain}}) = 2/7$  (in r.l.u. of the ladder).

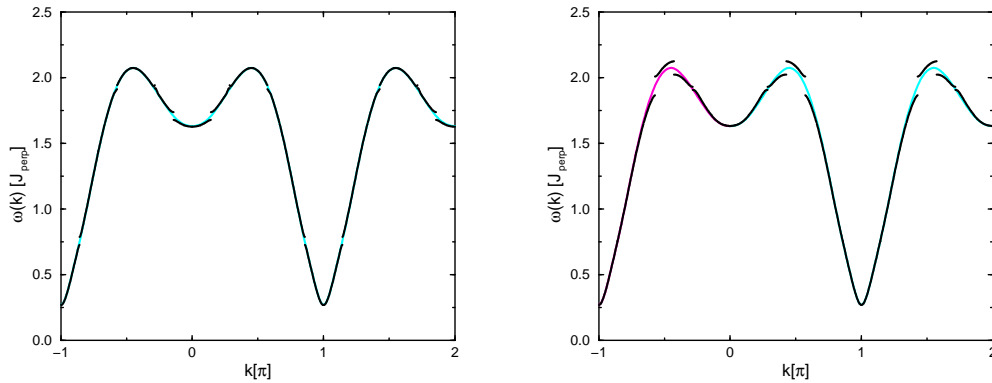


Fig. 8.25: One-triplon dispersion  $\omega(k)$  for  $x = 1.25$  with  $x_{\text{cyc}} = 0.09$  including the effect of structural modulations. Black lines correspond to modulated dispersions and grey lines to the unmodulated dispersions. **(Left panel)** Structural modulation  $Q_S = 6/7$  of strength  $\alpha_{6/7} = 5\%$ . **(Right panel)** Structural modulation  $Q_S = 3/7$  of strength  $\alpha_{3/7} = 10\%$ .

at low temperatures is an open problem.

Next the influence of the modulation on optical experiments is discussed. Obviously, the modulation gaps of the one-triplon dispersion are also present in the two-triplon channel. In addition, the same effect occurs also for two-triplon energies, i.e. energy gaps open in the dispersion of the two-triplon bound state for momenta connected by the modulation. The local two-triplon interaction is modified.

The effect of the modulation on the two-triplon contribution to the Raman response is shown in Fig. 8.26. Here both modulations are applied simultaneously. Since Raman scattering measures excitations with total momentum  $k_{\text{tot}}=0$ , the two-triplon response reflects the excitation of two

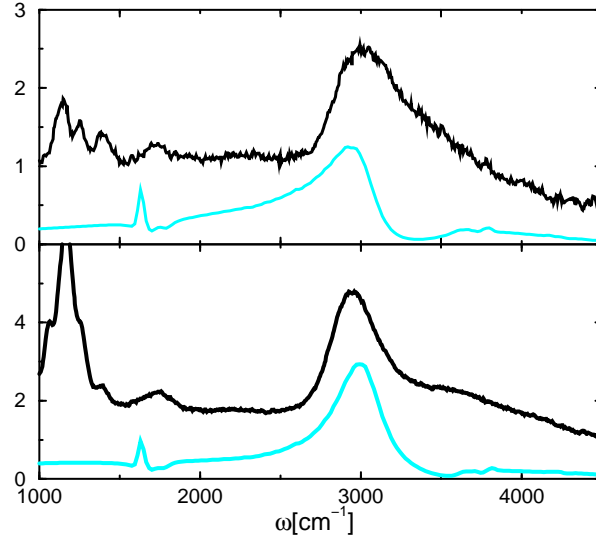


Fig. 8.26: Comparison of the Raman response of  $\text{La}_6\text{Ca}_8\text{Cu}_{24}\text{O}_{41}$  (black lines) [349] with the calculated two-triplon contribution for  $x = 1.25$  with  $x_{\text{cyc}} = 0.09$  and  $J_{\perp} = 1100\text{cm}^{-1}$  including the effect of a modulation (grey lines). An additional broadening of  $\Gamma = 0.02$  is used. A modulation  $Q_S = 6/7$  of strength  $\alpha_{6/7} = 5\%$  and a modulation of  $Q_S = 3/7$  of strength  $\alpha_{3/7} = 10\%$  are applied simultaneously. (**Upper panel**) rung polarization and (**lower panel**) leg polarization.

triplons with momenta  $k_2 = -k_1$  and energies  $\omega(k_1) = \omega(k_2)$ . Thus a gap in the one-triplon dispersion at  $\omega_g$  causes a corresponding feature in the Raman line at  $2\omega_g$ .

The most striking change in the Raman line shape is a new feature at about  $1600\text{cm}^{-1}$ . Looking at the one-triplon dispersions in Fig. 8.25, the only low-energy gap introduced by the modulations is caused by the  $Q_S = 6/7$  modulation which causes a gap in the Raman response at two times this energy. But there is an additional sharp peak inside this gap region where the width of the peak is given by the broadening  $\Gamma$ . A mid-gap two-triplon bound state is therefore found in the Raman response which originates from the structural modulation  $Q_S = 6/7$ . Indeed, additional structures are also found in the experiment at about  $1700\text{cm}^{-1}$  in both polarizations and in almost all members of the telephone number compounds [349]. The structural modulation  $Q_S = 3/7$  only influences the spectrum slightly at high energies.

The experimental relevance of the modulation on the infrared absorption in  $\text{La}_{5.2}\text{Ca}_{8.8}\text{Cu}_{24}\text{O}_{41}$  is rather small. This is due to the relatively broad spectra. A relatively large broadening has to be used which washes out the introduced new structures. In addition, there are actually two different phonons involved in every polarization [351] so that fine structures are averaged out.

Generically, the largest effect of the modulations is on the two low-energy peaks originating from the two-triplon bound state. In analogy to the one-triplon dispersion, the modulations also induce gaps in the dispersion of the two-triplon bound state and therefore new minima and maxima are introduced which give rise to van Hove singularities in the density of states. Consequently, new

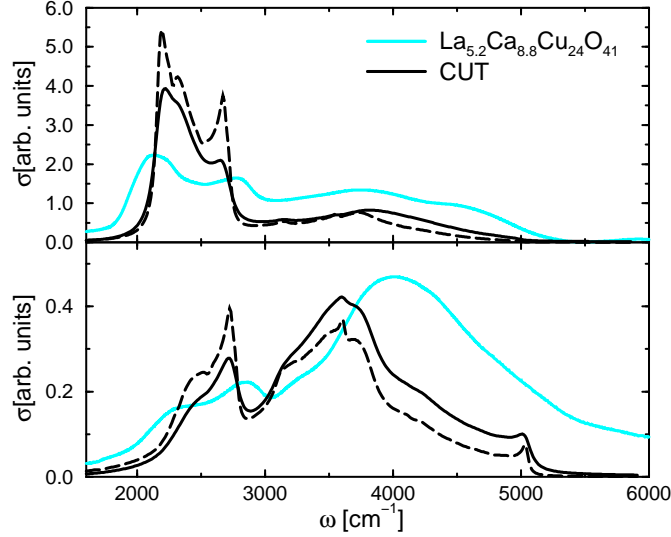


Fig. 8.27: Comparison of the infrared absorption of  $\text{La}_{5.2}\text{Ca}_{8.8}\text{Cu}_{24}\text{O}_{41}$  (grey lines) at  $T = 4$  K with the two-triplon contribution calculated by CUT (black lines) including the effect of structural modulations  $Q_S = 6/7$  of strength  $\alpha_{6/7} = 5\%$  and  $Q_S = 3/7$  of strength  $\alpha_{3/7} = 10\%$  for  $J_{\parallel}/J_{\perp} = 1.25$ ,  $J_{cy}/J_{\perp} = 0.09$ ,  $J_{\perp} = 1060 \text{ cm}^{-1}$ ,  $\omega_{ph}^{\text{leg}} = 570 \text{ cm}^{-1}$ ,  $\omega_{ph}^{\text{rung}} = 620 \text{ cm}^{-1}$ . Solid black line corresponds to a finite broadening of  $\Gamma = 0.05J_{\perp}$  and long dashed black line displays  $\Gamma = 0.02J_{\perp}$ . (**Top panel**) Polarization parallel to the legs. (**Bottom panel**) Rung polarization.

usually small peaks arise in the infrared absorption spectra.

In Fig. 8.27 the infrared absorption including the effect of structural modulations is displayed in analogy to Fig. 8.21. Simultaneous modulations  $Q_S = 6/7$  of strength  $\alpha_{6/7} = 5\%$  and  $Q_S = 3/7$  of strength  $\alpha_{3/7} = 10\%$  are used. The main effect at low energies is the appearance of an additional but very small feature between the two peaks originating from the  $S = 0$  two-triplon bound state. The additional structure is a consequence of the  $Q_S = 6/7$  modulation opening a gap in the dispersion of the bound state. It is almost invisible due to the additional broadening  $\Gamma = 0.05J_{\perp}$  being of the same size as  $\alpha_{6/7}$  (solid black line). The principle effect can be seen for the long dashed line depicting the case of  $\Gamma = 0.02J_{\perp}$ . The  $Q_S = 3/7$  modulation affects mostly the high energy part of the spectrum.

One can conclude that the effect of modulated exchange couplings in the ladder can be conveniently studied by adding the modulation on the level of the effective system, i.e. after the continuous unitary transformation. The modulation induced by the differing periodicity of chains and ladders in the telephone number compounds give rise to small but physical interesting structures. Note that the influence on the spectroscopic line shapes is small because the induced gaps open for energies where the spectral weight is small. In contrast there are strong changes if a gap opens at energies where the spectral weight is concentrated [338]. The latter can happen if the modulation has a different wave vectors  $Q$ , e.g. in the presence of charge order.

### 8.8.3 $\text{SrCu}_2\text{O}_3$ and $\text{Sr}_{14}\text{Cu}_{24}\text{O}_{41}$

In this subsection the compounds  $\text{SrCu}_2\text{O}_3$  and  $\text{Sr}_{14}\text{Cu}_{24}\text{O}_{41}$  are discussed focusing especially on the Raman response.  $\text{SrCu}_2\text{O}_3$  is an undoped two-leg spin-ladder while  $\text{Sr}_{14}\text{Cu}_{24}\text{O}_{41}$  as a member of the telephone-number compounds consists of ladders and chains. These two compounds show different line shapes in Raman spectroscopy compared to the previously discussed  $\text{La}_6\text{Ca}_8\text{Cu}_{24}\text{O}_{41}$ . Therefore it is important to understand the origin of these differences in order to establish that the results found for  $\text{La}_6\text{Ca}_8\text{Cu}_{24}\text{O}_{41}$  are generic findings for two-leg ladders.

It was discussed above that the Raman line shape of a two-leg ladder should be almost the same in both ladder polarizations. This was confirmed experimentally in the case of  $\text{La}_6\text{Ca}_8\text{Cu}_{24}\text{O}_{41}$  [349]. In contrast to the latter case, the Raman line shapes in  $\text{SrCu}_2\text{O}_3$  and  $\text{Sr}_{14}\text{Cu}_{24}\text{O}_{41}$  of rung and leg polarizations are very different [317, 349, 359]. One observes in both compounds a very sharp intensive peak in leg-polarization and a relatively broad structure in rung polarization. This cannot be explained within a purely magnetic model of a two-leg ladder.

At the moment there is no theory describing both compounds in an unified way. It was argued in the  $\text{Sr}_{14}\text{Cu}_{24}\text{O}_{41}$  case that a charge ordering in the spin-chain material induces an additional modulation in the ladders ( $Q_{\text{CO}} = 2/7$ ) causing the sharp feature in experiment [338]. There are 6 holes per unit cell in  $\text{Sr}_{14}\text{Cu}_{24}\text{O}_{41}$  which are assumed to order in the chains as displayed in Fig. 8.24. The charge order gives rise to a modulation of the two-leg ladder which causes a sharp Raman peak. Obviously this mechanism cannot be the explanation in the  $\text{SrCu}_2\text{O}_3$  compound which only consists of undoped spin-ladders. Nevertheless, in the meanwhile also a charge ordering directly in the spin-ladders of  $\text{Sr}_{14}\text{Cu}_{24}\text{O}_{41}$  has been observed which should modulate the exchange couplings in this material and influence also the spectral properties (see last subsection) [361–363]. The origin and properties of the observed charge order is unclear at the moment.

The most striking observation by looking at the experimental data is the fact that the measured Raman response for both materials depends strongly on the laser excitation energy pointing to a resonating contribution to the Raman spectrum. Indeed, the Raman line-shape is similar in both polarization when decreasing the laser frequency [317, 359]. It could be concluded that the Raman spectra measured with low laser frequency represent the true non-resonant Raman response as calculated in this work.

Infrared absorption of  $\text{Sr}_{14}\text{Cu}_{24}\text{O}_{41}$  shows that the exchange couplings are a bit different from the  $\text{La}_6\text{Ca}_8\text{Cu}_{24}\text{O}_{41}$  compound [360]. It is found that  $x \approx 1.35 - 1.4$  and  $x_{\text{cyc}} \approx 0.11 - 0.12$ . Clearly, the theory presented is not valid in a quantitative manner in this parameter regime. Nevertheless it can be concluded that the Raman response should show a sharper two-triplon peak as discussed in Sect. 8.7. This is also found when looking at the above mentioned experimental data obtained by using a low laser frequency [317, 359] compared to the Raman response of  $\text{La}_6\text{Ca}_8\text{Cu}_{24}\text{O}_{41}$  [349]. The similar width of the two-triplon Raman peak in  $\text{Sr}_{14}\text{Cu}_{24}\text{O}_{41}$  and  $\text{SrCu}_2\text{O}_3$  suggests that also the exchange couplings are similar in both materials.



## 8.9 Chapter summary

In this chapter the effect of four-spin interaction on the energy and the spectral properties of the two-leg ladder is investigated focusing on the parameter regime relevant for the experimental realizations of spin-ladders. The first part describes the origin and the importance of the four-spin interactions for cuprate systems.

The perturbative CUT is performed about the limit of isolated rung dimers in analogy to the Heisenberg ladder discussed in the last chapter. It is shown that the clusters needed to calculate the various amplitudes in the thermodynamic limit are larger than in the pure Heisenberg case. In addition, the expansion has to be performed in two perturbation parameters  $x = J_{\parallel}/J_{\perp}$  and  $x_{\text{cyc}} = J_{\text{cyc}}/J_{\perp}$  so that the maximum order that could be reached is smaller by three.

The extension of the rung-singlet phase is determined in the  $x - x_{\text{cyc}}$  plane by applying the method of internal parameters as introduced in Sect. 5.4 for the one-triplon gap [209]. The experimental realizations of spin-ladders are always in the rung-singlet phase.

The destabilization of the rung-singlet phase by the four-spin interaction affects also the spectral weights. It is found for total spin zero and total spin one that spectral weight is shifted from the leading channels to channels with more triplons. It is to be expected that the spectral weight is distributed over more and more channels upon approaching the phase transition line. Nevertheless, the one- and two-triplon channel dominate the physics for realistic values of the couplings relevant for cuprate ladders.

The main effect of the four-spin interaction is a global red shift of all energies. As a consequence, all continua approach each other, especially the two- and the four-triplon continua overlap strongly. This is also seen in severe extrapolation problems in the  $S = 0$  channel. Here the four-triplon contribution is located lower in energy and has a sizable weight so that possible life-time effects can be expected. The results obtained are quantitative up to  $x \approx 1$  in both spin channels. The extrapolation in the  $S = 1$  channel are rather straightforward. They are quantitative also for  $1 < x < 1.5$ . For such values of  $x$  only semi-quantitative results can be obtained in the  $S = 0$  channel.

The second sizable effect of the four-spin interaction is to lower the attractive two-triplon interaction. Thereby the binding energy of the two-triplon bound states is reduced upon turning on  $x_{\text{cyc}}$  and spectral weight is shifted from the bound state to the two-triplon continuum. The  $S = 1$  bound state disappears for realistic values of cuprate ladders due to this effect.

Therefore the spectral properties of the two-triplon continuum for total spin one changes drastically for finite four-spin interaction. The disappearance of the two-triplon bound state causes sharp structures at the lower band edge of the two-triplon continuum. The overall shape of the  $S = 0$  spectral density is not changed by  $x_{\text{cyc}}$ .

Results for the Raman response are shown for different values of  $x$  and  $x_{\text{cyc}}$ . The spectra are dominated by the two-triplon peak which becomes sharper for increasing  $x$ . The Raman line shape is identical for leg and rung polarization without four-spin terms. The Raman response displays a zero in the spectrum for  $x > 0.7$  accompanied by a second high energy peak. It is expected that the high energy features are changed by life-time effects. The line-shape in rung polarization is almost unchanged by the four-spin interaction while the two-triplon peak in leg polarization is

sharpened by  $x_{cyc}$ .

The infrared absorption spectrum is shown for various values of  $x$  and  $x_{cyc}$ . In addition, the effect of various phonon form factors are demonstrated. The line shape of the infrared absorption displays mainly three different peaks in both polarizations. The first two low-energy features originate from the two extrema of the two-triplon bound state dispersion. The different intensities of the first two peaks in both polarizations can be explained nicely by the different symmetries of the observables. The third peak results from the two-triplon continuum.

The last part of the chapter provides information on the current status of the spectral properties of magnetic excitations in cuprate ladders. It can be concluded that in the case of the undoped member of the telephone-number compounds all available experimental data can be understood using a unique set of exchange couplings. Experimentally, a high resolution INS study of this compound is missing so that only the gap energy is reliably known for this compound.

The results obtained by the CUT can semi-quantitatively explain INS data, Raman response and infrared absorption. A sizable three-triplon contribution is missing in leg polarization in the infrared absorption. The two-triplon peak in the Raman response can be reproduced nicely. There are some differences at high energies which are most probably caused by life time effects.

Besides the spectral properties of pure two-leg ladders, also the effect of modulations of the magnetic exchange couplings are discussed which simulate the indirect influence of the spin-chain subsystem on the ladders relevant for all members of the telephone-number compounds. The modulation considered have wave vectors  $Q_S = 3/7$  and  $Q_S = 6/7$ . The modulations are included on the level of the effective model. They induce small gaps in the one-triplon dispersion which could be measured directly by inelastic neutron scattering. In addition, also the effect of the modulation on optical experiments is investigated. It is shown that the structural modulations create a mid-gap bound state in the Raman response which can be also identified in the experimental data. The effect on the infrared absorption is rather small.

Although the influence of the modulation induced by the differing periodicity of chains and ladders is small, generically modulations can have a strong effect on the spectroscopic line shape. The latter corresponds to a situation where a modulation gap opens at an energy where the spectral weight of the spectrum is concentrated.

The last part of the chapter deals with the compounds  $SrCu_2O_3$  and  $Sr_{14}Cu_{24}O_{41}$ . It is concluded that the large differences between rung and leg polarization as observed by Raman spectroscopy cannot be explained in a purely magnetic model. Some suggestions are made for the origin of these differences and how they relate to the findings for  $La_6Ca_8Cu_{24}O_{41}$ . Therefore the previously discussed findings for  $La_6Ca_8Cu_{24}O_{41}$  can be viewed as generic for a two-leg ladder.

## 9 Concluding summary

In this chapter the findings of this thesis are summarized. The discussion is divided into aspects concerning the technical approach and into aspects concerning the application to chains and ladders. The end of the chapter gives future perspectives and possible extensions are presented.

### 9.1 Methodical aspects

In this work, particle-conserving continuous unitary transformations are used to study the energies and especially the spectral properties at zero temperatures of quasi one-dimensional quantum antiferromagnets. The method is well-suited for gapped spin liquids defined on a lattice.

The initially given operators like the Hamiltonian or the observables are transformed to effective operators in a continuous fashion. The initial Hamiltonian must allow for a perturbative decomposition

$$H = H_0 + xV \quad , \quad (9.1.1)$$

such that the unperturbed part  $H_0$  has an equidistant spectrum bounded from below. The perturbing part  $V$  has to be decomposed into ladder operators  $T_n$

$$V = \sum_{n=-N}^N T_n, \quad \text{with } N \in \mathcal{N} \quad \text{and} \quad [H_0, T_n] = nT_n \quad . \quad (9.1.2)$$

The quantized energy spectrum of  $H_0$  defines the quasi-particle description of the system. The quasi-particles are renormalized by the transformation leading to dressed particles in the effective model.

The transformation is realized in a perturbative manner such that the transformation is exact to a certain order in  $x$ . The effective Hamiltonian  $H_{\text{eff}}$  conserves the number of quasi-particles, i.e.  $[H_{\text{eff}}, H_0] = 0$ , hence the name particle-conserving continuous unitary transformation.

The latter property is crucial since it reduces the complex many-body problem to an effective few-body problem. This allows the calculation of multi-particle properties of the to be studied system [142, 143]. A similar orthogonal transformation was constructed by Trebst and coworkers [177].

The effective Hamiltonian and the effective observables decompose into  $n$ -particle irreducible operators, which are defined on the full Hilbert space of  $H_{\text{eff}}$ . The problem splits into different sectors uniquely characterized by the number of quasi-particles. The zero-particle irreducible part  $H_0$  measures the ground state energy,  $H_1$  measures the one-particle dispersion,  $H_2$  the true two-particle interaction and so on. In this thesis the discussion is concentrated on  $H_{n \leq 2}$  usually representing the physically most important parts of  $H_{\text{eff}}$ .

Generally the effective observables  $\mathcal{O}_{\text{eff}}$  do not conserve the number of particles. Zero-temperature

observables can be decomposed into irreducible parts injecting a definite number of particles in the system. This allows the separate determination of  $n$ -particle contributions to the spectral density. The way of decomposing the full Hamiltonian defines the choice of quasi-particles by which one will describe the physical system. To which extent the chosen quasi-particle is suitable to describe the physical system, can be studied by examining the  $n$ -particle spectral weights defined by the decomposition of the effective observables. A quasi-particle description is well suited for the given problem if most of the spectral weight remains in the particle-sectors with a small number of particles. Otherwise the spectral weight is distributed over multi-particle sectors, and an effective multi-particle problem has to be solved to describe the physics of the system.

The effective operators are calculated on finite clusters yielding results in the thermodynamic limit due to the linked-cluster theorem. The states are characterized by the number of quasi-particles and the position of the particles on the lattice. Therefore the calculation is done in real space.

The effective operators are given by a high-order series expansion in the parameter  $x$ . Each perturbative order represents virtual processes of the initially present particles. The obtained maximum order is proportional to the maximum range of virtual processes depending on the range of the initially given Hamiltonian. The resulting particle can be visualized as the local particle with a dressing of virtual processes.

A successful use of the method described above requires that the correlations in the considered physical system are not larger than the maximum range of processes one has included in the calculation. This is especially important in cases of critical systems exhibiting long-range correlations.

The use of extrapolation tools extends the parameter space in which reliable results can be found. In this way an analysis of locally defined quantities like spectral weights is possible even in the limit of a critical point. A variety of extrapolation tools are described. An effective extrapolation is found by combining the use of internal parameters of the system with Padé and dlogPadé techniques.

The use of continued fraction techniques makes the calculation of spectral densities possible. In this work the discussion is restricted to one- and two-particle spectral densities.

The decomposition of the Hamiltonian of a large class of low-dimensional quantum antiferromagnets can be obtained by starting from a totally dimerized state. Then the ground state is the product-state of singlets. Excitations are local triplets with total spin one and magnetic quantum numbers  $m = -1, 0, 1$ . The excitation spectrum is equidistant and the use of the perturbative particle-conserving continuous unitary transformation is straightforward. The quasi-particles in this context are named triplons [82] or elementary triplets corresponding to dressed triplet excitations. They are hardcore-bosons since only one triplon can be excited on one dimer.

## 9.2 Chains

The first system studied is the dimerized and frustrated antiferromagnetic spin-chain. The starting point is the totally dimerized state. This system shows a critical point at zero dimerization. Therefore the regime of small or zero dimerization is the most challenging regime for the method. The applicability of the chosen quasi-particle, the triplon, is analyzed by investigating the multi-

triplon spectral weights. For zero frustration it is found that most of the spectral weight is in the one- and two-triplon sector for all values of the dimerization including the case of vanishing dimerization [82]. The case of strong frustration is more subtle. Some indications are found that the triplon-picture is also applicable in this case. It can be concluded that the triplon is an appropriate quasi-particle for describing the dimerized and frustrated spin-chain in a large parameter regime.

The analysis of spectral densities is restricted to large or intermediate values for the dimerization. Quantitative results are obtained for all important spectral densities. Additionally, precursors of the physics of the uniform chains are identified and described. One has the expectation that everything should work even down to  $\delta = 0$ .

The discussion of the spectral density is split into the case of total spin one and total spin zero. The dynamical structure factor is dominated in the considered parameter regime by the one-triplon contribution. The one-triplon dispersion increases for increasing dimerization and it is flattened for increasing frustration. The spectral weight is concentrated at momentum  $k = \pi$ .

The two-triplon contribution comprises two-triplon bound states and a two-triplon continuum. The line shape at the lower band edge depends strongly on the location of the two-triplon bound states. Generically, a  $\sqrt{\omega}$  behavior is found at the band edges which is the consequence of the hardcore property of the triplons. Here  $\omega$  denotes the energy of the two triplons near the band edges. In contrast, a  $1/\sqrt{\omega}$  diverging behavior is found if a two-triplon bound state is degenerate with the band edge of the two-triplon continuum.

The spectral weight of the two-triplon continuum is concentrated at the lower band edge and near  $k = \pi$ . The frustration shifts spectral weight to higher energies.

Two different observables are examined in the  $S = 0$  case: a nearest-neighbour coupling on the weak bonds and a next-nearest-neighbour coupling. The spectral density for both observables is dominated by a strongly bound two-triplon state. Consequently, the same holds true for the Raman response and the infrared absorption<sup>1</sup>

The comparison of the results with field-theoretical treatments mapping the spin-chain to a continuum theory led to a number of insights. The dimerized and frustrated spin-chain is usually mapped to a single sine-Gordon model. But it turns out that this reduction to a single sine-Gordon neglecting marginal operators is not appropriate for the considered values of the dimerization. The physics of the single sine-Gordon model will emerge only at much smaller values of the dimerization.

## 9.3 Ladders

The second physical system investigated are two-leg ladders. The analysis comprises the pure Heisenberg ladder and the extended two-leg ladder including the next-leading four-spin interaction. The starting point of the discussion is in both cases the limit of isolated rung dimers. Therefore the elementary particle chosen in this context is the rung-triplon.

---

<sup>1</sup>Note that in the unfrustrated case ( $\alpha = 0$ ) the two-triplon boundstate  $S_1$  does not exist. Here one observes a resonance at the lower band edge dominating the spectra.

### 9.3.1 Two-leg Heisenberg ladder

The energy spectrum of pure Heisenberg ladders consists of the one-triplon dispersion, one two-triplon bound state with total spin one and total spin zero and multi-triplon continua. In addition, there is an anti-bound state with total spin two which is not discussed in this thesis.

The one-triplon dispersion is of cosine-shape for  $x \leq 0.7$ . The one-triplon gap is located at  $k = \pi$ . If  $x > 0.6$ , the one-triplon dispersion displays an additional local minimum at  $k = 0$ . This can be either understood from the limit  $x \rightarrow \infty$  which is the case of two isolated spin-chains or directly in the triplon language. The dispersion of the spin-chain is gapless at  $k = 0$  so that the dip in the ladder can be interpreted as a precursor effect of the spin-chain physics. In the triplon language it is shown that the dip corresponds to a level repulsion effect due to the proximity of the three-triplon continuum.

The two-triplon contribution splits into the two-triplon bound states and the two-triplon continuum. The bound states emerge from the continuum at finite momentum. They have their maximum binding energy at  $k = \pi$ . The binding energy of the  $S = 0$  bound state is larger than the binding energy of the  $S = 1$  bound state.

Sectors of odd (even) number of triplons are only coupled among themselves due to the reflection parity at the centerline of the ladder. The relative positions of one-/three- and two-/four-triplon energies are given. At isotropic coupling, the one-triplon dispersion is lower than the three-triplon continuum but they are very close for small momenta. The two-triplon and four-triplon continua overlap strongly. The overlap in the  $S = 1$  channel is smaller due to the smaller binding energy.

Multi-triplon spectral weights are analyzed in both spin channels. It turns out that most of the spectral weight remains in the one- and two-triplon channel. But in contrast to the spin-chain case the weight in the three- and four-triplon sector is getting sizable for  $x \geq 1$ .

The latter two points give rise to severe extrapolation problems especially for two-triplon amplitudes. The extrapolations are performed by using the method of internal parameters plus additional Padé and dlogPadé extrapolations. The overlap of two- and four-triplon continuum is reflected by spurious poles in the extrapolation. Usually  $[n, 2]$ -Padé or  $[n, 2]$ -dlogPadé extrapolants are used in order to avoid these poles. The extrapolation ignores possible life-time effects which reflect the decay of two triplons into four triplons. The extrapolation is less complicated in the  $S = 1$  sector because the overlap is smaller. The extrapolation is quantitative up to  $x = 1$  in both spin channels. The extrapolation in the  $S = 1$  sector is even reliable for larger coupling ratios.

The dynamical structure factor is dominated by the one-triplon contribution in the considered parameter range. The spectral weight is concentrated at  $k = \pi$ . The two-triplon spectral weight is situated mostly in the two-triplon bound state. The spectral weight of the two-triplon continuum is located mainly at the lower band edge near  $k = \pi$  reflecting already precursors of the spin-chain physics.

There are two generic  $S = 0$  observables, one couples to the rungs of the ladder and the second to the legs of the ladder. The rung observable has even parity concerning the reflection at the centerline of the ladder. Therefore it excites only an even number of triplons. The leg observable possesses an even and an odd parity contribution.

Results for the most important two-triplon contributions are presented for both observables. At

small momenta no two-triplon bound state is present. At  $k = 0$ , the leading two-triplon Raman response, the spectrum is dominated by a two-triplon peak inside the two-triplon continuum. Note that the line-shape is the same for both observables at  $k = 0$ . At  $x > 0.6$ , a second peak at high energies is formed split from the two-triplon peak by a zero in the spectrum. The zero is a combined effect of the two-triplon interaction and the dip at  $k = 0$  in the one-triplon dispersion. It is expected that life-time effects will modify the high-energy line shape producing a structure resembling a shoulder.

The two-triplon contribution at larger momenta is dominated by the presence of the  $S = 0$  two-triplon bound state. The two observables display different spectral weight distribution at finite momentum. Especially the spectral weight of the two-triplon bound state differs. The intensity in leg polarization is maximal at  $k = \pi$  while it is strictly zero in rung polarization.

The latter gives rise to a definite signature of the two-triplon bound state in infrared absorption measurements [298]. The two extrema of the two-triplon bound state result in two low-energy peaks in the infrared absorption. Due to the different spectral weight distribution, the first peak is larger as the second one in leg polarization while in rung polarization the second peak is dominant and only a shoulder at lower energies is present. In addition, the infrared absorption displays a third structure at high energies corresponding to the two-triplon continuum.

### 9.3.2 Heisenberg ladder with four-spin interaction

The Heisenberg ladder with additional four-spin interaction is investigated. It is known to be the minimal model for cuprate ladder systems. It is shown that the inclusion of the four-spin interaction requires larger clusters compared to the pure two-leg ladder in a given order. In addition, the series expansion has to be performed with two perturbation parameters. Therefore the maximal perturbation order reached is reduced.

The one-triplon gap is analyzed focusing on the stability of the rung-singlet phase. It is shown that the one-triplon gap closes at finite  $x_{cyc}$  for a given  $x$ . The extension of the rung-singlet phase in the whole  $[x, x_{cyc}]$ -plane is calculated using a new extrapolation technique combining renormalization ideas and series expansion [209]. Cuprate ladder systems are always in the rung-singlet phase.

The rung-triplon picture is destabilized by the four-spin interaction. This is also discernible in the spectral weight distribution. Spectral weight is shifted from the leading one- and two-triplon channels to multi-triplon channels. It can be concluded that the rung-triplon picture breaks down at the phase transition point.

The main effect of the four-spin interaction on the energy spectrum of the two-leg ladder is a red shift of all energies. Consequently, all multi-triplon continua lie closer in energy. The extrapolation is done in a analogy to the pure Heisenberg case. The second effect of the four-spin interaction is the reduction of the attractive triplon-triplon interaction. Hence the binding energy of the two-triplon bound states is therefore reduced. The  $S = 1$  two-triplon bound state disappears already at  $x_{cyc} \approx 0.1$  for  $x = 1$  while the  $S = 0$  two-triplon bound state is still present for these exchange couplings due to the larger binding energy in this spin channel.

For finite  $x_{cyc}$ , the one-triplon contribution to the dynamical structure factor is more concentrated near  $k = \pi$  while the overall weight is reduced. There is a drastic change in the line-shape of

the two-triplon contribution due to the disappearance of the  $S = 1$  two-triplon bound state. The spectral weight is mostly distributed at the lower band-edge of the two-triplon continuum. At the point where the lower band-edge and the bound state are degenerate, a  $1/\sqrt{\omega}$ -like behavior is found similar to the findings in the spin-chain case.

For finite  $x_{\text{cyc}}$ , the two-triplon contribution in the  $S = 0$  channel is changed only quantitatively. Spectral weight is shifted from the bound state to the two-triplon continuum which becomes more pronounced.

The Raman response in leg and rung polarization is not equal for finite four-spin interaction. The line-shape in rung-polarization is almost unchanged while the two-triplon peak is sharpened for increasing  $x_{\text{cyc}}$  in leg polarization. Nevertheless, the overall line-shape remains similar in both polarizations for the exchange ratios discussed in this thesis.

The two-triplon contribution to the infrared absorption is analyzed in both polarization. The influence of different phonon form factors on the resulting infrared line-shape is presented. The contribution of the two-triplon continuum becomes more pronounced for increasing  $x$  and increasing  $x_{\text{cyc}}$ .

The last part of the chapter compares the results obtained with experimental data for cuprate ladders and gives an overview of the current understanding of magnetic excitations in these systems. A quantitative analysis of infrared absorption data on  $\text{La}_{5.2}\text{Ca}_{8.8}\text{Cu}_{24}\text{O}_{41}$  by T. Nunner and coworkers [324] using DMRG gives  $J_{\perp} = 1150 \pm 150 \text{cm}^{-1}$ ,  $x = 1.22 \pm 0.05$  and  $x_{\text{cyc}} = 0.105 \pm 0.015$ . This parameter set is very challenging for the perturbative realization of the continuous unitary transformations. Nevertheless, it is shown that all experimental data including infrared absorption, Raman spectroscopy and inelastic neutron scattering data can be understood at least on the semi-quantitative level. Unfortunately, there is no high-resolution inelastic neutron scattering data available probing the one-triplon properties of the materials, for which a clear prediction is made in this thesis.

The two-triplon Raman response shows differences at higher energies of the spectrum. The experiment shows the two-triplon peak with a high-energy shoulder. The theoretical curve displays an additional second peak at high energies plus a zero in the spectral density between the two peaks. It is concluded that the omitted life-time effects are strong in this energy region and that they will lead to a washing out of the zero implying to a shoulder-like structure.

Comparing the theoretical infrared absorption spectra with the experimental data for  $\text{La}_{5.2}\text{Ca}_{8.8}\text{Cu}_{24}\text{O}_{41}$ , it is seen that the two-triplon interaction is overestimated by the extrapolation pushing the spectrum and the spectral weight to too low energies. But the overall agreement between experiment and theory is good. A sizable three-triplon contribution is missing in leg-polarization [327]. It can be concluded from the developments over the last years in experiment and theory that there are strong quantum fluctuations in cuprate two-leg ladders resulting in sizable high-energy spectral weight in the infrared absorption and in the Raman response. Second, it is important to treat the strong triplon-triplon interaction on a quantitative level. The similarities between the experimental findings in cuprate ladders and cuprate planes point in the direction that the same physical ingredients like two-particle interactions and multi-particle contributions have to be taken into account to understand the magnetism in the cuprate planes.



It is argued that in the telephone number compounds  $A_{14}Cu_{24}O_{41}$  there is an effect of the second structural unit, the spin-chains, on the ladders resulting in modulations of the two-leg ladder exchange couplings. This effect is treated theoretically on the level of the effective system, i.e. after the transformation. The influence on one- and two-triplon properties is given for the realistic exchange ratios of cuprate ladders. The main effect of the modulations is to open small gaps in the one-triplon dispersion. The modulations could be directly measured by inelastic neutron scattering. In addition, the influence on optical experiments is discussed. The effect on the infrared absorption is rather weak due to the larger additional broadening and the presence of at least two phonon contributions. In the Raman response, the modulations induces a mid-gap bound state which can be also identified in the experimental data.

The influence of the modulation on the spectroscopic line shapes depends strongly on the wave vector of the modulation. It is found that the effect of the modulation induced by the differing periodicity of chains and ladders in the telephone number compounds is rather small. The latter follows from the fact that the modulation gaps open at energies where the spectral weight is small. If a modulation gap opens at an energy where the spectral weight is concentrated, a large effect on the line shape is seen. This can happen if the wave vector of the modulation is different, e.g. in the presence of charge order.

## 9.4 Perspectives

The last part is devoted to some perspectives concerning the methodical aspects and possible extensions of the physical systems studied in this work. The method used here has two major limitations: First, no long range processes can be treated with the perturbative realization of the continuous unitary transformation. This is discussed in the spin-chain case approaching the critical limit of vanishing dimerization. Second, the possibility of overlapping multi-particle energies give rise to severe extrapolation problems as was observed in the investigation of two-leg ladder systems for large coupling ratios [326].

To overcome the first problem, one has to switch from a perturbative realization to a renormalizing formulation of the continuous unitary transformation. A way of doing this is to truncate the proliferating terms not occurring to their formal order of some expansion parameter but according to their complexity and to solve the resulting differential equations using a Runge-Kutta algorithm [138, 161, 165, 166]. The most challenging problem in this context is to find an appropriate and controlled truncation scheme. Note that a major advantage of the perturbative realization is the absence of any error in a given perturbation order.

The treatment of long range order processes can be done also by switching to momentum space and solve the differential equations on a discretized momentum grid. Note that treating the usually real space constraints of the participating particles is complicated in momentum space but can be done exactly by changing the commutation relations.

The problems arising from overlapping continua is not healed in the renormalizing formulation. In contrast, the solution of the differential equation diverges in this case and one is left without physical result [326]. There are two cures: First, the physical processes connecting the continua

are not important and one can omit these processes. Second, if the processes are important, one does not attempt to eliminate these processes and deals with them afterwards by other techniques, e.g. diagrammatic treatments [326].

Using these methodical extensions it should be possible to answer some of the open issues not solved in this work. One major task is to study the relationship of the triplon and the spinon picture in more detail approaching the limit of vanishing dimerization. Especially the case of the massive but free spinons for  $\alpha > \alpha_c$  is very fascinating. An improved understanding of fractional and integer excitations in spin liquids should be also important for the study of undoped and doped two-dimensional quantum antiferromagnets.

In the case of cuprate ladder systems, an almost complete understanding of the spectral properties of magnetic excitations has been reached. Especially the necessity to include four-spin interaction in the minimal magnetic model for these systems seems to be settled. The results obtained by the perturbative continuous unitary transformations are affected by the overlapping continua so that only semi-quantitative results are possible especially in the  $S = 0$  case. Therefore a quantitative treatment in the realistic coupling regime including possible life-time effects is an open issue and should resolve the differences in Raman spectroscopy and infrared absorption. The calculation of the three-triplon contribution is another missing step in order to understand the infrared line shape in a complete fashion. First results are available [327].

The treatment of modulations in the two-leg ladder on the level of the effective system is a promising example for using the effective system as the starting point for a calculation. The important point is that once the effective system is given, a less demanding calculation can be easily put on top. This was also done recently by considering coupled two-leg ladder systems to describe inelastic neutron scattering data of striped ordered and superconducting cuprate superconductors [130, 131]. The crossover from one-dimensional to anisotropic two-dimensional physics comes into reach in this way.

The similarity between the experimental findings in optical experiments for cuprate ladders and cuprate planes suggests similar physical ingredients necessary to describe the two-dimensional case. A calculation based on magnons which includes magnon-magnon interactions in a quantitative manner and multi-magnon contributions might resolve the long-standing problem of large spectral weights at high energies in undoped cuprate superconductors.

Therefore the use of continuous unitary transformations for the undoped and also for the doped two-dimensional square lattice is a very exciting and promising route. Hopefully, the strong correlations in these systems can be treated in this way, so that new insights in the physics of cuprate superconductors can be gained.

## Bibliography

- [1] J.G. Bednorz and K.A. Müller, *Z. Phys. B* **64**, 189 (1986).
- [2] J. Bardeen, L.N. Cooper and J.R. Schrieffer, *Phys. rev.* **108**, 1175 (1957).
- [3] A. Schilling, M. Cantoni, J.D. Quo, and H.R. Ott, *Nature* **363**, 56 (1993).
- [4] M. Nunez-Regueiro, J.L. Tholence, E.V. Antipov, J.J. Capponi, and M. Marezio, *Science* **262**, 97 (1993).
- [5] J. Orenstein and A.J. Millis, *Science* **288**, 468 (2000).
- [6] P.W. Anderson, *Science* **235**, 1196 (1987).
- [7] V.J. Emery, *Phys. Rev. Lett.* **58**, 2794 (1987).
- [8] C.M. Varma, S. Schmitt-Rink, and E. Abrahams, in *Novel Mechanisms of Superconductivity*, edited by S.A. Wolf and V.Z. Kresin (plenum, New York), 355 (1987).
- [9] C.M. Varma, S. Schmitt-Rink, and E. Abrahams, *Solid State Commun.* **62**, 681 (1987).
- [10] F.C. Zhang and T.M. Rice, *Phys. Rev. B* **37**, 3759 (1988).
- [11] A. Damascelli, Z. Hussain and Z-X. Shen, *Rev. Mod. Phys.* **75**, 473 (2003).
- [12] E. Dagotto, A. Nazarenko, and M. Boninsegni, *Phys. Rev. Lett.* **73**, 728 (1994).
- [13] P.W. Anderson, *Phys. Rev.* **79**, 350 (1950).
- [14] P.W. Anderson, *Science* **288**, 480 (2000).
- [15] I. Affleck and J.B. Marston, *Phys. Rev. B* **88**, 3774 (1988).
- [16] G. Kotliar and J. Liu, *Phys. Rev. Lett.* **61**, 1784 (1988).
- [17] S. Maekawa, T. Matsuura, Y. Isawa, and H. Ebisawa, *Physica C* **152**, 133 (1988).
- [18] Y. Suzumura, Y. Hasegawa, and H. Fukuyama, *J. Phys. Soc. Jpn.* **57**, 3229 (1988).
- [19] P.A. Lee and N. Nagaosa, *Phys. Rev. B* **46**, 5621 (1992).
- [20] L.B. Ioffe and A.J. Millis, *Phys. Rev. B* **54**, 3645 (1996).
- [21] X.-G. Wen and P.A. Lee, *Phys. Rev. Lett.* **76**, 503 (1996).
- [22] R.B. Laughlin, *Phys. Rev. Lett.* **79**, 1726 (1997).
- [23] L. Balents, M.P.A. Fisher and C. Nayak, *Int. J. Mod. Phys. B* **12**, 1033 (1998).
- [24] L. Balents, M.P.A. Fisher and C. Nayak, *Phys. Rev. B* **60**, 1654 (1999).
- [25] L. Balents, M.P.A. Fisher and C. Nayak, *Phys. Rev. B* **61**, 6307 (2000).
- [26] D.-H. Lee, *Phys. Rev. Lett.* **84**, 2694 (2000).
- [27] J. Zaanen and O. Gunnarsson, *Phys. Rev. B* **40**, 7391 (1989).
- [28] V.J. Emery and S.A. Kivelson, *Physica C* **209**, 597 (1993).
- [29] A. Bianconi, N.L. Saini, A. Lanzara, M. Missori, T. Rossetti, H. Oyanagi, H. Yamaguchi, K. Oka, and T. Ito, *Phys. Rev. Lett.* **76**, 3412 (1996).

- [30] M.I. Salkola, V.J. Emery and S.A. Kivelson, Phys. Rev. Lett. **77**, 155 (1996).
- [31] S.A. Kivelson, E. Fradkin and V.J. Emery, Nature (London) **393**, 550 (1998).
- [32] V.J. Emery, S.A. Kivelson and J.M. Tranquada, Proc. Natl. Acad. Sci. U.S.A. **96**, 8814 (1999).
- [33] M. Ichioka and M. Machida, J. Phys. Soc. Jpn. **68**, 4020 (1999).
- [34] T. Tohyama, S. Nagai, Y. Shibita, and S. Maekawa, Phys. Rev. Lett. **82**, 4910 (1999).
- [35] J. Zaanen, Science **286**, 251 (1999).
- [36] A.L. Chernyshev, A.H. Castro Neto, and A.R. Bishop, Phys. Rev. Lett. **84**, 4922 (2000).
- [37] M. Fleck, A.I. Lichtenstein, E. Pavarini, and A.M. Oleś, Phys. Rev. Lett. **84**, 4962 (2000).
- [38] R.S. Markiewicz, Phys. Rev. B **62**, 1252 (2000).
- [39] S.R. White and D.J. Scalapino, Phys. Rev. B **61**, 6320 (2000).
- [40] M.G. Zacher, R. Eder, E. Arrigoni, and W. Hanke, Phys. Rev. Lett. **85**, 2585 (2000).
- [41] J.H. Han, Q.-H. Wang, and D.-H. Lee, Int. J. Mod. Phys. B **15**, 1117 (2001).
- [42] S. Chakravarty, B.I. Halperin, and D.R. Nelson, Phys. Rev. B **39**, 2344 (1989).
- [43] S. Chakravarty, R.B. Laughlin, D.K. Morr and C. Nayak, Phys. Rev. B **63**, 094503 (2001).
- [44] C.M. Varma, P.B. Littlewood, S. Schmitt-Rink, E. Abrahams, and A.E. Ruckenstein, Phys. Rev. Lett. **63**, 1996 (1989).
- [45] P.B. Littlewood and C.M. Varma, J. Appl. Phys. **69**, 4979 (1991).
- [46] S. Sachdev and J. Ye, Phys. Rev. Lett. **69**, 2411 (1992).
- [47] V.J. Emery and S.A. Kivelson, Phys. Rev. Lett. **71**, 3701 (1993).
- [48] A. Sokol and D. Pines, Phys. Rev. Lett. **71**, 2813 (1993).
- [49] C. Castellani, C. Di Castro, and M. Grilli, Phys. Rev. Lett. **75**, 4650 (1995).
- [50] C.M. Varma, Phys. Rev. B **55**, 14554 (1997).
- [51] A.A. Abrikosov, Physica C **341**, 97 (2000).
- [52] T.P. Devereaux, T. Cuk, Z.-X. Shen, and N. Nagaosa, cond-mat/0403766.
- [53] E. Manousakis, Rev. Mod. Phys. **63**, 1 (1991).
- [54] M.A. Kastner, R.J. Birgeneau, G. Shirane, and Y. Endoh, Rev. Mod. Phys. **70**, 897 (1998).
- [55] S.J. Clarke, A. Harrison, T.E. Mason, and D. Visser, Solid State Commun. **112**, 561 (1999).
- [56] S.M. Hayden, G. Aeppli, R. Osborn, A. D. Taylor, T. G. Perring, S.-W. Cheong, and Z. Fisk, Phys. Rev. Lett. **67**, 3622 (1991).
- [57] R. Coldea, S.M. Hayden, G. Aeppli, T. G. Perring, C.D. Frost, T.E. Mason, S.-W. Cheong, and Z. Fisk, Phys. Rev. Lett. **86**, 5377 (2001).
- [58] S.J. Clarke, A. Harrison, T.E. Morris, G.J. McIntyre, and D. Visser, J. Phys. Condens. Matter **4**, L71 (1992).
- [59] H.M. Rønnow, D.F. McMorrow, and A. Harrison, Phys. Rev. Lett. **82**, 3152 (1999).
- [60] A. Cuccoli, V. Tognetti, R. Vaia, and P. Verrucchi, Phys. Rev. Lett. **77**, 3439 (1996).
- [61] M. Roger and J.M. Delrieu, Phys. Rev. B **39**, 2299 (1989).
- [62] H.J. Schmidt and Y. Kuramoto, Physica C **167**, 263 (1990).

- [63] M. Takahashi, *J. Phys. C: Sol. State Phys.* **10**, 1289 (1977).
- [64] A. H. MacDonald, S. M. Girvin, D. Yoshioka, *Phys. Rev. B* **41**, 2565 (1990).
- [65] E. Müller-Hartmann and A. Reischl, *Eur. Phys. J. B* **28**, 173 (2002).
- [66] C.J. Calzado and J.P. Malrieu, *Phys. Rev. B* **63**, 214520 (2001).
- [67] A.A. Katanin and A.P. Kampf, *Phys. Rev. B* **66**, 100403 (2002).
- [68] J. Lorenzana, J. Eroles, and S. Sorella, *Phys. Rev. Lett.* **83**, 5122 (1999).
- [69] S. Sugai, M. Sato, T. Kobayashi, J. Akimitsu, T. Ito, H. Takagi, S. Uchida, S. Hosoya, T. Kajitani, and T. Fukuda, *Phys. Rev. B* **42**, 1045 (1990).
- [70] G. Blumberg, P. Abbamonte, M.V. Klein, W.C. Lee, D.M. Ginsberg, L.L. Miller, and A. Zibold, *Phys. Rev. B* **53**, R11930 (1996).
- [71] J.D. Perkins, J.M. Graybeal, M.A. Kastner, R.J. Birgeneau, J.P. Falck, and M. Greven *Phys. Rev. Lett* **71**, 1621 (1993).
- [72] J.D. Perkins, R.J. Birgeneau, J.M. Graybeal, M.A. Kastner and D.S. Kleinberg, *Phys. Rev. B* **58**, 9390 (1998).
- [73] M. Grüninger, D. van der Marel, A. Damascelli, A. Erb, T. Nunner, and T. Kopp, *Phys. Rev. B* **62**, 12422 (2000).
- [74] A.A. Katanin and A.P. Kampf, *Phys. Rev. B* **67**, 100404 (R) (2003).
- [75] P. Bourges, H. Casalta, A.S. Ivanov, and D. Petitgrand, *Phys. Rev. Lett.* **79**, 4906 (1997).
- [76] R.R.P. Singh and M.P. Gelfand, *Phys. Rev. B* **52**, R15695 (1995).
- [77] G. Aeppli, S.M. Hayden, P. Dai, H.A. Mook, R.D. Hunt, T.G. Perring, and F. Dogan, *Phys. Status Solidi*, (b) **215**, 519 (1999).
- [78] C.-M. Ho, V.N. Muthukumar, M. Ogata, and P.W. Anderson, *Phys. Rev. Lett.* **86**, 1626 (2001).
- [79] A.W. Sandvik and R.R.P. Singh, *Phys. Rev. Lett.* **86**, 528 (2001).
- [80] S. Sachdev, *Science* **288**, 475 (2000).
- [81] T. Senthil, A. Vishwanath, L. Balents, S. Sachdev, and M.P.A. Fisher, *Science* **303**, 1490 (2004).
- [82] K.P. Schmidt and G.S. Uhrig, *Phys. Rev. Lett.* **90**, 227204 (2003).
- [83] L.D. Faddeev and L.A. Takhtajan, *Phys. Lett.* **85A**, 375 (1981).
- [84] J. Zaanen, *Nature* **404**, 714 (2000).
- [85] S. Sachdev, in *Developments in Mathematical and Experimental Physics, Volume B: Statistical Physics and Beyond*, edited by A. Macias, F. Uribe, and E. Diaz (Kluwer Academic, New York).
- [86] E.W. Carlson, V.J. Emery, S.A. Kivelson, and D. Orgad, in *The Physics of Conventional and Unconventional Superconductors*, edited by K.H. Bennemann and J.B. Ketterson (Springer, Berlin).
- [87] N. Hasselmann, A.H. Castro Neto, and C. Morais Smith, *Phys. Rev. B* **69**, 014424 (2004).
- [88] S.A. Kivelson, I.P. Bindloss, E. Fradkin, V. Organesyan, J.M. Tranquada, A. Kapitulnik and C. Howald, *Rev. Mod. Phys.* **75**, 1201 (2003).
- [89] P.W. Anderson, cond-mat/0406038.
- [90] H.C. Fu, J.C. Davis, and D. Lee, cond-mat/0403001.
- [91] J.M. Tranquada, in *Neutron Scattering in Layered Copper-Oxide Superconductors*, edited by A. Furrer (Kluwer, Dordrecht, The Netherlands), 225 (1998).

- [92] J.M. Tranquada, *Physica B* **241-243**, 225. (1998).
- [93] J.M. Tranquada, B.J. Sternlieb, J.D. Axe, Y. Nakamura, and S. Uchida, *Nature* **375**, 561 (1995).
- [94] J.M. Tranquada, J.D. Axe, N. Ichikawa, A.R. Moodenbaugh, Y. Nakamura, and S. Uchida, *Phys. Rev. Lett.* **78**, 338 (1997).
- [95] N. Ichikawa, S. Uchida, J.M. Tranquada, T. Niemöller, P.M. Gehring, S.-H. Lee, and J.R. Schneider, *Phys. Rev. Lett.* **85**, 1738 (2000).
- [96] S. Wakimoto, J.M. Tranquada, T. Ono, K.M. Kojima, S. Uchida, S.-H. Lee, P.M. Gehring, and R.J. Birgeneau, *Phys. Rev. B* **64**, 174505 (2001).
- [97] M. Fujita, H. Goka, K. Yamada, and M. Matsuda, *Phys. Rev. Lett.* **88**, 167008 (2002).
- [98] C. Niedermayer, C. Bernhard, T. Blasius, A. Golnik, A. Moodenbaugh, and J.I. Budnick, *Phys. Rev. Lett.* **88**, 3843 (1998).
- [99] T. Suzuki, T. Goto, K. Chiba, T. Shinoda, T. Fukase, H. Kimura, K. Yamada, M. Ohashi, and Y. Yamaguchi, *Phys. Rev. B* **57**, R3229 (1998).
- [100] H. Kimura, K. Hirota, H. Matsushita, K. Yamada, Y. Endoh, S.-H. Lee, C.F. Majkrzak, R. Erwin, G. Shirane, M. Greven, Y.S. Lee, M.A. Kastner, and R.J. Birgeneau, *Phys. Rev. B* **59**, 6517 (1999).
- [101] S. Wakimoto, G. Shirane, Y. Endoh, K. Hirota, S. Ueki, K. Yamada, R.J. Birgeneau, M.A. Kastner, Y.S. Lee, P.M. Gehring, and S.-H. Lee, *Phys. Rev. B* **60**, R769 (1999).
- [102] M. Matsuda, Y.S. Lee, M. Greven, M.A. Kastner, R.J. Birgeneau, K. Yamada, Y. Endoh, P. Böni, S.-H. Lee, S. Wakimoto and G. Shirane, *Phys. Rev. B* **61**, 4326 (2000).
- [103] Q. Si, Y. Zha, K. Levin, and J.P. Lu, *Phys. Rev. B* **47**, 9055 (1993).
- [104] P. Bernard, L. Chen, and A.-M.S. Tremblay, *Phys. Rev. B* **47**, 15217 (1993).
- [105] P.B. Littlewood, J. Zaanen, G. Aeppli, and H. Monien, *Phys. Rev. B* **48**, 487 (1993).
- [106] Y.-J. Kao, Q. Si, and K. Levin, *Phys. Rev. B* **61**, R11898 (2000).
- [107] M.R. Norman, *Phys. Rev. B* **61**, 14751 (2000).
- [108] M.R. Norman, *Phys. Rev. B* **63**, 092509 (2001).
- [109] Y.S. Lee, R.J. Birgeneau, M.A. Kastner, Y. Endoh, S. Wakimoto, K. Yamada, R.W. Erwin, S.-H. Lee, and G. Shirane, *Phys. Rev. B* **60**, 3643 (1999).
- [110] P. Bourges, Y. Sidis, H.F. Fong, L.P. Regnault, J. Bossy, A. Ivanov, and B. Keimer, *Science* **288**, 1234 (2000).
- [111] D. Reznik, P. Bourges, L. Pintschovius, Y. Endoh, Y. Sidis, Y. Shiokara, and S. Tajima, *Phys. Rev. Lett.* **93**, 207003 (2004).
- [112] H.A. Mook, P.C. dai, and F. Dogan, *Phys. Rev. Lett.* **88**, 097004 (2002).
- [113] H.A. Mook, P.C. Dai, S.M. Hayden, G. Aeppli, T.G. Perring, and F. Dogan, *Nature* **395**, 580 (1998).
- [114] M. Arai, T. Nishijima, Y. Endoh, T. Egami, S. Tajima, K. Tomimoto, Y. Shiohara, M. Takahashi, A. Garrett, and S.M. Bennington, *Phys. Rev. Lett.* **83**, 608 (1999).
- [115] S.M. Hayden, H.A. Mook, Pengcheng Dai, T.G. Perring, and F. Dogan, *Nature* **429**, 531 (2004).
- [116] E.W. Carlson, D.X. Yao, and D.K. Campbell, *Phys. Rev. B* **70**, 064505 (2004).
- [117] J. Rossat-Mignod, L.P. Regnault, C. Vettier, P. Bourges, P. Burllet, J. Bossy, J.Y. Henry, and G. Lapertot, *Physica C* **185-189**, 86 (1991).

- [118] H.A. Mook, M. Yethiray, G. Aepli, T.E. Mason, and T. Armstrong, Phys. Rev. Lett. **70**, 3490 (1993).
- [119] H.F. Fong, B. Keimer, P.W. Anderson et al., Phys. Rev. Lett. **75**, 316 (1995).
- [120] H.F. Fong, B. Keimer, P.W. Anderson et al., Phys. Rev. B **54**, 6708 (1996).
- [121] P. Bourges, L.P. Regnault, Y. Sidis, and C. Vettier, Phys. Rev. B **53**, 876 (1996).
- [122] H.F. Fong, P. Bourges, Y. Sidis, L.P. Regnault, A.S. Ivanov, G.D. Gu, N. Koshizuka, and B. Keimer, Nature **398**, 588 (1999).
- [123] H. He, P. Bourges, Y. Sidis, C. Ulrich, L.P. Regnault, S. Pailhès, N.S. Berzigiarova, N.N. Kolesnikov, and B. Keimer, Science **295**, 1045 (2002).
- [124] Y. Sidis, S. Pailhès, B. Keimer, P. Bourges, C. Ulrich, and L.P. Regnault, phys. stat. sol. **241**, 1204 (2004).
- [125] M.R. Norman and C. Pépin, Rep. Prog. Phys. **66**, 1547 (2003).
- [126] E. Demler and S.C. Zhang, Nature **396**, 733 (1998).
- [127] S. Meixner, W. Hanke, E. Demler, and S.-C. Zhang, Phys. Rev. Lett. **79**, 4902 (1997).
- [128] E. Demler, W. Hanke, and S.-C. Zhang, cond-mat/0405038.
- [129] J.M. Tranquada, H. Woo, T.G. Perring, H. Goka, G.D. Gu, G. Xu, M. Fujita, and K. Yamada, Nature **429**, 534 (2004).
- [130] G.S. Uhrig, K.P. Schmidt and M. Grüninger, cond-mat/0402659.
- [131] G.S. Uhrig, K.P. Schmidt and M. Grüninger, submitted to Jour. of Magn. and Magn. Mat.
- [132] M. Vojta and T. Ulbricht, Phys. Rev. Lett. **93**, 127002 (2004).
- [133] F. Krüger and S. Scheidl, Phys. Rev. B **67**, 134512 (2003).
- [134] G. Seibold and J. Lorenzana, cond-mat/0406589. Phys. Rev. B **69**, 134513 (2004)
- [135] F.J. Wegner, Ann. Physik **3**, 77 (1994).
- [136] S.D. Glazek and K.G. Wilson, Phys. Rev. D **48**, 5863 (1993).
- [137] S.D. Glazek and K.G. Wilson, Phys. Rev. D **49**, 4214 (1994).
- [138] S. Dusuel and G.S. Uhrig, J. Phys. A: Math. Gen. **37**, 9275 (2004).
- [139] F.J. Wegner, Physics Reports **348**, 77 (2001).
- [140] K.G. Wilson, Rev. Mod. Phys. **47**, 773 (1975).
- [141] A. Mielke, Eur. Phys. J. B **5**, 605 (1998).
- [142] G.S. Uhrig and B. Normand, Phys. Rev. B **58**, R14705 (1998).
- [143] C. Knetter and G.S. Uhrig, Eur. Phys. J. B **13**, 209 (2000).
- [144] J. Stein, J. Stat. Phys. **88**, 487 (1997).
- [145] J. Stein, Eur. Phys. J. B **5**, 193 (1998).
- [146] S. Kehrein and A. Mielke, J. Phys. A: Math. Gen. **27**, 4259, corrigendum 5705 (1994).
- [147] S. Kehrein and A. Mielke, Ann. d. Physik **252**, 1 (1996).
- [148] S. Kehrein, A. Mielke, and P. Neu, Z. f. Physik B **99**, 269 (1996).
- [149] S. Kehrein, A. Mielke, Phys. Lett. A **219**, 313 (1996).

- [150] S. Kleff, S. Kehrein, and J. von Delft, cond-mat/0302357.
- [151] T. Stauber and A. Mielke, Phys. Lett. A **219**, 313 (1996).
- [152] T. Stauber and A. Mielke, Phys. Lett. A **305**, 275 (2002).
- [153] T. Stauber, Phys. Rev. B **68**, 125102 (2003).
- [154] T. Stauber and F. Guinea, Phys. Rev. B **69**, 035301 (2004).
- [155] S.K. Kehrein and A. Mielke, Ann. Physik **6**, 90 (1997).
- [156] S.K. Kehrein and A. Mielke, J. Stat. Phys. **90**, 889 (1998).
- [157] P. Lenz and F. Wegner, Nucl. Phys. B **482**, 693 (1996).
- [158] M. Ragwitz and F. Wegner, Eur. Phys. J. B **8**, 9 (1999).
- [159] S. Sykora, A. Hübsch, K.W. Becker, G. Wellein, and H. Fehske, cond-mat/0402184.
- [160] I. Grote, E. Koerding, and F.J. Wegner, J. Low Temp. Phys. **126**, 1385 (2002).
- [161] A. Reischl, E. Müller-Hartmann, and G.S. Uhrig, cond-mat/040102.
- [162] V. Hankevych, I. Grote, and F.J. Wegner, Phys. Rev. B **66**, 094516 (2002).
- [163] F.J. Wegner and V. Hankevych, Acta Physica Polonica B **34**, 497 (2003).
- [164] V. Hankevych and F.J. Wegner, Eur. Phys. J. B **31**, 333 (2003).
- [165] C.P. Heidbrink and G.S. Uhrig, Phys. Rev. Lett. **88**, 146401 (2002).
- [166] C.P. Heidbrink and G.S. Uhrig, Eur. Phys. J. B **30**, 443 (2002).
- [167] S. Kehrein, Phys. Rev. Lett. **83**, 4914 (1999).
- [168] S. Kehrein, Nucl. Phys. B **592**, 512 (2001).
- [169] K.W. Becker, A. Hübsch and T. Sommer, Phys. Rev. B **66**, 235115 (2002).
- [170] A. Hübsch and K.W. Becker, Eur. Phys. J. B **33**, 391 (2003).
- [171] C. Knetter, K.P. Schmidt, and G.S. Uhrig, J. Phys.: Condens. Matter **36**, 7889 (2003).
- [172] C. Knetter, K.P. Schmidt, and G.S. Uhrig, Eur. Phys. J. B **36**, 525 (2004).
- [173] L.D. Landau and E.M. Lifshitz, Statistical Physics (Pergamon, Oxford, 1980).
- [174] A.A. Abrikosov, L.P. Gor'kov and I.Y. Dzyaloshinskii, Quantum Field Theoretical Methods in Statistical Physics, (Pergamon Press, Oxford, 1965).
- [175] M.P. Gelfand and R.R.P. Singh, Adv. Phys. **49**, 93 (2000).
- [176] C. Knetter, A. Bühler, E. Müller-Hartmann, and G.S. Uhrig, Phys. Rev. Lett. **85**, 3958 (2000).
- [177] S. Trebst, H. Monien, C.J. Hamer, Z. Weihong, and R.R.P. Singh, Phys. Rev. Lett. **85**, 4373 (2000).
- [178] S.R. White, J. Chem. Phys. **117**, 7472 (2002).
- [179] C. Knetter, K.P. Schmidt, M. Grüninger, and G.S. Uhrig, Phys. Rev. Lett. **87**, 167204 (2001).
- [180] K.P. Schmidt, C. Knetter, and G.S. Uhrig, Europhys. Lett. **56**, 877 (2001).
- [181] W. Zheng, C.J. Hamer, R.R.P. Singh, S. Trebst, and H. Monien, Phys. Rev. B **63**, 144410 (2001).
- [182] M.P. Gelfand, R.R.P. Singh, and D.A. Huse, J. Stat. Phys. **59**, 1093 (1990).
- [183] M.P. Gelfand, Solid State Commun. **98**, 11 (1996).
- [184] W. Zheng, C.J. Hamer, R.R.P. Singh, S. Trebst, and H. Monien, Phys. Rev. B **63**, 144411 (2001).



- [185] S. Miyahara and K. Ueda, Phys. Rev. Lett. **82**, 3701 (1999).
- [186] R.R.P. Singh and Z. Weihong, Phys. Rev. B **59**, 9911 (1999).
- [187] W. Zheng, C.J. Hamer, and R.R.P. Singh, Phys. Rev. Lett. **91**, 037206 (2003).
- [188] C. Knetter, K.P. Schmidt, and G.S. Uhrig, Physica B **312-313**, 527 (2002).
- [189] M. Grüninger, M. Windt, T. Nunner, C. Knetter, K.P. Schmidt, G.S. Uhrig, T. Kopp, A. Freimuth, U. Ammerahl, B. Büchner und A. Revcolevschi, J. Phys. Chem. Solids **63**, 2167 (2002).
- [190] C. Knetter, E. Müller-Hartmann, and G.S. Uhrig, J. Phys.: Condens. Matter **12**, 9069 (2000).
- [191] E. Müller-Hartmann, R.R.P. Singh, C. Knetter, and G.S. Uhrig, Phys. Rev. Lett. **84**, 1808 (2000).
- [192] C. Knetter and G.S. Uhrig, Phys. Rev. B **63**, 94401 (2001).
- [193] W. Brenig and A. Honecker, Phys. Rev. B **65**, 140407 (2002).
- [194] W. Brenig, Phys. Rev. B **67**, 064402 (2003).
- [195] W. Brenig and M. Grzeschik, Phys. Rev. B **69**, 064420 (2004).
- [196] The coefficients  $C(\underline{m})$  and  $\tilde{C}(\underline{m})$  will be published on the web-pages [www.thp.uni-koeln.de/~gu](http://www.thp.uni-koeln.de/~gu) and [www.thp.uni-koeln.de/~ck](http://www.thp.uni-koeln.de/~ck).
- [197] O.P. Sushkov and V.N. Kotov, Phys. Rev. Lett. **81**, 1941 (1998).
- [198] V.N. Kotov, O.P. Sushkov, and R. Eder, Phys. Rev. B **59**, 6266 (1999).
- [199] R. Zwanzig, in *Lectures in Theoretical Physics*, edited by W.E. Brittin, B.W. Downs, and J. Downs (Interscience, New York, 1961), Vol III.
- [200] H. Mori, Prog. Theor. Phys. **34**, 399 (1965).
- [201] E.R. Gagliano and C.A. Balseiro, Phys. Rev. Lett. **26**, 2999 (1987).
- [202] D.G. Pettifor and D.L. Weaire, *The Recursion Method and its Applications*, Vol. 58 of *Springer Series in Solid State Science* (D.G. Pettifor and D.L. Weaire, Berlin, 1985).
- [203] V.S. Viswanath and G. Müller, *The Recursion Method: Application to Many-Body Dynamics*, Vol.m23 of *Lecture Notes in Physics* (Springer-Verlag, Berlin, 1994).
- [204] J. Stoer and R. Bulirsch, *Numerische Mathematik 2* (Springer-Verlag, Berlin, 1973).
- [205] A.C. Guttman, in "Phase Transitions and Critical Phenomena", Vol. 13 ed. C. Domb and J. Lebowitz (New York, Academic, 1989).
- [206] P.M. Stevenson, Phys. Rev. D **23**, 2916 (1981).
- [207] B.G. Nickel and B. Sharpe, J. Phys. A **12**, 1835 (1979)
- [208] K.P. Schmidt, C. Knetter, and G.S. Uhrig, Acta Physica Polonica B **34**, 1481 (2003).
- [209] K.P. Schmidt, H. Monien, and G.S. Uhrig, Phys. Rev. B **67**, 184413 (2003).
- [210] B. Bernu and G. Misguich, Phys. Rev. B **63**, 134409 (2001)
- [211] A. Bühler, U. Löw, K.P. Schmidt und G.S. Uhrig, Phys.Rev. B **67**, 134428 (2003)
- [212] C. Bender and T. Wu, Phys. Rev. **184**, 1231 (1969).
- [213] M. Hase, I. Terasaki, and K. Uchinokura, Phys. Rev. Lett. **70**, 3651 (1993).
- [214] M. Nishi, O. Fujita, and J. Akimitsu, Phys. Rev. B **50**, 6508 (1994).
- [215] J. Riera and A. Dobry, Phys. Rev. B **51**, 16098 (1995).
- [216] G. Castilla, S. Chakravarty, and V.J. Emery, Phys. Rev. Lett. **75**, 1823 (1995).

- [217] A.W. Garrett, S.E. Nagler, D.A. Tennant, B.C. Sales, and T. Barnes, Phys. Rev. Lett. **79**, 745 (1997).
- [218] G. Chaboussant, P.A. Crowell, L.P. Lévy, O. Piovesana, A. Madouri and D. Mailly, Phys. Rev. B **55**, 3046 (1997).
- [219] G. Xu, C. Broholm, D.H. Reich, and M.A. Adams, Phys. Rev. Lett. **84**, 4465 (2000).
- [220] D.A. Tennant, C. Broholm, D.H. Reich, S.E. Nagler, G.E. Granth, T. Barnes, K. Damle, G. Xu, Y. Chen, and B.C. Sales, Phys. Rev. B **67**, 054414 (2003).
- [221] S.E. Nagler, D.A. Tennant, R.A. Cowley, T.G. Perring, and S.K. Satija, Phys. Rev. B **44**, 12361 (1991).
- [222] T. Ami, M.K. Crawford, and R.L. Harlow, Phys. Rev. B **51**, 5994 (1995).
- [223] N. Motoyama, H. Eisaki, and S. Uchida, Phys. Rev. Lett. **76**, 3212 (1996).
- [224] H. Bethe, Z. Phys. **71**, 205 (1931).
- [225] L. Hulthen, Ark. Mat. Astron. Fys. A **26**, 11 (1938).
- [226] J. des Cloizeaux and M. Gaudin, J. Math. Phys. **7**, 1384 (1996).
- [227] C.N. Yang and C.P. Yang, Phys. Rev. **150**, 321 and 327 (1966).
- [228] R.J. Baxter, *Exactly Solvable Models in Statistical Mechanics* (Academic Press, London, 1982).
- [229] J. des Cloizeaux and J.J. Pearson, Phys. Rev. **128**, 2131 (1962).
- [230] A. Klümper, Z. Phys. B **91**, 507 (1993).
- [231] F.D.M. Haldane, Phys. Rev. Lett **47**, 1840 (1981).
- [232] F.D.M. Haldane, J. Phys. **C14**, 2585 (1981).
- [233] R. Heidenreich, R. Seiler, and U. Uhlenbrock, J. Stat. Phys. **22**, 27 (1980).
- [234] V.E. Korepin, N.M. Bogoliubov, and A.G. Izergin, *Quantum Inverse Scattering Method and Correlation Functions*, p. 63-79 and p. 502-516, Cambridge University Press, 1993 and references therein.
- [235] A.M. Tsvelik, *Quantum Field Theory in Condensed Matter Physics* (Cambridge University Press, Cambridge, 1995).
- [236] J.D. Johnson, B.M. McKoy and C.K. Lai, Phys. Lett. **38A**, 143 (1972).
- [237] J.D. Johnson, S. Krinsky and B.M. McKoy, Phys. Rev. Lett. **29**, 492 (1972).
- [238] J.D. Johnson, S. Krinsky and B.M. McKoy, Phys. Rev. **A8**, 2526 (1972).
- [239] R. Jullien and F.D.M. Haldane, Bull. Am. Phys. Soc. **28**, 344 (1983).
- [240] K. Okamoto and K. Nomura, Phys. Lett. **A169**, 433 (1992).
- [241] S. Eggert, Phys. Rev. B **54**, R9612 (1996).
- [242] C.K. Majumdar and D.K. Ghosh, J. Math. Phys. **10**, 1388 (1969).
- [243] C.K. Majumdar and D.K. Ghosh, J. Math. Phys. **10**, 1399 (1969).
- [244] P.M. van den Broek, Phys. Lett. **77A**, 261 (1980).
- [245] F.D.M. Haldane, Phys. Rev. B **25**, 4925 (1982).
- [246] B.S. Shastri and B. Sutherland, Phys. Rev. Lett. **47**, 964 (1981).
- [247] K.P. Schmidt, C. Knetter and G.S. Uhrig, Phys. Rev. B **69**, 104417 (2004)
- [248] R. Chitra, S. Pati, H.R. Krishnamurthy, D. Sen, and S. Ramasesha, Phys. Rev. B **52**, 6581 (1995).

- [249] A. Luther and I. Peschel, Phys. Rev. B **12**, 3908 (1975).
- [250] F.D.M. Haldane, Phys. Rev. Lett. **45**, 1358 (1980).
- [251] G.S. Uhrig and H.J. Schulz, Phys. Rev. B **54**, R9624 (1996); **58**, 2900(E) (1998).
- [252] A.O. Gogolin, A.A. Nersisyan, and A.M. Tsvelik, *Bosonization and Strongly Correlated Systems* (Cambridge University Press, Cambridge, UK, 1998).
- [253] S. Sachdev and R.N. Bhatt, Phys. Rev. B **41**, 9323 (1990).
- [254] I. Affleck, in *Dynamical Properties of Unconventional Magnetic Systems*, Vol. 349 of *NATO SCIENCE SERIES E: Applied Sciences*, edited by A.T. Skjeltorp and D. Sherrington (Kluwer Academic Publishers, Dordrecht, 1998).
- [255] A. Fledderjohann and C. Gros, Europhys. Lett. **37**, 189 (1997).
- [256] H. Bergknoff and H.B. Thacker, Phys. Rev. D **19**, 3666 (1979).
- [257] G. Bouzerar, A.P. Kampf, and G.I. Japaridze, Phys. Rev. B **58**, 3117 (1998).
- [258] P. Shevchenko, V.N. Kotov, and O.P. Sushkov, Phys. Rev. B **60**, 3309 (1999).
- [259] T. Barnes, J. Riera, and D.A. Tennant, Phys. Rev. B **59**, 11384 (1999).
- [260] P. Jordan and E. Wigner, Z.Phys. **47**, 42 (1928).
- [261] I. Affleck, Nucl. Phys. B **265**, 409 (1986).
- [262] I. Affleck and F.D.M. Haldane, Phys. Rev. B **36**, 5291 (1987).
- [263] G.S. Uhrig and M. Grüninger, Physik-Journal 1, 41 (2003).
- [264] S.R. White and I. Affleck, Phys. Rev. B **54**, 9862 (1996).
- [265] R. Chitra and T. Giamarchi, Phys. Rev. B **55**, 5816 (1997).
- [266] M.C. Cross and D.S. Fisher, Phys. Rev. B **19**, 402 (1979).
- [267] J.L. Black and V.J. Emery, Phys. Rev. B **23**, 429 (1981).
- [268] R.F. Dashen, B. Hasslacher, and A. Neveu, Phys. Rev. D **10**, 4114 (1974).
- [269] R.F. Dashen, B. Hasslacher, and A. Neveu, Phys. Rev. D **10**, 4130 (1974).
- [270] R.F. Dashen, B. Hasslacher, and A. Neveu, Phys. Rev. D **10**, 4138 (1974).
- [271] R.F. Dashen, B. Hasslacher, and A. Neveu, Phys. Rev. D **11**, 3424 (1975).
- [272] M. Karbach, G. Müller, A.H. Bougourzi, A. Fledderjohann and K.H. Mütter, Phys. Rev. B **55**, 12510 (1997).
- [273] A.H. Bougourzi, Mod. Phys. Lett. B **10**, 1237 (1996).
- [274] A. Abada, A.H. Bougourzi, and B. Si-Lakhal, Nucl. Phys. B **497**, 733 (1997).
- [275] A. Abada, A.H. Bougourzi, B. Si-Lakhal, and S. Seba, cond-mat/9802271.
- [276] B. Si-Lakhal and A. Abada, J. Phys. A: Math. Gen. **37**, 497 (2004).
- [277] J. Lorenzana and G.A. Sawatzky, Phys. Rev. Lett. **74**, 1867 (1995).
- [278] J. Lorenzana and G.A. Sawatzky, Phys. Rev. B **52**, 9576 (1995).
- [279] I. Affleck, in *Fields, Strings and Critical Phenomena* (Elsevier, North-Holland, Amsterdam, 1990), p. 566.
- [280] J. Voit, Rep. Prog. Phys. **58**, 977 (1995).

- [281] A. Luther and I. Peschel, Phys. Rev. B **9**, 2911 (1974).
- [282] C.J. Hamer, W. Zheng, and R.R.P. Singh, Phys. Rev. B **68**, 214408 (2003).
- [283] T. Papenbrock, T. Barnes, D.J. Dean, M.V. Stoitsov, and M.R. Strayer, Phys. Rev. B **68**, 024416 (2003).
- [284] M. Müller, H.-J. Mikeska, and N. Cavadini, J. Phys.: Condens. Matter **15**, 8513 (2003).
- [285] K. Fabricius and U. Löw, Phys. Rev. B **57**, 13371 (1998).
- [286] W.J. Caspers and W. Magnus, Phys. Lett. **88A**, 103 (1982).
- [287] W.J. Caspers, K.M. Emmett, and W. Magnus, J. Phys. A: Math. Gen. **88A**, 103 (1982).
- [288] F.A. Smirnov, *Form Factors in Completely Integrable Models of Quantum Field Theory* (World Scientific, Singapore, 1992).
- [289] R.F. Dashen, B. Hasslacher, and A. Neveu, Phys. Rev. D **12**, 2443 (1975).
- [290] T. Nakano and H. Fukuyama, J. Phys. Soc. Jpn. **49**, 1679 (1980).
- [291] T. Nakano and H. Fukuyama, J. Phys. Soc. Jpn. **50**, 2489 (1981).
- [292] G.S. Uhrig, Habilitation 1999, [www.thp.Uni-Koeln.DE/gu/veroeffentlichungen.html](http://www.thp.Uni-Koeln.DE/gu/veroeffentlichungen.html)
- [293] I. Affleck, D. Gepner, H.J. Schulz, and T. Ziman, J. Phys. A: Math. Gen. **22**, 511 (1989); corr. **23**, 4725 (1990).
- [294] E. Müller-Hartman and G.S. Uhrig, unpublished.
- [295] P.A. Fleury and R. Loudon, Phys. Rev. **166**, 514 (1968).
- [296] B.S. Shastry and B.I. Shraiman, Phys. Rev. Lett. **65**, 1068 (1990).
- [297] J. Lorenzana and R. Eder, Phys. Rev. B **55**, R3358 (1997).
- [298] M. Windt, M. Grüninger, T. Nunner, C. Knetter, K.P. Schmidt, G.S. Uhrig, T. Kopp, A. Freimuth, U. Ammerahl, B. Büchner, and A. Revcolevschi, Phys. Rev. Lett. **87**, 127002 (2001).
- [299] H. Suzuura, H. Yasuhara, A. Furusaki, N. Nagaosa, and Y. Tokura, Phys. Rev. Lett. **76**, 2579 (1996).
- [300] E. Dagotto and T.M. Rice, Science **271**, 618 (1996).
- [301] E. Dagotto, J. Riera and D.J. Scalapino, Phys. Rev. B **45**, 5744 (1992).
- [302] R. Hirsch, thesis, Universität Köln (1988).
- [303] E. Dagotto and A. Moreo, Phys. Rev. B **38**, 5087 (1988).
- [304] T. Barnes, E. Dagotto, J. Riera and E.S. Swanson, *ibid.* **47**, 3196 (1993).
- [305] D.G. Shelton, A.A. Nersisyan and A.M. Tsvelik, Phys. Rev. B **53**, 8521 (1996).
- [306] Y. Ueda and M. Isobe, J. Magn. Magn. Mater. **177**, 741 (1998).
- [307] Z. Hiroi, M. Azuma, M. Takano and Y. Bando, J. Solid State Chem. **95**, 230 0.22640(1991).
- [308] M. Uehara, T. Nagata, J. Akimitsu, H. Takahashi, N. Mori and K. Kinoshita, J. Phys. Soc. Jpn. **65**, 2764 (1996).
- [309] J.B. Goodenough, Phys. Rev. **100**, 564 (1955).
- [310] J. Kanamori, J. Phys. Chem. Solids **10**, 87 (1959).
- [311] E.M. McCarron, M.A. Subramanian, J.C. Calabrese and R.L. Harlow, Mater. Res. Bull. **23**, 1355 (1988).

- [312] T. Siegrist, L.F. Schneemeyer, S.A. Sunshine, J.V. Waszczak and R.S. Roth, *Mater. Res. Bull.* **23**, 1429 (1988).
- [313] H. Iwase, M. Isobe, Y. Ueda and H. Yasuoka, *J. Phys. Soc. Jpn.* **65**, 2397 (1996).
- [314] M. Onoda and N. Nishiguchi, *J. Solid. State. Chem.* **127**, 359 (1996).
- [315] D.C. Johnston, M. Troyer, S. Miyahara, D. Lidsky, K. Ueda, M. Azuma, Z. Hiroi, M. Takano, M. Isobe, Y. Ueda, M.A. Korotin, V.I. Anisimov, A.V. Mahajan, and L.L. Miller, *cond-mat/0001147* .
- [316] A. Löffert, C. Cross and W. Assmus, *J. Crust. Growth* **237-239** (1), 796 (2002).
- [317] A. Gößling, U. Kuhlmann, C. Thomsen, A. Löffert, C. Cross and W. Assmus, *Phys. Rev. B* **67**, 052403 (2003).
- [318] N. Nücker, M. Merz, C.A. Kuntscher, S. Gerhold, S. Schuppler, R. Neubert, M.S. Golden, J. Fink, D. Schild, S. Stadler, V. Chakarian, J. Freeland, Y.U. Idzerda, K. Conder, M. Uehara, T. Nagata, J. Goto, J. Akimitsu, M. Motoyama, H. Eisaki, S. Uchida, U. Ammerahl and A. Revcolevschi, *Phys. Rev. B* **62**, 14384 (2000).
- [319] Y. Mizuno, T. Tohyama and S. Maekawa, *J. Phys. Soc. Jpn* **66**, 397 (1997).
- [320] W.H. Zheng, V. Kotov, and J. Oitmaa, *Phys. Rev. B* **57**, 11439 (1998).
- [321] A.A. Nersesyan and A.M. Tselik, *Phys. Rev. Lett.* **78**, 3939 (1997).
- [322] J. Oitmaa, R.R.P. Singh and Z. Weihong, *Phys. Rev. B* **54**, 1009 (1996).
- [323] S. Brehmer, H.-J. Mikeska, M. Müller, N. Nagaosa and S. Uchida, *Phys. Rev. B* **60**, 329 (1999).
- [324] T.S. Nunner, P. Brune, T. Kopp, M. Windt, and M. Grüninger, *Phys. Rev. B* **66**, 180404 (2002)
- [325] K. Damle and S. Sachdev, *Phys. Rev. B* **57**, 8307 (1998).
- [326] A. Reischl, K.P. Schmidt and G.S. Uhrig, in preparation.
- [327] S. Kirschner, diploma thesis, Univ. of Cologne (2004).
- [328] N. Haga and S. Suga, *Phys. Rev. B.* **66**, 132415 (2002).
- [329] P. A. M. Dirac, *Proc. Roy. Soc. A* **123**, 714 (1929).
- [330] D. J. Thouless, *Proc. Phys. Soc.* **86**, 893 (1965).
- [331] M. Roger, J. H. Heatherington and J. M. Delrieu, *Rev. Mod. Phys.* **55**, 1 (1983).
- [332] H. J. Schmidt and Y. Kuramoto, *Physica B* **163**, 443 (1990).
- [333] Y. Mizuno, T. Tohyama And S. Maekawa, *J. Low Temp. Ph.* **117**, 389 (1999).
- [334] M. Müller, T. Vekua and H.-J. Mikeska, *Phys. Rev. B* **66**, 134423 (2002).
- [335] R. S. Eccleston, M. Uehara, J. Akimitsu, H. Eisaki, N. Motoyama and S. Uchida, *Phys. Rev. Lett.* **81**, 1702 (1998).
- [336] S. Brehmer, H.J. Mikeska, M. Müller, N. Nagaosa and S. Uchida, *Phys. Rev. B* **60**, 329 (1999).
- [337] M. Matsuda, K. Katsumata, R.S. Eccleston, S. Brehmer and H.J. Mikeska, *J. Appl. Phys.* **87**, 6271 (2000).
- [338] K.P. Schmidt, C. Knetter, M. Grüninger, and G.S. Uhrig, *Phys. Rev. Lett.* **90**, 167201 (2003).
- [339] A. Läuchli, G. Schmid and M. Troyer, *Phys. Rev. B* **67** 100409(R) (2003).
- [340] T. Hikihara, T. Momoi and X. Hu, *Phys. Rev. Lett.* **90**, 087204 (2003).
- [341] T. Momoi, T. Hikihara, M. Nakamura and X. Hu, *Phys. Rev. B* **67**, 174410 (2003).

- [342] V. Gritsev, B. Normand and D. Baeriswyl, Phys. Rev. B **69**, 094431 (2004) .
- [343] Y. Honda and T. Horiguchi, cond-mat/0106426.
- [344] K. Hiji and K. Nomura, Phys. Rev. B **65** (1), 104413 (2002).
- [345] M. Greven, R.J. Birgeneau, and U.-J. Wiese, Phys. Rev. Lett. **77**, 1865 (1996).
- [346] A. Bühler, Doktorarbeit, Universität zu Köln (2003).
- [347] P.J. Freitas and R.R.P. Singh, Phys. Rev. B **62** 14113 (2000).
- [348] C. Jurecka, V. Grützun, A. Friedrich and W. Brenig, Eur. Phys. J. B **21** 469 (2001).
- [349] S. Sugai and M. Suzuki, Phys. Status Solidi B **215** 653 (1999).
- [350] C. Jurecka and W. Brenig, Phys. Rev. B **61**, 14307 (2000).
- [351] T.S. Nunner, P. Brune, T. Kopp, M. Windt, and M. Grüninger Acta Physica Polonica B 34, 1545 (2003).
- [352] U. Ammerahl and A. Revcolevschi, J. Crystal Growth **197**, 825 (1999); U. Ammerahl, PhD thesis, Univ. of Cologne, 2000.
- [353] M. Matsuda, K. Katsumata, R.S. Eccleston, S. Brehmer and H.-J. Mikeska, Phys. Rev. B **62**, 8903 (2000).
- [354] A. Frost-Jensen, V. Petříček, F. Krebs-Larsen, and E.M. McCarron III, Acta Cryst. **B53**, 125 (1997).
- [355] L.P. Regnault, J.P. Boucher, H. Moudden, J.E. Lorenzo, A. Hiess, U. Ammerahl, G. Dhalenne, and A. Revcolevschi, Phys. Rev. B **59**, 1055 (1999).
- [356] M. Matsuda, T. Yoshizawa, K. Kakurai, and G. Shirane, Phys. Rev. B **59**, 1060 (1999).
- [357] T. Fukuda, J. Mizuki, and M. Matsuda, Phys. Rev. B **66**, 012104 (2002).
- [358] M. Braden, private communication.
- [359] A. Gozar, G. Blumberg, B.S. Dennis, B.S. Shastry, N. Motoyama, H. Eisaki, and S. Uchida, Phys. Rev. Lett. **87**, 197202 (2001).
- [360] M. Windt, PHD thesis, University of Cologne (2003).
- [361] B. Gorshunov, P. Haas, T. Rößler, M. Dressel, T. Vuletić, B. Korin-Hamzić, S. Tomić, J. Akimitsu, and T. Nagata, Phys. Rev. B **66**, 060508(R) (2002).
- [362] A. Gozar, G. Blumberg, P.B. Littlewood, B.S. Dennis, N. Motoyama, H. Eisaki, and S. Uchida, Phys. Rev. Lett. **91**, 087401 (2003).
- [363] M.v. Zimmermann, J. Geck, S. Kiele, R. Klingeler, and B. Büchner, cond-mat/0406215.

## List of publications

- M. Windt, M. Grüninger, T. Nunner, C. Knetter, K.P. Schmidt, G.S. Uhrig, T. Kopp, A. Freimuth, U. Ammerahl, B. Büchner und A. Revcolevschi, Observation of two-magnon bound state in the two-leg ladders of  $(Ca, La)_{14}Cu_{24}O_{41}$ , *Phys.Rev.Lett.* **87**, 127002 (2001)
- C. Knetter, K.P. Schmidt, M. Grüninger und G.S. Uhrig, Fractional and integer excitations in quantum antiferromagnetic spin 1/2 ladders, *Phys.Rev.Lett.* **87**, 167204 (2001)
- K.P. Schmidt, C. Knetter und G.S. Uhrig, Raman response in antiferromagnetic spin 1/2 ladders, *Europhys.Lett.* **56**, 877 (2001)
- C. Knetter, K.P. Schmidt und G.S. Uhrig, Multi-particle excitations and spectral densities in quantum spin-systems, *Physica B* **312**, 527 (2002)
- M. Grüninger, M. Windt, T. Nunner, C. Knetter, K.P. Schmidt, G.S. Uhrig, T. Kopp, A. Freimuth, U. Ammerahl, B. Büchner und A. Revcolevschi, Optical spectroscopy of  $(Ca, La)_{14}Cu_{24}O_{41}$  spin ladders: comparison of experiment and theory, *Physica B* **312**, 617 (2002)
- M. Grüninger, M. Windt, T. Nunner, C. Knetter, K.P. Schmidt, G.S. Uhrig, T. Kopp, A. Freimuth, U. Ammerahl, B. Büchner und A. Revcolevschi, Magnetic excitations in two-leg spin 1/2 ladders: experiment and theory, *J. Phys. Chem. Solids* **63**, 2167 (2002)
- K.P. Schmidt, C. Knetter und G.S. Uhrig, Novel Extrapolation for Strong Coupling Expansions, *Acta Physica Polonica B* **34**, 1481 (2003)
- K.P. Schmidt, C. Knetter, M. Grüninger und G.S. Uhrig, Charge order induced Raman peak in  $Sr_{14}Cu_{24}O_{41}$ , *Phys.Rev.Lett.* **90**, 167201 (2003)
- A. Bühler, U. Löw, K.P. Schmidt und G.S. Uhrig, Thermodynamic Properties of Spin Ladders with Cyclic Exchange, *Phys.Rev. B* **67**, 134428 (2003)
- K.P. Schmidt, H. Monien und G.S. Uhrig, Rung-singlet phase of the  $S=1/2$  two-leg spin-ladder with four-spin cyclic exchange, *Phys.Rev. B* **67**, 184413 (2003)
- K.P. Schmidt und G.S. Uhrig, Excitations in one-dimensional  $S=1/2$  quantum antiferromagnets, *Phys.Rev.Lett.* **90**, 227204 (2003)
- C. Knetter, K.P.Schmidt und G.S. Uhrig, The Structure of effective Hamiltonians and Observables Obtained by Continuous Unitary Transformation, *J. Phys. A: Math. Gen.* **36**, 7889 (2003)
- M. Grueninger, M. Windt, E. Benckiser, T.S.Nunner, K.P. Schmidt, G.S. Uhrig und T. Kopp, Optical Spectroscopy of Low-Dimensional Quantum Spin Systems, *Adv.Sol.Stat.Phys.* **43**, 95-112 (2003)
- K.P. Schmidt, C. Knetter und G.S. Uhrig, Spectral properties of the dimerized and frustrated spin chain, *Phys.Rev. B* **69**, 104417 (2004)
- C. Knetter, K.P. Schmidt and G.S. Uhrig, High Order Perturbation Theory for Spectral Densities of Multi-Particle Excitations:  $S=1/2$  Two-Leg Heisenberg Ladder, *Eur. Phys. J. B* **36**, 525 (2004)





## Danksagungen

Mein besonderer Dank gilt Herrn Priv.-Doz. Dr. Götz S. Uhrig für die Vergabe sowie die intensive Betreuung der vorliegenden Arbeit. Unzählige Gespräche und Diskussionen bilden die Grundlage für die gewonnenen Erkenntnisse. Eine in dieser Art stattfindende Arbeitsatmosphäre wünsche ich mir auch für die Zukunft.

Desweiteren bedanke ich mich bei Herrn Prof. Dr. E. Müller-Hartmann für die konstruktive und kritische Begleitung meiner Arbeit insbesondere während der Mitarbeiterseminare. Herrn Prof. Dr. B. Mühlshlegel gilt mein Dank für den unterstützenden und motivierenden Einfluss.

Ein besondere Dank gilt Dr. Markus Grüninger für unzählige Ideen und Gespräche, die mir insbesondere die experimentelle Sicht näher gebracht haben und zu einem großen Verständnisgewinn geführt haben.

Bedanken möchte ich mich auch bei Prof. Dr. M. Braden und bei Prof. Dr. F. Mila für die Begutachtung meiner Arbeit. Prof. Dr. A. Freimuth gilt ein Dank für die Übernahme des Prüfungsvorsitzes. Bei Alexander Reischl, Alexander Bühler, Christian Knetter, Sebastian Kirschner und Sébastien Dusuel bedanke ich mich für die produktive und schöne Stimmung im Büro 110. Ein besonderer Dank gilt auch Carsten Raas und Alexander Bühler für die Lösung vieler numerischer und computerorientierter Probleme.

Ein gesonderter Dank gilt Christian Knetter für die effektive und erfolgreiche Zusammenarbeit. Dies ist ein Beispiel dafür, dass die häufig in der Physik nicht praktizierte Teamarbeit sehr nützlich sein kann und eher mehr als weniger eingesetzt werden sollte.

Weiterhin danke ich Alexander Gößling, Marco Windt, Tamara Nunner, Andreas Läuchli, Prof. Dr. Thilo Kopp and Prof. Dr. Hartmut Monien für hilfreiche und fruchtbare Diskussionen.

Meiner Familie danke ich für die durchgehende Unterstützung. Birgit Zhorzel gilt das größte Dankeschön in jeder Hinsicht.



## Zusammenfassung

In dieser Arbeit wird eine perturbative Realisierung Teilchenzahl erhaltender kontinuierlicher Transformationen benutzt, um die energetischen und spektralen Eigenschaften quasi-eindimensionaler Quantenantiferromagnete zu studieren. Die betrachteten Systeme sind auf einem Gitter definiert und erlauben eine perturbative Behandlung. Es wird jeweils ein komplett dimerisierter Ausgangszustand für die Transformation ausgewählt. Der Grundzustand ist der Singulett-Produktzustand und das Anregungsspektrum ist äquidistant. Das zugehörige Energiequant wird Triplon genannt. Die kontinuierliche Transformation führt zu einem effektiven Hamiltonoperator, der die Zahl der Triplonen erhält, und effektiven für das Experiment relevanten Observablen.

Die effektiven Operatoren liegen nach der Transformation als Reihenentwicklung in den Störungsparametern vor. Alle Berechnungen werden auf endlichen Clustern im Ortsraum durchgeführt. Die Resultate werden so im thermodynamischen Limes bestimmt, so dass auf Grund des linked-cluster Theorems die Resultate für  $\infty$ -große Systeme gelten.

Die Ergebnisse sind exakt in der gegebenen Störungsordnung. Um eine verbesserte Darstellung der Ergebnisse zu erhalten, werden Extrapolationstechniken angewendet. Eine detaillierte Beschreibung verschiedener Extrapolationswerkzeuge wie Padé- und DlogPadé-Extrapolation, optimierte Störungstheorie und die Benutzung interner Systemvariablen wird angegeben.

Die dimerisierte und frustrierte Kette wird zuerst besprochen. Die Analyse der spektralen Gewichte bei verschwindender Frustration zeigt, dass sich fast das gesamte spektrale Gewichte im Grenzfall verschwindender Dimerisierung im Zwei-Triplon Kanal befindet. Demnach kann das Triplon neben dem Spinon auch als Elementaranregung des eindimensionalen Heisenberg-Modells benutzt werden. Die Extrapolationen für die spektralen Gewichte bei endlicher Frustration sind schwieriger.

Ein vollständiger Überblick der Ein- und Zwei-Triplon Spektraldichten bei großer und mittlerer Dimerisierung wird angegeben. Die Ergebnisse werden mit feldtheoretischen Resultaten verglichen. Weiterhin wird der Raman response und die optische Leitfähigkeit untersucht.

Die antiferromagnetische zweibeinige Leiter mit zusätzlicher Vier-Spin-Wechselwirkung wird als Zweites untersucht. Die Transformation startet vom Fall isolierte Sprossen. Die Anregungen sind Sprossen-Triplonen. Die Energien der Ein-Triplon-Zustände, der Zwei-Triplon gebundenen Zustände sowie der Multi-Triplon Kontinua wird für diverse Kopplungsverhältnisse angegeben. Optische Observablen werden im Detail untersucht.

Die Ausdehnung der Sprossen-Singulett-Phase wird in der gesamten  $[x, x_{cyc}]$ -Ebene berechnet. Es wird gezeigt, dass sich die experimentellen Realisierungen zweibeiniger Leitern immer in dieser Phase befinden. Das spektrale Gewicht befindet sich hauptsächlich im Ein- und Zwei-Triplon Kanal für die experimentell relevanten Kopplungsverhältnisse. Das Gewicht im Drei- und Vier-Triplon Kanal wird aber nennenswert groß.

Einen Überblick über das aktuelle Verständnis der spektroskopischen Befunde von magnetischen

Anregungen in Kuprat-Leiter-Systemen wird angegeben. Die berechneten Ergebnisse werden mit experimentellen Daten der inelastischen Neutronstreuung, Raman-Spektroskopie und optischer Leitfähigkeit verglichen. Der erste experimentelle Nachweis eines Zwei-Triplon gebundenen Zustandes in zweibeinigen Leitern wird besprochen.

## **Erklärung**

Ich versichere, daß ich die von mir vorgelegte Dissertation selbständig angefertigt, die benutzten Quellen und Hilfsmittel vollständig angegeben und die Stellen der Arbeit - einschließlich Tabellen, Karten und Abbildungen -, die anderen Werken im Wortlaut oder dem Sinn nach entnommen sind, in jedem Einzelfall als Entlehnung kenntlich gemacht habe; daß diese Dissertation noch keiner anderen Fakultät oder Universität zur Prüfung vorgelegen hat; dass sie - abgesehen von unten angegebenen Teilpublikationen - noch nicht veröffentlicht worden ist, sowie, daß ich eine solche Veröffentlichung vor Abschluß des Promotionsverfahrens nicht vornehmen werde. Die Bestimmungen dieser Promotionsordnung sind mir bekannt. Die von mir vorgelegte Dissertation ist von Herrn Privat-Dozent Dr. Götz S. Uhrig betreut worden.



## Lebenslauf

### Persönliche Daten

Name: Kai P. Schmidt  
Geburtsdatum: 13. Juni 1975  
Geburtsort: Neunkirchen  
Familienstand: ledig  
Staatsangehörigkeit: deutsch

### Schulbildung

1981-1985: Kath. Grundschule Viktoriastraße, Troisdorf  
1985-1994: Städt. Gymnasium Troisdorf-Sieglar  
1994: Abitur

### Hochschulstudium

Okt. 1994: Immatrikulation an der Friedrich-Wilhelm Universität Bonn, Studiengang: Physik, Diplom  
Okt. 1995: Immatrikulation an der Friedrich-Wilhelm Universität Bonn, Studiengang: Mathematik, Diplom  
Jun. 1996: Vordiplom Physik  
1997: Stipendium an der University of New South Wales, Sydney, Australien  
Febr. 2000: Abschluß der Diplomarbeit bei Prof. Dr. H. Monien  
Seit März 2000: Anfertigung der vorliegenden Dissertation unter Anleitung von Priv. Doz. Dr. G.S. Uhrig

### Arbeitsverhältnisse

1998-2000: Studentische Hilfskraft am Institut für theoretische Physik der Universität Bonn  
2000: Wissenschaftliche Hilfskraft am Institut für theoretische Physik der Universität zu Köln  
Seit 2001: Wissenschaftlicher Mitarbeiter am Institut für theoretische Physik der Universität zu Köln